Design of Dual-band Reconfigurable Smart Antenna

Hamid Torpi and Yasin Damgacı
Yıldız Technical University, Department of Electronics and Communication Engineering, Turkey

Abstract— This paper presents use of reconfigurable microstrip patch antenna elements in adaptive arrays. Adaptive antenna systems are referred to smart antennas. The combination of both reconfigurability and adaptivity in a single array is investigated in this study. For this purpose a dual-band inset-fed reconfigurable antenna is designed. The switching between the different frequency bands is achieved by using capacitive series RF-MEMS switches. On the second phase of the study, the designed reconfigurable antenna is used as a single element in smart antenna. Four element linear array performance is investigated and simulated.

1. INTRODUCTION

With the tramendous advencement in communication technology followed by ever growing consumer demands the need for multifunctional wireless communication devices is more than ever felt. Currently, different systems work with different standards such like cellular phones, WLAN and satellite communications [1, 2]. These different standards have different requirements. Many of the systems are being designed for to be compatible with more than one of these standards. For this reason they require to design for different RF circuits and antennas.

Reconfigurable antennas have recently received significant attention for their applications in communications, electronic surveillance and countermeasures, by adapting their properties to achieve selectivity in frequency, bandwidth, polarization and gain. In reconfigurable antennas, changing the shape of radiating element is achieved by switching. The switching property allows the user to roam any existing network and have only a single handset to access a great number of services [3].

A smart antenna is an array of antenna elements that is able to change its radiation pattern dynamically for preventing from noise, interference, and multipath fading. A smart antenna has the potential to reduce noise, to increase signal to noise ratio and enhance system capacity. The smart antenna systems can be divided into two categories. These are: switched beam system, and adaptive arrays. In this paper adaptive arrrays are investigated and used for smart antenna model. In adaptive beamforming, the goal is to adapt the beam by adjusting the gain and phase on each antenna element such that a desirable pattern is formed.

In this paper the design of reconfigurable microstrip antenna operating at two different frequency bands will be presented. Frequency bands are chosen as 2.4 GHz and 3.5 GHz which are used in WLAN and WiMAX applications. RF-MEMS switches is used for switching. It is also possible to use PIN diodes as switching element but we preferred MEMS switch for their significant better RF characteristics than conventional PIN diodes or FET switches and consumes less power [4]. Both switches and antenna are designed by simulations on Ansoft HFSS.

The designed reconfigurable antenna is used as a single element in smart antenna. The combination of both reconfigurability and adaptivity in a single array performance is investigated. LMS algorithm is used for this purpose. Four element linear array configuration is investigated and simulations are performed by MATLAB and Ansoft Designer.

2. RECONFIGURABLE MICROSTRIP PATCH ANTENNA DESIGN

The patch antenna was first designed based on the equations from the transmission line model (TLM) approximation [7]. That approximation states that the operating frequency of a patch antenna is given by:

$$f_r = \frac{1}{2(L + \Delta L)\sqrt{\varepsilon_{eff}}\sqrt{\mu_0\varepsilon_0}} \tag{1}$$

where L is the length of the antenna, ε_0 and μ_0 are the free space dielectric permitivity and permeability, ε_{reff} is the effective dielectric permitivity [6]:

$$\varepsilon_{reff} = \frac{\varepsilon_r + 1}{2} + \frac{\varepsilon_r - 1}{2}\left[1 + 12\frac{h}{W}\right]^{\frac{1}{2}} \tag{2}$$

where ε_r and h are the relative dielectric permitivity and thickness of the substrate, and W is thewidth of the patch. Because of fringing effects, the antenna looks larger than its physical dimensions. ΔL takes this effect in account and can be computed from [7]:

$$\Delta L = 0.412h \frac{(\varepsilon_{reff} + 0.3) \cdot (W/h + 0.264)}{(\varepsilon_{reff} - 0.258) \cdot (W/h + 0.8)} \tag{3}$$

The input impedance of the antenna must be matched to the feed line by choosing the correct position for the feeding point. Because the antenna must be fed with the microstrip, the connection to a point inside the metal patch requires the use of an inset.

Using the values given by TLM approximation, parameters for the antenna was calculated for 2.4 GHz and 3.5 GHz bands. The dielectric substrate is chosen to be corning glass ($\varepsilon_r = 5.75$) and substrate width $h = 0.5$ mm is used. To provide dual frequency operation another U-like shaped patch is attached to 3.5 GHz antenna for enlarging the radiating length. (Figure 1) For connecting two patches six capacitive RF-MEMS switches are used. This new antenna resonates at 2.40 GHz (Switch ON) and 3.48 GHz (Switch OFF). RF-MEMS switches designed on the same substrate. The RF-MEMS switches are modelled as two port devices with s-parameter data.

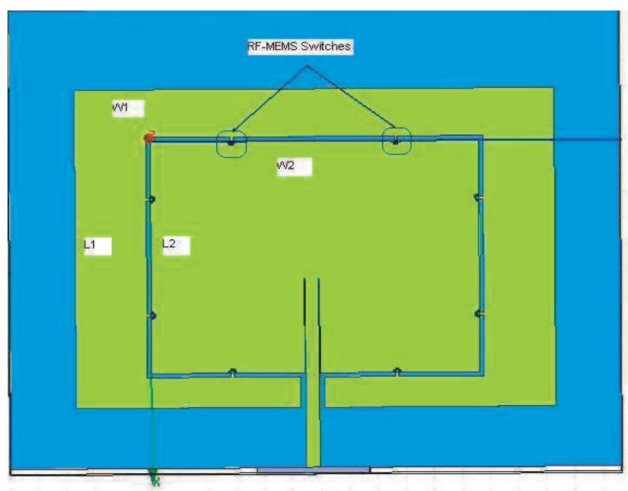

Figure 1: Designed reconfigurable antenna with six RF-MEMS switches. $L1 = 25.9$ mm, $W1 = 34$ mm for 2.4 GHz antenna and $W2 = 23.3$ mm, $L2 = 17.68$ mm for 3.5 Ghz antenna.

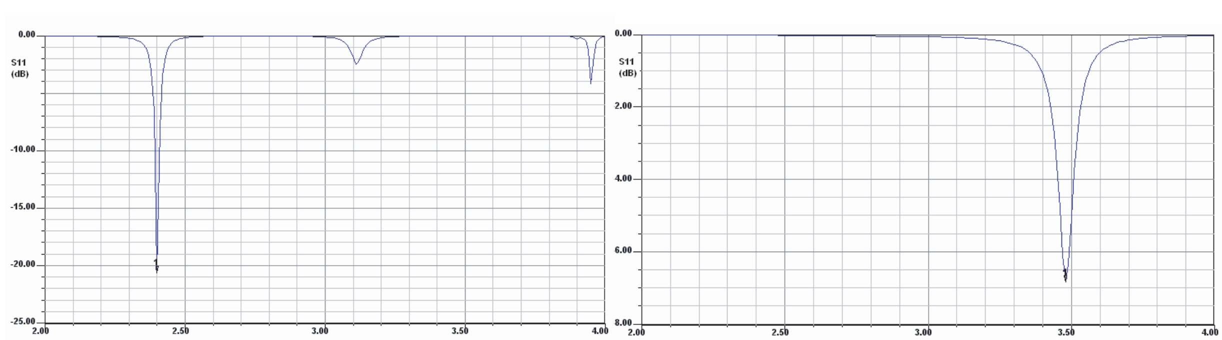

(a) (b)

Figure 2: Return loss of antenna in (a) switches ON position and (b) switches OFF position.

3. ADAPTIVE ANTENNA ARRAY

An adaptive array is an antenna system that can modify its beam pattern or other parameters, by means of internal feedback control while the antenna system is operating. Adaptive arrays are also known as adaptive beam formers or smart antennas. Smart antenna technology can have great effect on many important parameters in the wireless communication. Benefits to be gained are among others in the area of bandwidth, bit rates, interference rejection, power economy, and reliability [8]. The basic idea behind smart antennas is that multiple antennas processed simultaneously allow static or dynamical spatial processing with fixed antenna topology. The pattern of the antenna in its totality is now depending partly on its geometry but even more on the processing of the signals of the antennas individually [9].

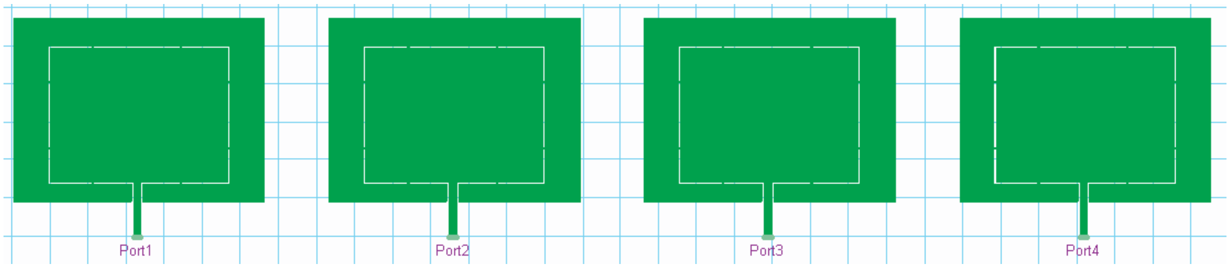

Figure 3: Dual band reconfigurable smart antenna.

Adaptive Beamforming is a technique in which an array of antennas is exploited to achieve maximum reception in a specified direction by estimatng the signal arrival from a desired direction (in the presence of noise) while signals of the same frequency from other directions are rejected. This is achieved by varying the weights of each of the sensors (antennas) used in the array [10]. In adaptive beamforming the optimum weights are iteratively computed using complex algorithms based upon different criteria.

Adaptive algorithms form the heart of the array-processing network. Several algorithms have been developed based on different criteria to compute the complex weights.

The LMS is a low complexity algorithm and can be used here as an example that provides a first insight on how a smart antenna system operates. The LMS algorithm calculates the weights in a time recursive manner [8]. The steps in the derivation are given as follows:

$$\text{output, } y(n) = w^H x(n) \tag{4}$$

$$\text{error, } e(n) = d^* - y(n) \tag{5}$$

$$\text{weights, } w(n+1) = w(n) + \mu x(n) e^*(n) \tag{6}$$

μ is a step size parameter which is related to the rate of convergence; however, convergence of the $w(n)$ is assured by the following condition:

$$0 < \mu < \frac{2}{\lambda_{maks}} \tag{7}$$

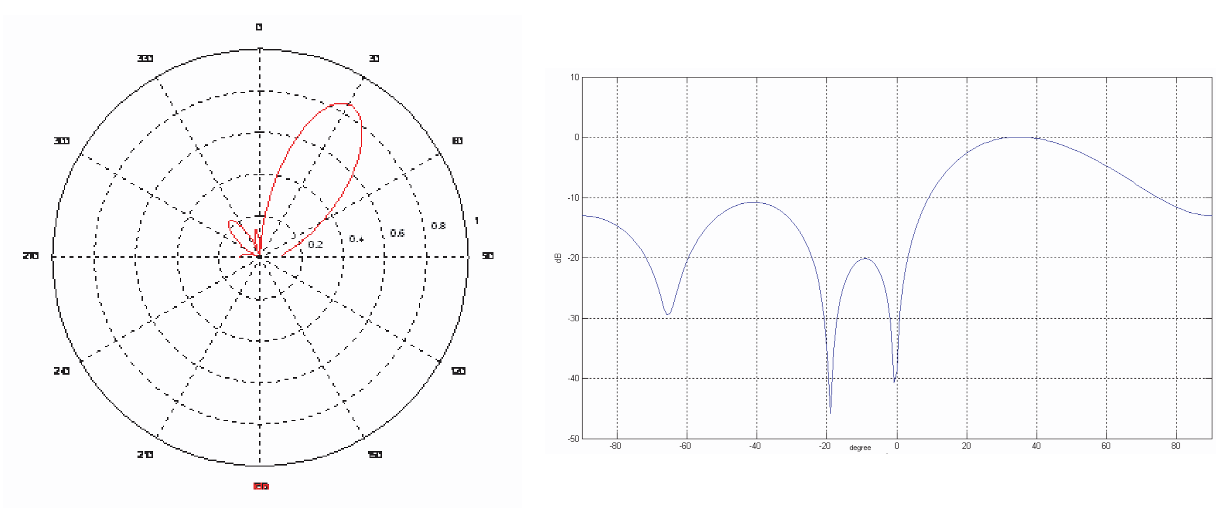

Figure 4: Antenna array gain pattern calculated with MATLAB simulation.

4. SIMULATION RESULTS

An adaptive array is simulated in MATLAB by using the LMS algorithm. When an array of 4 antennas is used with as separation of $\lambda/2$ (λ is wavelength), there is a maximum of 3 nulls that can eliminate the interferer. λ is determined for 2.4 GHz band. The true array output $y(t)$ is converging to the desired signal $d(t)$. The resulting antenna array gain pattern as shown in Figure 4. The interferers are cancelled by placing nulls in the direction of the interferers. The received signal arrives at an angle of 35 degrees, interferers arrives at 0 and -20 degrees and the array response is 0 dB. We have chosen step size = 0.05 for our simulation. After the calculating weights in MATLAB simulation we apply the normalized weights as excitations in the designed reconfigurable antenna array. In both frequencies antenna gains are calculated and results are similar the MATLAB simulation results (Figure 5).

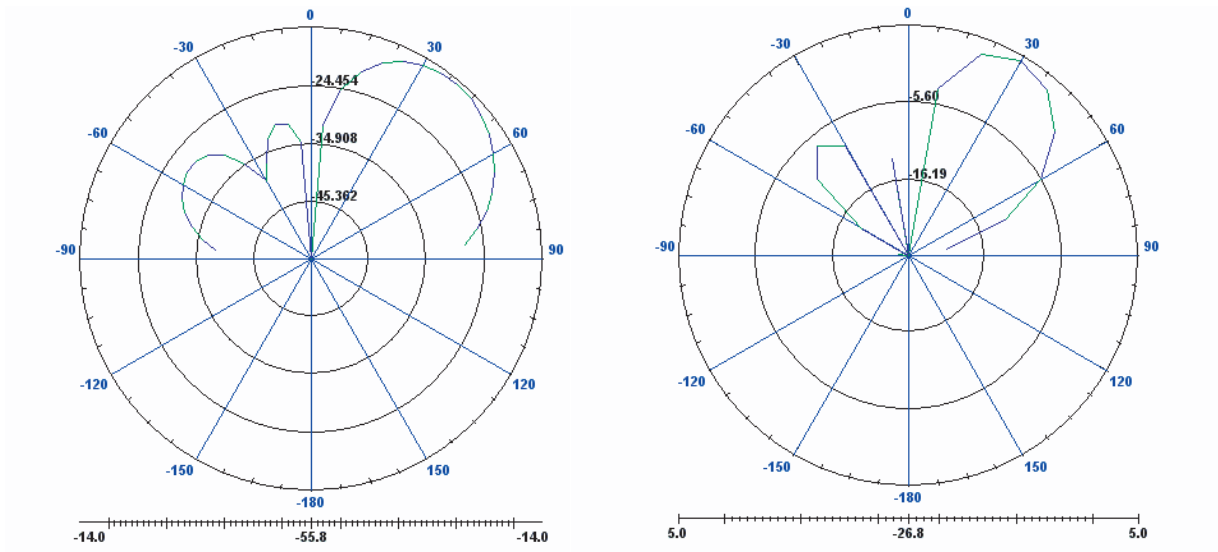

(a) (b)

Figure 5: (a) Reconfigurable antenna array gain pattern for 2.4 Ghz (switches ON). (b) Reconfigurable antenna array gain pattern for 3.5 Ghz (switches OFF).

5. CONCLUSION

A novel microstrip antenna capable of changing frequency operation using RF MEMS switches is introduced in this paper. Also this work demonstrates that these antennas are feasible for integration on smart antenna systems. Development of optimum signal processing algorithms and antenna designs will be studied to improve the reconfigurability and adaptivity performance of these systems.

REFERENCES

1. Peroulis, D., K. Sarabandi, and P. B. K. Katehi, "Design of reconfigurable slot antennas," *IEEE Transactions on Antennas and Propagation*, Vol. 53, 645–654, 2005.
2. Behdad, N., K. Sarabandi, and W. B. Hong, "Tri-band reconfigurable antenna for RF ID applications," *IEEE Antennas and Propagation Society Internation Symposium*, 2669, 2006.
3. Behdad, N. and K. Sarabandi, "A compact dual-/multi-band wireless LAN antenna," *IEEE Antennas and Propagation Society Internation Symposium*, Vol. 2B, 527–530, 2005.
4. Shynu, S. V., G. Augustin, C. K. Aanandan, P. Mohanan, and K. Vasudevan, "A reconfigurable dual frequency slot loaded microstrip antenna controlled by pin-diodes," *Microwave and Optical Technology Letters*, Vol. 44, 374–376, 2005.
5. Onat, S., L. Alatan, and Ş. Demir, "Design of triple-band reconfigurable microstrip antenna employing RF MEMS switches," *2004 IEEE AP-S International Symposium and USNC / URSI National Radio Science Meeting*, 2004.
6. Balanis, C. A., *Advanced Engineering Electromagnetics*, John Wiley & Sons, New York, 1989.
7. Hammerstad, E. O., "Equations for microstrip circuit design," *Proc. Fifth European Microwave Conf.*, 268–272, September 1975.

8. Widrow, B., P. E. Mantey, L. J. Grifiths, and B. Goode, "Adaptive antemna systems," *Proc. IEEE*, 2143–2159, December 1967.
9. Lehne, P. H. and M. Pettersen, "An overview of smart anltenna technology for mobile communlications systems," *IEEE Communications Sureys*, Vol. 2, No. 4, 373, 1999.
10. Winters, J., "Smart antennas for wireless systems," *IEEE Personal Communications*, Vol. l, 23–27, 1998.

Inversion Reconstruction of Signals Measured by the NMR Techniques

Pavel Fiala[1], **Eva Kroutilova**[1], **Miloslav Steinbauer**[1], **Michal Hadinec**[1], **and Karel Bartušek**[2]

[1]Brno University of Technology, Czech Republic
[2]Academy of science of the Czech Republic, Czech Republic

Abstract— The paper describes the magnetic resonance imaging method applicable mainly in MRI and MRS in vivo studies. We solved the effect of changes of magnetic fields in MR tomography. This article deals with the reverse reconstruction results obtained from the numerical simulation of MR signals by various techniques, which will be usable for the experimental results verification.

1. GEOMETRICAL MODEL

Figure 1 describes the sample geometry for the numerical modeling. On both sides, the sample is surrounded by the referential medium. During the real experiment, the reference is represented by water, which is ideal for obtaining the MR signal.

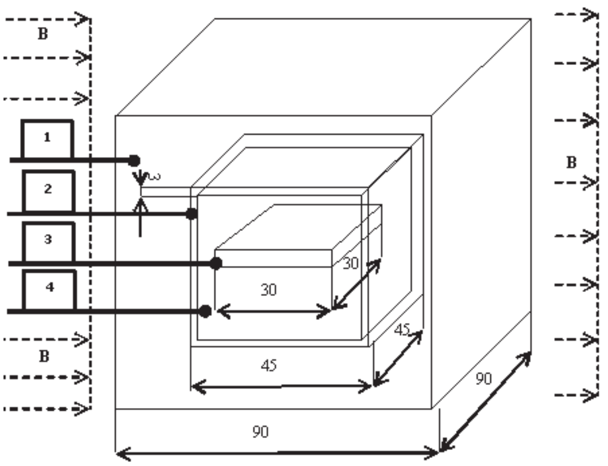

Figure 1: The sample geometry for numerical modeling.

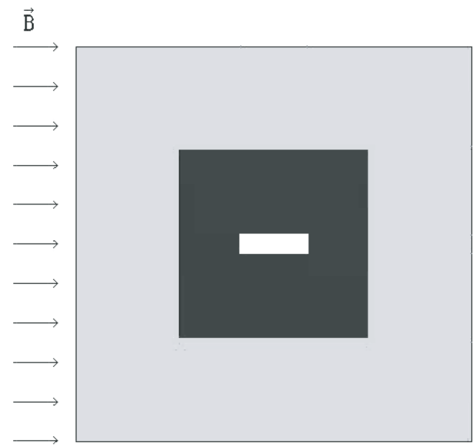

Figure 2: The geometrical model in the system Ansys.

As shown in Fig. 1, in the model there are defined four volumes with different susceptibilities. The materials are defined by their permeabilites: material No. 1 — the medium outside the cube (air), $\chi = 0$, material No. 2 — the cube walls (sodium glass), $\chi = -11,67 \cdot 10^{-6}$, material No. 3 is the sample material (sodium glass), $\chi = -11,67 \cdot 10^{-6}$, quartz glass, $\chi = -8,79 \cdot 10^{-6}$, the simax glass (commercial name), $\chi = -8,82 \cdot 10^{-6}$, material No. 4 is the medium inside the cube (water with nickel sulfate solution NiSO4, $\chi = -12,44 \cdot 10^{-6}$). The permeability rate was set with the help of the relation $\mu = 1 + \chi$. For the sample geometry according to Fig. 1, the geometrical model was built in the system. In the model there was applied the discretization mesh with 133584 nodes and 126450 elements, type Solid 96 (Ansys). The boundary conditions (1) were selected for the induction value of the static elementary field to be $B_0 = 4,7000\,\mathrm{T}$ in the direction of the z coordinate (the cube axis) — corresponds with the real experiment carried out using the MR tomograph at the Institute of Scientific Instruments, ASCR Brno.

2. NUMERICAL ANALYSIS

The numerical modelling was realized using the finite element method together with the Ansys system. As the boundary condition, there was set the scalar magnetic potential φ_m by solving Laplace's equation

$$\Delta\varphi_m = \mathrm{div}\mu(-\mathrm{grad}\varphi_m) = 0 \tag{1}$$

together with the Dirichlet boundary condition

$$\varphi_m = konst. \quad \text{on the areas } \Gamma_1 \text{ and } \Gamma_2 \tag{2}$$

and the Neumann boundary condition

$$\mathbf{u}_n \cdot \text{grad}\varphi_m = 0 \quad \text{on the areas } \Gamma_3 \text{ and } \Gamma_4. \tag{3}$$

The continuity of tangential elements of the magnetic field intensity on the interface of the sample region is formulated by the expression

$$\mathbf{u}_n \times \text{grad}\varphi_m = 0 \tag{4}$$

The description of the quasi-stationary model MKP is based on the reduced Maxwell's equations

$$\text{rot}\mathbf{H} = \mathbf{J} \tag{5}$$
$$\text{div}\mathbf{B} = 0 \tag{6}$$

where $\mathbf{H}$ is the magnetic field intensity vector, $\mathbf{B}$ is the magnetic field induction vector, $\mathbf{J}$ is the current density vector. For the case of the static magnetic irrotational field, the Equation (5) is reduced to the expression (7).

$$\text{rot}\mathbf{H} = 0 \tag{7}$$

Material relations are represented by the equation

$$\mathbf{B} = \mu_0\mu_0\mathbf{H} \tag{8}$$

where μ_0 is the permeability of vacuum, $\mu_r(B)$ is the relative permeability of ferromagnetic material. The closed area Ω, which will be applied for solving the Equations (6) and (7), is divided into the region of the sample Ω_1 and the region of the medium Ω_2. For these, there holds $\Omega = \Omega_1 \cup \Omega_2$. For the magnetic field intensity H in area Ω there holds the relation (7). The magnetic field distribution from the winding is expressed with the help of the Biot-Savart law, which is formulated as

$$\mathbf{T} = \frac{1}{4\pi}\int_{\Omega} \frac{\mathbf{J} \times \mathbf{R}}{|\mathbf{R}|^3} \text{d}\Omega \tag{9}$$

where $\mathbf{R}$ is the distance between a point in which the magnetic field intensity $\mathbf{T}$ is looked for and a point where the current density $\mathbf{J}$ is assumed. The magnetic field intensity $\mathbf{H}$ in the area can be expressed as

$$\mathbf{H} = \mathbf{T} - \text{grad}\phi_m \tag{10}$$

where $\mathbf{T}$ is the preceding or estimated magnetic field intensity, ϕ_m is the magnetic scalar potential. The boundary conditions are written as

$$\mathbf{u}_n \cdot \mu(\mathrm{T} - \text{grad}\phi_m) = 0 \quad \text{on the areas } \Gamma_3 \text{ and } \Gamma_4. \tag{11}$$

where $\mathbf{u}_n$ is the normal vector, $\Gamma_{\text{Fe}-0}$ is the interface between the areas Ω_{Fe} and $\Omega_0 \cup \Omega_{\text{W}}$. The area Ω_0 is the region of air in the model, the area Ω_{W} is the region with the winding. The continuity of tangential elements of the magnetic field intensity on the interface of the area with ferromagnetic material is expressed

$$\mathbf{u}_n \times (\mathrm{T} - \text{grad}\phi_m) = 0 \tag{12}$$

By applying the relation (10) in the relation (11) we get the expression

$$\text{div}\mu_0\mu_r\mathrm{T} - \text{div}\mu_0\mu_r\text{grad}\phi_m = 0 \tag{13}$$

The equation can be discretized (13) by means of approximating the scalar magnetic potential

$$\varphi_m = \sum_{j=1}^{NN} \varphi_j W_j(x, y, z) \quad \text{pro} \quad \forall(x, y, z) \subset \Omega \tag{14}$$

where φ_j is the value of the scalar magnetic potential in the jth node, W_j the approximation function, NN the number of nodes of the discretization mesh. By applying the approximation

(14) in the relation (13) and minimizing the residues according to the Galerkin method, we get the semidiscrete solution

$$\sum_{j=1}^{NN} \varphi_j \int_{\Omega} \mu \mathrm{grad} W_i \cdot \mathrm{grad} W_j \mathrm{d}\Omega = 0, \quad i = 1, \ldots NN. \tag{15}$$

The system of Equations (15) can be written briefly as

$$[k_{ij}] \cdot [\varphi_i]^{\mathrm{T}} = 0, \quad i, j \in \{1, \ldots NN\} \tag{16}$$

The system (16) can be divided into

$$\mathrm{K} \begin{bmatrix} \mathrm{U_I} \\ \mathrm{U_D} \end{bmatrix} = \begin{bmatrix} 0 \\ 0 \end{bmatrix}, \tag{17}$$

where $\mathrm{U_I} = [\varphi_1, \ldots, \varphi_{\mathrm{NI}}]^{\mathrm{T}}$ is the vector of unknown internal nodes of the area Ω including the points on the areas Γ_3 and Γ_4. $\mathrm{U_D} = [\varphi_1, \ldots, \varphi_{\mathrm{ND}}]^{\mathrm{T}}$ is the vector of known potentials on the areas Γ_1 and Γ_2 (the Dirichlet boundary conditions). NI in the index marks the number of internal nodes of the discretization mesh, ND is the number of the mesh boundary nodes. Then, the system can be written further in 4 submatrixes.

The system of Equations (16) can be solved with the help of standard algorithms. The scalar magnetic potential value is then used for evaluating the magnetic field intensity according to (10).

3. NUMERICAL MODEL

The numerical modelling results are represented in Fig. 2 and Fig. 7. The numerical modelling results were then used for the representation of the module of magnetic induction **B** along the defined path. For the model meshing, the element size selected as optimum was $0,5 \cdot 10^{-3}$ m. The boundary conditions $\pm\varphi/2$ were set to the model edges, to the external left and right boundaries of the air medium, as represented in Fig. 1. The excitation value $\pm\varphi/2$ was set using again the relation (21). This is derived for the assumption that, in the entire area, there are no exciting currents, therefore there holds for the rot$\mathbf{H} = 0$ and the field is irrotational.

Consequently, for the scalar magnetic potential φ_m holds

$$H = -\mathrm{grad}\varphi_m \tag{18}$$

The potential of the exciting static field with intensity $\mathbf{H}_0$ is by applying (18)

$$\varphi_m = \int \vec{H}_0 \cdot \vec{u}_z dz = H_0 \cdot z \tag{19}$$

where

$$H_0 = \frac{B}{\mu_0 \cdot \mu_r}. \tag{20}$$

Then

$$\pm \frac{\varphi}{2} = \frac{B \cdot z}{2\mu_0} = \frac{4,7000\,\mathrm{T} \cdot 90\,\mathrm{mm}}{2\mu_0} \tag{21}$$

where z is the total length of the model edge.

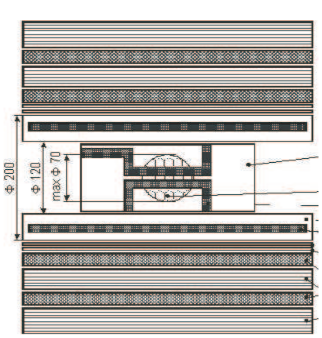

Figure 3: Elementary configuration of the MR magnet for the 200 MHz tomograph, ISI ASCR.

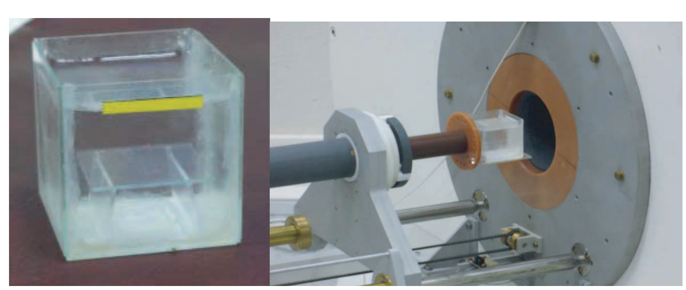

Figure 4: The measured preparation. The preparation seating in the tomograph.

4. EXPERIMENTAL VERIFICATION

The experimental measuring was realized using the MR tomograph at the Institute of Scientific Instruments, ASCR Brno. The tomograph elementary field $B_0 = 4,7000\,\mathrm{T}$ is generated by the superconductive solenoidal horizontal magnet produced by the Magnex Scientific company. The corresponding resonance frequency for the 1 H cores is 200 MHz.

5. THE COMPARISON OF RESULTS: NUMERICAL MODELLING AND MEASURING

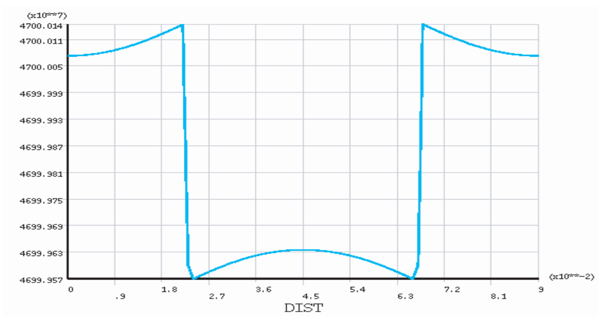

Figure 5: The magnetic induction B pattern, numerical model, without the sample.

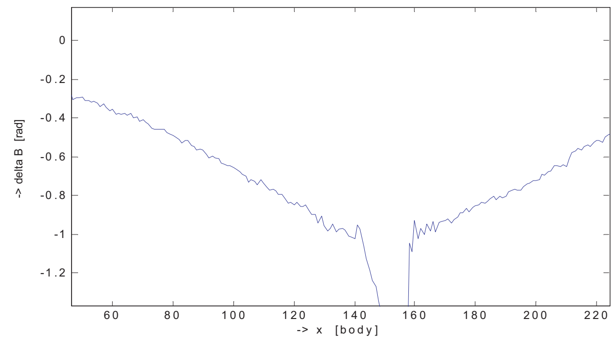

Figure 6: The measured pattern of magnetic induction B, through the medium, without the Hample.

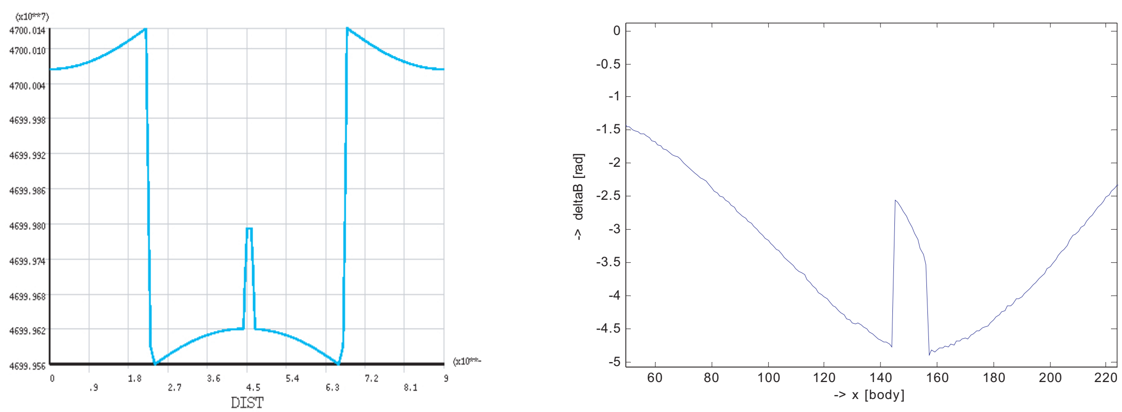

Figure 7: The magnetic induction B pattern, numerical model, quartz glass, $\Delta B = 17\,\mu\mathrm{T}$.

6. CONCLUSION

The numerical modelling and analysis of the task have verified the experimental results and, owing to the modificability of the numerical model, we have managed to advance further in the experimental qualitative NMR image processing realized at the ISI ASCR.

ACKNOWLEDGMENT

The research described in the paper was financially supported by research plans GAAV B208130603, MSM 0021630516 and GA102/07/0389.

REFERENCES

1. Fiala, P., E. Kroutilová, and T. Bachorec, Modelování elektromagnetických polí, počítačová cvičení, vyd. Brno: VUT v Brně, FEKT, Údolní 53, 602 00, s. 1–69, Brno, 2005.
2. Steinbauer, M., Měření magnetické susceptibility technikami tomografie magnetické rezonance. vyd. Brno: VUT v Brně, FEKT, Údolní 53, 602 00, Brno, 2006.

The Effect of Non-homogeneous Parts into Materials

Pavel Fiala[1], **Eva Kroutilova**[1], **Miloslav Steinbauer**[1], **Michal Hadinec**[1], **and Karel Bartusek**[2]

[1]Brno University of Technology, Czech Republic
[2]Academy of Sciences of the Czech Republic, Czech Republic

Abstract— This article deals with the verification of experimental results obtained by numerical simulation. We solved the effect of changes in the homogeneity of magnetic fields evoked by different samples from conductive and/or magnetic materials and the different types of inhomogeneity in the MR tomograph. Moreover, the paper will describe the suitable magnetic resonance techniques.

1. ANALYSIS OF THE TASK

The numerical modelling was realized using the finite element method together with the Ansys system. As the boundary condition, there was set the scalar magnetic potential φ_m by solving Laplace's equation

$$\Delta\varphi_m = \mathrm{div}\mu\left(-\mathrm{grad}\varphi_m\right) = 0 \tag{1}$$

together with the Dirichlet boundary condition

$$\varphi_m = konst. \quad \text{on the areas } \Gamma_1 \text{ a } \Gamma_2 \tag{2}$$

and the Neumann boundary condition

$$\mathbf{u}_n \cdot \mathrm{grad}\varphi_m = 0 \quad \text{on the areas } \Gamma_3 \text{ a } \Gamma_4. \tag{3}$$

The continuity of tangential elements of the magnetic field intensity on the interface of the sample region is formulated by the expression

$$\mathbf{u}_n \times \mathrm{grad}\varphi_m = 0 \tag{4}$$

The description of the quasi-stationary model MKP is based on the reduced Maxwell's equations

$$\mathrm{rot}\mathbf{H} = \mathbf{J} \tag{5}$$
$$\mathrm{div}\mathbf{B} = 0 \tag{6}$$

where $\mathbf{H}$ is the magnetic field intensity vector, $\mathbf{B}$ is the magnetic field induction vector, $\mathbf{J}$ is the current density vector. For the case of the static magnetic irrotational field, the Equation (5) is reduced to the Expression (7).

$$\mathrm{rot}\mathbf{H} = 0 \tag{7}$$

Material relations are represented by the equation

$$\mathbf{B} = \mu_0\mu_r\mathbf{H} \tag{8}$$

where μ_0 is the permeability of vacuum, $\mu_r(B)$ is the relative permeability of ferromagnetic material. The closed area Ω, which will be applied for solving the Equations (6) and (7), is divided into the region of the sample Ω_1 and the region of the medium Ω_2. For these, there holds $\Omega = \Omega_1 \cup \Omega_2$. For the magnetic field intensity H in area there holds the relation (7). The magnetic field distribution from the winding is expressed with the help of the Biot-Savart law, which is formulated as

$$\mathbf{T} = \frac{1}{4\pi}\int\limits_{\Omega}\frac{\mathbf{J}\times\mathbf{R}}{|\mathbf{R}|^3}d\Omega \tag{9}$$

where $\mathbf{R}$ is the distance between a point in which the magnetic field intensity $\mathbf{T}$ is looked for and a point where the current density $\mathbf{J}$ is assumed. The magnetic field intensity $\mathbf{H}$ in the area can be expressed as

$$\mathbf{H} = \mathbf{T} - \mathrm{grad}\phi_\mathrm{m} \tag{10}$$

where $\mathbf{T}$ is the preceding or estimated magnetic field intensity, ϕ_m is the magnetic scalar potential. The boundary conditions are written as

$$\mathbf{u}_n \cdot \mu\left(\mathrm{T} - \mathrm{grad}\phi_\mathrm{m}\right) = 0 \quad \text{on the areas } \Gamma_3 \text{ a } \Gamma_4. \tag{11}$$

where un is the normal vector, Γ_{Fe-0} is the interface between the areas Ω_{Fe} and $\Omega_0 \cup \Omega_W$. The area Ω_0 is the region of air in the model, the area Ω_W is the region with the winding. The continuity of tangential elements of the magnetic field intensity on the interface of the area with ferromagnetic material is expressed

$$\mathbf{u}_n \times \left(\mathrm{T} - \mathrm{grad}\phi_m\right) = 0 \tag{12}$$

By applying the relation (10) in the relation (11) we get the expression

$$\mathrm{div}\mu_0\mu_r\mathrm{T} - \mathrm{div}\mu_0\mu_r\mathrm{grad}\phi_m = 0 \tag{13}$$

The equation can be discretized (13) by means of approximating the scalar magnetic potential

$$\varphi_m = \sum_{j=1}^{NN} \varphi_j W_j(x,y,z) \quad \text{pro} \quad \forall(x,y,z) \subset \Omega \tag{14}$$

where φ_j is the value of the scalar magnetic potential in the j-th node, W_j the approximation function, NN the number of nodes of the discretization mesh. By applying the approximation (14) in the relation (13) and minimizing the residues according to the Galerkin method, we get the semidiscrete solution

$$\sum_{j=1}^{NN} \varphi_j \int_\Omega \mu \mathrm{grad} W_i \cdot \mathrm{grad} W_j d\Omega = 0, \quad i = 1, \ldots NN \tag{15}$$

2. GEOMETRICAL MODEL

Figure 1 describes the sample geometry for the numerical modeling. On both sides, the sample is surrounded by the referential medium. During the real experiment, the reference is represented by water, which is ideal for obtaining the MR signal. As shown in Fig. 1, in the model there are defined four volumes with different susceptibilities. The materials are defined by their permeabilites : material No. 1 – the medium outside the cube (air), $\chi = 0$, material No. 2 – the inhomogeneous sample, (clay), material No. 3 – the material of inhomogeneities inside the sample. The permeability rate was set with the help of the relation $\mu = 1 + \chi$.

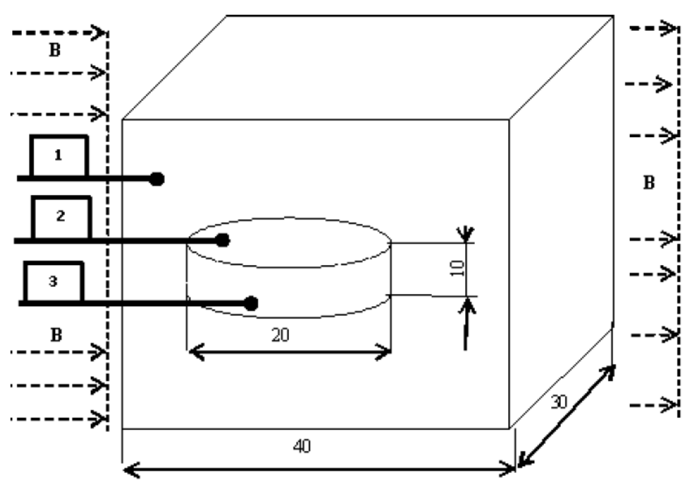

Figure 1: The sample geometry for numerical modeling.

For the sample geometry according to Fig. 1, the geometrical model was built in the system. In the model there was applied the mesh of elements, type Solid96 (Ansys). The boundary conditions (16) were selected for the induction value of the static elementary field to be $B_0 = 4,7000$ T in the direction of the z coordinate (the cube axis) — corresponds with the real experiment carried out using the MR tomograph at the Institute of Scientific Instruments, ASCR Brno.

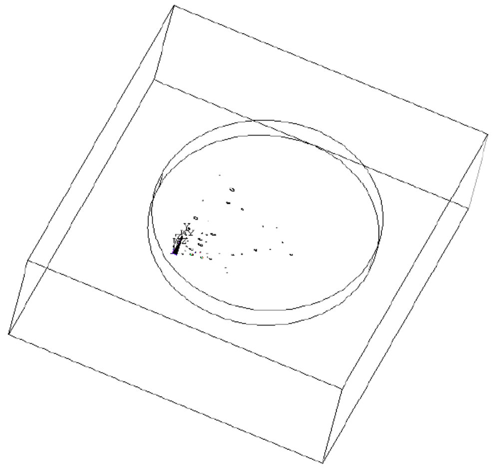

Figure 2: The geometrical model in the systém.

3. NUMERICAL ANALYSIS

The numerical modeling results are represented in Fig. 3. The numerical modeling results were then used for the representation of the module of magnetic induction B along the defined path. For the model meshing, the element size selected as optimum was $0.5 \cdot 10^{-3}$ m. The boundary conditions $\pm\varphi/2$ were set to the model edges, to the external left and right boundaries of the air medium, as represented in Fig. 1. The excitation value $\pm\varphi/2$ was set using again the relation (19).This is derived for the assumption that, in the entire area, there are no exciting currents, therefore there holds for the rot $H = 0$ and the field is irrotational. Consequently, for the scalar magnetic potential φ_m holds

$$H = -\mathrm{grad}\varphi_m \tag{16}$$

The potential of the exciting static field with intensity H_0 is by applying (17)

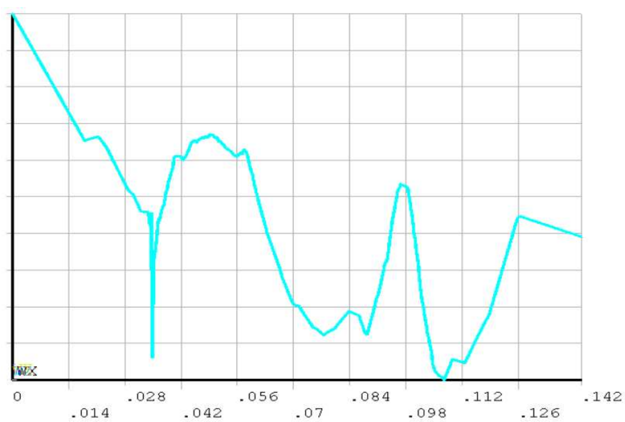

Figure 3: The distribution of the magnetic induction module in the section of the sample for material with $\chi_m = -8.79 \cdot 10^{-6}$.

$$\varphi_m = \int \vec{H}_0 \cdot \vec{u}_z dz = H_0 \cdot z \tag{17}$$

where

$$H_0 = \frac{B}{\mu_0 \cdot \mu_r} \tag{18}$$

Then

$$\pm\frac{\varphi}{2} = \frac{B \cdot z}{2\mu_0} = \frac{4,7000\,\mathrm{T} \cdot 90\,\mathrm{mm}}{2\mu_0} \tag{19}$$

where z is the total length of the model edge.

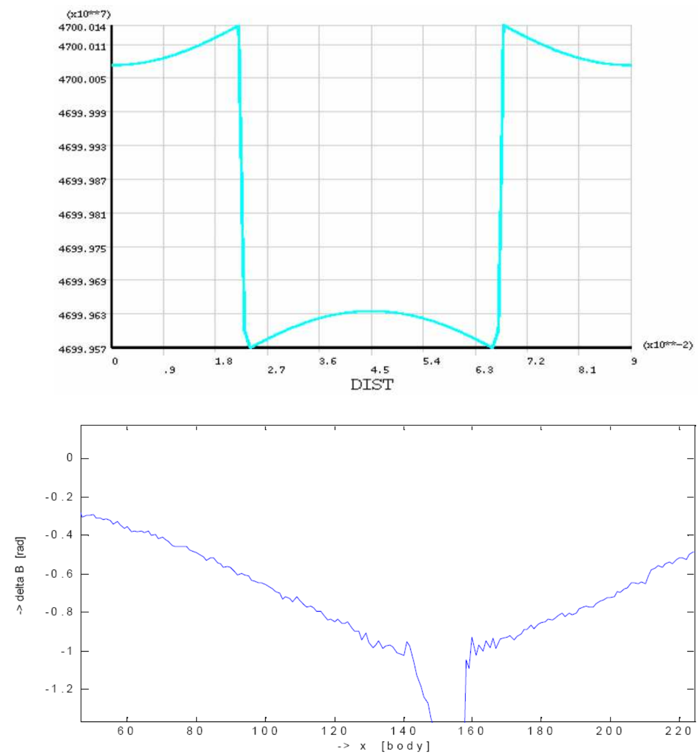

Figure 4: The measured pattern of magnetic inductione B, through the medium, without the Hample.

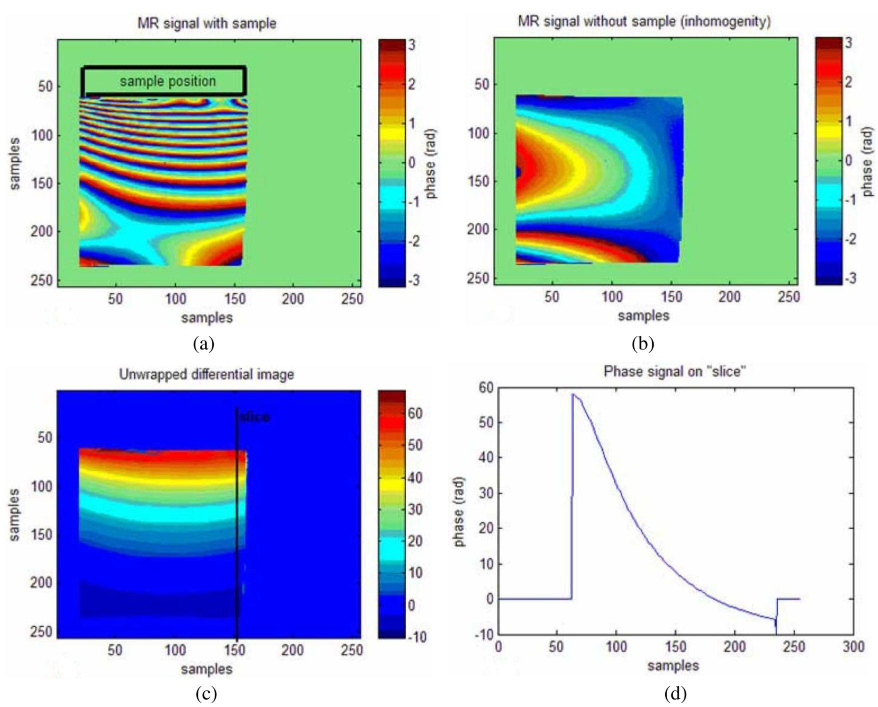

Figure 5: The measured patterns for the inhomogeneous sample, clay.

4. CONCLUSIONS

The experimental measuring was realized using the MR tomograph at the Institute of Scientific Instruments, ASCR Brno.

The tomograph elementary field $B_0 = 4,7000$ T is generated by the superconductive solenoidal horizontal magnet produced by the Magnex Scientific company. The corresponding resonance frequency for the 1H cores is 200 MHz. The numerical modeling and analysis of the task have verified the experimental results and, owing to the modifiability of the numerical model, we have managed to advance further in the experimental qualitative NMR image processing realized at the ISI ASCR.

ACKNOWLEDGMENT

The research described in the paper was financially supported by research plans GAAV B208130603, MSM 0021630516 and GA102/07/0389.

REFERENCES

1. *Ansys User's Manual*, Svanson Analysys System, Inc., Huston, USA, 1994–2006.
2. Fiala, P., E. Kroutilová, and T. Bachorec, Modelování elektromagnetických polí počítačová cvičení. vyd. Brno: VUT v Brně FEKT, Úolní 53, 602 00, s.1–69, Brno, 2005.
3. Steinbauer, M., Měřeni magnetické susceptibility technikami tomografie magnetické rezonance. vyd. Brno: VUT v Brně FEKT, Úolní 53, 602 00, Brno, 2006.

Magnetic Field Approximation in MR Tomography

Michal Hadinec[1], **Pavel Fiala**[1], **Eva Kroutilová**[1], **Miloslav Steinbauer**[1], **and Karel Bartušek**[2]

[1]Institute of Scientific Instruments of the ASCR, v.v.i
Královopolská 147, 612 64, Brno, Czech Republic
[2]Department of Theoretical and Experimental Electrical Engineering
Faculty of Electrical Engineering and Communication, Brno University of Technology
Kolejní 2906/4, 612 00, Brno, Czech Republic

Abstract— This paper describes a method, which can be used for creating map of magnetic field. Method has a great usage in magnetic resonance tomography, when we need to get information about homogeneity and characteristics of magnetic field inside the working space of the MR tomograph. The main purpose of this article is to describe basic principles of magnetic resonance phenomenon and mathematical method of Legendre polynoms which can be used for signal processing of FID (Free Induction Decay) signal obtained from tomograph detection coils. In the end of my article is experimental solution of magnetic field and models of magnetic field created by Matlab.

1. INTRODUCTION

Magnetic resonance tomography is an imaging technique used primary in medical setting to produce high quality images of the human body. Magnetic resonance imaging is based on the principles of nuclear magnetic resonance (NMR) and at the present time it is the most developed imaging technique at biomedical imaging [2]. Lately, medical science lays stress on the measuring of exactly defined parts of human body, especially human brain. If we want to obtain the best quality images we have to pay attention to homogeneity of magnetic fields, which are used to scan desired samples inside the tomograph. We should know how to reduce inhomogeneity, which can cause misleading information at the final images of samples. Generally, inhomogeneity of magnetic fields at magnetic resonance imaging cause contour distortion of images. To eliminate these inhomogeneity correctly, we need to know the map of the magnetic field and we also need to have an exact information about parameters of the magnetic field. This paper presents the experimental method, which can easily create the map of electromagnetic induction at any defined area inside the tomograph. This method uses mathematical theory of Legendre polynoms, which are used for approximation of magnetic field, if we know specific coefficients. The coefficients of Legendre polynoms, which are computed using measured values of magnetic induction at exactly defined discrete points are used for creating map of magnetic field. If we know these coefficients, we are able to compute magnetic induction at any point of defined area. At the ideal case, there should be no difference between measured data and approximated data.

2. MR PRINCIPLES

In quantum mechanics, spin [2] is important for systems at atomic length scales, such as individual atoms, protons or electrons. One of the most remarkable discoveries associated with quantum physics is the fact, that elementary particles can possess non zero spin. Elementary particles are particles that cannot be divided into any smaller units, such as the photon, the electron and the various quarks. The spin carried by each elementary particle has a fixed value that depends only on the type of particle, and cannot be altered in any known way. Particles with spin can possess a magnetic dipole moment, just like a rotating electrically charged body in classical electrodynamics. The main principle of magnetic resonance spectroscopy and magnetic resonance imagining is, that radiofrequency fields (RF pulses) excite transitions between different spin states in a magnetic field.

The information content can be retrieved as resonance frequency, spin to spin couplings and relaxation rates. We can imagine, that protons are rotating along their axes and there is also a wobbling motion called precession, that occurs when a spinning object is the subject of an external force. Thanks to the positive charge of protons and its spin, protons generate a magnetic field and gets a magnetic dipole moment. If the protons are placed in a magnetic field, the magnetic moment will precess about the direction of magnetic field with specific frequency. This frequency is called Larmor frequency and can be described by the Larmor equation [5]

$$\Omega = \gamma \cdot B \tag{1}$$

where Ω [MHz] is the frequency of precession, [MHz/T] is the gyromagnetic ratio and B is strength of external magnetic field. In ordinary materials, the magnetic dipole moments of individual atoms produce magnetic fields that cancel one another, because each dipole points in a random direction. In ferromagnetic materials however, the dipole moments are all lined up with another, producing a macroscopic, non-zero magnetic field. If there is no external magnetic field, magnetic moments of atoms are chaotically spread and there is nearly no resulting magnetization vector M_0. If we place a sample into the stationary magnetic field B_0, we realize, that there is a vector of magnetization M_0 which is created as a sum of magnetic moments of each atom. The direction of this vector is the same as the direction of external magnetic field B_0. This state is called longitudinal magnetization. Now we apply a high frequency magnetic field of induction B_1, which is vertical to stationary magnetic field B_0. This high-frequency magnetic field causes resonance effect and magnetization vector M_0 starts to rotate with specific angular frequency. To measure vector M_0, we need to drop it into the xy plain (on condition that B_0 has direction of z axes). This dropping is done by a high-frequency excitation pulse B_1, which has a proper shape. This state is called transversal magnetization. Set of these pulses is called pulse sequence. Pulse sequence is a pre-selected set of defined RF and gradient pulses, usually repeated many times during a scan. Pulse sequences control all hardware aspects of the measurement process. At the x-y plain, there is scanning coil, which is used for scanning of FID signal

After excitation pulses, the spins has tendency to minimize transverse magnetization and to maximize longitudinal magnetization. The transverse magnetization decays toward zero with characteristic time constant T2 and the longitudinal magnetization returns towards maximum with a characteristic time constant T1.

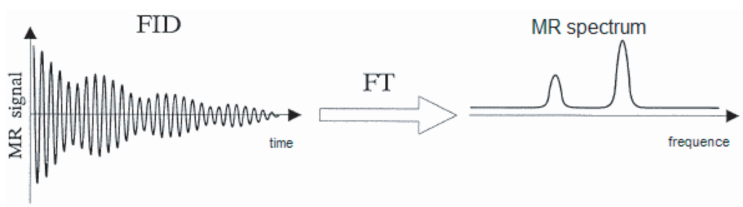

Figure 1: Fid signal and MR spectrum.

3. LEGENDRE POLYNOMS THEORY

If we want to determine the magnetic induction values in the specific points of measured area, we should use Legendre polynoms [4] which are defined according to equation (2)

$$P_n(z) = \frac{1\cdot 3\cdot 5\cdot \ldots \cdot (2n-1)}{n!}\cdot\left[z^n - \frac{n(n-1)}{2(2n-1)}z^{n-2} + \frac{n(n-1)(n-2)(n-3)}{2\cdot 4(2n-1)(2n-3)}Z^{n-4} - \ldots\right] \quad (2)$$

Legendre polynoms of zero and first order

$$P_0(z) = 1 \quad (3)$$
$$P_1(z) = z = \cos v \quad (4)$$

Legendre polynoms of of higher order are defined according to recursion formula

$$P_{n+1}(z) = \left[(2n+1)\cdot z\cdot P_n(z) - n\cdot P_{n-1}(z)\right]/(n+1) \quad (5)$$

Now we can define functions associated to Legendre polynoms, which are derivation of Legendre polynoms

$$P_0^1(z) = 0 \quad (6)$$
$$P_2^1(z) = \frac{1}{2}(3z^2-1) \quad (7)$$
$$P_{n+1}^m(z) = \left[(2n+1)\cdot z\cdot P_n^m(z) - (n+m)\cdot P_{n-1}^m(z)\right]/(n-m+1) \quad (8)$$
$$P_n^{m+2}(z) = \frac{2\cdot(m+1)\cdot z}{\sqrt{1-z^2}}\cdot P_n^{m+1} - (n-m)\cdot(n+m+1)\cdot P_n^m(z) \quad (9)$$

Magnetic field induction can be approximated at any point of measured area. These points can be selected using spherical coordinates $[r,\, \theta,\, \varphi]$, so we can define approximation formula as follows

$$B_a(r,\, \theta,\, \varphi) = \sum_{k=0}^{N_K} \sum_{m=0}^{m=K} \cdot r^k \cdot P_{m,\,k}(\cos\theta) \cdot [A_{m,\,k} \cos m \cdot \varphi + B_{m,\,k} \sin m \cdot \varphi] \tag{10}$$

where N_K is the highest order of Legendre polynom for chosen approximation, A_{mk} a B_{mk} are unknown coefficients. N_K is defined according to sampling theorem and depends on number of measured points N_b:

$$N_k = \frac{N_b}{2} - 1 \tag{11}$$

Coefficients A_{mk} a B_{mk} is then possible to find like the minimum value of this formula:

$$\Psi = \min \sum_{i=1}^{N_m} (B_{im} - B_{ia})^2 \tag{12}$$

where B_m are measured values of magnetic induction at the desired area (circle, sphere, cylinder) and B_a. are approximated values of magnetic induction. This method is known as Least Square method.

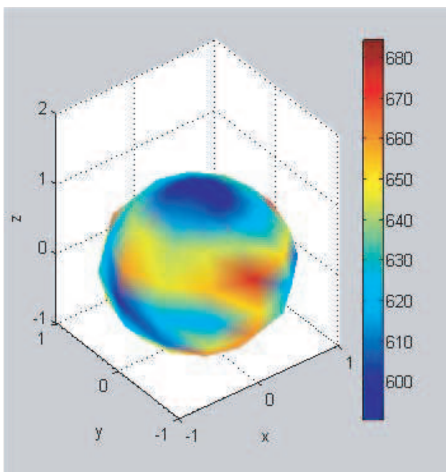

Figure 2: 3D map on the surface (measured values).

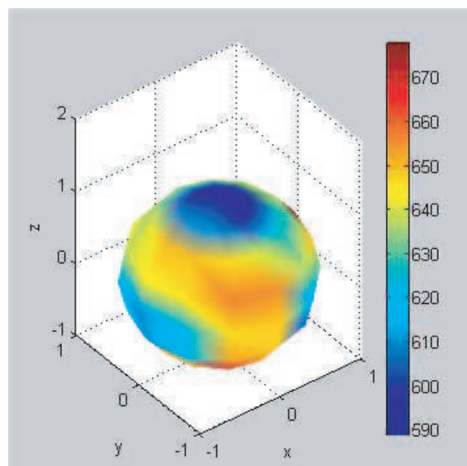

Figure 3: 3D map on the surface (computed values).

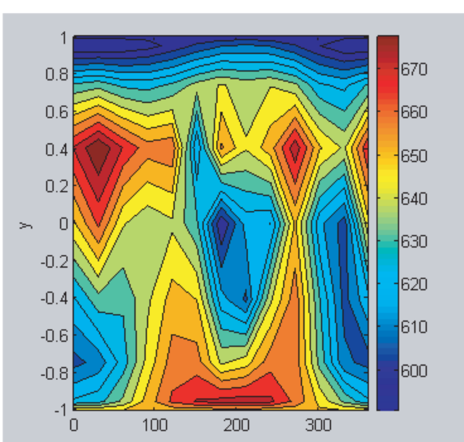

Figure 4: Contour map of the field (measured values).

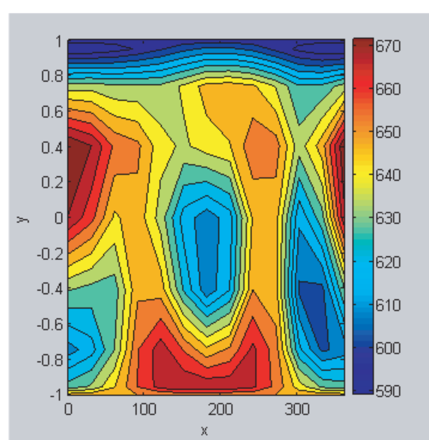

Figure 5: Contour map of the field (computed values).

4. EXPERIMENTAL RESULTS

All values of magnetic induction on following figures are presented at $[\mu T]$ unit. Fig. 2 shows three-dimensional map of the field on the surface of sphere, which is created only from measured values. Fig. 3 is map created from computed values, it means values which were computed during minimum searching (least square method) in Matlab. At the Fig. 4 and Fig. 5 is a comparison using 2D contour plot.

Finally if we want to get values of magnetic field induction inside the sphere, we use computed coefficients. Then we generate new coordinates of desired points inside the sphere and compute map of the field. This map can be any slice through the sphere as we can see in the Fig. 6.

5. CONCLUSION

We proposed a method for magnetic field mapping and approximation on the basis of measured values along specific area. As we can see from results, the map created from measured and computed values are quite similar. Future work can be directed towards minimization of differences between measured values of magnetic induction and approximated values, so we can obtain exact coefficients for approximation inside the sphere.

REFERENCES

1. Fiala, P., E. Kroutilová, and T. Bachorec, Modelování elektromagnetických polí, počítačová cvičení vyd. Brno: VUT v Brně FEKT, Údolní, 53, 60200, Brno, 2005.
2. Haacke, E. M., R. W. Brown, M. R. Thomson, and R. Venkatesan, *Magnetic resonance imaging-physical principles and sequence design*, John Wiley & Sons, ISBN 0-471-48921-2, 2001.
3. Stratton, J. A., *Teorie elektromagnetického pole*, SNTL Praha, 1961.
4. Angot A., Užitá matematika, Státní nakladatelství technické literatury, Praha 1972.
5. Morris, P. G., *Nuclear Magnetic Resonance Imaging in Medicine and Biology*, Clearendon Press, Oxford, 1986.

Progress in Gain Performance of Parametrically Amplifying Travelling-wave Antennas (PATA): PATA Analogous to Travelling-wave Tube Amplification and Negative Resistivity of Esaki Diodes

H. Kikuchi[1], **S. Tsuruoka**[2], **and T. Obata**[3]

[1]Institute for Environmental Electromagnetics, 3-8-18, Komagome, Toshima-ku, Tokyo 170, Japan
[2]Takuwa Corporation, 1-4-15, Uchi-Kanda, Chiyoda-ku, Tokyo 101, Japan
[3]Gunma National College of Technology, 580, Toriba-machi, Maebashi 371-0845, Japan

Abstract— Progress in gain performance of Parametrically amplifying travelling-wave antennas (PATA) invented by one of the present authors is presented at a range of frequencies 2∼5 GHz where its eigen surface wave becomes a fast eave, being amplified by the sky (space) wave due to a strong coupling, and its guide wavelength reaches as long as 2∼4 λ (λ: wavelength in free space), thus increasing the amplification ratio as high as 0.26∼0.4 dB/cm. Specifically, for a range of 2∼5 GHz, the sky (space) wave dominates near the input side but the induced surface wave tends to be dominant, guide-wavelength increasing as long as 2∼4 λ (λ: wavelength in free space) and thus increasing the amplification ratio as high as 0.26∼0.4 dB/cm as approaching the output end.

1. INTRODUCTION

Parametrically amplifying travelling-wave antennas (PATA) [1, 2] invented by one of the present authors are somewhat analogous to travelling-wave tubes [3] and Esaki diodes [4] in function and characteristics, though there are essential differences. PATA correspond to amplification of travelling-wave tubes and the incident waves along the line play a role of electron beams. There are, however, essential differences between them. The role of electron beams in travelling-wave tubes is an amplification only when an external microwave is passing through a helical circuit. In contrast, there are twofold roles of an incident wave in PATA. One is to induce a current wave along the line. The other is to amplify its induced current wave at the same time. Further, there is a difference that the coupling of electron beams to a helical circuit is capacitive for travelling-wave tubes but the coupling of incident waves to the line is inductive for PATA. While PATA is expressed by an equivalent active distributed parameter line whose shunt conductance G is negative in the transition region, the resistance in an equivalent lumped circuit of Esaki diodes is also negative. In

Figure 1: Experimental setup of PATA.

this respect, there is some correspondence or analogy between them, though those negative effects are different. The negative shunt conductance of PATA leads to new results that the attenuation constant of the induced wave decreases with increasing frequency and the wave-mode becomes a fast wave, while the negative resistance of Esaki diodes causes current decrease with voltage increase as a result of quantum-meechanical tunnel effects. Progress in gain performance of PATA is presented at a range of frequencies 2∼5 GHz where its eigen surface wave becomes a fast eave, being amplified by the sky (space) wave due to a strong coupling. and its guide wavelength reaches as long as 2∼4 λ (λ: wavelength in free space), thus increasing the amplification ratio as high as 0.26∼0.4 dB/cm.

2. EXPERIMENTAL SETUP

Whole setup of PATA is composed of a bare copper (or aluminum) wire (tube) or its array (1 m long with (outer) diameter 2.75 cm) connected with a guide-horn above a lossy dielectric (foam polyethylene) base-plate and wire or tube centre is 2.7∼8 cm high) above the base-plate whose bottom side is grounded as seen in Fig. 1.

3. EXPERIMENTAL RESULTS

3.1. Phase Characteristics Showing a Fast Wave Induced (λ_g=guide wavelength > 2λ∼4λ)

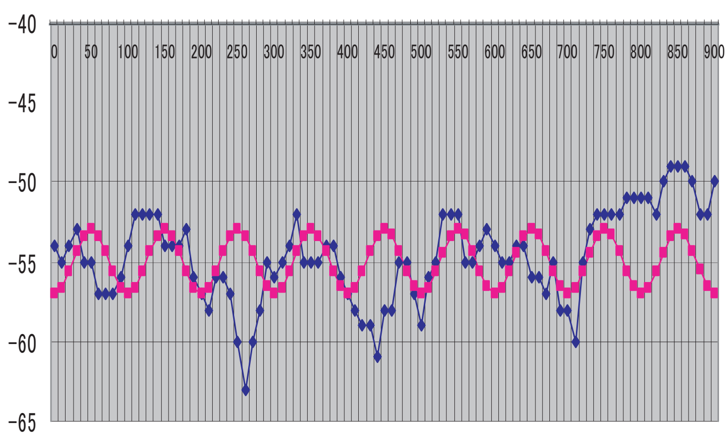

Figure 2: Sample data of the standing wave induced along the line (blue), showing a decrease of the guide wavelength (λ) in comparison with the space wave in free space (purple). The centre of Almi-pipe is 27 mm high above the base plate. $F = 3$ GHz.

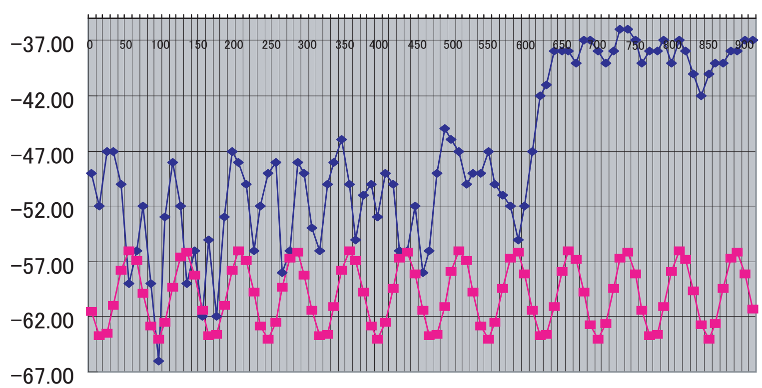

Figure 3: Another sample data of the standing wave induced along the line (blue), showing a decrease of the guide wavelength (λ) in comparison with the space wave in free space (purple). The centre of Almi-pipe is 27 mm high above the base plate. $F = 3$ GHz.

3.2. Frequency Dependence of Phase Velocity Showing a Fast Wave Region (0.4∼5 GHz)

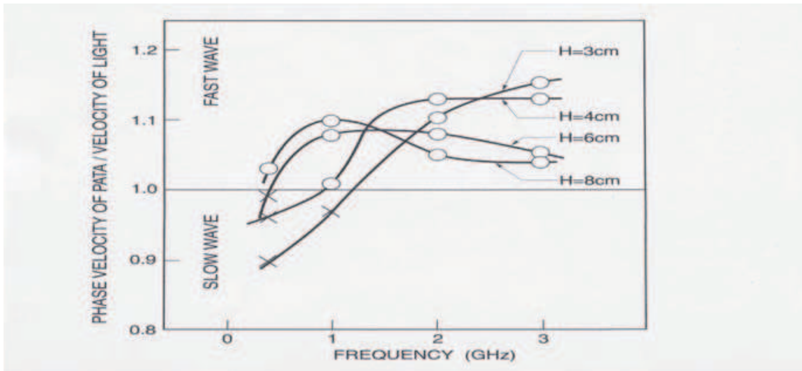

Figure 4: Frequency dependence of phase velocity showing a fast wave region (0.4∼5 GHz).

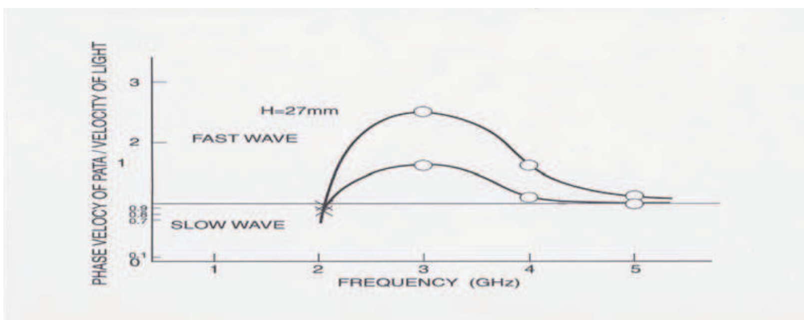

Figure 5: Another example of frequency dependence of phase velocity showing a fast wave region (0.4∼5 GHz.)

3.3. Amplification Characteristics (0.4∼5 GHz)

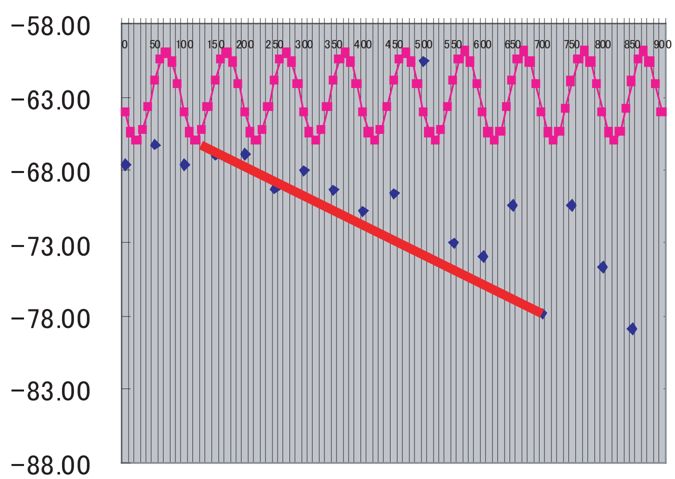

Figure 6: $H = 27$ mm, $f = 3$ GHz, amplification rises upto 0.4 dB/cm as approaches the end. In general, wave fields are composed of space waves and surface waves induced. As is shown in Fig. 6, most of wave fields are the incident space waves near the input end. But become the induced surface waves as approaching the output end, being amplified by the space waves, increasing its amplification ratio as high as 0.4 dB/cm.

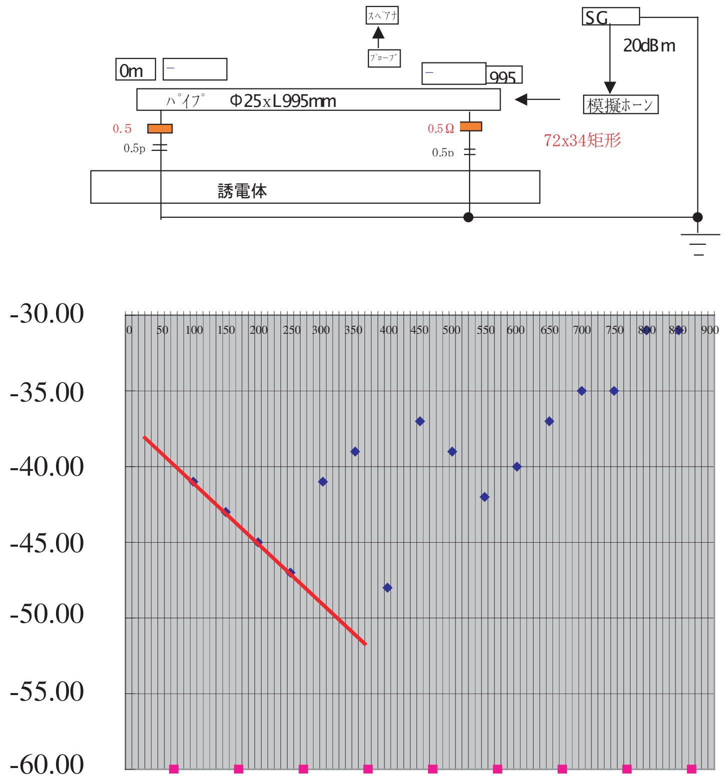

Figure 7: Another sample data: $H = 27$ mm, $f = 3$ GHz, amplification rises upto 0.4 dB/cm as approaches the end. In general, wave fields are composed of space waves and surface waves induced. As is shown in Fig. 6, most of wave fields are the incident space waves near the input end. But become the induced surface waves as approaching the output end, being amplified by the space waves, increasing its amplification ratio as high as 0.4 dB/cm.

4. CONCLUSION

Progress in gain performance of PATA reveals the following results:

1. At a range of frequencies 0.4∼5 GHz, the eigen surface wave induced becomes a fast wave and its guide wavelength reaches as long as 2∼4 λ (λ: wavelength in free space).
2. Its induced wave is strongly coupled to the sky (space) wave, since the phase velocities coincide with each other.
3. As a result the induced surface wave is parametrically amplified by the sky (space) wave due to a strong coupling, thus increasing the amplification ratio as high as 0.26∼0.4 dB/cm.
4. Thus, the present antenna is thought to be feasible for high gain ad directivity.
5. If the antenna is made to be rotationable towards any direction, however, it virtually constitutes non directivity with maximum sensitivity and may be used for this purpose.

REFERENCES

1. Kikuchi, H., Parametrically Amplifying Travelling-Wave Antenna, UK Patent 2276985, 1996; US Patent 5,469,179, 1995; French Patent 9404020, 1997; Japanese Patent 2636164, 1997; German Patent 4411720, 2004.
2. Kikuchi, H., “Similarities and differences among parametrically amplifying travelling-wave antennas, travelling-wave tubes, and esaki diodes,” *Proc. PIERS 06*, Tokyo, Japan.
3. Pierce, J. R., *Travelling Wave Tubes*, D. Van Nostrand, Princeton, 1950.
4. Esaki, L., *Phys. Rev.*, Vol. 109, 603, 1958.

Design, Simulation and Realization the Specfic Source of Light

Eva Kroutilova, **Miloslav Steinbauer**, **and Zoltán Szabó**
Department of Theoretical and Experimental Electrical Engineering
Faculty of Electrical Engineering and Communication, Brno University of Technology
Kolejni 2906/4, Brno 612 00, Czech Republic

Abstract— This paper presents information about design of special light sources, which is intended for photosynthesis process research. Required properties were continuous spectral characteristic with respect to photosynthetically active wavelength area, possibility of luminous flux regulation and practically zero thermal effect to illuminated object. Owing to new high-performance LED this type of light source was selected. Design of light source consisting of high efficient white LED's, as well as experimental results, are presented. The special light source was designed and constructed for the research activity on the lichen structure in the Antarctica. This research is made by the Institute of Experimental Biology, Masaryk University, Faculty of Science.

1. BIOENERGETICS OF PHOTOSYNTHESIS

Photosynthesis is a physiological phenomenon that converts solar energy into photochemical energy. This physiological phenomenon may be described thermodynamically in terms of changes in energy, entropy and free energy. The energetic of photosynthesis, driven by light, causes a change in entropy that in turn yields a usable source of energy for the plant. On earth, there are two sources of free energy: light energy from the sun, and terrestrial sources, including volcanoes, hot springs and radioactivity of certain elements. The biochemical value of electromagnetic radiation has led plants to use the free energy from the sun in particular. Visible light, which is used specifically by green plants to photosynthesize, may result in the formation of electronically excited states of certain substances called pigments. For example, Chl a is a pigment which acts as a catalyst, converting solar energy into photochemical energy that is necessary for photosynthesis. With the presence of solar energy, the plant has a usable source of energy, which is termed the free energy of the system. However, thermal energy is not completely interconvertible, which means that the character of the solar energy may lead to the limited convertibility of it into forms that may be used by the plant.

There is known effects of light intensity (irradiance) and temperature on the rate of photosynthesis. At constant temperature the rate of photosynthesis varies with irradiance, initially increasing as the irradiance increases. However at higher irradiance this relationship no longer holds and the rate of photosynthesis reaches a plateau. The effect on the rate of photosynthesis of varying the temperature at constant irradiance can be seen in image to the left. At high irradiance the rate of photosynthesis increases as the temperature is increased over a limited range. At low irradiance, increasing the temperature has little effect on the rate of photosynthesis.

2. SOURCE OF LIGHT

On luminous characteristics sources were laying following requirements

- continuous spectra in visible area from 400 to 800 nm
- shape of the spectrum characteristic should be very similar as the daylight
- the source should radiate in IR area as low as possible
- defined shape and size of the illuminated surface
- very high and homogenous intensity of the light on the defined surface

These requirements are met by used power LEDs, which are illustrated on Fig. 1(a). Shape of this LEDs spectrum is on Fig. 1(b).

3. VERIFICATION OF THE HOMOGENEITY BY THE SIMULATION

MATLAB modeling of light source arrangement was designed for first verification of the lighting systems design and it is given in the Fig. 2. The main advantages of the MATLAB simulation are the simplicity of the submission for the initial figures and the high speed of the calculations for the simple assignments. This modeling is suitable for the verification of the results, which are received from other type of the modeling method.

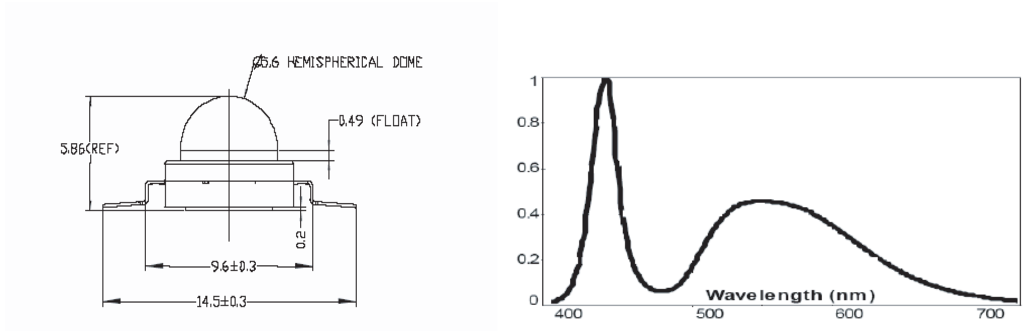

(a) (b)

Figure 1: (a) Geometrical illustration of the LED light source and (b) its relative spectral characteristic.

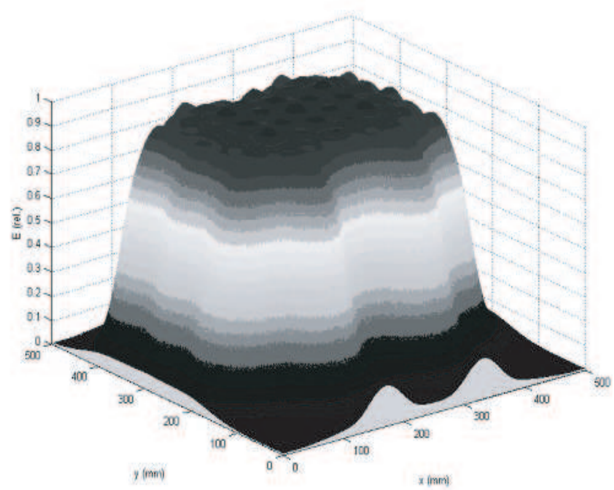

Figure 2: Simulated intensity of illumination for LEDs arrangement.

4. VERIFICATION OF THE DESIGN VIA EXPERIMENTS

The results of the design verification via experiments are given in Fig. 3. There are differences between the values obtained by modeling and experimental measurement, ranging to the 20%, depending on the distance. When the light is into the requested distance, the differences are also lower. Experimental measurements were used as second verification.

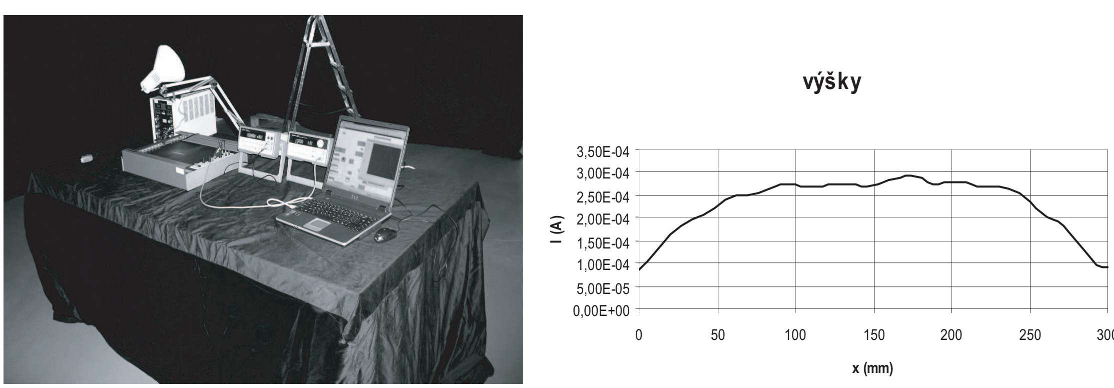

Figure 3: The research workplace and measured homogeneity of illumination.

5. POWER SUPPLY

Power consumption of whole arrangement consisting of 17 LEDs is about 85 W. Whenever wide range of power source voltage was required, pulsed source was chosen. Designed power supply is voltage driven current source 0 to 10 A operating on 180 kHz with efficiency over 80%, input voltage can be from 12 to 30 V.

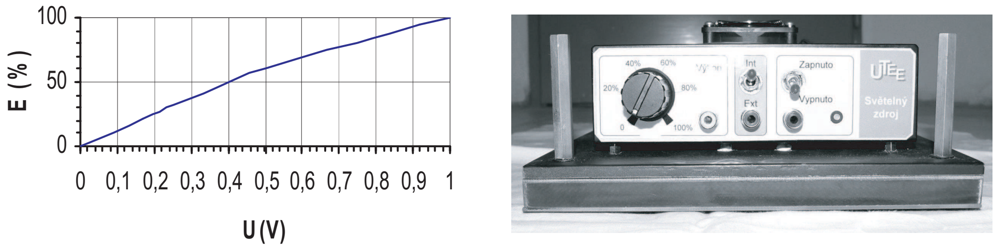

Figure 4: Regulation characteristic of source and control panel of arrangement.

6. CONCLUSIONS

The research workplace is given in the Fig. 3. There were measured some parameters of the special source of light, which was designed and constructed.

The final parameters of the special light source are:

- The distance from the illuminate area is 18–21 cm for the best homogeneity
- The illuminate area is 200 × 300 mm
- The intensity of the light is 500 μEinstein·cm-2·s-1 • (in the distance 19 cm)
- The homogeneity of the light is better than 10% into the area 100 × 200 mm (in the distance 19 cm)
- The lifetime of used LEDs is 1000 hours around at upper-most setting power
- The storage and container temperature −40 − +85°C
- The working temperature is −25 − +30°C
- The direct power supply is into range 12 V/9 A till 30 V/3,5 A

The source of light agrees with extreme climatic conditions in the Antarctica and it is constructed with regard to the environmental resistance, thermal shocks, weatherproofness and protection against shaking. To achieve this corresponding climatic class components were chosen, the screws and the components were fixed against the movement, the silver PCB was used, etc. Designed prototype of the special source of light reached all requirements. Increasing intensity of the light will be possible, as soon as the LED diodes with higher powers will be available.

ACKNOWLEDGMENT

The research described in the paper was financially supported by research plans GAAV B208130603, MSM 0021630516 and GA102/07/0389.

REFERENCES

1. GM Electronic, Katalog elektronických součástek 2005.
2. Světlo, ISSN 1212-0812, FCC Public s.r.o., Pod Vodárenskou věží4, 182 08, Praha 8, ČR.
3. Plch, J., J. Mohelníková, and P. Suchánk, "Osvětlení neosvětlitelných prostor," *ERA*, 2004.
4. *LEOS Newsletter Magazine*, Lasers and Electro-Optics Society of the Institute of Electrical and Electronics Engineers, Inc., Corporate Office: 3 Park Ave., 17th Floor, New York, NY 10016-5997, USA.
5. Plch, J., "Světelná technika v praxi," Praha, IN-EL 1999, 210 stran, ISBN 80-86230-09-0.
6. Habel, J., a kol. Světelná technika a osvětlování, Praha, FCC PUBLIC 1995, 448 stran, ISBN 800-901985-0-3.
7. Govindjee, *Bioenergetics of Photosynthesis*, Academic Press, New York, 1975.
8. Campbell, N. and J. Reece, *Biology*, 7th ed., Benjamin Cummings., San Francisco, 2005.
9. http://www.esim.ca/2002/documents/Proceedings/other2.pdf.

Preemphasis Coreection of Gradient Magnetic Field in MR Thomograph

Eva Gescheidtova, **Radek Kubasek**, **and Zoltan Szabo**
Faculty of Electrical Engineering and Communication, Brno University of Technology
Kolejni 2906/4, Brno 612 00, Czech Republic

Abstract— The magnetic resonance (MR) imaging techniques of tomography and spectroscopy are exploited in many applications. For the MR instruments to function properly it is necessary to maintain a high quality of homogeneity of the fundamental magnetic field. The pre-emphasis compensation of the generated gradient field increases the homogenity of the generated magnetic field and reduces the minimum switching times of the gradients. This enables measuring the MR images of incisions in the human body, the relaxation properties of nuclei, self-diffusion processes, flows of liquids and movements of solids faster and more accurately.

1. INTRODUCTION

When defining the area being measured in localized spectroscopy and tomography, the gradient field is excited by very short pulses of sufficient magnitude. This gives rise to a fast changing magnetic field, which induces eddy currents in the conducting material near the gradient coils. These currents then cause retrospectively unfavourable deformation of the total magnetic field [1]. The effect of eddy currents acts against the fast temporal changes in the magnetic field. The basic idea of a method that compensates this effect consists in replacing the missing leading edge of the field waveform by an overshoot of excitation current as shown in Fig. 1.

To have the best possible compensation it is necessary to find an optimum shape of excitation pulse. Basically, this consists in obtaining the spectrometer response pulse, inverting it and using this inversion to filter the excitation (usually square) pulse. The term pre-emphasis compensation method is based on the fact that the compensation filter is in the nature of a differentiating element (high-pass filter).

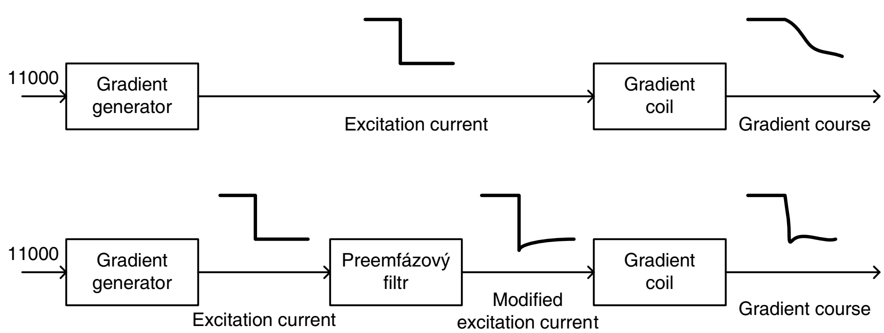

Figure 1: Principle of pre-emphasis compensation.

2. MEASURING METHOD

The principle of measuring the waveform of gradient pulse consists in determining the changes in instantaneous frequency [2] of an MR signal produced by the resonance of nuclei excited in two thin layers positioned symmetrically about the gradient field centre, as shown in Fig. 2. The average inductions of magnetic field $B(r_n, t)$ are measured in the excited layer in the $+r_n$ and $B(-r_n, t)$ positions in the $-r_n$ layer; r is one of the (x, y, z) directions.

From the differences of the two inductions measured the magnitude of gradient can be calculated according to the relation

$$G_r(t) = \frac{1}{2r_n} \left[B\left(r_n, t\right) - B\left(-r_n, t\right) \right]. \tag{1}$$

The sum of the $B(r_n, t)$ and $B(-r_n, t)$ inductions measured determines the change in basic homogeneous magnetic field according to the relation

$$B_{0r}(t) = \frac{1}{2} \left[B(r_n, t) + B(-r_n, t) \right]. \tag{2}$$

Under the above conditions the instantaneous frequency of MR signal will be directly proportional to the induction of magnetic field $B(\pm r_n, t)$. The measuring sequence has two stages, as illustrated in Fig. 3.

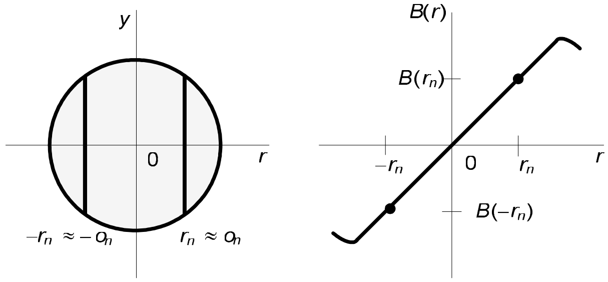

Figure 2: Position of excited thin layers in working space of MR device.

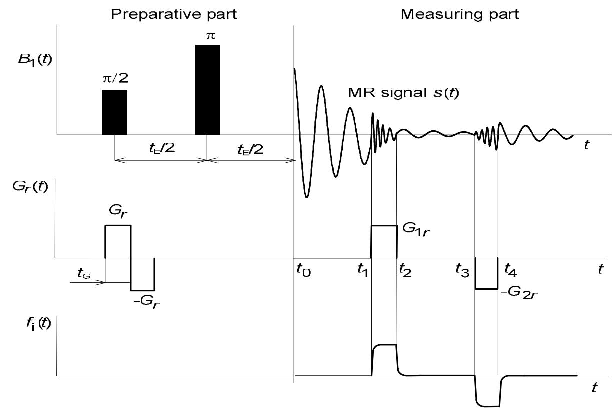

Figure 3: Measuring sequence for measuring the time characteristics of gradient pulses.

If in the measuring part of the sequence no pulsed gradient is applied, the instantaneous frequency of MR signal carries the information about the average value of magnetic field induction in the excited layer, inclusive of the inhomogeneities of basic magnetic field. In the application of pulsed gradients (G_{1r} and $-G_{2r}$) during the signal decay there is a change in the instantaneous frequency of the MR signal, which is proportionate to the magnetic field induction at the place of excited layer.

The measured waveform of magnetic inductions $B(r_n, t)$ and $B(-r_n, t)$ is much distorted due to noise, as shown in Fig. 4. The gradient $G_r(t)$ calculated according to Equation (2) is even more distorted, due to the incorrelatibility of noise. To obtain an accurate and undistorted waveform of the gradient $G_r(t)$, we must remove the noise.

Figure 5 gives the waveform of magnetic inductance $B(r_n, t)$ subsequent to filtering. As can be seen, there has been considerable noise attenuation. The gradient $G_r(t)$ is free from noise and, at the same time, measured with sufficient accuracy to be used in determining the coefficients of the pre-emphasis filter.

3. PREEMFASIS COMPENZATION

In the Academy of Sciences of the Czech Republic in Brno the lay-out of pre-emphasis filters is as shown in Fig. 6. Pre-emphasis filters are basically inverse filters to the model of tomographic

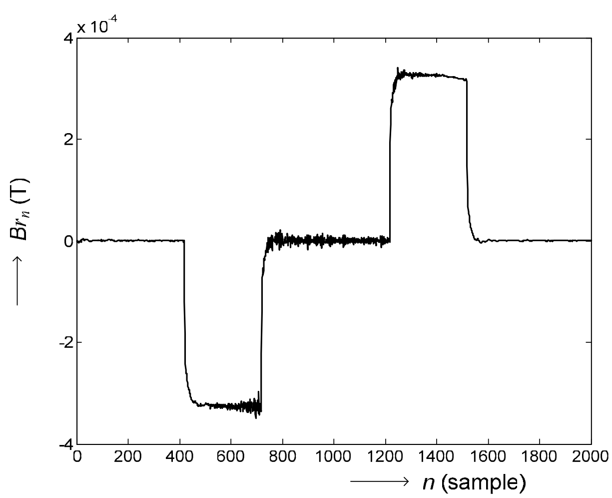

Figure 4: Measured waveform of magnetic inductance $B(r_{n,n})$.

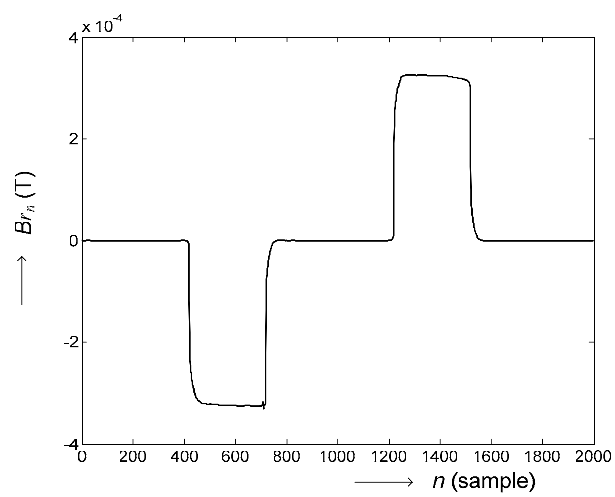

Figure 5: Waveform of magnetic inductance $B(r_{n,n})$ after denoising filtering.

scanner. Thein task is to generace a waveform of the gradient $G'_\alpha(t)$ pre-distorted to such a degree that subsequent to the action of eddy currents the generated gradient $g_\alpha(t)$ is of the required waveform, i.e., $G_\alpha(t)$.

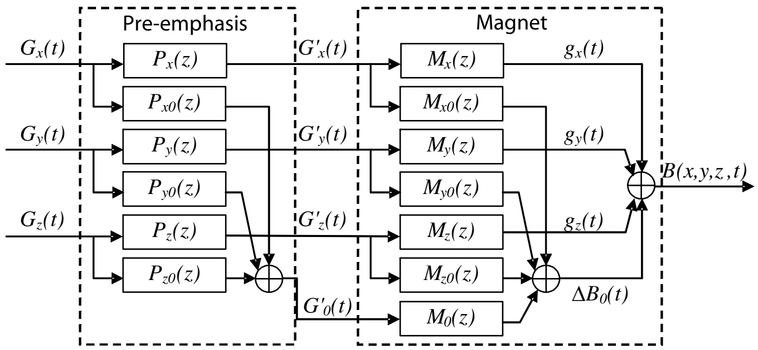

Figure 6: Pre-emphasis kompenzace a model magnetu MR tomografu.

The effect of eddy currents will be compensated under the conditions

$$P_\alpha(z) = M_\alpha^{-1}(z) = \frac{G_\alpha(z)}{g_\alpha(z)}. \tag{3}$$

The measurement itself must be performed for the setting $P_\alpha(z) = 1$, preferably for $P_{\alpha 0}(z) = 0$. The transfer of the coil $M_0(z)$, which compensates the basic magnetic field B_0 will be measured for quite the opposite setting, namely $P_\alpha(z) = 0$ and $P_{\alpha 0}(z) = 1$. The basic field B_0 is excited directly by the gradient in the respective direction. The compensation of the basic field using the cross pre-emphasis filter $P_{\alpha 0}(z)$ will take place if a basic field of opposite polarity is generated.,

$$P_{\alpha 0}(z) = -\frac{\Delta B_0(z)}{G_\alpha(z) M_0(z)}. \tag{4}$$

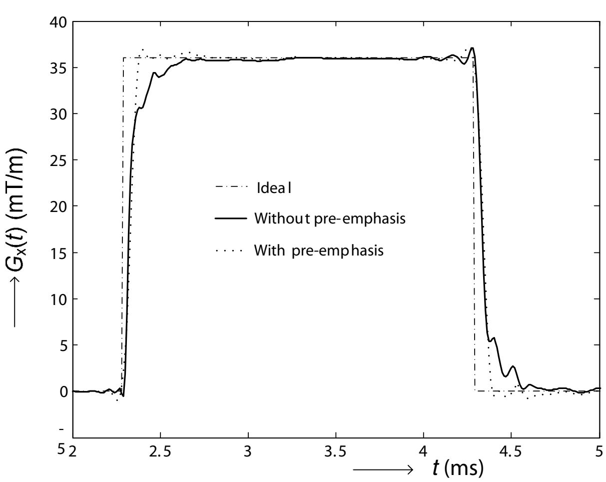

Figure 7: Comparison of positive gradient impulse G_x 2 ms s long, with and without pre-emphasis compensation.

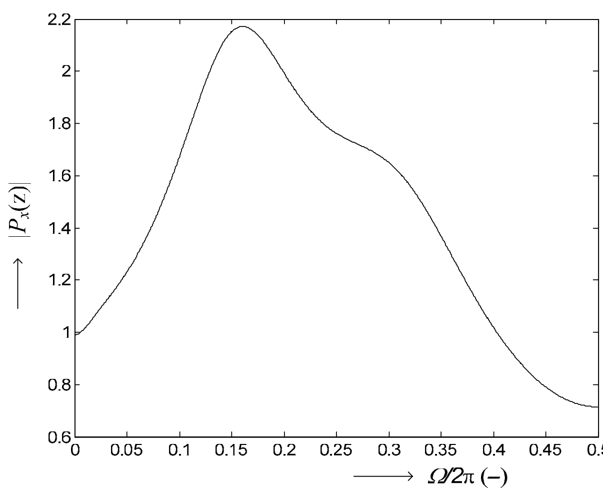

Figure 8: Magnitude frequency response of pre-emphasis filter.

Figure 7 gives the waveform of positive gradient impulse with and without pre-emphasis compensation in the direction of the axis x. The most essential change consists in the shortening of the leading and trailing edges of the gradient impulse. While for the gradient without pre-emphasis the rise time to 97% of the gradient measured is 250 µs, for the gradient with pre-emphasis the rise time to 97% of the gradient measured is less than 80 µs. The leading edge has been shortened ca. three times.

Figure 8 shows the magnitude frequency response of the adjusted pre-emphasis filter, with typoval unit transfer of the DC component. Fig. 9 and Fig. 10 give the waveforms of the positive gradient impulse with pre-emphasis compensation for the y and z directions. In the course of the gradient impulse 2 ms long the resonating nuclei got out of phase and the signal got lost. The gradient impulse was therefore shortened to 1.76 ms. The results obtained for the pre-emphasis compensation of gradient in the direction of the axis y are similar to those obtained for the axis x. Both gradient coils, in the direction of the axes x and y, are of identical design, they are only rotated by 90°.

The design of the gradient coil in the direction of the axis z differs from the design of gradient coils in the direction of the x and y axes. The waveform of the gradient impulse is therefore different. The rise time and the decay time of the edges are longer, and the ripple in the waveform of the magnetic field gradient is much greater. The length of the leading and the trailing edges of the gradient impulse is ca. 350 μs. Due to pre-emphasis compensation it was reduced to 60 μs.

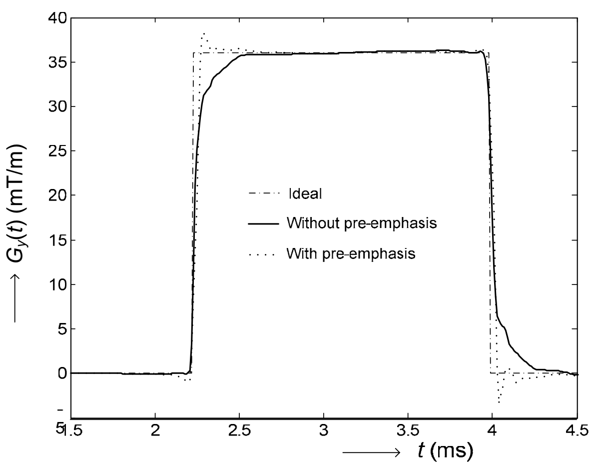

Figure 9: Comparison of positive gradient impulse G_y, length 1.76 ms, with and without pre-emphasis compensation.

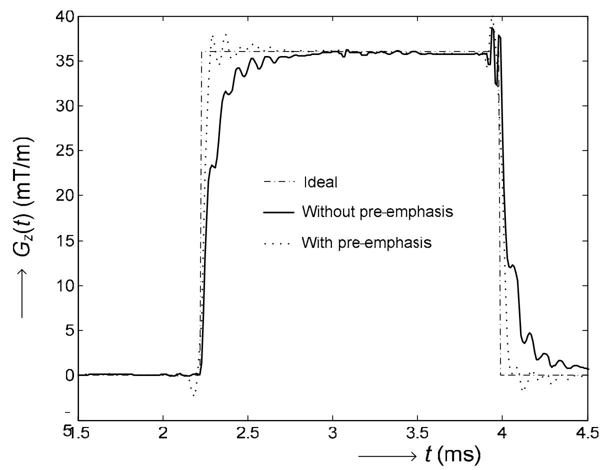

Figure 10: Comparison of positive gradient impulse G_z, length 1.76 ms, with and without pre-emphasis compensation.

4. CONCLUSION

The application of pre-emphasis compensation of gradient magnetic field has led to a qualitative improvement in the parameters of the magnetic field generated in an MR tomograph. It can therefore be expected that better results will be obtained in all regions of MR tomography and spectroscopy where the generation of gradient fields of a defined waveform with minimum switching times is required. Today the minimum applicable switching time of gradients in MR tomography is a limiting factor in the application of fast imaging sequences im MRI. Shortening the gradient edges and improving the magnetic field homogenity after a gradient impulse result in shortening the minimum applicable switching time of magnetic field gradients and the waiting time between gradient impulses, when the magnetic field is required to drop to the level of the homogenity of the basic magnetic field B_0. In that case the images of incisions in the human body can be measured faster and more accurately.

ACKNOWLEDGMENT

This work was supported within the framework of the research plans MSM 0021630516, GA102/07/0389 and project B208130603 of the Grant Agency of the Academy of Sciences of the Czech Republic.

REFERENCES

1. Vlaardingerbroek, M., *Magnetic Resonance Imaging*, Springer-Verlag, 2000.
2. Kubásek, R., E. Gescheidtová, and K. Bartušek, "Measurements of time characteristics of the gradient magnetic field," *27th Annual International Conference Medicine and Biology Society Shanghai*, 1–4, 2005.
3. Rajmic, P., "Statistical properties of wavelet spectrum thresholding rules," *48th International Scientific Colloquium*, 87–88, Ilmenau, 2003.

4. Gescheidtová, E., R. Kubásek, Z. Smékal, and K. Bartušek, "Automatic adjustment of time-variant thresholds when filtering signals in MR tomography," Lecture Notes in Computer Science (IF 0,513), 384–391, 2005.
5. Ljung, L., *System Identification: Theory for the User*, Prentice-Hall, Englewood Cliffs, NJ.

Optimization Method of EMI Power Filters

J. Sedláček, M. Hadinec, and Zoltan Szabó
BUT FEKT Brno, Czech Republic

Abstract— Electromagnetic interference (EMI) can be reduced to acceptable level using EMI filter circuits. Unfortunately, many known methods of filter design and optimization cannot be applied directly to power electronics, which has it own peculiarities. In comparison to EMI data communication filters EMI power filters operate typically under mismatched impedance conditions. One from important manner of a filter design and optimization process there is a filter modeling. The paper deals with methods of filter design and optimization useful in area of EMI power filter synthesis. Synthesis and optimization of different types of EMI power filters with required insertion loss and using of their equivalent models here are discussed are discussed in some practical examples.

1. INTRODUCTION

In present time the world is becoming more densely populated with devices that are increasingly sensitive to electromagnetic disturbances. In industrial spheres, electronic control systems, data processing equipment and other sensitive devices play an increasingly important role. Therefore solution of problems coupled with problematic of EMC (electromagnetic compatibility) is very important. In electrical engineering practice now are used many new circuit elements for electromagnetic interference (EMI) suppression. We can observe, that in area of EMC are growing different requirements to solve problems of electromagnetic emissions and electromagnetic susceptibility.

In area of EMC there are very often used EMI filters. Their using can be differed to solution of two different problems. At first it is the essential decreasing of undesirable electromagnetic pollution, on the other hand are used to increase electromagnetic immunity of any electrical equipments.

In telecommunications adequate methods for computing and solving EMC problems have been developed over the last years. Unfortunately, many of these methods cannot be applied directly to power electronics, which has it own peculiarities [1].

2. EMI FILTERS

Electromagnetic interference (EMI) can be reduced to acceptable level using filter circuits usually referred as EMI or RFI filters. EMI filters are usually low-pass filter circuits with serial choke coils and parallel capacitors. These filters can be generally divided to two different groups. First group are named as data filters — are used namely in telecommunication systems. EMI data filters are performed as well known low-pass filter configurations (LC ladder circuits). Because these filters are constructed for constant load and generator impedances, design and optimization of filters can be realized according known design and optimization procedures.

The second group of EMI filters are filters used in power electronic. In comparison to EMI data communications filters EMI power filters operate typically under mismatched impedance conditions. This major problem of EMI filter design for power electronic equipment is caused by the arbitrary generator and load impedances. These impedances are really arbitrary because neither their value can be known, filters are installed in different equipments and supply network. The design of power EMI filters is different then well known procedures of classical filter design and requires some special view and procedures.

EMI filters are generally two-ports characterized by insertion loss (IL) rather then voltage attenuation. An insertion loss definition and measurement method is clear from Fig. 1. The difference between the measured voltage appearing beyond the insertion point before (switch position1) and after the filter insertion (switch position 2) can be expressed as :

$$IL = 20\log\left(\frac{U_{L1}}{U_{L1}}\right). \tag{1}$$

The voltage U_{L1} can be expressed using resistances of load and generator, and then insertion loss is given:

$$IL = 20\log\left(\frac{U_g}{U_{L2}}\frac{R_L}{R_g+R_L}\right). \tag{2}$$

The requirement of insertion loss value must be fulfill in wide frequency range from DC to frequencies about hundred MHz. Thus analysis and measurement of the insertion loss must be made by filter design process in wide frequency range for many frequencies. Such a measurement procedure is not highly desirable in practical engineering. The chart in Fig. 2 presents typical frequency characteristic of insertion loss of EMI filters. In the pass band insertion loss must be negligible, from cut-off frequency f_c it monotonically increases. At the stop frequency f_s reaches insertion loss required value, up the stop frequency f_s due to parasitic effects exhibit curve some imperfections and usually decreases. After determining the required insertion loss in the stop band-pass, the next step of filter design is to choose a circuit configuration. Important factors may include a limitation on capacitive current for grounded equipments or the acceptable voltage drop across power line filters. For stringent suppression requirements must be also consider the mismatched impedance conditions. In area of power electronic EMC filter most often are used low-pass LC ladder filters in L, PI or T configurations. For high-performance applications are used also multistage LC circuits with higher number of basic sections. In power engineering practice, multistage filters having more then four stages are not very common. To suppress EMI on all wires, filter prototypes must be inserted in every wire of power lines. Thus power filter network becomes more complex with an increase in the number of wires to be filtered. The two-wire EMI filter should be studied as a six-terminal network. EMI power filters are inserted most often in three phase main supply lines and then must be filtered each wires including neutral. The complexity of EMI filters then significantly increases. The measurement of insertion loss in this case must be realized separately for all terminal pairs. According of used measurement system (symmetric, asymmetric or non-symmetric) the unused terminal pairs must be connected together to obtain the lowest insertion loss value. These specifications require the unused terminals to be grounded, ungrounded, or linked to ground through specific impedance [4].

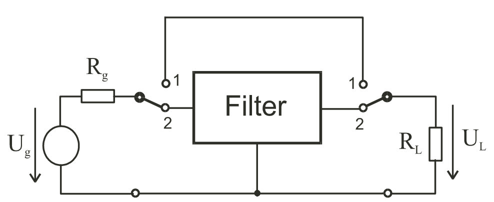

Figure 1: Insertion loss definition and measurement.

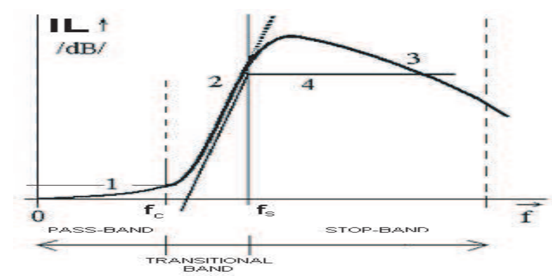

Figure 2: Typical frequency characteristic of EMI filter.

3. MODELING OF EMI POWER FILTERS

The synthesis of proper filter models (equivalent circuits) including function elements as well as parasitic elements is one from important parts of successful EMI filter design and optimization. Using modeling techniques can be analyzed the effects of parasitic phenomena and impedance mismatch.

In present time PC technique enables to apply direct calculation method very easy. The direct calculation method is also the simplest approach for generating a complete EMC filter model. This modeling method is based on equivalent filter circuit synthesis by means of built-in filter elements. The models can be synthesized from the limited data available from manufacturers but also with measured data. To express filter performance in required wide frequency range, the basic filter elements must be assumed not ideal. Basic electrical element must be replaced by equivalent circuit including their parasitic elements (Fig. 3). The approximate values of parasitic elements of most often used EMI filter elements (inductors and capacitors) are summarized in Table 1 [1].

4. OPTIMIZATION OF EMI FILTERS

As an example of EMC filter model synthesis and optimization a filter model for three phase power FN 3280H-64-34 and is here presented. The first step of filter model synthesis was grown from known basic (given in manufacturer's data sheet) filter topology (Fig. 4). In the second step the given topology with ideal basic elements was for each from three lines rebuilt using real models of each (R, L, C) filter elements. The initial filter value parameters was approximated and filter

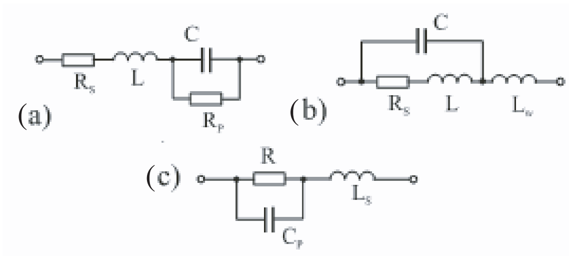

Figure 3: Equivalent circuits: (a) of capacitor, (b) of inductor, (c) of resistor.

C	$L_{parasitic}$	Remark
< 10 nF 10 nF - 1 µF >1 µF	10 - 20 nH 40 nH 30 - 100 nH	feedthrough type capacitors in orders lower then 1/10 values
L	R_S	$C_{parasitic}$
< 10 µH 50 µH - 200 µH >200 µH	1,5 mΩ 10 mΩ 0,5 Ω	2 pF 5 pF 10 - 30 pF

Table 1: Typical element values of real filter elements.

with equal load and generator resistors (50 Ω) was analyzed using commercially available analyzers MicroCap, TINA and P-SPICE 9. After circuit analysis frequency curve of insertion loss was compared with frequency curve presented by the same measuring conditions in manufacturer's data sheet. Using optimizer routines from analyzers was step by step optimized frequency curve of filter model. As result of optimization procedures the values of each filter model elements were obtained. The resulting circuit diagram of filter model with their parameter values is shown in Fig. 5.

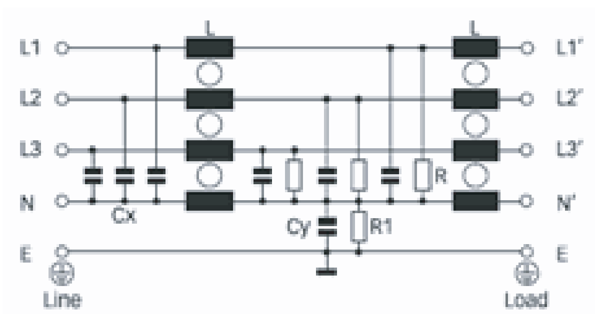

Figure 4: Circuit topology of power EMI filter.

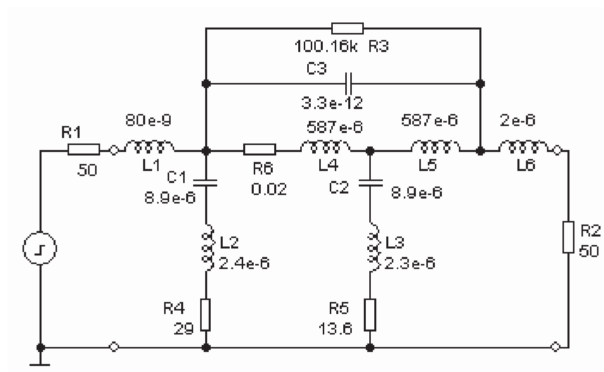

Figure 5: Circuit diagram of filter model.

Using created filter model an influence of resistance of generator R_1 and resistance load R_2 on insertion loss curve of filter was investigated to determine worst case of operation. How it is seen from curves (Fig. 6, Fig. 7), effect of mismatch conditions in worst case can decrease initial insertion loss about 15 dB in entire working frequency range what must be by in real filter work respected. We can see also from figures that in a practice operating filter conditions must be to mismatch conditions, which are leading to worst case operating stage of filters taken in account for this filter types mainly parameters of load resistance of filter.

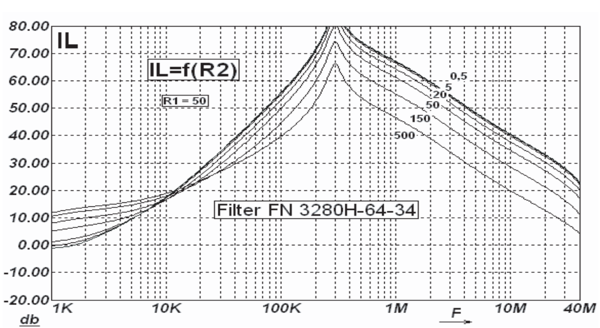

Figure 6: Insertion loss as function of load R_2.

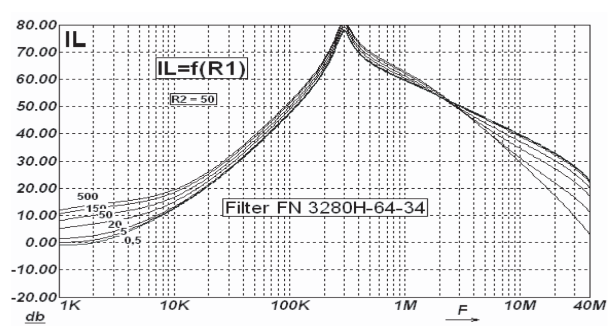

Figure 7: Insertion loss as function of resistance R_1.

5. CONCLUSIONS

In the paper was shortly discusses problems of power EMC filter design and optimization. In a practical example of the power EMC filter was prescribed a synthesis method which enable to set and optimize equivalent filter model including their element value parameters. The created model enables to investigate influence of mismatched condition very quickly without measurement of filter. The great advantage of optimization method is that enable to optimize resulting filter model parameters by usage of usually accessible software for network analysis without requirement of special numerical programs what brings new possibility for many designers in area of EMC filter design and optimization.

ACKNOWLEDGMENT

This work has been supported by the Research Project: MSM 0021630513 and Grant Agency of the Czech Republic under Grant 102/03/1181, 102/04/0442.

REFERENCES

1. Thayne, L., *Electromagnetic Compatibility in Power Electronics*, IEEE Press, J. K. Eckert, Sarasota, 1995, USA, 2004.
2. Wiliams, T. and K. Armstrong, *EMC for Systems and Installations*, Newnes, Butterworth-Heineman, Oxford, Great Britain, 2000.
3. Rybak, T. and M. Steffka, *Automotive Electromagnetic Compatibility (EMC)*, Kluwer Academic Publishers, Norwell, Massachusetts, USA, 2004.
4. Dřínovský, J. and J. Svačina, "Estimation of EMI filter performance for the "Worst-Case" system," *Radioengineering*, Vol. 15, No. 4, ISSN 04-510-79, Brno, 2006.

T_1 Relaxation Time of the Xenon 129 Influenced by Magnetic Susceptibility of the Laboratory Glasses

K. Bartušek[1,2], **J. Rychnovský**[1,2], **and P. Fiala**[1]

[1]Institute of Scientific Instruments of the ASCR, v.v.i
Královopolská 147, Brno 612 64, Czech Republic
[2]Department of Theoretical and Experimental Electrical Engineering
Faculty of Electrical Engineering and Communication, Brno University of Technology
Kolejni 2906/4, Brno 612 00, Czech Republic

Abstract— Every substance has its own susceptibility, which can affect homogenous magnetic field in magnetic resonance measuring. T_1 and T_2 relaxation times of measured materials or gasses can be reduced by the deformation of the local homogenous magnetic field. By the laboratory glasses magnetic susceptibilities measurement, we obtained theirs walls influence to thermally polarized ^{129}Xe T_1 relaxation times.

1. INTRODUCTION

The magnetic susceptibility is the degree of magnetization of a material in response to an applied magnetic field. The dimensionless volume magnetic susceptibility, represented by the symbol $\chi(\kappa, K)$, is defined by the relationship

$$M = \chi \mathbf{H}, \tag{1}$$

where M is the magnetization of the material (the magnetic dipole moment per unit volume) [A/m], $\mathbf{H}$ is the applied field [A/m].

The magnetic induction $\mathbf{B}$ is related to $\mathbf{H}$ by the relationship

$$\mathbf{B} = \mu_0(\mathbf{H} + M) = \mu_0(1+\chi)\mathbf{H} = \mu\mathbf{H}, \tag{2}$$

where μ_0 is the permeability of vacuum, $(1+\chi)$ is the relative permeability of the material. If χ is positive, then $(1+\chi) > 1$ and the material is called paramagnetic. In this case, the magnetic field is strengthened by the presence of the material. If χ is negative, then $(1+\chi) < 1$, and the material is diamagnetic. The magnetic field is weakened in the presence of the material [1]. Influence of the magnetic susceptibility of laboratory glass tubes to ^{129}Xe relaxation times was observed. It can help us to choose eligible material for others gas experiments, relaxation times and hyperpolarized noble gases measuring.

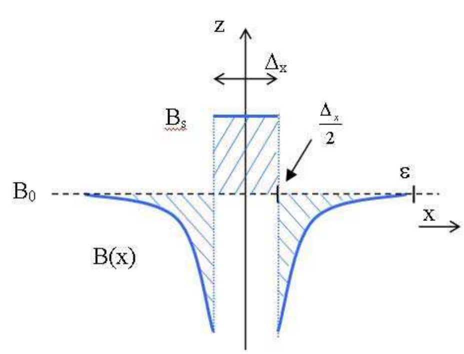

Figure 1: Idealized shape of magnetic induction field in paramagnetic sample and its vicinity.

2. THE USED METHOD

The method of the magnetic susceptibility measurement is based on presumption of constant magnetic flux in working space of superconducting magnet. Inserting the sample of thickness Δx and with magnetic susceptibility χ_s into the homogenous magnetic field, causes local deformation of this homogeneous magnetic field (idealized case is in Fig. 1)

$$B_s = B_0 \cdot (1 + \chi_s). \tag{3}$$

If we can determine the course of $B(x)$ (using suitable MRI (Magnetic Resonance Imaging) technique and reference substance giving MR signal in vicinity of material), we can also enumerate B_s and χ_s values of the investigated sample material. From principal case in Fig. 1 and using (3) we can derive:

$$\chi_s \cong \frac{2 \int\limits_{\Delta_x/2}^{\varepsilon} [B(x) - B_0] \cdot dx}{\Delta_x \cdot B_0}. \tag{4}$$

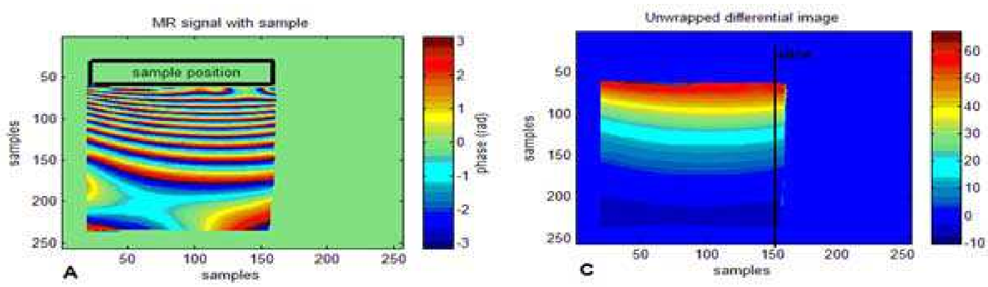

Figure 2: Images obtained from experimental verification of the method, processed in MATLAB 7.1. In the left picture is shown sample position of silica glass affecting magnetic field in reference water sample.

Described method was numerically in Ansys modeled. The method of the magnetic susceptibility measurement was experimentally verified with number of samples on 200 MHz MR tomograph in ISI AS Brno. Reference substance was water ($\chi_{\mathrm{H_2O}} = -9.04 \cdot 10^{-6}$) filled into cell. The method of Gradient echo [2] was used to acquire MR image with contrast corresponding to the magnetic induction changes in measured volume of sample vicinity. For the used MR technique the phase change $\Theta(x)$ response to the magnetic induction change

$$B(x) = \frac{\Theta(x)}{2\pi\gamma T_E} + B_0, \tag{5}$$

where γ is gyromagnetic ratio of water, $T_E = 5.56$ ms was used echo-time. In this way we can identify the course of magnetic induction change in water nearby the sample. From known thickness Δx of the sample with use of (5) the susceptibility of samples can be calculated.

3. PREPARATION OF A SAMPLE

A main part of the sample is made from two Delrin pieces — the cylindrical body (inner diameter 28 mm, length a bit longer than 130 mm, because of sealing rubber o-ring) and the screw cap with a pasted-in Teflon sealed glass valve. Through the valve is the sample evacuated and filled by xenon gas. A laboratory glasses tube can be inserted in to the cylindrical body of the Delrin sample. Length of glass tube is 130 mm and outer diameter 28 mm. Tube wall thickness is for Si glass 1.6 mm, SIMAX 1.4 mm, SCHOTT 1 mm. Teflon in spray (Boehlender).

Figure 3: Delrin sample is shown in the left picture. In the right picture are shown Schott glass (right hand side) and Si glass + Teflon coating (left hand side). Both pictures are not in the same scale.

Delrin sample was always (single or with a glass tube) evacuated by up to $\approx 10^{-3}$ Pa and than filled with natural xenon gas to 300 kPa. After it was the glass valve shut and the sample was disconnected of the vacuum apparatus by rubber tube. Finally was the sample inserted into the 200 MHz NMR (nuclear magnetic resonance) system for relax.

4. RESULTS

The glass samples were measured by means of described NMR method. Thermally polarized ^{129}Xe relaxation times were by common saturation recovery method measured. Longitudinal magnetization was by ten RF (radiofrequency) pulses with repetition time $T_R = 2\,\mathrm{s}$ lowered to zero. Nuclei were excited by 90° RF pulse at the time ti and transversal magnetization was measured. The measurement was repeated with variable time ti and from approximation transversal magnetization course was the T_1 relaxation time determined — Table 1.

Table 1: Measured relaxation times T_1 and magnetic susceptibility χ for selected materials.

	SCHOTT	SIMAX	Si	Si + Teflon	Delrin
$\chi[x10\,\mathrm{exp}^{-6}]$	−11.7	−8.8	−8.79	−8.79	−8
T_1 [s]	1788	1349	1025	1459	1242

Contexture of relaxation times of ^{129}Xe and walls susceptibility of glass material susceptibility shows Fig. 4 using SCHOTT glass preferable to obtain longer relaxation time.

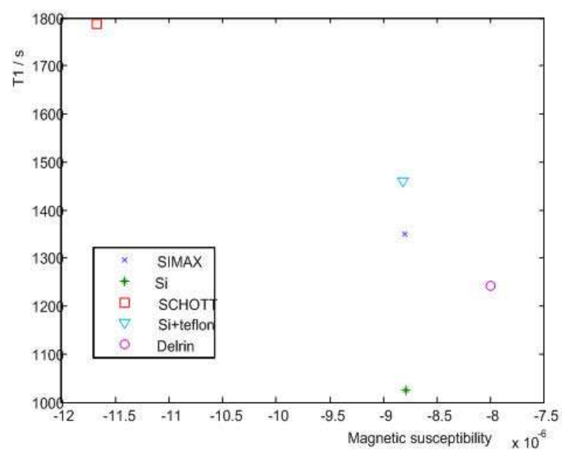

Figure 4: Contexture of ^{129}Xe relaxation times and walls material susceptibility.

5. DISCISSION

As results shows, SCHOTT glass is more inclinable to obtain longest relaxation times. But technically, it is soft glass, and it is hardy for joining with other harder glasses. More important is ratio between Si and Si + Teflon glass, which is cheaper and mostly used for glass cells. It would be attractive, to compare results with PYREX glass. SIMAX has a little bit shorter relaxation time than Si + Teflon, and the question is about Teflon heat and fire resistance when foreheads are mounting to the tube by reason of a laser beam use.

6. CONCLUSION

The magnetic susceptibility of laboratory glasses and its influence to ^{129}Xe relaxation times were measured. The results are shown in Fig. 4 and Table 1. SCHOTT glass has the longest relaxation time, but there are some difficulties with jointing with others glass types. SIMAX glass and silica glass with Teflon coating has comparable results for relaxation times. The disadvantage for Teflon is its abrasion sensitive and SIMAX is more expensive than silica glass.

ACKNOWLEDGMENT

This work is supported by GAAV ČR IAA1065303 and by GAČR 102/07/0389.

REFERENCES

1. "Definition of the magnetic susceptibility," February 2007. [on line] http://en.wikipedia.org/wiki/Magnetic_susceptibility.

2. Levitt, M. H., *Spin Dynamics: Basics of Nuclear Magnetic Resonance*, ISBN: 0-471-48921-2, John Wiley & Sons, 2001.
3. Steinbauer, M. and K. Bartušek, "Magnetic properties of materials-comparison of NMR and inductive measuring methods," *28th International Conference SPETO 2005, 28th International Conference on Fundamentals of Electrotechnics and Circuit Theory (ICSPETO 2005)*, ISBN 83-85940-27-8, Silesian University of Technology, Gliwice, Polsko, 67–70, 2005.

Experiments of Accuracy Air Ion Field Measurement

K. Bartušek[1], **P. Fiala**[2], **T. Jirků**[2], **and E. Kadlecová**[2]

[1]Institute of Scientific Instruments Academy of Sciences of the Czech Republic
Královopolská 147, 612 64 Brno, Czech Republic
[2]Department of Theoretical and Experimental Electrical Engineering, University of Technology Brno
Kolejni, 4, 612 00 Brno, Czech Republic

Abstract— An analysis of the electric state of air shows the presence of various ion sorts. The therapeutic effect of negative high-mobility ions of proper concentration is known. This positive effect was observed in caves that are used for speleotherapy. This article presents the capability of methods for measuring ion concentration and for ion spectral analysis. Here are new gerdien tube design steps based on numerical analysis and its experimental verification. Article describe of any experiments with different air ion generator.

1. INTRODUCTION

Air ion concentration and composition belong to the frequently monitored parameters of the atmosphere [5]. Their influence on living organisms has been the subject of intensive studies. Earlier research has demonstrated the positive influence of light negative ions and air cleanness on human health. The Department of the Theoretical and Experimental Electrical Engineering of Brno University of Technology and the Institute of Scientific Instruments of the Academy of Sciences of the Czech Republic are involved in the research of ion field in office and living spaces. The objective is to increase the concentration of light air ions in these spaces. Another task is to set up a simulated therapy room, with conditions similar to speleotherapy caves. It sets the requirements for accurate measurement of ion field with good repeatability. The article deals with the design of gerdien condenser and peripheral measuring devices. An optimal design is important for eliminating the inaccuracy of ion concentration measurement.

2. MEASURING METHOD

Several methods are currently used to measure air ion fields: the dispersion method, the ionspectrometer method, the Faraday cage method, and the gerdien condenser method, whose principle is shown in Figure 1. Here is $d1$-inner electrode diameter, $d2$-outer electrode diameter, l-length of gerdien condenser, M-air flow volume rate, v-air flow velocity, e-elementary charge of electron, $\oplus$ positive air particle (ion), $\ominus$ negative air particle (ion). The gerdien condenser consists of two electrodes. There is an electric field between the inner electrode (the collector) and the outer electrode. The field is imposed by voltage source U. Air ions flow from the fan through the gerdien condenser. Negative ions in the electric field impact the collector, and the current produced is measured by a pA-meter. The current measured is proportional to air ion concentration. The model of the measuring system is shown in Figure 2. The values measured carry systematical measurement errors. This is due to leakage currents and parasitic capacitances (modeled by I_{LEAK} in Figure 2) [6]. We have to consider leakage resistances R_{AK} of gerdien condenser, leakage resistances and capacitance of the pA-meter input (R_{EH}, C_{EH}, R_{EL}, C_{EL}), insulation resistance (R_V) of the collector voltage source. The current measured is further affected by the input resistance of pA-meter and the input resistance of voltage source (R_U, C_U). To minimize the measurement error, R_{AK}, and R_V should be much larger than R_I, and R_{EH}, and R_{EL} should also be much larger than R_{OUT}. Time constant $R_U C_U$ has to be much larger than the measuring time.

3. NEW DESIGN OF GERDIEN CONDENSER

The inner and outer electrodes are elliptical in shape. This shape ensures that the flow of air is laminar. Air flow turbulence can distort the accuracy of measurement. The surface of the electrodes is required to be as smooth as possible. These aspects make the design of gerdien condenser quite demanding (fine grinding, lapping, etc.). The new design of gerdien condenser is shown in Figure 3.

Since in the measurement of air ion concentration very small currents are detected, it is necessary to eliminate the influence of ambient electric charge. The influence of magnetic fields has to be minimized too.

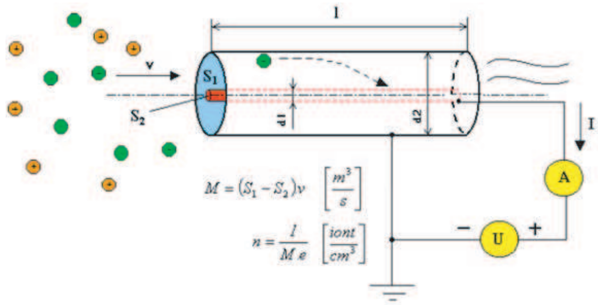

Figure 1: Principle of gerdien condenser method.

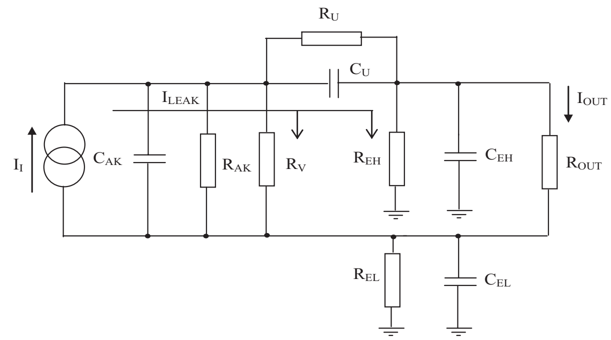

Figure 2: Model of a system for measuring air ion concentration - the gerdien condenser method.

Figure 3: New gerdien condenser.

4. WEAK CURRENT AMPLIFIER

The current flowing through the gerdien condenser is due to the ion concentration. Current intensity depends on polarization voltage, on the dimension and parameters of gerdien condenser, and on ion concentration. The specific current range for the designed gerdien condenser is 10^{-10}A–10^{-13}A. For the following measurement it is suitable to convert the current to voltage. Because the current is very weak, it is suitable to do this near the gerdien condenser. The low-level amplifier is realized with INA 116-Figure 4. The INA 116 has a very low input bias current $I_{b,\max} = 100\,\text{fA}$. The design of the amplifier is shown in Figure 5. The gain of INA 116 is set by resistor R_{10}.

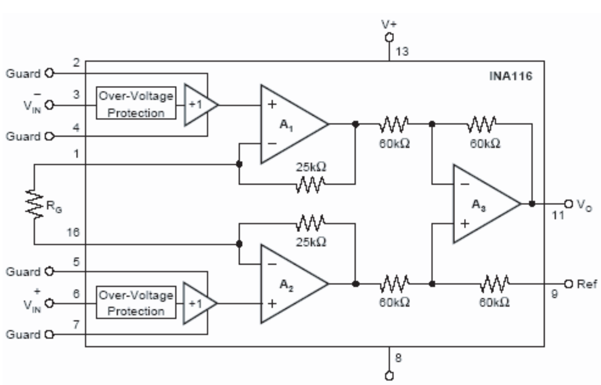

Figure 4: Principal scheme of INA 116.

Figure 5: Design of low-level amplifier.

5. NUMERICAL MODELING, VERIFICATION

It is possible to carry out analysis of a MG model as a numerical solution by help of Finite element method (FEM). The electromagnetic part of the model is based on the solution of full Maxwell's equations. It was solved like simply electrostatic field. This results showed to new facts in gerdien condenser design. The new knowledge were tested in many experiments and our measurement system had approximately 50% better characteristics. In Figure 6 is shown one effect of light negative ion inside of gerdien condenser. There are showed the non-primitive moving of one electron. Therefore the sensor has higher noise then sensor with filter. New design of gerdien condenser was made with filter for the specific particles. Result of new experiments are showed in Figure 7.

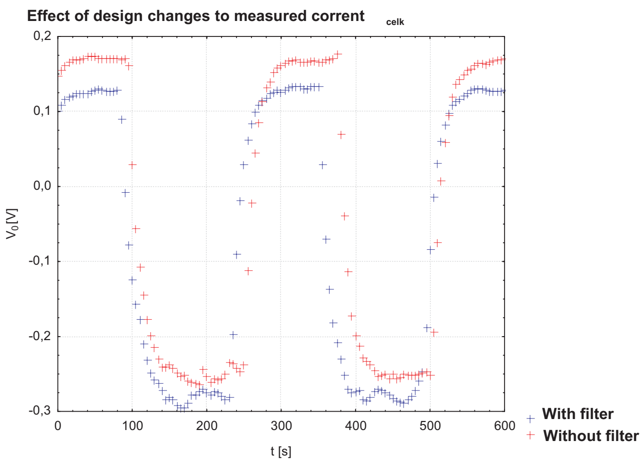

Figure 6: Result-characteristics of gerdien condenser with filter, time depend.

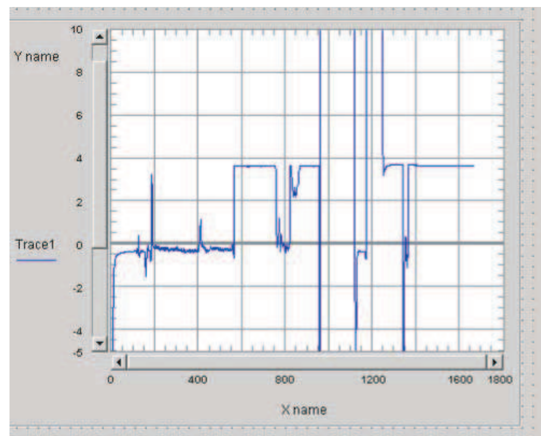

Figure 7: Result-characteristics of gerdien condenser with filter.

6. TESTS OF GERDIEN CONDENSERS

The gerdien condenser of new design was tested according to the special measuring methodology. The scheme of this method is shown in table 1. The test of the gerdien condenser method was tested on several sources of ion generators. The experiments are shown in Fig. 8 and Fig. 9.

Table 1: Air ion concentration methodology.

Measuring type		Fan	Voltage	Ion generator	Air flow Regulation	Comment
	Mode	F	V	I	R	
Absolute	Testing A	0	0	0	0	A
		0	1	0	0	A
		1	0	0	0	AF
		1	1	0	0	AFV
Diferential	Testing D	0	0	0	0	D
		0	1	0	0	DV
		1	0	0	0	DF
		1	1	0	0	DV
	Measuring D	0	0	1	0	DI
		0	1	1	0	DVI
		1	1	1	1	**DVIF**
Legend: 0-device is **off**, 1- device is **on**						

Table 1. Table of gerdien tube measurement method.

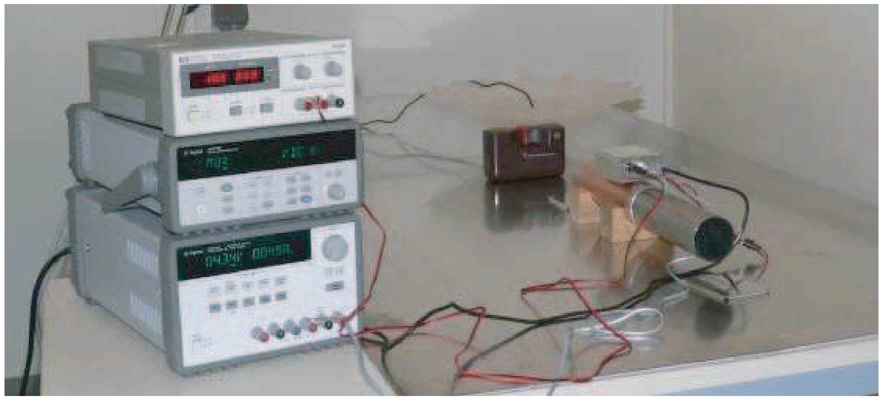

Figure 8: Gerdien condenser measuring method- test by electronic generator.

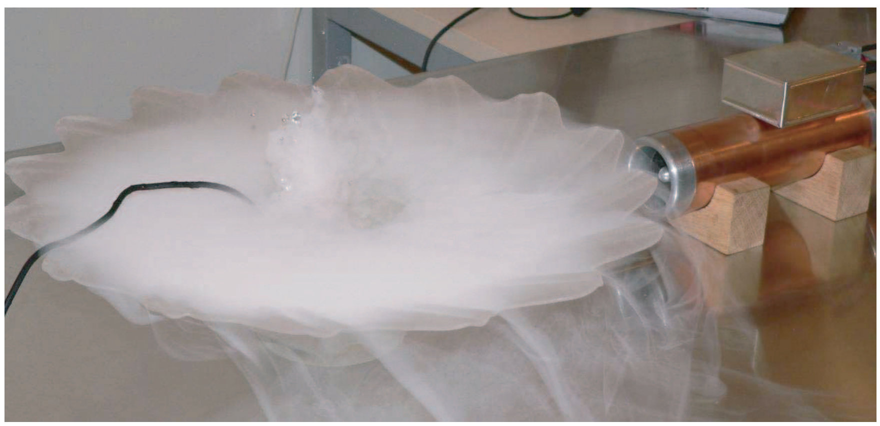

Figure 9: Gerdien condenser measuring method- test by water "natural" generator.

7. CONCLUSION

The new design of gerdien condenser and the optimization of peripheral measuring devices have minimized the systematic error of measurement. The new system allows measuring air ion concentration with a sensitivity $> 100\,\text{ions/cm}^3$. The ion mobility is in the interval $0.3 - 100\,\text{cm}^2\text{V}^{-1}\text{s}^{-1}$. The system is used to measure ion field distribution in living and office spaces.

ACKNOWLEDGMENT

The paper were prepared within the framework of VUT Brno of the Czech Republic and with the support of the research plan MSM 0021630516 and grant GAAV No. B208130603.

REFERENCES

1. Bartušek, K., Měření speleoterapeutických parametrů jeskyní pro lékařské účely. Interní text UPT AV ČR 1997.
2. Buřival, Z., Vliv prostorového náboje v atmosféře na znečištění vzduchu v technologických provozech. Knižnice odborných a vědeckých spisů VUT Brno.
3. Spurný, Z., Atmosferická ionizace. Praha. Academia 1985.
4. Puškeilerová, L., Nové poznatky o měření volných záporných iontů v laboratorním prostředí. Příspěvek k VŠTČ FEI. Brno 2000.
5. Israël, H., Atmosphärische Elektrizität. Akademische Verlagsgesellschaft Leipzig 1957.
6. Smutný, T, Vliv obvodových prvků na přesnost měření iontových polí Diplomová práce 2004 VUT Brno
7. Kafka, V, Saturační a spektrální charakteristika iontového pole, Diplomová práce 2004 VUT Brno

The Calculation of the V-shape Microstrip Line Impedance by the Conformal Mapping Method

Václav Šádek, **Pavel Fiala**, **and Michal Hadinec**
Faculty of Electrical Engineering and Communication, Brno University of Technology
Kolejni 2906/4, 612 00 Brno, Czech Republic

Abstract— The boundary element method (BEM) is used for the strip centered coaxial line (SCCL). The common microstrip line has one disadvantage — a lot of electromagnetic field is spread outside the dielectric substrate. This field moves $\sqrt{}$er times faster than field under the microstrip inside the dielectric substrate. This deformation of the field (HEM wave) complicates the application of the microstrip line on frequencies over c. 20 GHz. Described complication can be eliminated in the structure, which cumulates major portmon of power density of the EM field in dielectric substrate to the detriment of free space above the strip.

1. INTRODUCTION

A lot of different electronic equipments have to work together. Unfortunately the power levels among them are over 200 dB very often. Coaxial structures are widely used because of their good shielding effect, which suppress the fields around strong distortion sources (e.g., transmitting antenna feeder) and protect sensitive parts of receivers, measurements etc. [1, 2].

Whereas coaxial line (two concentric cylindrical electrodes) is widely known, strip-centered coaxial line (SCCL, Fig. 1.) is mentioned rarely (founded only in very special literature like [3]).The SCCL structure also offers a very attractive occasion of matching to microstrip line, coplanar waveguide, etc.

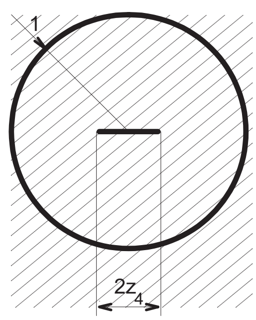

Figure 1: Normalized strip-centered coaxial line.

The sequence of three conformal mappings (used also in [1, 2]) faces to the formula for the characteristic wave impedance of the V-shape microstrip line

$$Z_0 = \frac{30 \cdot \pi^2}{\sqrt{\varepsilon_{r,ef}}\,\mathrm{arctanh}\sqrt{\frac{2\beta}{\alpha+\beta}}}. \tag{1}$$

where

$$\alpha = \sqrt{\left(\frac{h}{\sin\varphi}\right)^{\frac{\pi}{\varphi}} + \left(\frac{b}{\tan\varphi}\right)^{\frac{\pi}{\varphi}}} \quad \textbf{and} \quad \beta = \sqrt{\left(\frac{h}{\sin\varphi}\right)^{\frac{\pi}{\varphi}} + \left(\frac{b}{\sin\varphi}\right)^{\frac{\pi}{\varphi}}} \tag{2}$$

The effective relative permittivity is given as

$$\varepsilon_{r,ef} = \varepsilon_r - (\varepsilon_r - 1)\frac{\mathrm{arctanh}\sqrt{2 + 2\frac{\alpha}{\beta}}}{\mathrm{arctanh}\sqrt{\frac{2\beta}{\alpha+\beta}}}. \tag{3}$$

The result (1) was compared to numerical solution in *sc-toolbox* in MATLAB$^{\mathrm{TM}}$ [3]. The conformal mapping is not absolutely exact; there is an approximation in the method, which causes the error. This error depends on h/b ratio and in a mild way also on the angle φ. and the result (1) is always bigger than numerical result. The worst case is for small h/b ratio (for $h/b = 1.5$ is error approximately 15%), for higher ratios increase (for $h/b = 5$ is only 10% and for $h/b = 50$ less then 5%). The error of calculated effective relative permittivity is hard to determine, but influence of this error would be very small, because of square root in (1).

2. BOUNDARY ELEMENT METHOD

The boundary element method (BEM) [5] is based on integral Maxwell's equations (Laplace's equation is solved along boundary of the structure only). We need values of the field intensity just along PEC's for characteristic impedance determination according formula below:

$$Z_0 = \frac{\int E dy}{\int H dx} = 120\pi \frac{U}{\int\limits_0^{z_4} E_y dx}, \tag{4}$$

where U is voltage between conductors and E_y is electric field y-component along central electrode. (The integrals in first fraction are only informative; they both are not displayed in exact form). Two different strategies have been tested. First of them is based on constant number of boundary elements ($n = 50$) per one basic element. The flat inner electrode is divided onto $n = 50$ elements, the round outer electrode is divided also onto $n = 50$ elements and both the magnetic walls are also divided each into $n = 50$ pieces. That means total sum of all boundary elements is $4n = 200$. The lengths of element are not the same, especially in case of $z_4 \neq 0.5$.

The second strategy is based on equidistant division of the border (except outer electrode). The inner electrode is divided to z_4 times n pieces, the continuing magnetic wall into $(1 - z_4)$ times n pieces, the outer electrode into n elements and last magnetic wall also n elements. On the ground of calculation in wide range of z_4, the number of elements was $n = 100$.

Table 1: Results of analysis (error compared to Wadell [3]).

Z_0 [Ω] / error [%]				
z_4	Wadell [3]	scCtoolbox	BEM-1	BEM-2
0,01	317,89	317,86 / 0,01	651,5 / 105	323,4 / 1,73
0,05	221,33	221,31 / 0,02	273,3 / 23,5	223,2 / 0,85
0,1	179,74	179,71 / 0,02	206,8 / 15,1	180,8 / 0,55
0,2	138,16	138,11 / 0,03	152,7 / 10,5	138,6 / 0,35
0,3	113,83	113,73 / 0,08	122,8 / 7,52	114,1 / 0,25
0,4	96,57	96,34 / 0,24	96,5 / 0,03	96,63 / 0,06
0,5	82,63	82,66 / 0,04	82,9 / 0,32	82,9 / 0,34
0,6	71,19	71,17 / 0,03	71,42 / 0,32	71,39 / 0,28
0,7	60,98	60,94 / 0,06	60,98 / 0,38	61,15 / 0,28
0,8	51,22	51,17 / 0,08	51,48 / 0,50	51,38 / 0,32
0,9	40,70	40,64 / 0,15	41,03 / 0,81	40,89 / 0,48
0,95	33,98	33,89 / 0,25	34,44 / 1,35	34,24 / 0,76
0,99	24,73	24,57 / 0,64	26,14 / 5,71	25,39 / 2,68

3. RESULTS

Results of all mentioned methods are displayed in Table 1. All results are compared to relevant results of method mentioned in Wadell's book [3], however he doesn't inform about the accuracy of the mentioned formula. He only cites his sources — Bongianni [6] and Hilberg [7]. Bongianni made an experiment which confirms this method (the accuracy is in range of measurement errors), Hilberg is the author of this method, but he only describes it, not compare to any other method.For each value of z_4 has been also numerical Schwarz-Christoffel method used [4]. The result of this method is in very good agreement with Wadell's results [3].

4. CONCLUSION

One method founded in literature [3] is easy, but with the chicken-to-egg problem of choosing one of two formulae according to their results. The error of designed method compared to [3] is very small, grows for both methods for z_4 very close to 0 or 1, but for middle values of z_4 (range 0.4 to 0.9 in 1st variant and 0.05 to 0.95 in 2nd one) is the error under the level 1% There is a wide space for next work on this thema. First of them is a suppression of the error, next different variants of the dielectric substrate (multiple layers, segments, gaps ...). Also different numerical models should be calculated for better verification of results. Also experimental results will be heplful for next work.

REFERENCES

1. Svačna, J., *Electromagnetic Compatibility — Lectures*, Textbook of Brno University of Technology, FEKT VUT Brno, 2002.
2. Armstrong, K., *Design Techniques for EMC*, http://www.compliance-club.com/keith_armstrong.asp.
3. Wadell, B. C., *Transmission Line Design Handbook*, Artech House, Boston/London, 1991.
4. Driscoll, T. A., *SC-Toolbox, for MATLAB*, http://www.math.edu/ driscoll/SC/.
5. Paris, F. and J. Canas, *Boundary Element Method*, Oxford University Press, Oxford, 1997.
6. Bongianni, W. L., "Fabrication and performance of strip-centered microminiature coaxial cable," *Proceeding of the IEEE*, Vol. 72, No. 12, 1810–1811, December 1984.
7. Hilberg, W., *Electric characteristics of Transmission Lines*, 122, Artech House Nooks, Dedham, MA, 1979.

Experimental Results of a Wave Guide Using a Photorefractive Material SBN:Ce

Francisco Marroquín Gtz[1,2], **Nikolai Korneev**[2], **A. Apolinar Iribe**[3], **and A. García B.**

[1]Universidad Politécnica de Pachuca (UPP), Departamento de Mecatrónica
Carretera Cd. Sahagun-Pachuca, Hidalgo, Km. 20, C. P. 43830, México
[2]Instituto Nacional de Astrofísica, Óptica y Electrónica (INAOE)
Apdo. Postal 51 y 516, C. P. 72000, Puebla, México
[3]Universidad de Sonora (UNISON), Apdo. Postal 1626, C. P. 83000, Hermosillo, Sonora, México

Abstract— The photorefractive effect is a physical phenomenon whereby the local index of refraction is modified by spatial variations of light intensity. It is strongly observed when coherent rays interfere with each other in a photorefractive material, which forms spatially varying patterns of illumination. In this investigation, we report experimental results obtained when the light place of laser of He-Ne by an arrangement of photoinduced waveguides in a Strontium Barium Niobato (SBN), which it has a large electro-optic coefficient delivering a fast response time and high two wavelength maxing gain. The results reveal the important role that carrier out the phenomenon of transverse modulation instability in the control of light. The possible applications can be scientific and technological, the optic wave guides as well we know they transport the light in a transparent medium, in this case SBN:Ce, in a controlled way, so, also it is possible the fabrication of devices for communication systems or optoelectronic integrated.

1. INTRODUCTION

The study of non-linear effects on photonic periodic structures (lattices) is of great importance due to the possibilities of controlling propagation and trapping of light. These structures are present on biological systems [1], non-lineal optic guides [2], solid-state systems [3] and Bose-Einstein condensates [4]. The stability analysis of solitary and periodic waves is of vital importance for controlling trapping of light. Recently, a review on the topic was presented [5]. In the spatial domain, a light wave propagating through nonlinear auto-focusing media is auto-compressed on its initial state's intensity profile; resulting on an interesting phenomena named auto-compression of periodic patterns [6], interesting because it can produce a periodical array of waveguides. These structures have the particular property of being able to change sign and value of the non-linearity, as well as the typical property of changing refraction index's period and modulation. However, experimental studies on the stability of these patters in photorefractive materials are few when compared to theoretical studies on the same topic. Lately, it was shown that the compression of a periodic light pattern is limited by the creation of sub-fringes inside the original fringe pattern. This behavior is explained using a transitory instability that amplifies the running waves inside the crystal [7]. On this experiment a Barium Niobate Oxide (BTO) photorefractive crystal was used. In [8] compression was limited by fringe pattern breaking on the transverse direction; this limitation was explained by transverse modulation instability using a Barium Strontium Niobate (SBN:Ce) crystal.

On this article we report experimental results on guiding a He-Ne Gauss laser beam. Beam control and guidance is produced by an array of photoinduced waveguides created on a SBN crystal by an external electric field. We present optimal optics requirements for the involved physical variables.

2. EXPERIMENTAL ARRAY

Figure 1 shows the experimental array used to control and guide the light beam. As optical material, a cerium doped Strontium Barium Niobate ($Sr_{0.6}Ba_{0.39}Nb_2O_6$:Ce = SBN:Ce) photorefractive crystal was used, an external electric field was applied to increase the non-linearity. Crystal's dimensions are $5 \times 5 \times 5\,\mathrm{mm}^3$. A Nd:Yag (532 nm, 100 mW) emitted and expander laser beam was used to illuminate the crystal. A shadowing obstacle (1 mm width) was placed in the trajectory of the green beam before the crystal, producing a 1.5 mm wide shadow on the whole crystal. Additionally, two green beams impinged on the crystal producing an interference pattern. The propagation plane of those two green beams was perpendicular to the plane of the shadow on the crystal. These beams were obtained slitting, with a 50/50 beam splitter, a laser beam from a solid-state device

(532 nm, 45 mW). Finally, a red Gaussian beam with lineal vertical polarization from a He-Ne laser (633 nm, 10 mW) impinged on the shadow zone of the crystal and in between the green beams. The red and green beams propagated on the same plane. This array leads to concentration of all the high voltage applied to the crystal's faces on the shadow zone, raising the electric field threshold for superficial discharges on the crystal when compared to traditional geometry used for writing on photorefractive crystals. The external voltage is applied to the plane formed by the green and red beams producing a high contribution to the non-lineal part of the refraction index [7, 8], and raising the auto-focusing of the green fringes.

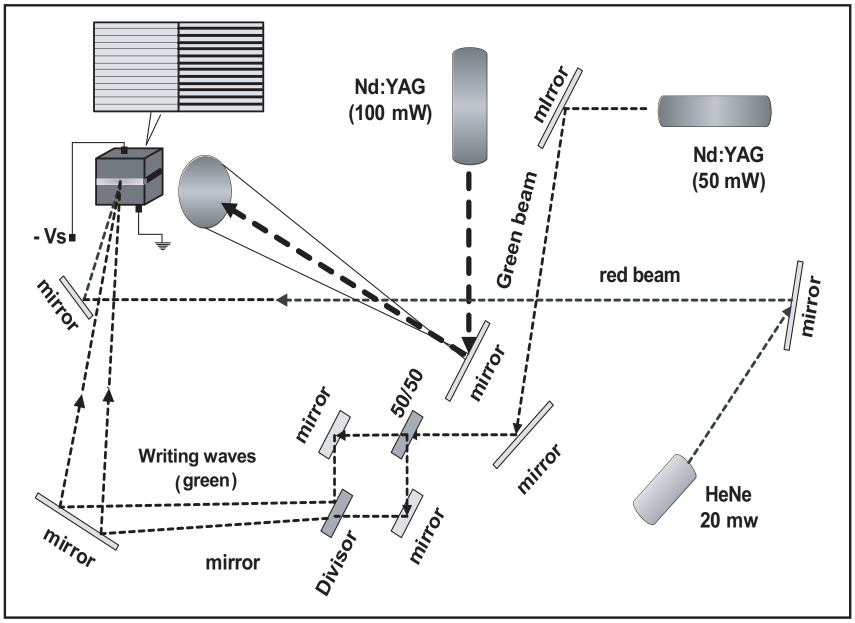

(a)

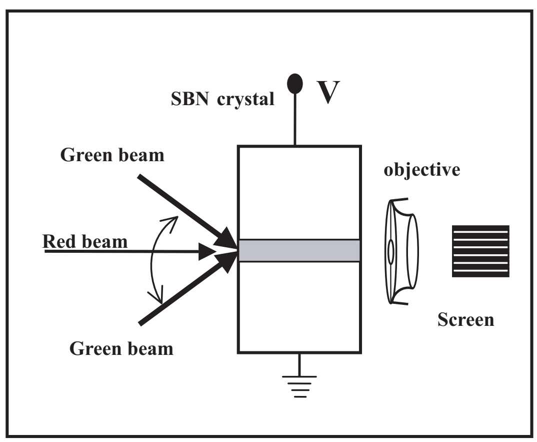

(b)

Figure 1: (a) Array experimental and b) The pictures of the green fringes were obtained using a red filter to block the red and viceversa. Additionally, the entire SBN:Ce crystal was illuminated perpendicularly to the optical axis with one expanded green beam of frequency-doubled Nd:YAG laser to produce the uniform illumination of the interelectrode space.

In order to observe the fringe patter and the waveguide array, a microscope objective focused on the back face of the crystal was used. The fringe patter was projected on a screen 1 meter away from the crystal.

Intensity profiles were obtained impinging the fringe pattern on a detector. The fringe patter is rotated using a plane mirror coupled to a step motor in such a way that the detector captures over a perpendicular line to the fringe pattern. In order to detect small intensities a lock-in amplifier synchronized to a chopper was used. Data was visualized on a oscilloscope and captured to a computer.

3. EXPERIMENTAL RESULTS

Figure 2(b) presents photographs showing the variation of the fringe patter as a function of the external voltage applied and the red beam angle respect to the bisector of the writing beams. The pictures were taken on the far field using a digital camera. In order to get the photographs, a microscope objective was focused on the back face of the crystal, Fig. (1). The pictures of the green fringes were obtained using a red filter to block the red beam and vice versa. The compression rate was limited to level 4–5, approximately, in order to develop transversal modulation instability [7, 9].

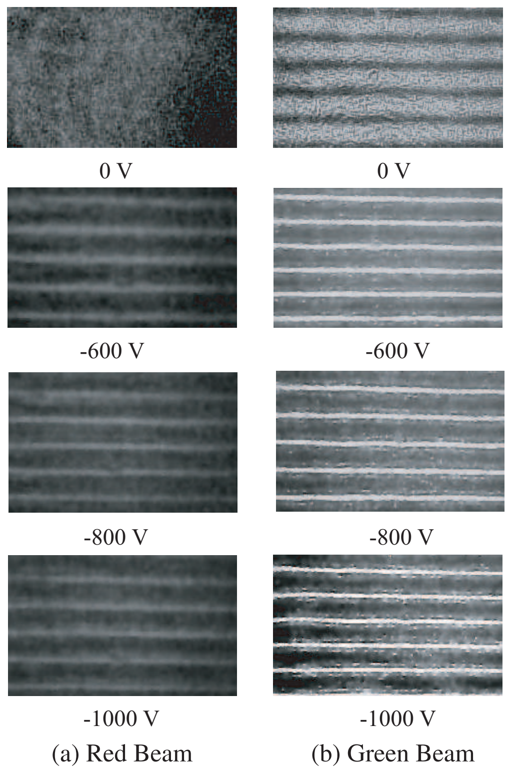

Figure 2: (a) The red light beam was trapped by this array of self-tightening photoinduced lattices. (b) Presents photographs showing the variation of the fringe patter as a function of the external voltage applied and the red beam angle respect to the bisector of the writing beams. The pictures were taken on the far field using a digital camera. In order to get the photographs, a microscope objective was focused on the back face of the crystal.

We consider the main effect produced by the external voltage particularly the self-compression of the green fringes (interference) where the red light ($\lambda = 632\,\text{nm}$) is trapped and guided in photorefractive materials SBN:Ce (Fig. 2(a) and Fig. 2(b)). The crystal sized at $5 \times 5 \times 5\,\text{mm}^3$ with two silver paste electrodes deposited an to the faces of the crystal perpendicular to the C axis.

The high voltage was wave guided is observed; also the self-focusing is noted in the red beam. Interest in laser beam self-action in photorefractive material SBN:Ce has been stimulated by its low threshold power and possible applications in light by light guiding and control [10].

In the Fig. 3 presents graphs showing the transversal profiles of the green fringe patterns as a function of voltage, optimal angle between writing beams and optimal angle of the red beam to the bisector of the green beams. It is possible to show that the main effect of the external voltage is the fringe compression and increase of the fringes intensity.

On the spatial frequency domain, the external voltage applied to the crystal produces high orders of diffraction; these can be seen on Fig. 4. We observe that the main effect of the external field is the generation of higher and higher diffraction orders and optical noise around these.

The intensity of the high orders of diffraction was measured using a detector placed behind a screen with a small orifice on it 1 meter away from the crystal. The screen was used as filter,

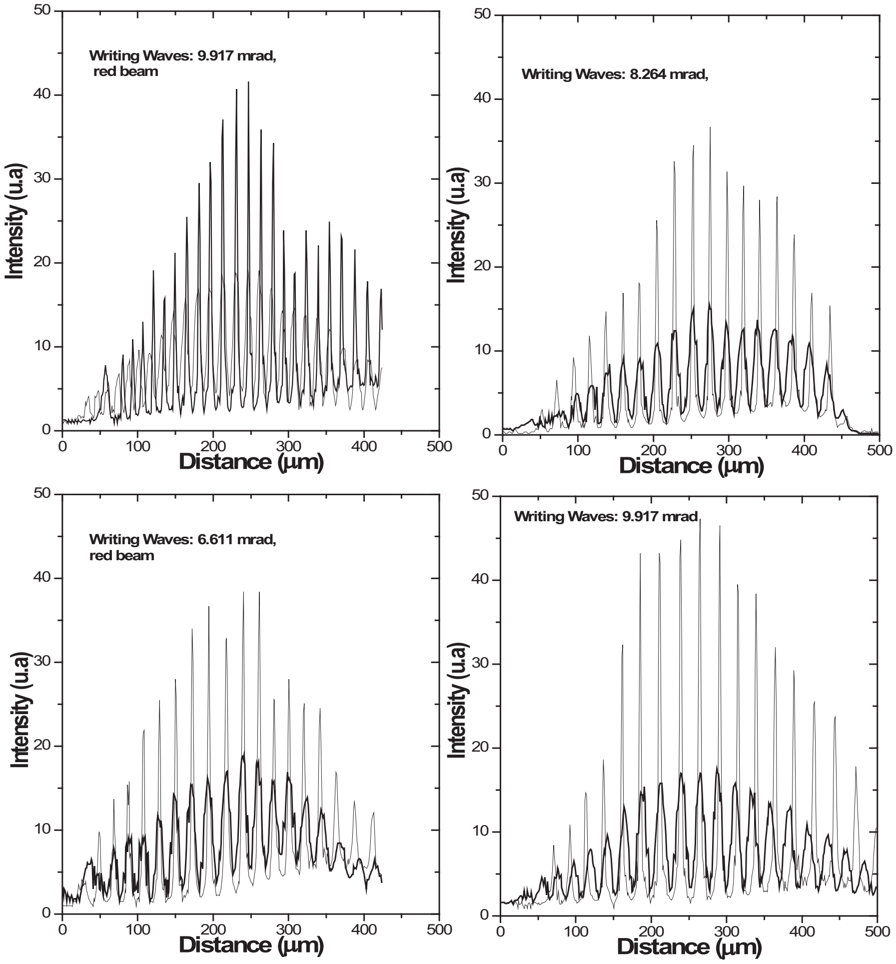

Figure 3: Presents graphs showing the transversal profiles of the green fringe patterns as a function of voltage, optimal angle between writing beams and optimal angle of the red beam to the bisector of the green beams. It is possible to show that the main effect of the external voltage is the fringe compression and increase of the fringes intensity.

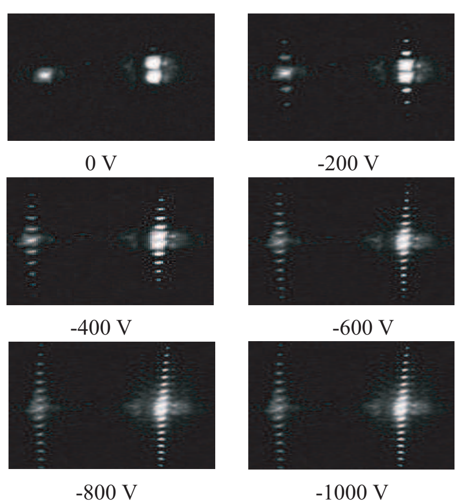

Figure 4: We observe high order diffraction generation as a function of external voltage applied to the crystal. Experiment conditions are the same as those of Fig. 2 (left side, red light; right side, green light).

blocking all but one of the diffraction orders. Fig. 5 presents the intensity variation for the first three diffraction orders as a function of the applied external voltage.

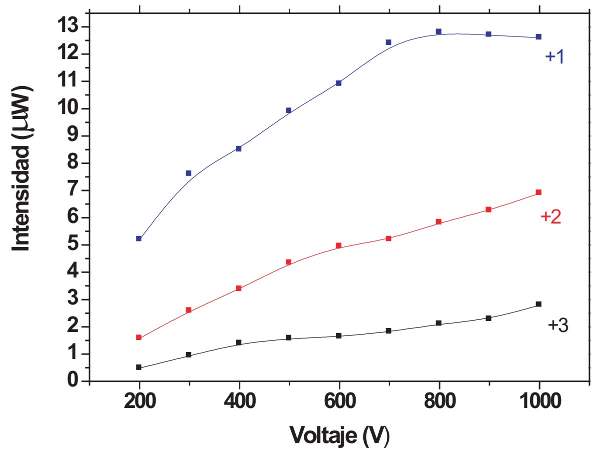

Figure 5: We present the intensity variation for the first three diffraction orders as a function of the applied external voltage.

4. CONCLUSIONS

Optimal experimental conditions were found for the control and guidance of a Gaussian beam emitted by a He-Ne laser using a periodical array of non-lineal light transforming gradually in a waveguide inside the range of transversal modulation instability phenomenon.

ACKNOWLEDGMENT

The author thanks Nikolai Korneev for help. The CONACyT aid (project 39681) is gratefully acknowledged.

REFERENCES

1. Davydov, A. S. and N. I. Kislukha, "Solitary excitations in one-dimensional molecular chains," *Phys. Status Solidi B*, Vol. 59, 465–470, 1973.
2. Christodoulidies, D. N. and R. I. Joseph, "Discrete self-focusing in nonlinear arrays of coupled waveguides," *Optics Letters*, Vol. 13, 794–797, 1988.
3. Su, W. P., J. R. Schieffer, and A. J. Heeger, "Solitons in polyacetylene," *Phys. Rev. Lett.*, Vol. 42, 1968–1971, 1979.
4. Trombettoni, A. and A. Smerzi, "Discrete solitons and breathers with dilute Bose-Einstein condesates," *Phys. Rev. Lett.*, Vol. 86, 2353–2356, 2001.
5. Kivshar, Y. S. and D. E. Pelinovsky, "Self-focusing and transverse instabilities of solitary waves," *Physics Reports*, Vol. 331, 117, 2000.
6. "Experimental evidence of modulation instability in a photorefractive BTO crystal," *Optics Letters*, Vol. 20, 1853, 1995.
7. Korneev, N., A. Apolinar-Iribe, V. A. Vysloukh, and M. A. Basurto-Pensado, "Self-compression of 1+1D cnoidal wave in photorefractive BTO crystal: an experimental evidence," *Optics Communications*, Vol. 197, 209, 2001.
8. Korneev, N., "Current anisotropy influence on beam self-focusing in photorefractive materials," *Journal of Modern Optics*, Vol. 48, 751, 2001.
9. Apolinar-Iribe, A., N. Korneev, V. A. Vysloukh, and C. M. Gomez-Sarabia, "Transverse modulation instability of periodic light patterns in photorefractive strontium barium niobate crystal," *Optics Letters*, Vol. 27, 2088, 2002.
10. Stegeman, G. I. and M. Segev, *Science*, Vol. 286, 1518, 1999.

A Higher-order Accurate FDTD Solution to Scalar SHG Problems

M. A. Alsunaidi[1] **and F. S. Al-Hajiri**[2]

[1]King Fahd University of Petroleum & Minerals, Saudi Arabia
[2]King Faisal University, Saudi Arabia

Abstract— A higher-order accurate FDTD simulation algorithm for the solution of the phase-dependent SHG problem is presented. This algorithm approximates the spatial derivatives in the propagation direction using 4th order FD schemes. It has been shown that this scheme guarantees the convergence of the solution using significantly less computation time and less memory requirement as compared to 2nd order schemes.

1. INTRODUCTION

Higher order FDTD schemes allow the modeling of electromagnetic wave interaction in structures that have very long electrical lengths without jeopardizing the limit on phase error accumulation set by standard 2nd order methods. These higher order schemes become even more attractive in problems involving nonlinear interactions. For example, in a second harmonic generation (SHG) problem, the energy coupling between the propagating input optical beam and the generated beam is a strong function of the phase shift between the two waves. Failing to accurately estimate the phase of the waves at any given distance along the propagation direction results in errors in the calculation of both coherence length and the amount of coupled energy. Several researchers have attempted the FDTD solution of wave propagation in both linear as well as nonlinear optical structures using higher order methods to overcome the limitations of 2nd order explicit schemes [1–3].

In this paper, the FDTD-SHG solution reported in [4] is revisited. The second order accurate approximations of the spatial derivatives are replaced by 4th order accurate schemes. Such a scheme has not been yet discussed in literature in the context of the nonlinear wave equation representing SHG.

2. FORMULATIONS

A time-domain formulation of the SHG problem in nonlinear optical waveguides has been proposed in [4]. The equations representing the propagating waves are derived using a nonlinear wave equation such that the problem is reduced to an equivalent scalar problem. This new formulation of the SHG problem offers great advantages over both the classical BPM technique and other frequency-domain methods. While it completely accounts for the wave-medium interactions, it avoids the limitations associated with conventional asymptotic behavior and paraxial propagation. On the other hand, it provides an efficient method for the time-domain characterization of nonlinear optical structures by focusing on such quantities as beam intensity, nonlinear depletion and phase shift, characteristic lengths, etc., in which detailed analysis of the field components is not necessary. For a 2D SHG problem, the proposed time-domain algorithm solves for only two fields; the fundamental field and the second harmonic field. In addition, the algorithm is capable of incorporating different matching techniques in the SHG process including quasi-phase matching and it can simulate CW second-order nonlinear effects as well as operations with short time-varying envelops. The SHG model equations are given by:

$$\nabla^2 E^f = \mu_o \varepsilon_o n_f^2 \frac{\partial^2 E^f}{\partial t^2} + 2\mu_o \varepsilon_o \chi^{(2)} \left\langle E^f \frac{\partial^2 E^s}{\partial t^2} + E^s \frac{\partial^2 E^f}{\partial t^2} + 2 \frac{\partial E^f}{\partial t}\frac{\partial E^s}{\partial t} \right\rangle \tag{1}$$

$$\nabla^2 E^s = \mu_o \varepsilon_o n_s^2 \frac{\partial^2 E^s}{\partial t^2} + 2\mu_o \varepsilon_o \chi^{(2)} \left\langle E^f \frac{\partial^2 E^f}{\partial t^2} + \frac{\partial E^f}{\partial t}\frac{\partial E^f}{\partial t} \right\rangle \tag{2}$$

where E^f and E^s are the fundamental and the second harmonic fields, respectively, n is the material refractive index and $\chi^{(2)}$ is the dispersionless nonlinear susceptibility. The second order FD approximation of the laplacian is systematically used in many wave propagation problems. Provided that the spatial step size in the propagation direction is made a small fraction of the shortest wavelength, the amount of numerical dispersion of a 2nd order scheme is generally acceptable. It will be interesting to investigate this general criterion when the simulation involves phase-dependent interactions between coexisting waves, such as the case of a SHG problem. Using the 4th order scheme, which is proposed to replace the 2nd order scheme, the spatial derivative of the fundamental wave, for example, in the propagation direction will be given by:

$$\frac{\partial^2 E^f}{\partial y^2} \cong \frac{1}{12(\Delta y)^2}\left[-E^f(i,\, j-2)+16E^f(i,\, j-1)-30E^f(i,\, j)+16E^f(i,\, j+1)-E^f(i,\, j+2)\right] \quad (3)$$

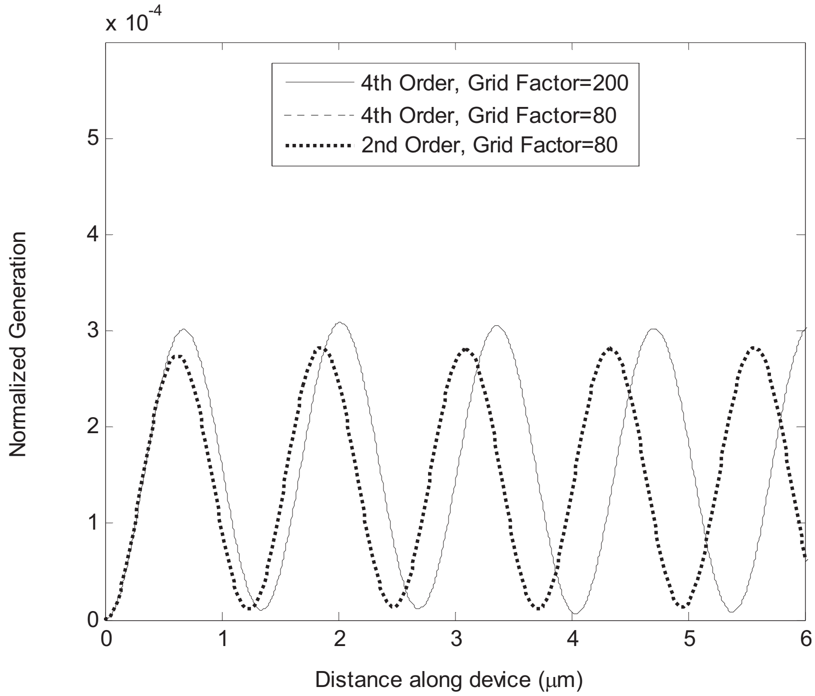

Figure 1: SHG results for 2nd and 4th order FDTD schemes.

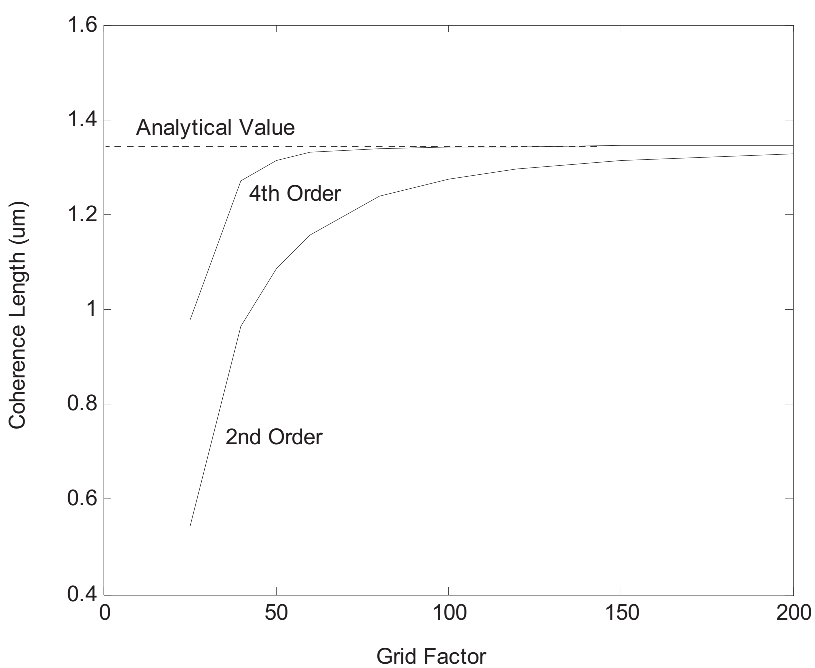

Figure 2: Coherence length vs. Grid factor using 4th order and 2nd order schemes.

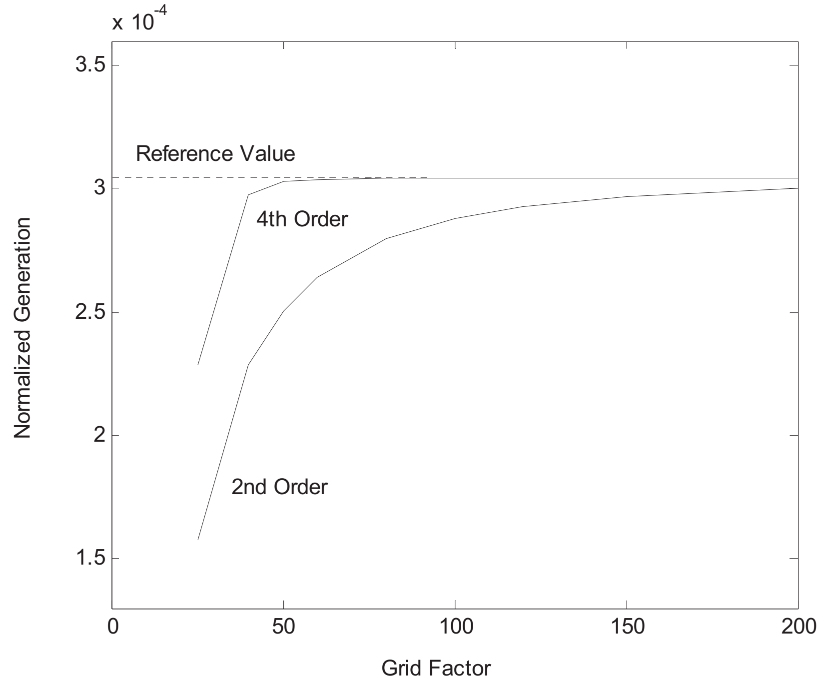

Figure 3: Peak value of second harmonic power vs. Grid factor using 4th order and 2nd order schemes.

3. SOLUTION METHOD AND NUMERICAL RESULTS

To study the effectiveness of the proposed 4th order method, a symmetric AlGaAs-based dielectric slab waveguide is considered. It consists of a 0.44-μm thick guiding layer sandwiched between two 3-μm thick AlAs layers. The excitation field is a CW signal at a fundamental wavelength of $\lambda_f = 1.064\,\mu\text{m}$. The transverse profile of the excitation corresponds to the first guided mode at the given operating frequency. For the sake of comparison, both 2nd and 4th order schemes were considered. No matching technique is used such that the level of coupling between the input and the generated waves depends entirely on the phase shift between them. This phase shift is defined by the effective refractive indices of the two coexisting guided modes. The coherence length is given by $L_C = \lambda_f / 2(n_s - n_f)$, where n is the effective refractive index. Because of the nature of the

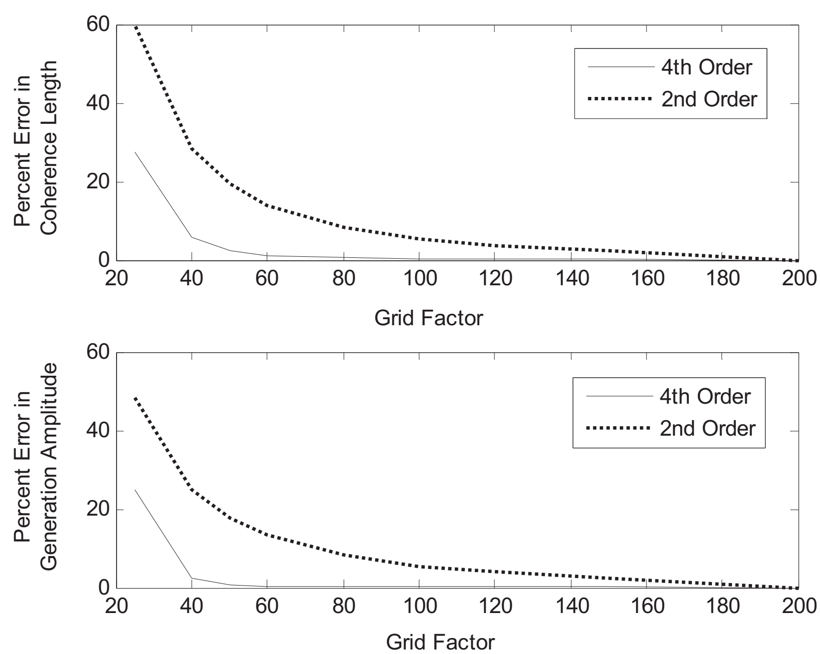

Figure 4: Error analysis for 4th order (solid) and 2nd order (dashed) schemes.

problem, propagation occurs in only one direction. Several numerical experiments have shown that negligible gain in accuracy is achieved by applying the 4th order scheme to the transverse direction. Figures 1 to 3 summarize the effectiveness of the 4th order scheme in speeding up convergence. In the figures, the grid factor is defined as the ratio of the wavelength to the spatial step size. For this particular problem, a grid factor of 80 in the 4th order scheme is sufficient to ensure low levels of numerical dispersion. By applying the 4th order scheme to the spatial derivatives in the propagation direction only, an overall increase of 26% in computation time per time step is expected, but no additional memory resources are necessary. As shown in Figure 4, this additional computation time is insignificant if compared to the savings made by relaxing the spatial step and hence the time step. For the same error tolerance, the 4th order scheme uses spatial steps with more than double the size required by the 2nd order scheme.

4. CONCLUSIONS

A 4th order accurate FDTD simulation algorithm for the solution of the phase-dependent SHG problem has been presented. This algorithm guarantees the convergence of the solution using significantly less computation time and less memory requirement as compared to 2nd order schemes.

ACKNOWLEDGMENT

The authors would like to acknowledge the support of King Fahd University of Petroleum & Minerals.

REFERENCES

1. Taflove, A., *Computational Electrodynamics: The Finite-Difference Time-Domain Method*, Artech House, Norwood, MA, 1995.
2. Hwang, K. and J. Ihm, "A Stable fourth-order FDTD method for modeling electrically long dielectric waveguides," *J. Lightwave Tech.*, Vol. 24, 1048–1056, Feb. 2006.
3. Shlager, K. and J. Schneider, "Comparison of dispersion properties of several low-dispersion finite-difference time-domain algorithms," *IEEE Trans. Antenna Propagat.*, Vol. 51, 642–653, March 2003.
4. Alsunaidi, M. A., H. M. Masoudi, and J. M. Arnold, "A Time-domain algorithm for second harmonic generation in nonlinear optical structures," *IEEE Photonics Tech. Lett.*, Vol. 12, 395–397, April 2000.

Full-wave Solution of the Second Harmonic Generation Problem Using a Nonlinear FDTD Algorithm

H. M. Al-Mudhaffar, M. A. Alsunaidi, and H. M. Masoudi
King Fahd University of Petroleum & Minerals, Saudi Arabia

Abstract— A vectorial time-domain simulator of integrated optical structures containing second order nonlinearities is presented. The simulation algorithm is based on the direct solution of nonlinear Maxwell's equations representing the propagating fields and is solved using the FDTD method. Because the proposed algorithm accounts for the full optical coefficient tensor, the inaccuracies associated with the scalar and paraxial approximations are avoided. It should find application in a wide range of device structures and in the analysis of short-pulse propagation in second order nonlinear devices.

1. INTRODUCTION

The increased progress in materials technology and fabrication methods for integrated optics has resulted in a growing need for accurate models that closely predict the behavior of the electromagnetic fields inside new optical devices. Fortunately, the advent of fast and powerful computers has made detailed numerical modeling an efficient and reliable tool for researchers and engineers. Because many of the nonlinear optical devices are waveguide-based, the paraxial approximation of the energy flow direction was utilized in the early numerical models. The Beam Propagation Method (BPM) [1] is one approach of this type of modeling. The BPM method has been successfully used in the analysis of Second Harmonic Generation (SHG) in nonlinear optical structures [2, 3]. Although this method is relatively less computationally intensive than other methods, the formulation of the fields for the SHG is scalar and the method is aimed at modeling wave propagation in devices where the primary flow of energy is along a single principal direction. Other modeling methods in this area are the Finite element method (FEM) and the Finite-Difference Time-Domain (FDTD) method.

Since the introduction of the Yee algorithm for the numerical solution of Maxwell's equations in 1966 [4], the FDTD method has been applied to the simulation of a large number of linear as well as nonlinear electromagnetic problems [5]. The FDTD is substantially more robust than other methods because it directly solves for fundamental quantities. It also avoids the simplifying assumptions of conventional asymptotic behavior and paraxial propagation. Recently, a FDTD approach that solves the nonlinear scalar wave equation was applied to the second harmonic generation problem [6]. This scalar model offered a number of attractive advantages. All the effects due to the wave-medium interaction are included in the analysis under the scalar formulation. Further, as compared to the BPM solution, the approach takes into account wave reflection due to discontinuities in the simulated structure as well as outside boundaries. However, the scalar model is only suited for problems that do not involve change in polarization. In most practical nonlinear integrated optical devices, wave polarization does occur. For example, in a GaAs-based nonlinear structure a TM incident field can couple to a TE second harmonic field.

In this paper, a formulation of the full-wave model for SHG in optical structures containing second order nonlinearity is presented. This formulation is suitable for implementation using the vectorial FDTD. The algorithm is applied to a GaAs-based waveguiding structure.

2. FORMULATION OF THE SHG IN GAAS-BASED STRUCTURES

The propagation of electromagnetic radiation through certain class of crystals causes the nonlinear dielectric properties of the material to be polarized. This polarization, P, can be expressed mathematically using terms proportional to the nonlinear susceptibility, $\chi^{(2)}$, and to the propagating electric field components inside the structure. The nonlinear response of the material to such property leads to an exchange of energy between fields propagating at different frequencies. This response is utilized in the SHG in which energy from one field propagating at frequency ω_f, the fundamental field, is transferred to a field propagating at double the frequency $\omega_s = 2\omega_f$, the second harmonic field.

The formulation starts with Maxwell's equations:

$$\frac{\partial H}{\partial t} = -\frac{1}{\mu_o}\nabla \times E \tag{1}$$

$$\frac{\partial E}{\partial t} = -\frac{1}{\varepsilon_o}\nabla \times H - \frac{1}{\varepsilon_o}\frac{\partial P}{\partial t} \tag{2}$$

where E is the electric field intensity and H is the magnetic field intensity. P is the total (linear and non-linear) electric polarization given by

$$P = P^L + P^{NL} \tag{3}$$

where

$$P^L = \varepsilon_o([\varepsilon_r] - 1)E \tag{4}$$

$$P^{NL} = 2\varepsilon_o[d]E \cdot E \tag{5}$$

and $[d]$ is the nonlinear optical coefficient tensor. In vectorial form, the nonlinear polarizations of the fundamental and the second harmonic waves are given by

$$\begin{bmatrix} P_x^{NL,\omega} \\ P_y^{NL,\omega} \\ P_z^{NL,\omega} \end{bmatrix} = 2\varepsilon_o[d] \begin{bmatrix} E_x^\omega E_x^{2\omega} \\ E_y^\omega E_y^{2\omega} \\ E_z^\omega E_z^{2\omega} \\ E_z^\omega E_y^{2\omega} + E_y^\omega E_z^{2\omega} \\ E_z^\omega E_x^{2\omega} + E_x^\omega E_z^{2\omega} \\ E_x^\omega E_y^{2\omega} + E_y^\omega E_x^{2\omega} \end{bmatrix} \quad \begin{bmatrix} P_x^{NL,2\omega} \\ P_y^{NL,2\omega} \\ P_z^{NL,2\omega} \end{bmatrix} = \varepsilon_o[d] \begin{bmatrix} E_x^\omega E_x^\omega \\ E_y^\omega E_y^\omega \\ E_z^\omega E_z^\omega \\ 2E_z^\omega E_y^\omega \\ 2E_x^\omega E_z^\omega \\ 2E_x^\omega E_y^\omega \end{bmatrix} \tag{6}$$

Consider now a GaAs-based waveguide with crystal axes matching the principal axes. The nonlinear optical coefficient tensor is given by

$$[d] = \begin{bmatrix} 0 & 0 & d_{14} & 0 & 0 \\ 0 & 0 & 0 & d_{14} & 0 \\ 0 & 0 & 0 & 0 & d_{14} \end{bmatrix} \tag{7}$$

In this case, coupling of a TM fundamental field to a TE second harmonic field is possible. The resulting differential equations are:

TM fundamental input

$$\varepsilon_x \frac{\partial E_x^f}{\partial t} = -\frac{\partial H_y^f}{\partial z} - 2\varepsilon_o d_{14}\frac{\partial}{\partial t}\left(E_z^f E_y^s\right) \tag{8}$$

$$\varepsilon_z \frac{\partial E_z^f}{\partial t} = \frac{\partial H_y^f}{\partial x} - 2\varepsilon_o d_{14}\frac{\partial}{\partial t}\left(E_x^f E_y^s\right) \tag{9}$$

$$\mu \frac{\partial H_y^f}{\partial t} = \frac{\partial E_z^f}{\partial x} - \frac{\partial E_x^f}{\partial z} \tag{10}$$

TE second harmonic field

$$\varepsilon_y \frac{\partial E_y^s}{\partial t} = \left(\frac{\partial H_x^s}{\partial z} - \frac{\partial H_z^s}{\partial x}\right) - 2\varepsilon_o d_{14}\frac{\partial}{\partial t}\left(E_x^f E_z^f\right) \tag{11}$$

$$\mu \frac{\partial H_x^s}{\partial t} = \frac{\partial E_y^s}{\partial z} \tag{12}$$

$$\mu \frac{\partial H_z^s}{\partial t} = -\frac{\partial E_y^s}{\partial x} \tag{13}$$

3. SOLUTION METHOD AND NUMERICAL RESULTS

The finite-difference time-domain (FDTD) method is used to numerically solve Equations (8) to (13). The method is suitable for this application because of its ability to include different structures and different media. It is also capable of producing results for multiple frequencies using a single

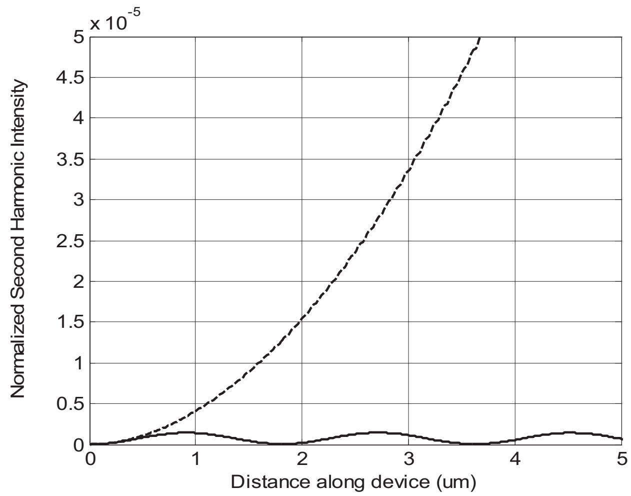

Figure 1: SHG along the nonlinear waveguide (solid: no matching, dashed: perfect match).

simulation. To increase the accuracy of the computations, the PML absorbing boundaries are used for the truncation of the computation domain. A symmetric GaAs-based dielectric slab waveguide is considered to test the proposed FDTD algorithm. It consists of a 0.44-μm thick guiding layer sandwiched between two 3-μm thick AlAs layers. The arrangements of the field components for both the fundamental and second harmonic are made according to the standard Yee cell. The excitation field is a CW TM signal at a fundamental wavelength of $\lambda_f = 1.064\,\mu\text{m}$ and an amplitude of $5.0\,\text{A}/\mu\text{m}$. The transverse profile of the excitation corresponds to the first TM guided mode at the given operating frequency. For the sake of illustration, two matching scenarios are considered. First, no matching technique is used such that the level of coupling between the input and the generated waves depends entirely on the phase shift between them. This phase shift is defined by the difference between the effective indices of the two coexisting guided modes. Second, the effective refractive index of the first odd guided mode of the TE field at $\lambda_s = 0.533\,\mu\text{m}$ is perfectly matched to the first even guided mode of the TM input field by numerically changing the value of the refractive index of the guiding layer at λ_s. The results for both scenarios are shown in Figure 1. As expected, energy exchange between the fundamental field and the second harmonic field takes place periodically during every coherence length if no matching technique is implemented. If, however, the two waves are perfectly matched, the energy exchange will be continuous, resulting in a coherent build-up of the second harmonic energy. The transverse profiles for the fundamental TM mode and the second harmonic TE mode are shown in Figure 2. The simulation verifies the

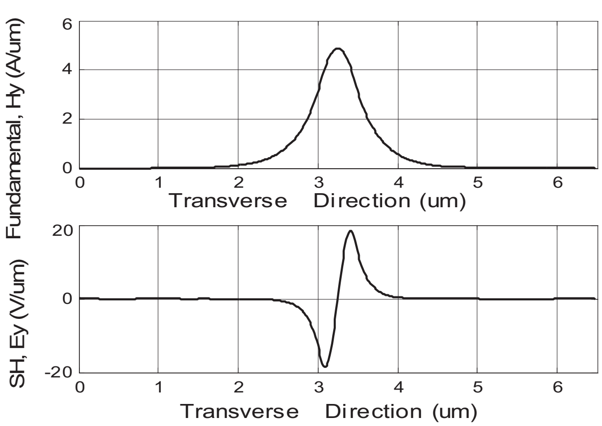

Figure 2: TM input (fundamental) and generated TE second harmonic profiles.

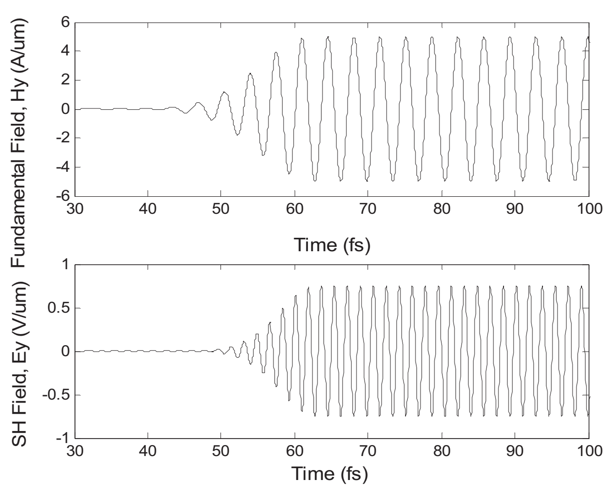

Figure 3: Time-domain results for the fundamental and second harmonic fields at a point along the device at the center of the guiding layer.

coupling of second harmonic energy on the first odd TE mode. Finally, time-domain results of the input fundamental field and the generated second harmonic field at a point along the device are shown in Figure 3. The results confirm the relative frequency between the two propagating beams.

4. CONCLUSIONS

The developed model can be utilized to efficiently analyze and study different optical structures with second order nonlinearities. Instead of calculating the total field inside the structure and then performing spectral analysis to separate the two propagating waves, the presented model solves directly for the fundamental as well as the second harmonic fields. It should find application in a wide range of device structures and in the analysis of short-pulse propagation in second order nonlinear devices. The extension of the model for applications involving pulsed excitations and different device geometries is a future work.

ACKNOWLEDGMENT

The authors would like to acknowledge the support of King Fahd University of Petroleum & Minerals.

REFERENCES

1. Feit, M. and J. Fleck, "Light propagation in graded-index optical fibers," *App. Opt.*, Vol. 17, 3990–3998, 1978.
2. Hermansson, V. and D. Yevick, "A propagation beam method analysis of nonlinear effects in optical waveguides," *Opt. Quantum Elect.*, Vol. 16, 525–534, 1984.
3. Masoudi, H. and J. Arnold, "Parallel beam propagation method for the analysis of second harmonic generation," *IEEE Photonics Tech. Lett.*, Vol. 7, No. 4, 400–402, April 1995.
4. Yee, K. S., "Numerical solution of initial boundary value problems involving Maxwell's equations in isotropic media," *IEEE Trans. Antenna Propagat.*, Vol. AP-14, 302–307, May 1966.
5. Taflove, A., *Computational Electrodynamics: The Finite-Difference Time-Domain Method*, Artech House, Norwood, MA, 1995.
6. Alsunaidi, M. A., H. M. Masoudi and J. M. Arnold, "A time-domain algorithm for second harmonic generation in nonlinear optical structures," *IEEE Photonics Tech. Lett.*, Vol. 12, 395–397, April 2000.

Spectral Monte-Carlo Simulations of Photon Penetration in Biotissue in Visible and Near Infrared

M. Hülsbusch, D. Hölscher, and V. Blažek
Institute of High Frequency Technology, RWTH Aachen University, Aachen, Germany

Abstract— For design and optimization of optoelectronic sensor concepts the photon-tissue interaction has to be evaluated. The Monte Carlo method is a well suited tool for this task. This paper discusses different virtual skin models and the optical properties of biotissue in the visible and near infrared spectrum. Based on these fundamentals a simulation tool is presented, which is capable of handling arbitrary complex simulation scenarios. Apart from the assessment and quantification of penetration depth of different sensor concepts also dynamical simulations are presented, which allow simulations of blood volume pulses. These simulations permit the evaluation of the DC and also the AC component of the detector signal.

1. INTRODUCTION

Optoelectronic sensor concepts are gaining importance in modern medicine. They are noninvasive, allow cheap and flexible measurements and are widely accepted by the patients. The design and optimization of theses sensors require knowledge of photon-tissue interaction. An established tool for simulation of this interaction is the Monte Carlo method.

2. MONTE CARLO SIMULATION

Monte Carlo simulations are based on the method of statistical sampling for the solution of quantitative problems. They were first introduced by Metropolis and Ulam in 1949 for the prediction of neutron distributions in uran [1]. In the presented optical domain the interaction between photons and tissue is simulated by distribution functions of the interaction processes and generation of random numbers. Light is considered as particles, which can be absorbed or scattered in turbid media like tissue or blood. The photon path is then calculated using ray tracing algorithms.

One advantage of the Monte Carlo method is the simple description of biotissue, only the absorption coefficient μ_a, the scattering coefficient μ_s and the anisotropic factor g of the simulation media have to be specified. μ_a and μ_s define the probability for absorption of a photon, g allows the specification of a scattering angle according to the Henyey-Greenstein phase function.

3. OPTICAL PROPERTIES OF BIOTISSUE

Human skin is a strongly scattering turbid medium. In the visible and also in the near infrared spectrum the probability of scattering is about 100–1000 times higher than that of absorption. This fact generally allows measurements using optical sensors.

Quantitative values for anisotropic factor g and absorption and scattering coefficient μ_a, μ_s for discrete wavelengths in the range of 300–900 nm can be found in the literature. These parameters have usually been gained by parameter matching between macroscopic measurements and simulations. Unfortunately there are strong variabilities in these parameters. They could be generated by differing probe preparation or different measurement techniques.

Different research groups try to not only estimate simulation parameters for discrete wavelengths, but to produce measurements for the whole optical spectrum from 300–900 nm. Measurement data for oxyhemoglobin and reduced hemoglobin have been published by Prahl [2]. Jacques [3] further published functional approximations for absorption and scattering coefficients of different skin components. As a functional description of the anisotropic parameter g linear interpolation have been used throughout this paper. The continuous representation of simulation parameters (Fig. 1, 2) in relation to wavelengths permit simulations at arbitrary wavelengths, which offers great advantage for parameterising simulation runs. Optimizations of different sensor concepts in regard to wavelength are thus possible.

4. SKIN MODEL

The skin is the largest human organ, it has a surface of about 1.5–1.8 m^2 and a weight of about 5 kg. It's thickness varies from 1 to 4 mm. In first approximation it can be regarded as a multilayer

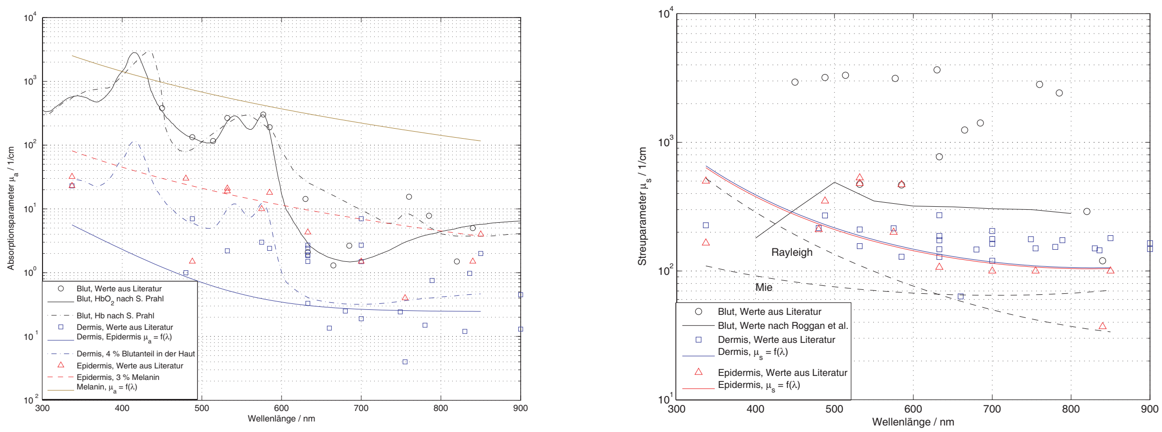

μ_a μ_s

Figure 1: Absorption and scattering parameters for epidermis, dermis und blood. Discrete measurements from literature are depicted as well as functional representations of μ_a and μ_s for different skin components.

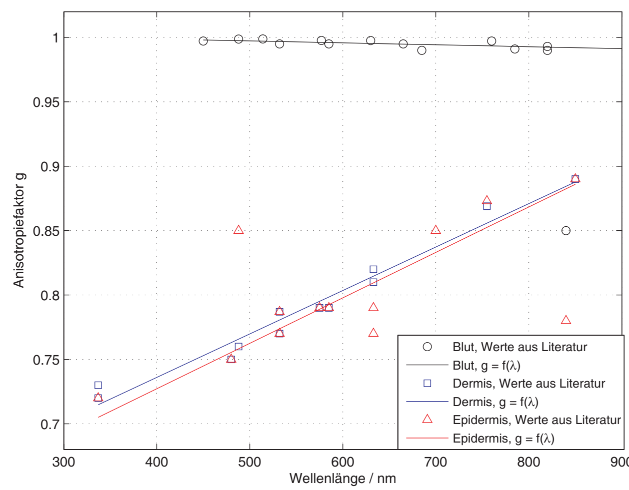

Figure 2: Anisotropic factor for epidermis, dermis and blood. Discrete Measurements from literature ate depicted as well as linear interpolations of g.

structure where the different layers can be divided by function or vessel density (Fig. 3). Different authors published layered skin models with differing layer thickness and differing blood contents fblood in the functional layers [4–6] (Tab. 1).

Different simulations have been performed for these skin models. Despite strongly differing layer dimensions, no significant differences in regard to penetration depth and backscattered light intensity could be found. Since the skin model of Meglinskii & Matcher seems to be the newest and most widely used model, it has been utilised in this work.

5. EXPERIMENTAL VERIFICATION OF SIMULATION RESULTS

For the Monte Carlo simulations a lot of approximations and simplifications have to be used. The simulation parameter μ_a, μ_s and g which were found in the literature show discrepancies or are interpolated, the layered skin model represents a strong simplification and the consideration of only a few skin components melanin, epidermis, dermis and blood could also potentially reduce simulation accuracy. An experimental validation of simulation results has been performed. The skin is punctually illuminated by a laser light source with wavelength $\lambda = 632\,\text{nm}$. A detector with varying lateral distance then measures the backscattered light intensity. The lateral intensity profile from experimental measurements at different skin positions and also from the simulation are shown in Fig. 4. For measurements on the palm of the hand a good correlation to simulation results could be found. This emphasises the general suitability of the presented virtual skin model

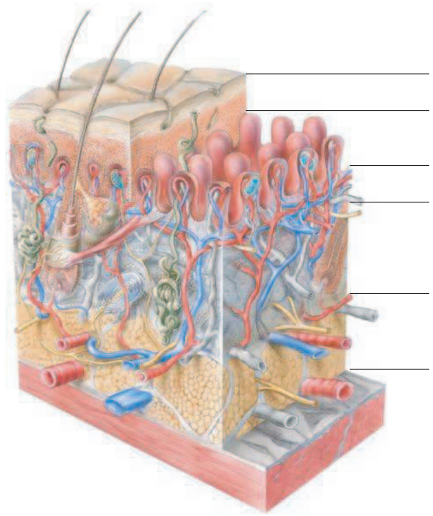

Figure 3: Structure of human skin. According to varying vessel density it can be divided into different layers. (Source: http://www.medizininfo.de/hautundhaar/images/haut1.gif).

Table 1: Thickness and blood volume concentration f_{blood} for different skin layers for skin models from [4], [5] and [6].

Hautmodell	Meglinskii & Matcher		Mühl		Tuchin[1]	
Skin layer	thickness	f_{blood}	thickness	f_{blood}	thickness	f_{blood}
Epidermis	100 µm	0%	200 µm	0%	100 µm	0%
Capillary layer	150 µm	4%	200 µm	4%	200 µm	3%
upper vessel plexus	80 µm	30%	200 µm	10%	200 µm	20%
supply layer cutis	1500 µm	4%	900 µm	5%	900 µm	3%
deeper vessel plexus	100 µm	10%	500 µm	15%	600 µm	25%
supply layer subcutis	3000 µm	5%	3000 µm	4%		

[1] Tuchin does not specify blood volume concentration but uses weighted mean values of simulation parameters μ_a, μ_s and g.

and the simulation parameters.

6. SIMULATION RESULTS

For visualisation and qualitative inspection of the simulation results a 3D model can be generated (Fig. 5). The full photon path of all photons that are registered by the detector and contribute to the sensor signal is displayed. Despite the qualitative analysis from the visualisation the penetration depth can be assessed quantitatively.

A sensitivity profile in relation to skin depth can be calculated when the light intensity $I(x, y, z)$ at different locations are regarded. The contribution of any skin depth dz to the whole detector signal can be specified as

$$I(z) = \frac{\int\int I(x, y, z)dxdy}{dz} \tag{1}$$

Figure 6 shows the sensitivity profiles for different wavelength in green (550 nm), red (650 nm) and infrared (900 nm) wavelengths. A strong influence of wavelength on penetration depths can be observed. The green sensor, which only measures the upper skin layers up to a depth of about 0.3 mm will provide measurements solely of the skin microcirculation. While sensors utilising red or infrared light will additionally collect information of deeper and larger vessels in the skin and thus gather information of the macro circulation.

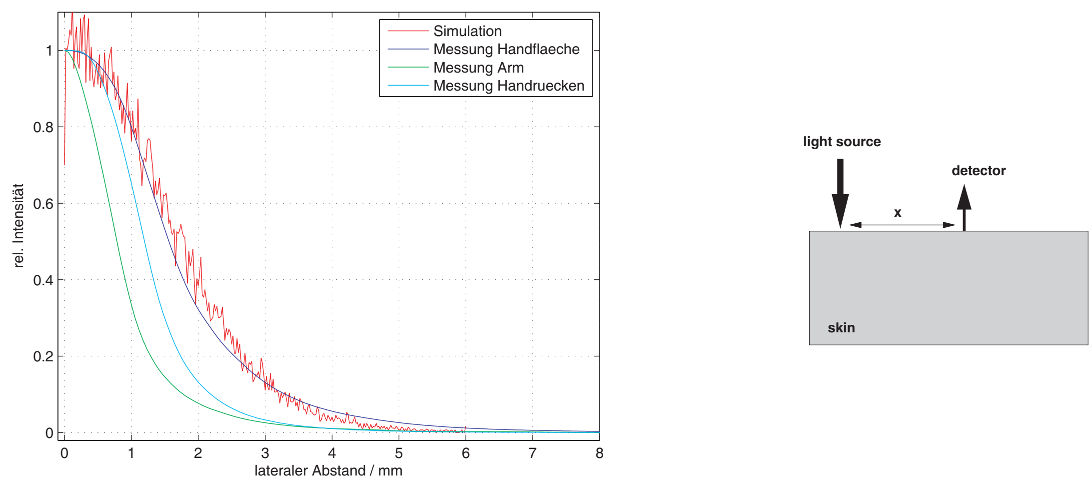

Figure 4: Verification of simulation results by experimental measurements. The skin is punctually illuminated by a laser light source. At a variable lateral distance x a detector is placed, which measures the backscattered light intensity. Experimental measurements have been performed on different skin areals, at the palm of the hand a good correlation to the simulation results could be found.

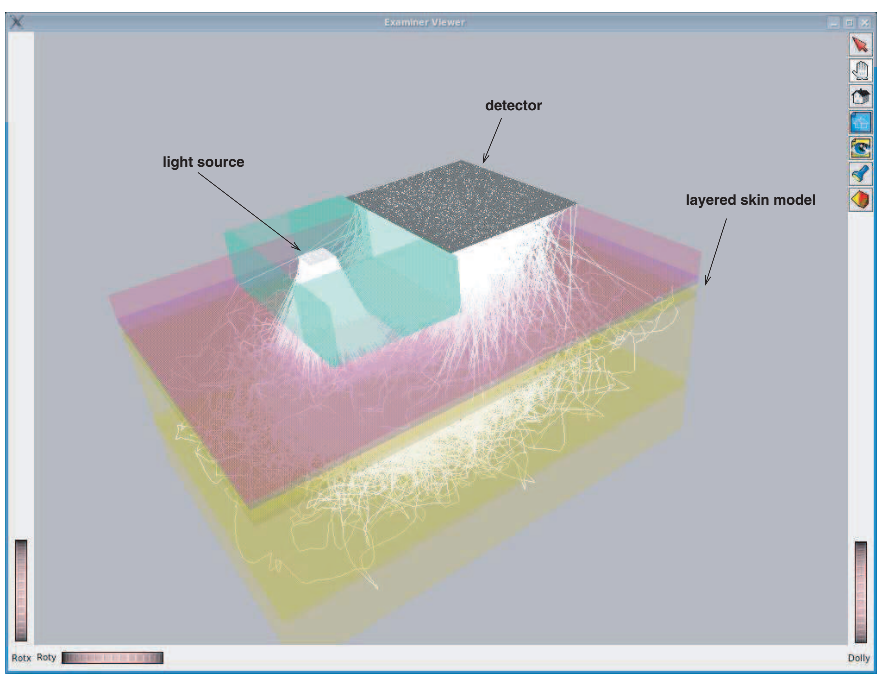

Figure 5: 3D visualisation of photon simulations for infrared illumination. The full photon paths of all registered photons are depicted.

7. DYNAMIC SIMULATIONS

Due to increasing computing power also parameterised simulations can be done. In repeated simulation runs different scenario properties can be changed. As an example the blood volume contents in the capillary layer have been chosen as dynamic parameter. These dynamic simulation runs thus model the contraction of one heart beat. It will result mainly in an increase of blood volume in the capillaries by about 10%, that is from 4% to 4.4%. Figure 7 shows the simulation results. With increasing blood volume the light intensity at the detector will decrease due to increased absorbance in the skin. Despite statistical variations the relation seems to be linear. The slope of

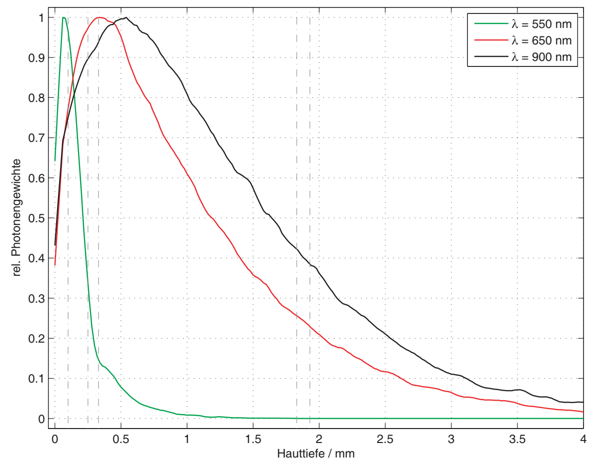

Figure 6: Sensor sensitivity in relation to skin depths for different wavelengths of $\lambda = 550$, 650 and 900 nm.

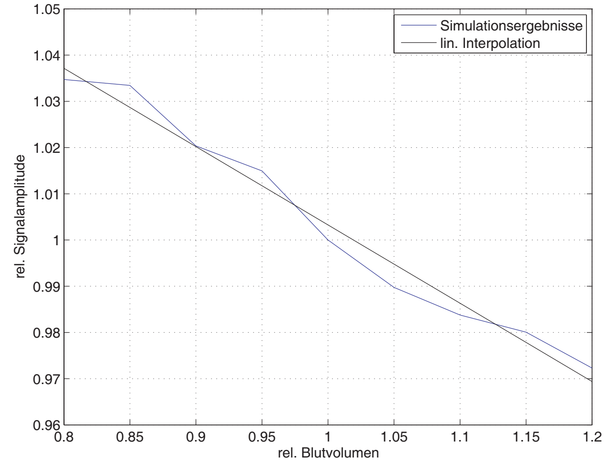

Figure 7: Expected intensity changes in relation of blood contents in the skin. The blood volume in the capillary layer has been changed by ±20%, in different simulation runs the number of photons registered at the detector have been calculated. A linear relation between blood contents and sensor intensity could be found.

the interpolation line represents the sensor sensitivity and is proportional to the AC component of the sensor signal. The DC component can be determined by the number of photons registered at the detector.

8. CONCLUSION

Advances in computing power allow new appliances of Monte Carlo simulations. Apart from static simulations for the quantification of penetration depth, measurement volume etc., also parameterised simulation runs are possible. For sensor optimisations in regard to working wavelength functional representations of the simulation parameters have been collected and extended from the literature. Layered skin models from different authors have been found to lead to comparable results despite their differing layer dimensions. The general suitability of these simulation models could be approved by experiments.

Due to the modularised concept of the implemented simulation tool dynamic simulation runs could be realised. As a result the skin can not only be simulated as a static scenario, but modelling of vital functions like the heart beat is possible.

REFERENCES

1. Metropolis, N. and S. Ulam, "The Monte Calro Method," *J. Am. Statistics Association*, 335–341, 1949.
2. Prahl, S. A., *Optical absorption of hemoglobin, Oregon Medical Laser Center*, http://omlc.ogi.-edu/spectra/hemoglobin/index.html, 1999.
3. Jacques, S. L., *Skin Optics*, Oregon Medical Laser Center News, 1998.
4. Meglinskii, I. V. and S. Matcher, "Quantitative assessment of skin layers absorption and skin reflectance spectra simulations in the visible and near-infrared spectreal regions," *Phys. Meas.*, Vol. 23, 741–753, 2002.
5. Mühl, T. M., *Berechnung von Lichtintensittsverteilungen in streuenden Medien*, PhD thesis, RWTH Aachen, 1988.
6. Tuchin, V. V., "Light scattering study of tissue," *PhysicsCUspekhi*, Russian Academy of Sciences, 495–515, 1997.

Modeling and Analysis of Crosstalk between Differential Lines in High-speed Interconnects

F. Xiao and Y. Kami

University of Electro-Communications, Japan

Abstract— The crosstalk between a single-ended line and a differential pair, and between differential pairs are investigated in this paper. First, the telegrapher's equations for multiconductor line are applied. Then the telegrapher's equations are solved by using the mode decomposition technique. Finally the mixed-mode S-parameters are derived to investigate the crosstalk and mode conversion.

1. INTRODUCTION

As clock frequency reaches the gigahertz band and signal transmission rate reaches the gigabit range, signal integrity issues, such as crosstalk between signals, are becoming serious problems in the interconnection of signals. Comparing with the single-ended signaling, differential traces are highly resistant to common-mode noise from other signals or external fields, reduce the common-mode radiation levels, and improve the signal integrity as well as the dynamic range [1–3]. Compared to single-ended signaling, differential signaling uses double the number of interconnects. N singleended signals need $N + 1$ interconnects, while N differential signals need $2N$ interconnects. As the circuit packaging density continues to increase, the number of interconnects will be a limiting factor. It is desirable to send as much data as possible between two points using a minimum number of interconnects. Inserting an extra signal information by using the common mode into the differential signaling is a promising technique [4]. Theoretically, the differential and common modes are orthogonal with each other, thus the two signals can be transmitted on the same physical channel without affecting each other. The circuit to implement this idea is illustrated in Fig. 1. The differential signal is generated by the switching array S_1 and S_2. Another signal is introduced which is connected to the center of two resistors at both ends. Since this signal only influences the common-mode signal, the original differential signal is not affected [5]. The schemes for commonmode transmission in differential pair is shown in Fig. 2. V_d and V_c are the original differential and common-mode signals. Since the two signals transmit on the same physical channel, the signal on the circuit will be the combination of the two signals. Here we denoted the combination signal as V_{out}. Since the differential and common modes are orthogonal, thus from the difference of the combined signal, the differential-mode signal can be obtained. On the other hand, from the sum of the combined signal, the common-mode signal can be extracted.

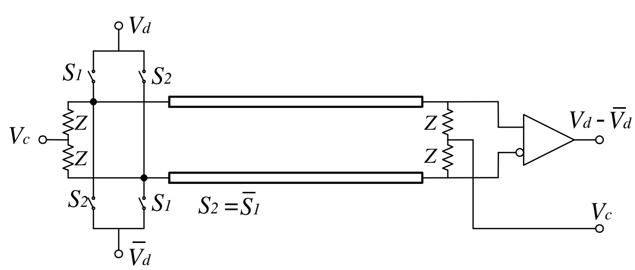

Figure 1: Circuit for both differential and common-mode signaling.

While in theory the differential and common modes are orthogonal, in practice, inevitable non-idealities, such as mismatch due to vias, connectors, and ground bounce, lead to crosstalk problems. The crosstalk may exist in several different manners. First, signal coupling between modes causes mode conversion between differential and common mode. Furthermore, if a differential pair is near to a single-ended trace or another differential pair, the crosstalk between them may occur. In this work, as a preliminary study, we consider the crosstalk to differential lines from a nearby singleended trace or another differential pair. First the crosstalk and mode conversion are analyzed.

In our analysis, the differential pairs are considered as parallel transmission lines thus the telegrapher's equations for multi-conductor lines can be applied [6]. Then the telegrapher's equations are solved by using a mode decomposition technique. The mixed-mode S-parameters are derived to investigate the crosstalk and mode conversion. The measurement of the crosstalk and mode conversion are also conducted. The characteristics of the near-end crosstalk (NEXT) and far-end crosstalk (FEXT) are also examined and discussed.

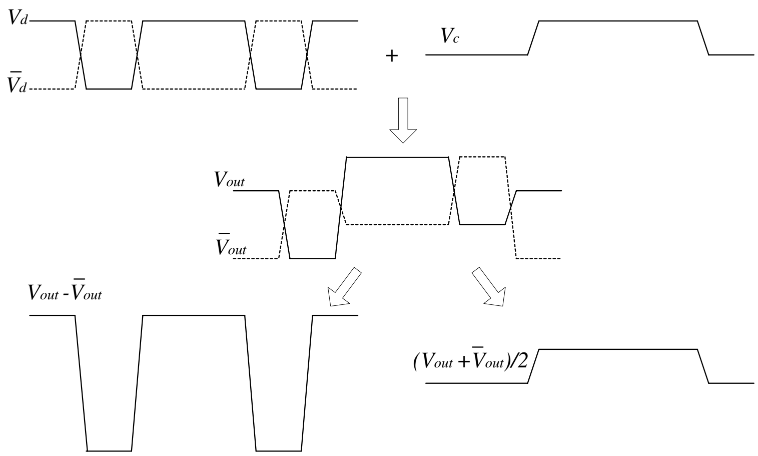

Figure 2: Scheme for differential and common-mode signaling.

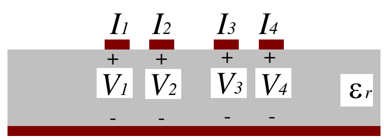

Figure 3: Schematic of four conductor lines above ground plane and definition of line voltages and currents.

2. NETWORK EXPRESSION FOR (4+1)-CONDUCTOR LINES

Two pairs of differential traces run parallel on a PCB is shown in Fig. 3. The line voltages V_i and line currents I_i $(i = 1, 2, 3, 4)$ for each trace are also shown in the figure. At the first step, we just consider the traces as four conductor transmission lines above a reference conductor, i.e., (4+1)-conductor lines. If the traces are x-oriented, then the telegrapher's equations are

$$\frac{\partial \boldsymbol{V}}{\partial x} = -j\omega \boldsymbol{L}\boldsymbol{I}, \quad \frac{\partial \boldsymbol{I}}{\partial x} = -j\omega \boldsymbol{C}\boldsymbol{V} \tag{1}$$

where $\boldsymbol{V} = [V_1, V_2, V_3, V_4]^T$ and $\boldsymbol{I} = [I_1, I_2, I_3, I_4]^T$ are respectively the line voltage and current vectors with the superscript T denoting the transpose of the vector, $\boldsymbol{L}$ and $\boldsymbol{C}$ are the per-unit-length inductance matrix and capacitance matrix, respectively. Both $\boldsymbol{L}$ and $\boldsymbol{C}$ are symmetric matrices. The equations in (1) are a set of eight, coupled, first-order partial differential equations. They can be solved using the mode decomposition technique [6]. This technique decomposes the line voltages and currents into four independent modes, then the eight coupled telegrapher's Equation (1) are transformed to eight uncoupled equations. The primary solution process of the mode decomposition technique is to find transformation matrices $\boldsymbol{T}_v$ and $\boldsymbol{T}_i$, which change the actual line voltages and currents, $\boldsymbol{V}$ and $\boldsymbol{I}$, to the mode voltages and currents $\boldsymbol{V}_m$ and $\boldsymbol{I}_m$, i.e.,

$$\boldsymbol{V} = \boldsymbol{T}_v \boldsymbol{V}_m, \quad \boldsymbol{I} = \boldsymbol{T}_i \boldsymbol{I}_m \tag{2}$$

The solution of the eight uncoupled equations can be easily obtained in the same fashion of solving a bifilar transmission line. For example, without loss of generality, for lines of length ℓ, we can express the network expression between the mode voltages and currents in chain matrix as

$$\begin{bmatrix} \boldsymbol{V}_m(0) \\ \boldsymbol{I}_m(0) \end{bmatrix} = \begin{bmatrix} \boldsymbol{A}_m & \boldsymbol{B}_m \\ \boldsymbol{C}_m & \boldsymbol{D}_m \end{bmatrix} \begin{bmatrix} \boldsymbol{V}_m(\ell) \\ \boldsymbol{I}_m(\ell) \end{bmatrix} \tag{3}$$

where the matrices $\boldsymbol{A}_m$, $\boldsymbol{B}_m$, $\boldsymbol{C}_m$, and $\boldsymbol{D}_m$ can be easily calculated from the mode impedances, phase constants, and the line length. Thus for the actual line voltages and currents we have

$$\begin{bmatrix} \boldsymbol{V}(0) \\ \boldsymbol{I}(0) \end{bmatrix} = \begin{bmatrix} \boldsymbol{T}_v & \boldsymbol{O} \\ \boldsymbol{O} & \boldsymbol{T}_i \end{bmatrix} \begin{bmatrix} \boldsymbol{A}_m & \boldsymbol{B}_m \\ \boldsymbol{C}_m & \boldsymbol{D}_m \end{bmatrix} \begin{bmatrix} \boldsymbol{T}_v^{-1} & \boldsymbol{O} \\ \boldsymbol{O} & \boldsymbol{T}_i^{-1} \end{bmatrix} \begin{bmatrix} \boldsymbol{V}(\ell) \\ \boldsymbol{I}(\ell) \end{bmatrix} \equiv \begin{bmatrix} \boldsymbol{A} & \boldsymbol{B} \\ \boldsymbol{C} & \boldsymbol{D} \end{bmatrix} \begin{bmatrix} \boldsymbol{V}(\ell) \\ \boldsymbol{I}(\ell) \end{bmatrix} \tag{4}$$

This is the obtained chain matrix expression for the (4+1)-conductor transmission line system. From the above admittance matrix, the standard scattering matrix can be derived. This standard S-parameters can be further transformed to the mixed-mode S-parameters [7], with which the crosstalk is analyzed.

3. MODELING AND ANALYSIS RESULTS FOR A SINGLE-ENDED LINE AND A DIFFERENTIAL PAIR

The mixed-mode S-parameters actually completely define the relations between the modes in the multi-conductor lines. For a single-ended line and a differential pair, i.e., three-conductor lines, Fig. 4, the mixed-mode S-parameters are

$$S_{mixed} = \begin{bmatrix} S_{ss11} & S_{ss12} & S_{sd13} & S_{sd14} & S_{sc13} & S_{sc14} \\ S_{ss21} & S_{ss22} & S_{sd23} & S_{sd24} & S_{sc23} & S_{sc24} \\ S_{ds31} & S_{ds32} & S_{dd33} & S_{dd34} & S_{dc33} & S_{dc34} \\ S_{ds41} & S_{ds42} & S_{dd43} & S_{dd44} & S_{dc43} & S_{dc44} \\ S_{cs31} & S_{cs32} & S_{cd33} & S_{cd34} & S_{cc33} & S_{cc34} \\ S_{cs41} & S_{cs42} & S_{cd43} & S_{cd44} & S_{cc43} & S_{cc44} \end{bmatrix} \tag{5}$$

The S_{ss11}, S_{dd33}, and S_{cc33} provide the input impedance information for the single-ended trace, and the differential and common mode respectively. The S_{dc43} and S_{cd43}, provide the mode conversion information between differential and common modes. And the four parameters S_{ds31}, S_{ds41}, S_{cs31}, and S_{cs41} provide the near-end and far-end crosstalk information from the single-ended trace to the differential mode and common mode. Since the crosstalk is actually a function of the traces separation, we will investigate the effect of the trace separation on the crosstalk. Parametric simulations were conducted for this investigation. All geometries were fixed except the center-to-center distance between the single-ended trace and the differential pair, D, Fig. 4, is changed.

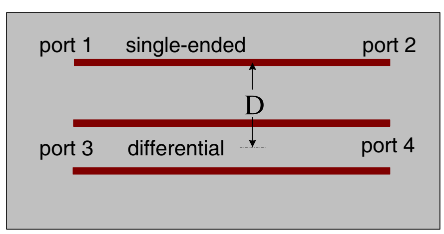

Figure 4: A single-ended line and a differential pair.

First, the effect of the trace separation on the input impedance of the single-ended trace, the differential-mode, and the common-mode are shown in Fig. 5. The separation is changed from 4.5 mm to 9.5 mm. First, one can see the input impedance of the common mode is almost not affected by the changing of the separation D. On the contrary, the effect on the input impedance of the differential mode, and the single-ended line is obvious, especially for the differential mode. Next, let's look at the resonance frequency. One can see the resonance frequency of the common mode is always less than that of the differential mode. In other words, the differential mode propagates faster than the common mode. This is because the differential mode has more electric flux in the air, leading to a lower effective permittivity and higher phase velocity. Furthermore, one can see that, narrowing the space between the single-ended trace with the differential pair will cause the differential mode faster.

The mode conversion between differential and common modes is shown in Fig. 6(a). One can see, up to 3 GHz, the mode conversion is less than −20 dB. In Fig. 6(b), the mode conversion at 2 GHz is shown as a function of the separation D. One can see the mode conversion falls off quickly as the separation is increased. With doubling the separation, the reduction in the mode conversion is about 22 dB.

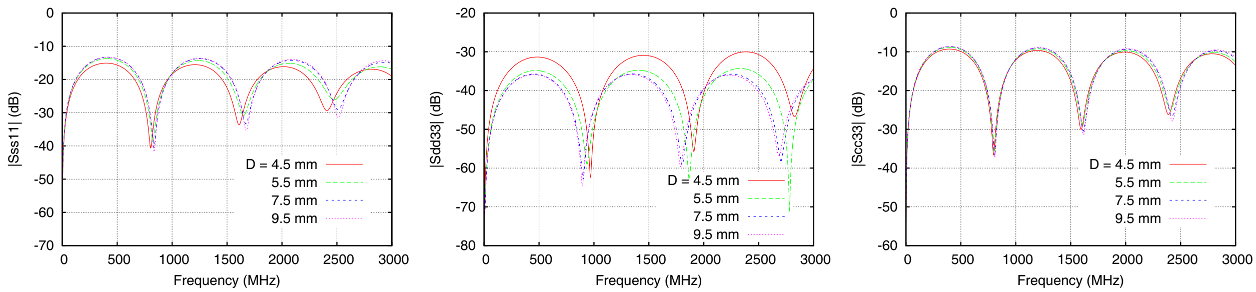

(a) (b) (c)

Figure 5: Input impedance of each mode affected by the trace separation, (a) single-ended, (b) differential mode, and (c) common mode.

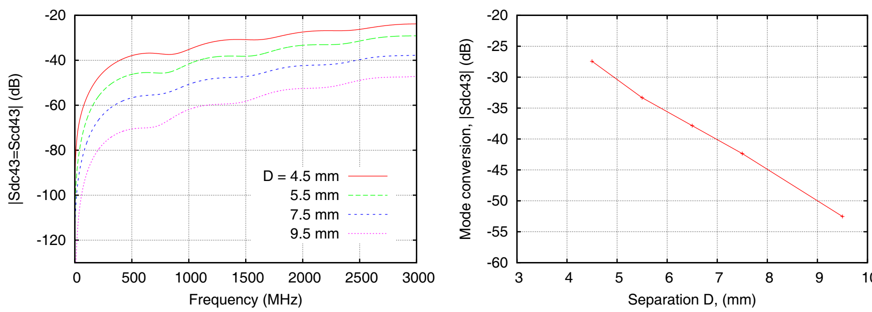

(a) (b)

Figure 6: Mode conversion between the differential mode and common mode affected by the trace separation, (a) with D as parameter, (b) at 2 GHz.

In Figs. 7 and 8, the crosstalk from the single-ended trace to the differential mode and common mode are shown respectively. For both near- and far-end crosstalk, one can see the levels for the differential mode are lower than those of the common mode. When the separation D is 4.5 mm, for the near-end crosstalk, the common-mode response is about -17 dB, where the differential mode response is about -20 dB. For the far-end crosstalk, the common-mode response can be up to -7 dB, where the differential response is about -15 dB. In Fig. 9, the crosstalk levels are shown versus the separation D. One can see the crosstalk falls off quickly as the separation is increased. With doubling the separation, the reduction in the near-end crosstalk from the single-ended trace to the differential mode is about 16 dB, and the reduction in the far-end crosstalk to the differential-mode is about 9 dB. On the other hand, the reduction in the near-end crosstalk to the common-mode is about 11 dB, and the reduction in the far-end crosstalk to the common-mode is about 8 dB. That is, the reduction for the crosstalk to the common mode is not as effective as for those of the differential mode. Furthermore, the reduction for the far-end crosstalk, both for the differential mode and common mode, is not as effective as for the near-end crosstalk. The crosstalk between differential pairs are smaller than those for the case of a single-ended line to a differential pair. But the behaviors for both the near- and far-end crosstalks are similar to those discussed above.

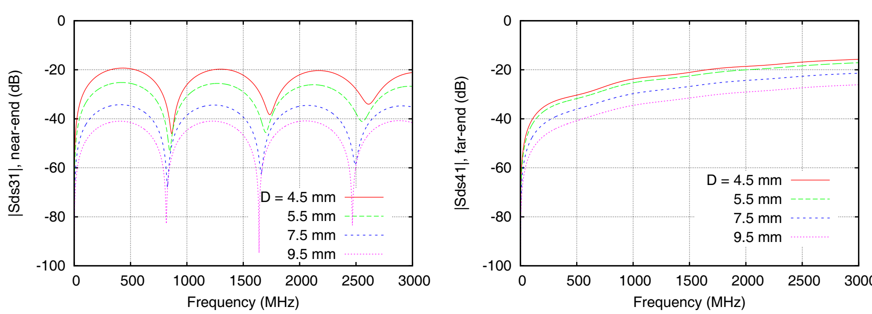

(a) (b)

Figure 7: Crosstalk from the single-ended trace to the differential mode (a) near end, and (b) far end.

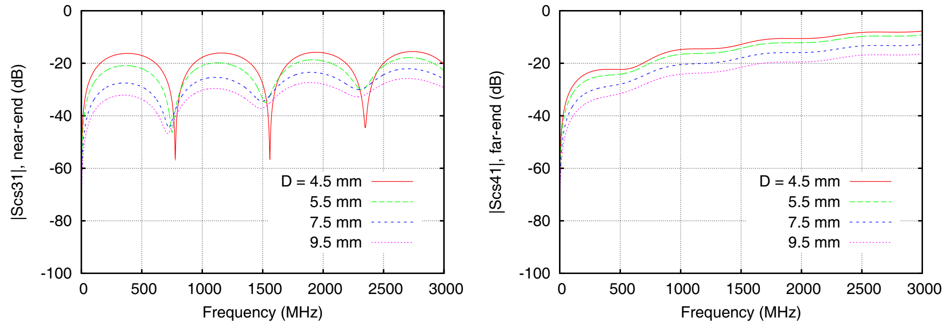

(a) (b)

Figure 8: Crosstalk from the single-ended trace to the common mode (a) near end, and (b) far end.

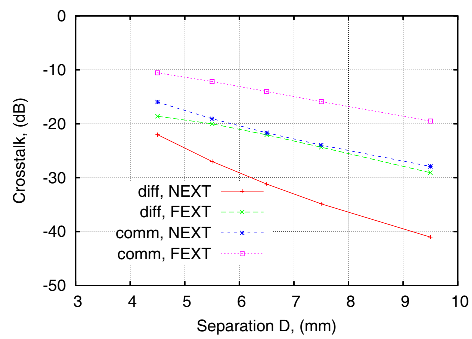

Figure 9: Crosstalk levels versus trace separation at 2 GHz.

4. CONCLUSION

The crosstalk between a single-ended line and a differential pair, and the crosstalk between differential pairs have been analyzed based on the telegrapher's equations for multi-conductor lines. The obtained results can give guidelines for design the differential interconnects for minimizing the crosstalk. That is the goal of this work. Several possible differential-line structures will be considered, including the co-planar lines, stacked-pair lines, diagonal-pair lines, to find a design of the interconnects that minimizes the crosstalk. Different structures may exhibit different crosstalk characteristics, and the crosstalk may be decreased by properly setting the differential pair. Furthermore, the effect of routing guard traces and ground tracks will also be examined.

REFERENCES

1. Johnson, H. W. and M. Graham, *High Speed Digital Design: A Handbook of Black Magic*, Prentice Hall, NJ, 1993.
2. Hall, S., G. W. Hall, and J. A. McCall, *High-Speed Digital System Design: A Handbook of Interconnect Theory and Design Practices*, John Wiley & Sons, INC., New York, 2000.
3. Johnson, H. W. and M. Graham, *High Speed Signal Propagation: Advanced Black Magic*, Prentice Hall, NJ, 2003.
4. Gabara, T., "Phantom mode signaling in VLSI system," *Proc. Conf. on Advances Research in VLSI*, 88–100, Salt Lake City, UT, Mar. 2001
5. Kimura, M., H. Ito, H. Sugita, K. Okada, and K. Masu, "Zero-crosstalk bus line structure for global interconnects in Si ultra large scale integration," *Japanese Journal of Applied Physics*, Vol. 45, No. 6A, 4977–4981, 2006.
6. Paul, C. R., *Analysis of Multiconductor Transmission Lines*, John Wiley & Sons, INC., New York, 1994.
7. Eisenstadt, W. R., B. Stengel, and B. M. Thompson, *Microwave Differential Circuit Design Using Mixed-Mode S-Parameters*, Artech House, Norwood, MA, 2006.

A Novel Time-domain Approach Using TDR/TDT for Synthesizing SPICE-compatible Models of Power Delivery Networks with Resonance Effect

Chen-Chao Wang[1], Chih-Wen Kuo[1], Alex Wang[2], and Hung-Hsiang Cheng[2]

[1]Department of Electrical Engineering, National Sun Yat-Sen University, Kaohsiung, Taiwan
[2]Advanced Semiconductor Engineering Group, Kaohsiung, Taiwan

Abstract— A novel time-domain approach for synthesizing SPICE-compatible models of power delivery networks with resonance effect using time-domain reflected/transmitted waveforms either measured by TDR/TDT or simulated by FDTD method has been developed. The step responses of the power/ground planes are solved in terms of rational functions by the generalized Pencil-of-Matrix (GPOM) method, and the pole-residue representation of the time-domain step responses of the planes structure is obtained. The macro-π model in terms of the rational functions pairs is obtained through a Y matrix transformation. The equivalent lumped circuits of the macro-π model are synthesized by a lumped circuit extraction method. It is found that the extracted models accurately predict the power/ground bouncing or resonance behavior in a wide-band range. The developed models can be efficiently incorporated into the HSPICE simulator for considering the power/ground bouncing noise in high-speed circuits.

1. INTRODUCTION

In recent high-speed digital circuits with pico-second rising/falling edges, it is reasonable to consider the power/ground planes as a dynamic electromagnetic system [1]. The simultaneous switching noise (SSN) or ground bounce noise, resulting from the transient currents flowing between power planes during the state transitions of the logic gates, has become a critical factor to degrade the signal integrity (SI) and power integrity (PI) in PCB or package design [2]. In order to accurately perform overall system-level power integrity simulation, extracting the SPICE-compatible models of the power/ground planes with resonance effect and incorporating the model into the conventional circuit simulator, such as SPICE, is essential.

In the early development, the power delivery network consisting of the power/ground planes was modeled as a lumped inductor or inductive network [3]. At high frequencies where the wave phenomenon is more significant, more accurate modeling of the power delivery network is necessary. Various numerical methods based on the cavity models [4] and partial element equivalent circuit method [5], among others, were proposed to model the power/ground planes. Full-wave numerical methods such as finite-element (FEM), finite-difference time-domain (FDTD) and moment methods (MoM) were also adapted to analyze the complicated resonance effect of the simultaneous switching noise [6]. Recently, based on time-domain responses either from simulations or measurements, the resonance effect of the power/ground planes was characterized using a complicated process [7].

In this paper, a time-domain approach is proposed for synthesizing the SPICE-compatible circuits of the power/ground planes based on a two-port π-model. According to either the measured or simulated time-domain reflected waveforms, the generalized pencil of matrix method (GPOM) [8] is employed to construct the time-domain step response of the power/ground planes in terms of rational functions. The equivalent model in terms of the rational functions pairs is obtained through a two-port Y-matrix transformation. The equivalent circuits of the model are finally transformed by a systematic lumped-model extraction technique (SLET) [9].

2. SIMULATION OR MEASUREMENT SETUP

Time-domain waveforms are employed to obtain the step response of the power/ground planes. The time domain waveforms are made available either through FDTD simulation or a TDR/TDT measurement. Fig. 1 shows an example of the power/ground planes for a two-layer board ($\varepsilon_r = 4.3$). For the simulation setup, a resistive voltage source injects a step waveform into the power/ground planes, and receives transmitted waveform on the other end. In addition, for measurement setup, we can use a general TDR, such as Tektronix CSA8000B or Agilent DCA86100C, to launch a step waveform into the power/ground planes. This setup is used for the power/ground planes model extraction both from the FDTD simulation or the TDR/TDT measurement.

3. STEP RESPONSES AND MODE EXTRACTION

As shown in Fig. 1, a step source with rise time τ is injected into port1 and port2, respectively, and the reflected and transmitted voltage waveforms are recorded. The step responses of the power/ground planes at these two ports can be obtained by normalizing the reflected and transmitted waveforms with the incident wave amplitude, and are denoted as $y_{mn}(t)$, where m is the receiving port and n is the injecting port. By employing the GPOM method, the step responses can be obtained as a summations of the complex exponential terms (modes) as

$$y_{mn}(t) = \sum_{i=1}^{L_{mn}} r_{mn}^{i} \exp\left(-p_{mn}^{i} t\right) \tag{1}$$

where $m, n = 1$ or 2, r_{mn}^{i} and p_{mn}^{i} are the residues and poles in the Z planes, and L_{mn} is the number of exponential term synthesized by the GPOM. The objective of the GPOM is to find the best estimates of L_{mn}, r_{mn}^{i}, p_{mn}^{i} and with $i = 1, \ldots, L_{mn}$.

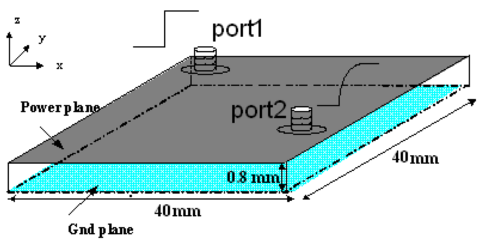

Figure 1: An equivalent two-layer PCB to model a power/ground planes pair.

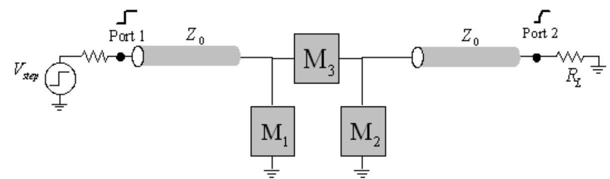

Figure 2: The proposed equivalent π-model module.

4. MODULES OF π-MODEL

The corresponding impulse responses of the power/ground planes in frequency domain is obtained through the Laplace transformation of (1) as the rational functions

$$\xi_{mn}(s) = s \sum_{i=1}^{L_{mn}} \frac{r_{mn}^{i}}{s + p_{mn}^{i}} \tag{2}$$

Figure 2 shows the proposed equivalent π-model of the power/ground and the corresponding ports. By using the two-port transformation and the definition of the impulse response in (2), the corresponding models with three modules M_1, M_2, and M_3 can be derived as

$$M_1(s) = \frac{1}{Z_0} \frac{(1-\xi_{11})(1+\xi_{22}) + (\xi_{12})(\xi_{21}) - 2\xi_{21}}{(1+\xi_{11})(1+\xi_{22}) - (\xi_{12})(\xi_{21})} \tag{3a}$$

$$M_2(s) = \frac{1}{Z_0} \frac{(1+\xi_{11})(1-\xi_{22}) + (\xi_{12})(\xi_{21}) - 2\xi_{21}}{(1+\xi_{11})(1+\xi_{22}) - (\xi_{12})(\xi_{21})} \tag{3b}$$

$$M_3(s) = \frac{1}{Z_0} \frac{2\xi_{21}}{(1+\xi_{11})(1+\xi_{22}) - (\xi_{12})(\xi_{21})} \tag{3c}$$

where Z_0 is the impedance of the terminated transmission line. Each of the modules (M_1, M_2, or M_3) is derived based on the admittance definition in frequency domain.

5. LUMPED CIRCUITS EXTRACTION METHOD (LCEM)

The final step is to synthesize the equivalent lumped circuits π modules. M_i in (3) can be rearranged as

$$M_i(s) = s \sum_{\substack{i=1 \\ q_i>0}}^{K_0} \frac{q_i}{s+h_i} + s \sum_{\substack{i=1 \\ v_i>0}}^{K_i} \frac{r_i s + v_i}{s^2 + u_i s + m_i} + \frac{P(s)}{Q(s)} + K_i \tag{4}$$

where q_i, h_i, r_i, v_i, u_i, m_i are real numbers and $i = 1, 2$, or 3. The corresponding circuit models for the first-order terms in the first summation of (4) can be realized by a parallel connection of series R-C, as shown in Fig. 3(a), with

$$R_{Ci} = 1/q_i \tag{5a}$$
$$C_i = 1/\left(h_i \cdot R_{Ci}\right) \tag{5b}$$

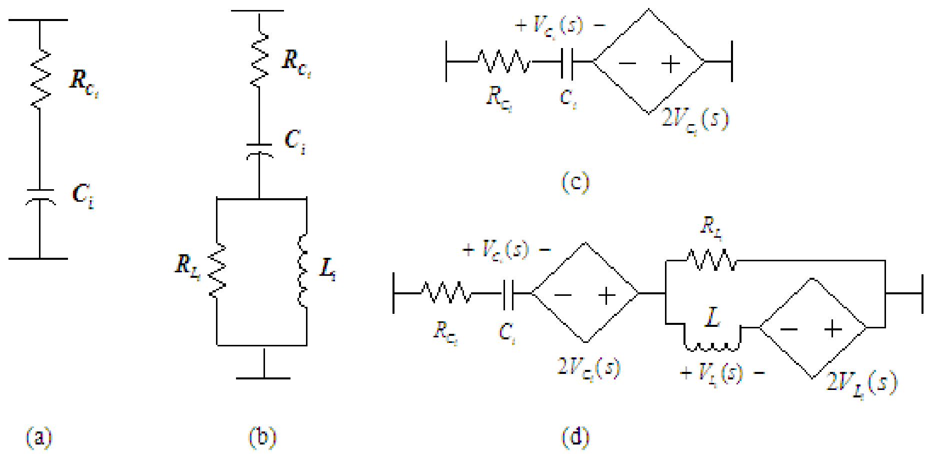

Figure 3: Four types of the equivalent model extracted from the pole-residue representation.

The equivalent circuits of the second-order terms in the second summation of (4) are shown in Fig. 3(b) with corresponding values derived as

$$C_i = v_i/m_i \tag{6a}$$
$$R_{Ci} = \left(u_i - r_i/C_i\right)/v_i \tag{6b}$$
$$R_{Li} = 1/r_i - R_{Ci} \tag{6c}$$
$$L_i = R_{Li} \cdot r_i/\left(C_i \cdot m_i\right) \tag{6d}$$

The remaining term $P(s)/Q(s)$ in (4) can also be converted to a summation of first-order and second-order terms with negative value q_i and v_i, respectively. By employing the voltage-controlled voltage-source (VCVS), they can be synthesized as the circuit models shown in Figs. 3(c) and 3(d) for the first-order and second-order terms, respectively. The corresponding values for the first-order term can be derived as

$$R_{Ci} = 1/q_i \tag{7a}$$
$$C_i = -1/\left(h_i \cdot R_{Ci}\right) \tag{7b}$$

and the values of second-order terms can be derived as

$$C_i = -v_i/m_i \tag{8a}$$
$$R_{Ci} = \left(u_i + r_i/C_i\right) v_i \tag{8b}$$
$$R_{Li} = 1/r_i - R_{Ci} \tag{8c}$$
$$L_i = R_{Li} \cdot r_i/\left(C_i \cdot m_i\right) \tag{8d}$$

$V_{Ci}(s)$ in Fig. 3(c) and $V_{Li}(s)$ in Fig. 3(d) are the voltage drop crossing on the corresponding capacitor and inductor, respectively.

6. MODELING RESULT AND DISCUSSION

An FDTD simulation with a 0.4 V step source of 10 ps rise-time was launched to port 1 to obtain the reflected and transmitted time domain response. Using the proposed approach, the equivalent model of the power/ground planes can be extracted successful. The accuracy of the equivalent lumped model is verified in frequency-domain. For comparing the results in the frequency-domain, S_{11} and S_{21} calculated by the extracted model and Ansoft HFSS is shown in Fig. 4, and Fig. 5. Both the magnitude and phase agree reasonably well. Good agreement both in magnitude and phase is also seen in frequency range from DC to 3 GHz.

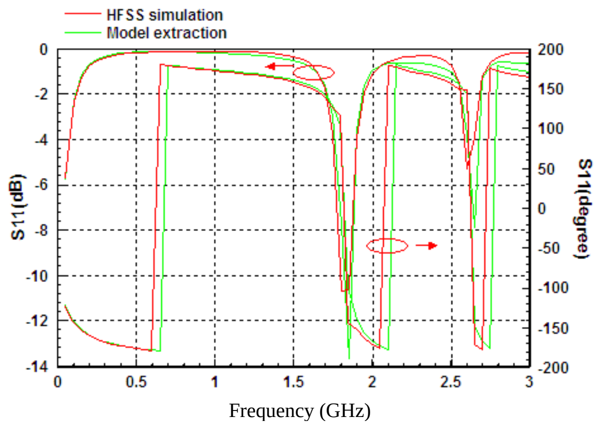

Figure 4: Comparison of S_{11} with extracted model in ADS and HFSS simulations for magnitude and phase.

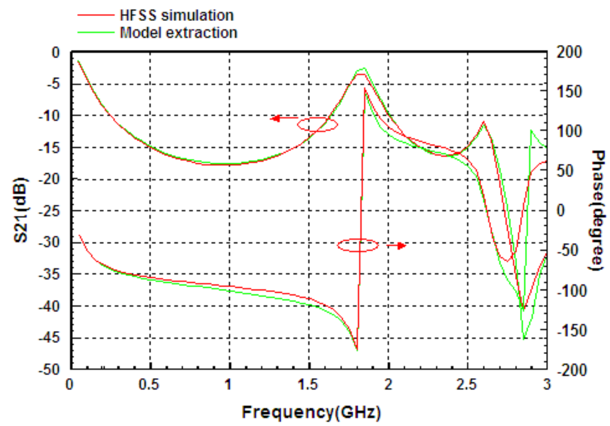

Figure 5: Comparison of S_{21} with extracted model in ADS and HFSS simulations for magnitude and phase.

7. CONCLUSION

Based on the TDR/TDT-measured or FDTD-computed time-domain data, an efficient systematic approach has been proposed to extract the SPICE-compatible models of the power delivery networks. According to either the measured or simulated time-domain waveforms, the GPOM is employed to construct the time-domain step response of the power/ground planes in terms of rational functions. The rational functions are then used to extract the lumped circuits of DUT by SLET. The good accuracy of the proposed approach in frequency-domain has been demonstrated.

REFERENCES

1. Van den Berghe, S., F. Olyslager, D. De Zutter, J. De Moerloose, and W. Temmerman, "Study of the ground bounce caused by power plane resonances," *IEEE Trans. Electromagn. Compat.*, Vol. 40, May 1998.
2. Nuebel, J., T. Roy, and S. Das, "An investigation on power plane decoupling for high speed multiprocessor boards," *Proc. IEEE Int. Symp. Electromagn. Compat.*, 355–360, 1999.
3. Ruehli, A. E. and H. Heeb, "Circuit models for three-dimensional geometries including dielectrics" *IEEE Trans. Microw. Theory Tech.*, Vol. 40, 1507–1516, July 1992.
4. Shi, W. and J. Fang, "New efficient method of modeling electronics packages with layered power/ground planes," *IEEE Trans. Adv. Packag.*, Vol. 25, No. 3, 417–423, Aug. 2002.
5. Pinello, W., A. C. Cangellaris, and A. Ruehli, "Hybrid electromagnetic modeling of noise interactions in packages electronics based on the partial-element equivalent-circuit formulation," *IEEE Trans. Microwave Theory Tech.*, Vol. 45, 1889–1896, Oct. 1997.
6. Van der Berghe, S., F. Olyslager, D. De Zutter, J. De Moerloose, and W. Temmerman, "Study of the ground bounce caused by power plane resonances," *IEEE Trans. Electromagn. Compat.*, Vol. 40, No. 2, 111–119, May 1998.
7. Pannala, S., J. Bandyopadhyay, and M. Swaminathan, "Contribution of resonance to ground bounce in lossy thin film planes," *IEEE Trans. Advanced Packaging*, Vol. 22, 248–258, Aug. 1999.
8. Sarkar, T. K. and O. Pereira, "Using the matrix pencil to estimate the parameters of a sum of complex exponentials," *IEEE Antenna and Propagation Magazine*, Vol. 37, 48–55, 1995.
9. Wu, T. L., C. C. Wang, C. C. Kuo, and J. S. Hsieh, "A novel time-domain method for synthesizing broadband macro-pi models of differential via," *IEEE Microwave and Wireless Components Letters*, Vol. 15, 378–380, May 2005.

A Study of Layout Strategies in RF CMOS Design

John Richard E. Hizon, **Marc D. Rosales**, **Honee Lynn B. Tan**
Maria Cecilia N. Gutierrez, **Louis P. Alarcon**, **and Delfin Jay Sabido IX**
Microelectronics and Microprocessors Laboratory
Department of Electrical and Electronics Engineering
University of the Philippines, Diliman, Quezon City, Philippines

Abstract— In this paper, the different issues confronting designers of RF blocks in digital CMOS are presented. These issues include the various implementations for the successful integration of spiral inductors and capacitors in CMOS for RF operation as well as the evaluation of Q enhancement techniques to improve inductor Q. Another barrier considered is RF MOSFET modeling because MOSFET parasitics become important as the operating frequency increases and enters the GHz range. Likewise, knowledge of the effects of layout on these parasitics is vital in improving RF design effectiveness. To improve RF design capability, it is therefore essential that actual measurement results be used to quantify realizable performance for both passive and active devices in CMOS. Structures presented in this paper were fabricated on a 0.25 μm digital CMOS process but the results obtained will be crucial for deep submicron CMOS processes.

1. INTRODUCTION

The widespread use of mobile wireless communication systems provides challenging opportunities for research and development. Cellular phone users, for example, want affordable, lightweight and compact handsets, which have all the benefits the latest technology can offer. Thus, the development of low cost, low power and high performance mobile handsets continues to be a major endeavor. A possible solution to the stringent requirements of mobile handsets is the single-chip integration of the baseband, the intermediate frequency (IF), and the radio frequency (RF) modules in digital CMOS. The continuous reduction of the minimum feature size for CMOS technology allows it to achieve cut-off frequencies suitable for RF applications. This development, along with its inherent (1) low cost, (2) high integration density, (3) mixed signal compatibility, (4) low voltage capability, and (5) production maturity, makes CMOS technology a viable contender in single-chip integration [1]. As such, research on both active and passive devices is important in realizing the ultimate goal of single-chip RF CMOS design.

On-wafer characterization of both active and passive devices is important in realizing the ultimate goal of single-chip RF CMOS design. In this paper, inductors, capacitors and transistors were implemented in a 0.25 μm digital CMOS process and characterized to enable RF circuit integration. Spiral Inductors are first discussed in Section 1 highlighting the best option available to increase isolation and inductor Q. Capacitors are introduced next in Section 2 and the various available topologies are analyzed to present the options on how to implement area efficient capacitors with acceptable Qs. Techniques in improving transistor performance are analysed next in Section 4. Several layout strategies were implemented to determine how it affects the transistor parasitics at RF. Finally, conclusions are drawn in Section 5.

All on-wafer measurements conducted used a Micromanipulator Probing station, Microwave Probe Link Arms, GSG Picoprobes 40A-GSG-160-P, an Agilent 8753ES Vector Network Analyzer, a HP 4156A Precision Semiconductor Parameter Analyzer, and HP 11590B bias tees. All test structures were enclosed in test fixtures with GSG pads for de-embedding processes. It was determined that open pad de-embedding was sufficient for frequencies up to 6 GHz.

For a more concise discussion on the merits of this research, results published previously by the authors on inductors [2–4] are summarized in this paper. For the details for on-wafer characterization of capacitors and transistors please refer to [5, 6].

2. SPIRAL INDUCTORS

For integration in current commercial CMOS process, octagonal and square spiral inductors were implemented. ASITIC was used in the initial design and simulations then on wafer characterization was done using the inductor model proposed by Yue [7]. Q-enhancement techniques were implemented with the inductors. These techniques are patterned ground shields [7], halo substrate contacts [8] and shunted metal layers [9]. The halo substrate contacts and patterned ground shields

Table 1: Summary of extracted parammeters for 1.8 nH inductor at 2.4 GHz.

Technique Used	Parameters			
	L (nH)	**R_S (Ω)**	**C_P (fF)**	**Q**
Plain	2	10.5	60	2.8
PGS	2	12.5	95	2.5
Halo	2	11.5	90	2.6
S.M.	2	9	130	3
S.M.+ PGS	2	9.8	150	2.8

Table 2: Summary of capacitors implemented.

Group 1			**Group 2**		
Capacitor Type	**Value (fF)**	**Area (μm^2)**	**Capacitor Type**	**Value (pF)**	**Area (μm^2)**
HPP	634.9	4984.36	VPP	4.98	14,522.66
VPP	593.97	1802	VPP min width	5.003	11,549.8
VPP min width	598.18	1430.27	VPP 9 sqrs	5	11,994.75
VB	467.7	1062.7	VB	3.93	8949.16
Fractal 1	617.2	2410.83	Fractal 1	5.01	18664.56
Fractal 2	601.2	2507.98	Fractal 2	4.95	19892.21
Fractal 3	601.2	2178.51	Fractal 3	4.95	17,166.71
Interdigital	600.7	928.87	Interdigital	5.02	7252.83
Woven	583.7	994.77	Woven	5.01	7839..33

were then later evaluated in improving the isolation in an epitaxial CMOS process [4]. Shown in Table 1 is a summary of the inductor parameters derived for a 1.8 nH square spiral inductor at 2.4 GHz. It can be noted that there were no significant improvements that were observed when the techniques mentioned above were used. This can be accounted for by the increased parasitics associated with these techniques. Notable is the increase in parasitic resistance associated with using PGS and halo substrate contacts. The use of shunted metals does lessen resistive losses but brings the inductor closer to the substrate, thereby lessening its effectiveness at higher frequencies. From experiments done, highest Q achieved was 4.5 for a 1.8 nH inductor and only 3 for a 10 nH inductor. The f_o of the 10 nH spiral was below 4 GHz while those for the 1.8 nH were beyond 6 GHz.

The general guidelines that were derived from the various inductor structures characterized are the following:

1. Patterned ground shields are better than halo substrate contacts in limiting substrate losses. Using patterned ground shields also improves the isolation between inductors.
2. Inductors should be placed in a diagonal configuration to improve isolation since coupling can be both magnetic and through the substrate. Measured results prove that a further 5 dB of isolation can be achieved with this layout configuration.
3. Placing a PGS under an inductor with shunted metal layers can help alleviate reduce substrate losses.
4. Use small inductors as much as possible since it offers higher Qs and smaller area leading to higher resonant frequencies.
5. Octagonal spirals offer a more hallow implementation than a square spiral and higher inductance values can be achieved for the same area compared with a square spiral.

3. CAPACITORS

Capacitors like inductors play an important role in RF blocks as well as in other circuits like converters and switched capacitor circuits. These structures often consume large areas, and this has been the focus of various researches on how to come up with area-efficient, high-density and high Q capacitors. Capacitors with smaller areas tend to have smaller resistances leading to higher Qs and smaller parasitic inductance leading to higher resonant frequencies. With newer CMOS processes, lateral flux has become increasingly dominant due to fringing capacitance. In this regard, a number of capacitor topologies have been proposed to take advantage of the increasing lateral flux component such as Vertical Bars (VB) and Vertical Parallel Plates (VPP) [10]. Other novel structures tend to exploit both the vertical and lateral flux capacitances thereby increasing capacitance densities. These structures include the interdigital [11], woven and quasi-fractal capacitors [10]. Research done on capacitors focused on the realization of three distinct groups of capacitors: with capacitance of 600 fF, with a capacitance range of 3 to 6 pF and with a capacitance of 6 to 12 pF. The range was needed since a highly reliable 3D electromagnetic field solver was not available to approximate the value of the capacitance designed and formal procedures for actual design were not outlined in literature. For a more detailed discussion on the capacitance estimation used in designing each capacitor, please refer to [12]. Each of the given topologies was implemented for the three identified groups except for the horizontal parallel plate (HPP) capacitor which was implemented only for the small capacitance. Table 2 illustrates the structures implemented for Group 1 and Group 2 with the corresponding simulated capacitance and area consumed. Note that the HPP capacitor is included in Group 1 for comparison.

The extracted results using a simple pi-model used in [5] is presented in Table 3 for three sets of capacitors, Group A in the range of 5–7 pF, Group B one in the vicinity of 400 pF and Group C with a range of 3–4 pF. It can be observed from the table that after fabrication, there were some discrepancies in the computed and extracted capacitances due to the oversimplification of the fringing capacitance among the different structures considered. This required a new grouping for better comparison and analysis to determine the best option in capacitor implementations.

Table 3: Summary of measured capacitor characteristics at 1 GHz.

	C(fF)	ΔC(%)	Density (aF/μm^2)	DF (%)	Q	L_S (nH)	f_O (GHz)
Group A							
VPP	5700	-14.42	392.49	4.61	21.69	0.356	3.54
VPP m.w.	5350	-7.02	463.2	4.96	20.16	0.087	7.38
VPP 9sqrs	5900	-17.84	491.88	9.76	10.24	0.121	5.96
Fractal 1	5790	1.31	310.21	7.24	13.81	0.192	4.77
Fractal 2	6360	2.47	319.72	5.65	17.71	0.139	5.36
Fractal 3	6250	4.12	364.07	7.67	13.04	0.117	5.88
VB	6730	8.36	377.05	5.97	16.75	0.175	4.64
Interdigital	5500	29.27	384.19	18.69	5.35	0.247	4.32
Woven	7370	26.67	475.17	43.28	2.31	0.255	3.67
Group B							
VB	384.04	12.93	361.3657	1.32	75.79	0.321	14.33
Interdigital	333.08	28.87	358.5857	1.15	87.20	0.360	14.53
Woven	469.132	19.63	471.5975	1.14	87.49	0.418	11.36
Group C							
VB	3990	-8.17	445.85	4.42	22.61	0.246	5.06
Interdigital	2880	26.09	382.68	3.71	26.99	0.262	5.79
Woven	4190	16.49	534.38	4.31	23.18	0.166	6.03

Results presented in [5] show that using capacitors that take advantage of lateral flux like the VPP resulted in 3.5 times increase in capacitor density compared with a standard HPP topology while fractal capacitors had at least 2 times the capacitor density. This clearly shows that area can be saved by optimizing lateral flux. Looking at Group A in Table 3 for both VPP capacitors and fractal capacitors, it can be observed that VPP capacitors achieved higher densities compared to fractal capacitors with very good Qs in the range of 10 to 20 which is better than inductors presented earlier. Among the VPP inductors, the VPP minimum width achieved the highest resonant frequency with high Q. The VPP 9 squares was implemented to minimize parasitic inductance which was achieved from Table 3. However, this particular topology suffers from a lot of losses as can be seen with the DF wherein, DF, dissipation factor, is the ratio of capacitor resistance to reactance. The increase in losses contributed to its very low Q. Incidentally, the capacitor with the best Q is the normal VPP capacitor. Fractal capacitors, on the other hand, offer good agreement between computed and actual measurements. Among fractal capacitors considered, the third option proved to be the best topology having the highest density, moderate Q and the highest f_o.

It is important to out point the three topologies that accounted for a wide margin between computed capacitance and measured capacitance. These topologies are: VPP, interdigital and woven. Interdigital and woven structures take advantage of both lateral and vertical flux. Interdigital capacitors were off by an average of 27% and woven structures were off by an average of 20%. This greatly highlights the shortcomings of the formula used in deriving the capacitance of these structures and merits further study. This is an important step given the capacitor densities achieved with these structures. Among the two, the woven capacitor offers the highest capacitor densities but this structure suffers from large losses as can be seen from measured DF for large capacitances. VPP and VB capacitors offer the best performance tradeoff between Q, f_O and L_S. Furthermore, its construction is fairly simple compared with the other structures.

4. MOS TRANSISTORS

In general, MOS transistors need large device widths are used to achieve the high g_m's and to maximize the operating frequency minimum gate length is used. To limit the noise contribution brought about by increased device widths due to increased gate resistance, R_g, a common layout practice is to decompose it into parallel transistors of smaller widths. This layout technique is referred as multi-finger distribution. This technique not only reduces R_g but it also reduces junction capacitances. Further reductions in gate resistance can be obtained by using double contacted gates. The disadvantages of multi-finger distribution include: (1) the increase in the required gate-source and gate-drain overpasses and (2) the increase in gate-bulk parasitics.

An offshoot to multi-finger distribution is the cluster of fingers (COF) approach [13]. This technique emphasizes a high degree of layout consistency so that all major MOSFET parasitics scale with device dimensions. A COF requires a consistent number of fingers between substrate contacts, a consistent length for drain, source and bulk diffusion areas for all transistors, and a constant finger width. This approach however may lead to reduced design flexibility and reduced performance because only multiples of the COF width can be implemented and the COF may not be optimum for all transistor widths.

Another implementation issue that must be considered is the tradeoff between the number of fingers for a given gate width. It was shown in [14] that for a W_f less than some critical finger width, R_g increases as W_f decreases due to Non-Quasi Static (NQS) effects. This is complicated further by the tradeoff between lower gate resistance and increased fringing effects. Other optimizations with gate geometry was presented in [15] which proposes the use of meander type gate structures to further improve the f_T's of MOS transistors.

Finally constraints on matching and symmetry must also be addressed requiring the use of dummy transistors/gates and limiting interference through the use of substrate contacts and guard rings. All these guidelines were considered in the study of MOS transistor implementations for RF applications. The objective is to determine the effects of the different layout techniques on the dominant MOS parasitics. Three MOS device widths were chosen: 150 µm, 300 µm and 450 µm using a minimum length and configured in a CS topology. Various gate structures were incorporated in the experiments and include: (1) single-contacted comb type, (2) single-contacted meander type, (3) double-contacted comb type, and (4) double-contacted meander type. Different finger widths were also considered for each device width as listed in Table 4.

Table 4: List of number of fingers/finger widths implemented in multi-finger distribution.

Width (µm)	# of Fingers	Finger (µm)
300	10	30
300	15	20
300	20	15
300	25	12
300	30	10
300	60	5

Extracted gate resistance presented in Table 5 reveal that double-contacted RF MOSFET's exhibit lower R_g compared to single-contacted RF MOSFET's. Smaller R_g's are observed as the number of fingers is increased. This is mainly attributed to smaller finger widths as the number of fingers is increased. Unlike in single-contacted transistors, there is a negligible difference (0.5 Ω) between R_g extracted from double-contacted meander type structures using 30 and 60 fingers which highlights that a critical width exists wherein an increase in the number of fingers and consequently, a decrease in the finger width, no longer result in a decrease in R_g. It was determined from measurements that drain resistance was not a strong function of the number of fingers. Also, there were no noticeable differences in terms of terminal resistance whether a transistor is implemented in multi-finger or COF technique. Using substrate contacts or guard rings does not affect the extracted terminal resistances.

Table 5: Variation of gate resistance in a multi-finger distribution.

Gate Type	No. of Fingers				
	10	15	20	30	60
SCM	56.44	37.59	34.76	29.23	24.05
DCM	37.08	30.13	28.67	21	21.5

In contrast to the trend noted in the terminal resistances, larger capacitances are extracted as the number of fingers used increases as can be observed, in general, in Table 6. This is attributed to greater capacitance due to the SDE regions and fringing effects. This trend is more apparent in C_{GD} because it is mainly due to the overlap capacitance. From measurements, the use of double-contacted gate structure results in larger capacitances. This is attributed to the amount of polysilicon used in these structures. In addition, compared to the doublecontacted comb type structure, the double-contacted meander type structure has more polysilicon, thus the meander type exhibit higher capacitance values. The use of substrate contacts, instead of guard rings, leads to a decrease in capacitances, with C_{GB} being the most significantly affected.

Table 6: Variation of gate capacitance in a multi-finger distribution.

Cap (fF)	No. of Fingers				
	10	15	20	30	60
C_{GG}	340	369.5	358.7	363.2	428.1
C_{GD}	93.72	100.8	100.2	104.7	124.1
C_{GS}	187.1	191.2	161.6	187.2	246.7
C_{GB}	74.3	77.7	68.8	71.3	57.3

Note there were no noticeable differences between the performances between COF or multi-finger transistors. The choice will therefore lie on which will provide the least amount of effort to generate the layout for a particular device width.

5. CONCLUSION

It is hoped that the results presented in this paper will be of great value to those research groups who will venture into the development of RF applications in digital CMOS. From studies conducted, spiral inductors have very limited Q. Proposed techniques were really not effective in improving Q. The use of shunted metals limits resistive losses but suffers from a larger capacitance with the substrate. The use of PGS offers the best solution in limiting crosstalk in epitaxial CMOS compared to halo substrate contacts. VPP and VB capacitors offer the best option for integrated capacitors due to it high capacitance densities and Q, although VPP capacitors are easier to design compared to VB. Quasi fractal 3 capacitors can also be used and offer comparable performance to VPP and VB, and can easily be designed but are more complex to implement. To limit MOS transistor parasitics, the use of guard rings, double contacted comb type gates and multi-finger techniques are highly recommended. Meander gates contribute to higher extracted capacitance thereby limiting high frequency capabilities of the transistor. The use COF technique is also recommended to achieve more regular layouts and improve matching.

ACKNOWLEDGMENT

The authors wish to acknowledge the assistance and support of Intel Higher Education Philippines and the Philippine Council for Advanced Science and Technology Research Development of DOST.

REFERENCES

1. Abidi, A., "RF CMOS comes of age," *IEEE J.S.S.C.*, Vol. 39, No. 4, 549–561, Apr. 2004.
2. Hizon, J. E., et al., "Characterization of monolithic inductors on a 0.25 μm digital CMOS process," *Proc. IEEE Region 10 Conference*, 21–24 Nov., 2004.
3. Rosales, M. D., et al., "Monolithic spiral inductors for a 0.25 μm digital CMOS process," *Proc. IEEE Region 10 Conference*, 21–24 Nov., 2005.
4. Hizon, J. E., et al., "Spiral inductor coupling on a 0.25 μm digital CMOS process," *Proc. IEEE Region 10 Conference*, 21–24 Nov., 2005.
5. Hizon, J. E., et al., "RF passives for a 0.25 μm digital CMOS process," *Mic. Con. Proc. APMC 2006*, 12–15 Dec., 2006.
6. Mangaser, J. E. R., et al., "A study on RF transistor implementations on a 0.25 μm digital CMOS process," *Proc. IEEE Region 10 Conference*, 14–17 Nov., 2006.
7. Yue, C. P., et al., "On chip spiral inductors with patterned ground shields for Si-based RF IC's," *IEEE J. Solid-State Circuits*, Vol. 33, 743–752, May 1998.
8. Burghartz, J. N., et al., "Novel substrate contact structure for high Q silicon integrated spiral inductors," *Tech. Digest International Electron Devices Meeting*, 55–58, 1997.
9. Soyuer, M., et al., "Multi-level monolithic inductors in silicon technology," *El. Letter*, Vol. 31, No. 5, 359–360, 1995.
10. Aparicio, R., et al., "Capacity limits and matching properties of integrated capacitors," *IEEE J. Solid-State Circuits*, Vol. 37, 384–393, March 2002.
11. Samavati, H., et al., "Fractal capacitors," *IEEE J. Solid-State Circuits*, Vol. 33, 2035–2041, Dec. 1998.
12. Tan, H. B., "Characterization, comparison and analysis of monolithic capacitors in silicon for RFICs," M.S. Thesis, U. P. Diliman, Oct. 2004.
13. Kolding, T., "Consistent layout techniques for succesful RF CMOS design," RF Integrated Systems and Circuits (RISC) Group, Aalborg University, Denmark.
14. Cheng, Y., et al., "On the high-frequency characteristics of substrate resistance in RF MOSFETs," *IEEE Electron Device Letters*, Vol. 21, No. 12, 604–606, December 2000.
15. Kim, C., et al., "Gate layout and bonding pad structure of a RF n-MOSFET for low noise performance," *IEEE Electron Device Letters*, Vol. 21, No. 12, 607–609, December 2000.

Ultra-wide Band Noise-signal Radar Utilizing Microwave Chaotic Signals and Chaos Synchronization

Shan Qiao[1], **Tao Jiang**[2], **Lixin Ran**[1,2], **and Kangsheng Chen**[1]

[1]Department of Information and Electronic Engineering, Zhejiang University, Hangzhou, 310027, China
[2]The Electromagnetics Academy at Zhejiang University, Zhejiang University, Hangzhou, 310058, China

Abstract— In this paper, we present a new scheme for the realization of a wide-band noise-signal RADAR utilizing wide-band chaotic signal generated from microwave chaotic Colpitts oscillator. System simulations show that such RADAR can still work in an environment when the signal-to-noise ratio (SNR) is $-20\,\mathrm{dB}$.

1. INTRODUCTION

RADAR, abbreviated from "Radio Detection and Ranging", might be the most important technical invention of human in the area of microwave engineering. From the invention of a primitive anti-collision marine RADAR by a Germany Christian Husmeyer in 1903, RADAR has gone through a history for more than 100 years. Nowadays, modern RADAR systems have been regarded to be very "mature" in all the aspects like performance, manufacturing technics and reliability, and have been widely applied in either military or civil uses. However, the development of RADAR is far from its end. For military RADAR, it would be better if the RADAR signal is more difficult to be detected or interfered, while for civil RADAR, EMC performance is more emphasized. A typical example is the anti-collision vehicle-borne RADAR: since the vehicle-borne RADAR on one car can not avoid the luminance from the adjacent lane, it has to work under the interference in a same frequency band. The number of cars is innumerous, meaning that for a vehicle-borne RADAR, it has to be co-existent with a number of RADARs with the same schemes, or it should be with the property of "multi-user", similar to a large-volume wireless communication system, such as a cellular system. The key requirement for modern military and civil RADARs is actually the same, i.e., how to let RADAR signals look more like wide-band noise. As the spread-spectrum technique has been widely used in military and civil communications, using ultra-wide band, noise-like signals in modern RADAR systems is also a trend. In this paper, we try to utilize microwave chaotic signals and chaos synchronizations in a new type of noise-signal RADAR.

2. MICROWAVE CHAOTIC COLPITTS OSCILLATOR

So far, various chaotic circuits and systems have been extensively studied to illustrate the evolution from DC to chaos. In early researches, chaotic circuits realized in laboratory only generated chaos spectra with kilohertz to megahertz bandwidth, but till now, chaotic Colpitts circuits operating at microwave frequencies have been reported [1, 2].

Figure 1(a) shows a Colpitts circuit realized by a bipolar junction transistor (BJT), which might be the most common oscillator widely used from very low frequencies to millimeter wave frequencies. Being a single-transistor circuit with inherent nonlinearity, Colpitts circuit has the potential to generate high frequency chaos [3]. Colpitts circuit in Figure 1(a) can be described by following circuit equations:

$$\begin{aligned} C_1\frac{dV_{C1}}{dt} &= -f(-V_{C2}) + I_L \\ C_2\frac{dV_{C2}}{dt} &= I_L - I_0 \\ L\frac{dI_L}{dt} &= -V_{C1} - V_{C2} - I_L R + V_{CC}, \end{aligned} \tag{1}$$

where $f(\cdot)$ is an exponential function representing the nonlinearity term of the BJT Model. Simulations by Agilent's Advanced Design System (ADS) show that when the circuit parameters are $C_1 = 5\,\mathrm{pF}$, $C_2 = 5\,\mathrm{pF}$, $L = 6\,\mathrm{mH}$, $I_0 = 5.26\,\mathrm{mA}$, $V_{CC} = 10\,\mathrm{V}$ and $R = 27\,\mathrm{Ohm}$, the Colpitts circuit exhibits chaotic oscillation. The realization of such a microwave chaotic oscillator in a module form and its output spectrum are shown in Figure 2. We see that the fundamental frequency of the Colpitts oscillator is up to about 1.6 GHz, and the discriminable continuous spectrum is extended to

10 GHz, indicating that although Colpitts circuit is with a simple structure, it can indeed generate ultra-wide band continuous spectrum. In this paper, we will try to utilize such ultra-wide band chaotic signal directly as RADAR signal.

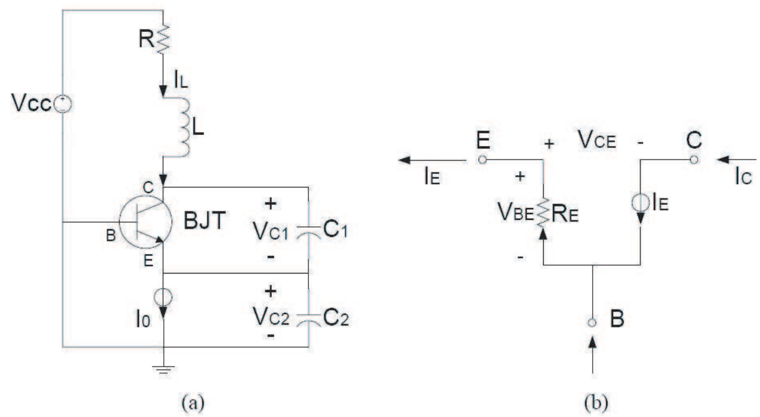

Figure 1: (a) Colpitts Oscillator and (b) the equivalent circuit model of the BJT in (a).

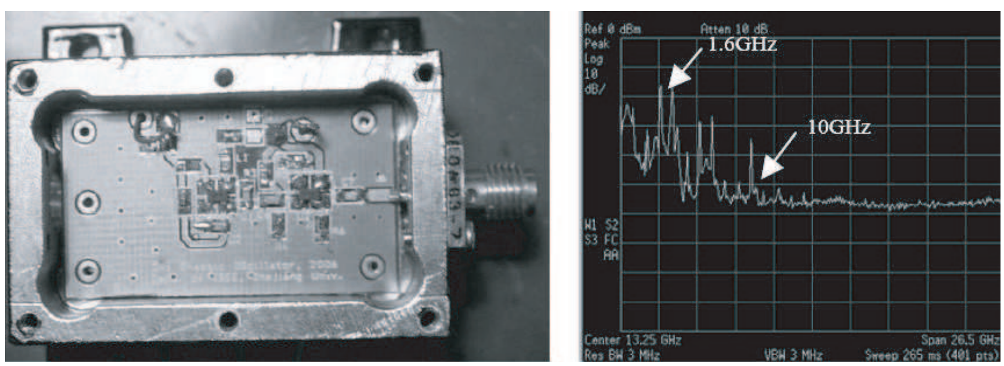

Figure 2: Modulized microwave Colpitts Oscillator (left) and its output spectrum (right).

3. CHAOS SYNCHRONIZATION

One thing interesting is that chaotic signals are controllable and synchronizable, which make them different from "real" noises. There are several kinds of chaos synchronization, such as identical synchronization and phase synchronization. In most cases the identical synchronization is used in chaotic communication. Generally there are two synchronization schemes for identical synchronization: Pecora-Carroll (or drive-response) synchronization and error feedback synchronization which is based on nonlinear observer method. The synchronization performance comparison of chaotic colpitts oscillators using the two schemes have been discussed in Ref. 4, where both the mathematical derivation and numeric simulations indicate that the error feedback synchronization scheme outperforms the former one when the chaotic signal is transmitted over a noisy channel with an additive white Gaussian noise and a channel filter .

In Figure 3, a chaotic Colpitts oscillator is used as a transmitter, and a "copy" of the transmitter with identical parameters is used as a receiver. The chaotic signal generated by the transmitter is sent into a wireless channel, where an additive Gaussian noise and an attenuation are introduced. In simulations, for the same set of the circuit parameters in the simulation for Figure 2 and with the initial conditions for the transmitter and receiver are $(10.5, -0.6, 0.01)$ and $(10.8, -0.61, 0.01)$, respectively, the simulation result shows that although at the beginning, transmitter and receiver oscillate independently, after a period of time (approximately 5 ns, figure not shown), the chaotic signal in receiver starts to synchronize with that in transmitter. This result shows that the chaos synchronization can be regarded as a signal retrieval process from noise, which is very suitable for the usage of recovering chaotic RADAR signals from noise and interference.

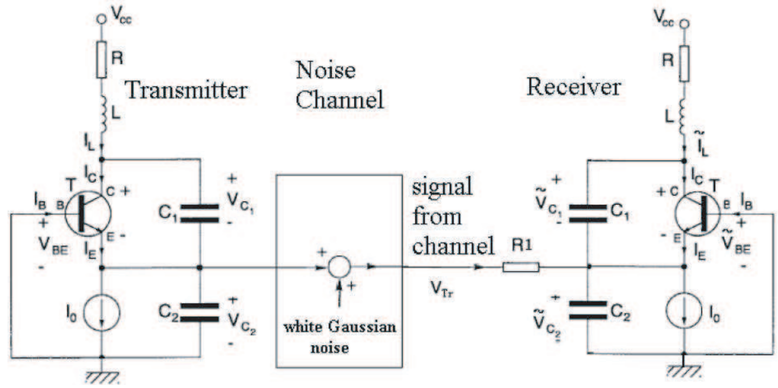

Figure 3: Simulation model for the error feedback chaos synchronization.

4. ARCHITECTURE OF THE PROPOSED CHAOTIC RADAR

We have shown that chaotic signals can be ultra-wide band and can be retrieved from noise. Applying the above properties, we can construct a RADAR like that in Figure 4 where a microwave chaotic oscillator is used as the source for generating RADAR signal. Such signal is isolated and driven by a buffer amplifier and then modulate with carrier, and then be radiated by a transmitter antenna after a power amplifier. If there is a target in air, the backscattered signal (echo) will be received by the receiver antenna, and after going through a low noise amplifier, a demodulator and an adaptive filter, the chaotic signal with noise and delay reaches the chaos synchronization circuit, where, as illustrated in Figure 3, a delayed copy of the source chaotic signal will be re-generated. After a correlation calculation of the original and recovered chaotic signal by synchronization, the echo signal can be finally detected.

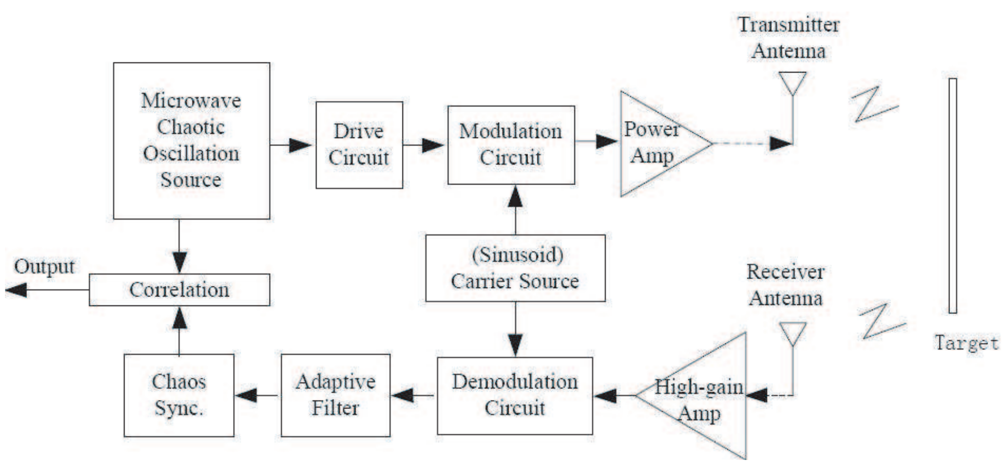

Figure 4: Illustration of the proposed RADAR.

According to above scheme, a system simulation can be run to illustrate how the RADAR works. In simulations, the circuit parameters are the same as those in Figure 3. In Figure 5, the cases when signal-noise ratio (SNR) is -15 and -20 dB are simulated, we see that even when the noise power is 100 times larger than signal's, we can still distinguish the echo signal from the noise floor.

Another interesting property of chaotic signals is the "butterfly effect", or the sensitivity to the initial conditions. For two chaotic circuits, even with identical circuit structures and parameters, their output can be irrelevant, or in other words, the signals are orthogonal with each other theoretically, for they can hardly have identical initial conditions. Since circuit parameters, i.e., capacitance, inductance and resistance, can be continuously tuned in wide ranges, the number of orthogonal chaotic signals can be infinite. This means for a correlation receiver, multiple chaotic signals are permitted to co-exist in a same channel. Thus, when there are multiple chaotic RADARs in one area simultaneously, since the chaotic signals generated from different chaotic sources are

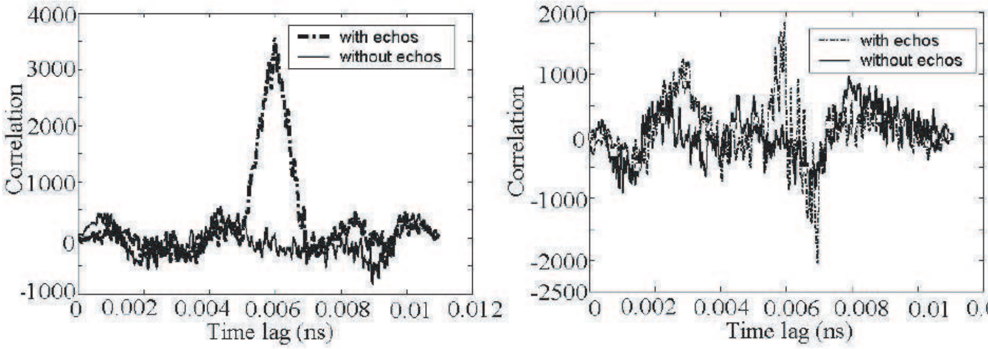

Figure 5: Echo signals when SNR is -15 and -20 dB, respectively.

irrelevant, therefore it could be filtered by the chaos synchronization circuit, and will not influence the basic function of the RADAR. The negative influence of the other chaotic signals is that they raise the noise floor and hence degrade the performance of the RADAR, which is very similar to the spectrum spread communications widely used in CDMA systems.

5. CONCLUSION

In this paper, the possibility of applying microwave chaotic signals and chaos synchronization in constructing a new kind of UWB RADAR is investigated. The system simulations show that such a RADAR system can work under severe interference and with a "multi-user" property like a public wireless communication systems. However, there are also challenges have to be overcome before these advantages can be realized, in which the most difficult one might be the realization of chaos synchronization in microwave band. Fortunately, researches in Ref. 5 have demonstrated the feasibility of the realization of chaos synchronization at very high frequencies.

ACKNOWLEDGMENT

This work was supported by National Natural Science Foundation of China (No. 60671003, No. 60531020) and Zhejiang Provincial Natural Science Foundation (No. R105253).

REFERENCES

1. Mykolaitis, G., A. Tamasevicius, and S. Bumeliene, "Experimental demonstration of chaos from Colpitts oscillator in VHF and UHF ranges, *Electronics Letters*, Vol. 40, No. 2, 91–92, 2004.
2. Shi, Z. G. and L. X. Ran, "Microwave chaotic Colpitts resonator: design, implementation and applications," *Int. J. of Electromagn. Waves and Appl.*, Vol. 20, No. 10, 1335–1349, 2006.
3. Kennedy, M. P., "Chaos in the Colpitts oscillator," *IEEE Transactions on Circuits and Systems*, Vol. 41, No. 11, 771–774, 1994.
4. Shi, Z. G., J. T. Huangfu, and L. X. Ran, "Performance comparison of two synchronization schemes for Colpitts circuits based chaotic communication system over noisy channel," *The 5th World Congress on Intelligent Control and Automation*, Vol. 6, 1276–1279, 2004.
5. Myneni, K. and T. A. Thomas, "New method for the control of fast chaotic oscillations," *Physical Review Letters*, Vol. 83, No. 11, 175–2178, 1999.

High-dimensional Chaotic Regimes in Distributed Radiophysical Systems Operating near the Cutoff Frequency

A. A. Balyakin and E. V. Blokhina
Saratov State University, 83 Astrakhanskaya St., Saratov 410012, Russia

Abstract— We present the results of computer modeling of chaotic dynamics in several radiophysical models (nonlinear ring cavity under external driving, one-dimensional Fabri-Perrot resonator and a gyrotron with non-fixed field structure). We calculated the set of Lyapunov exponents of chaotic attractors for these systems and estimated the dimensions of chaotic attractors from the Kaplan-Yorke formula. The dimensions were found to be anomalously high. We suppose this phenomenon to occur because all these systems operate near a critical frequency.

1. INTRODUCTION

Spatio-temporal chaos in distributed systems belongs to the most challenging and promising problems of nowadays physics. Recently, ideas and methods of nonlinear dynamics have been used extensively in application to distributed radiophysical systems as BWOs, gyrotrons, delayed feedback oscillators based on traveling-wave tubes (TWTs), klystrons and various distributed nonlinear resonators. As believed, analysis of Lyapunov exponents (LEs) would provide valuable complementary information concerning nature of the regimes observed in such systems. The Lyapunov exponents, that give the quantitative characteristics of the instability, define exponential growth (or decay) of perturbations near a typical phase trajectory, belonging to the attractor [1]. The total number of LEs corresponds to the phase system dimension. The presence of at least one positive LE reveals the existence of chaotic motion. If there is more than one positive LE, this regime is called hyperchaos.

For distributed systems, the dimension is infinite and a total number of LEs of their attractors is infinite, too. Thus, for systems with time delay that corresponds with the demand to specify the distribution of some physical quantity at the part of the length τ (τ — time delay). For spatially distributed systems situation can be rather more complicated. However, in practice, only a limited subset of LE is significant. We may restrict the number of LEs taking into account to only those of them which are enough to determine the so-called Lyapunov dimension of the attractor from the Kaplan-Yorke formula.

At the moment, it has been published several papers containing application of the LEs in distributed systems of radiophysical nature (see, for instance [2–6]). Some first works in that field were devoted to calculation of the set of LEs in system with time-delay [2]. It was found that the number of positive LEs increases with the growth of time delay and can reach 8–10, with Kolmogorov entropy remaining constant. By now the results of numerical simulations and of physical experiments have shown that chaos in such radiophysical system as BWO is certainly linked with the instability of the dynamics in respect to small perturbations of the initial state [3]. In [4] chaotic regimes in TWT were examined and several largest LEs were calculated. It was established that in dependence on the current of the electron beam the system can manifest chaotic regimes either with a single positive exponent (weak chaos) or with two or more positive exponents (developed chaos or hyperchaos).

2. NUMERICAL SCHEME

First, let us briefly discuss the numerical scheme applied for calculation the set of LEs. We have developed a code to calculate LEs spectra in such systems, based on a adapted Benettine algorithm using the approach proposed for the distributed electron-wave system in [3]. A finite number of N exponents is obtained from a numerical solution of $N+1$ sets of equations of the starting system. The initial conditions for the field are defined as close complex functions

$$F_k(\zeta) = F(\zeta) + \varepsilon \tilde{F}_k(\zeta), \quad \|\tilde{F}_k\| = \int_0^\tau |\tilde{F}_k|^2 d\zeta = 1, \ \varepsilon \ll 1. \tag{1}$$

For next moment in time $t_2 = t + \Delta t$ we obtain new set of functions: $\tilde{F}_k(\zeta) = \frac{F_K(\zeta) - F(\zeta)}{\varepsilon}$. After each time step Δt the perturbations are orthogonalized and normalized with the Gram-Schmidt algorithm:

$$\begin{aligned}
\tilde{F}_1^0 &= \tilde{F}_1/\|\tilde{F}_1\|, \\
\tilde{F}_2' &= \tilde{F}_2 - \left(\tilde{F}_2, \tilde{F}_1^0\right)\tilde{F}_1^0,\ \tilde{F}_2^0 = \tilde{F}_2'/\|\tilde{F}_2'\|, \quad (f,g) = \int_0^\tau f(\zeta)g^*(\zeta)d\zeta \\
\tilde{F}_3' &= \tilde{F}_3 - \left(\tilde{F}_3, \tilde{F}_1^0\right)\tilde{F}_1 - \left(\tilde{F}_3, \tilde{F}_2^0\right)\tilde{F}_2^0,\ \tilde{F}_3^0 = \tilde{F}_3'/\|\tilde{F}_3'\|, \\
&\dots
\end{aligned} \tag{2}$$

Then, N values of the accumulating sums Σ_n are calculated at each step, which indicate a growth or decrease of a logarithm of a norm of the n-th perturbation upon M steps of the procedure. From these sums, the LEs are estimated as follows:

$$\Sigma_k = \prod_{m=1}^{M} \|\tilde{\mathbf{x}}_k\|_{t=m\Delta t} \quad \Lambda_k = \lim_{t\to\infty}\left[\frac{\ln \Sigma_k}{t}\right]$$

Once a sufficiently large number N of the Lyapunov exponents have been calculated, the estimation of dimension of the chaotic attractor may be obtained from the Kaplan-Yorke formula [1]:

$$D = m + \sum_{i=1}^{m} \Lambda_i/|\Lambda_{m+1}|, \tag{3}$$

where m is a number determined by a condition that $\sum_{i=1}^{m} \Lambda_i > 0$, whereas $\sum_{i=1}^{m+1} \Lambda_i < 0$.

As known from numerous examples considered in the literature on nonlinear dynamics, the value D given by the formula (3) usually provides a good approximation for the fractal dimension of a chaotic attractor [1]. To be precise, D is called the Lyapunov dimension. Thus D gives the number of variables urgently necessary for thorough description of the studied system. This seems to be very useful in practical applications; we recall here the recent work [6] where this approach was applied to decrease the number of parameters used for weather forecast.

We verified the developed code having it tested in application to some well-known model systems of nonlinear dynamics, including both finite and infinite dimensional systems, such as the Lorenz system, the Roessler system, the one-dimensional BWO model [3], the single-cavity klystron model.

3. RESULTS OF NUMERICAL SIMULATION

First, let us consider resonator containing nonlinear medium with modulation instability. This system can be described with the help of nonlinear Schroedinger equation with a delay term [7].

$$i\left(\frac{\partial A}{\partial t} + V\frac{\partial A}{\partial x}\right) + \frac{\omega_0''}{2}\frac{\partial^2 A}{\partial x^2} + \beta|A|^2 A = 0. \tag{4}$$

The boundary condition is defined as follows: $A(0,t) = A_0\exp(-i\omega t) + RA(L, t - \Delta t)$.

Another simple model of distributed system can be performed as a piece of nonlinear medium with end reflections driven by an external harmonic signal. That is well known resonator of Fabri-Perrot type, described by a system of coupled nonlinear Schroedinger equations.

$$\begin{aligned}
&i\left(\frac{\partial A_+}{\partial t} + V\frac{\partial A_+}{\partial x}\right) + \frac{\omega_0''}{2}\frac{\partial^2 A_+}{\partial x^2} + \beta\left(|A_+|^2 + 2|A_-|^2\right)A_+ = 0, \\
&i\left(\frac{\partial A_-}{\partial t} - V\frac{\partial A_-}{\partial x}\right) + \frac{\omega_0''}{2}\frac{\partial^2 A_-}{\partial x^2} + \beta\left(|A_-|^2 + 2|A_+|^2\right)A_- = 0,
\end{aligned} \tag{5}$$

Boundary conditions have the form:

$$\begin{aligned}
A_+(0,t) &= A_0 e^{-i\omega t} + R_0 A_-(0,t), \\
A_-(L,t) &= R_L A_+(L,t),
\end{aligned} \tag{6}$$

here A — slowly varying complex wave amplitude, A_+ and A_- — forward und backward wave amplitudes on a carrying frequency ω_0, $V = \partial\omega_0/\partial k$ group velocity, $\omega_0'' = \partial^2\omega_0/\partial k^2$ — dispersion parameter, β — nonlinearity parameter, $R = \rho\exp(i\psi)$ — feedback coefficient, Δt — time delay, L — the length of nonlinear medium, A_0, ω — amplitude and frequency of the input signal.

Previously we have carried out the computer modeling of those systems in a wide range of parameters and shown that the complex dynamics in these systems is caused by modulation instability (some first remarks can be found in [7]). Here we present the results of calculations of the set of LEs for these two systems. As a perturbation we used the artificially constructed vector: For the model (4) — the value of A, defined in N points in a delay time, i.e., $F = (A(t), \ldots, A(t+\tau))$. For the model, expressed by Equations (5), the values of $A_\pm$ along the medium, i.e., $F = (A_+(0), \ldots, A_+(L), A_-(0), \ldots, A_-(L))$. The obtained results were found to be very similar and we proved that the origin of the observed peculiarities in both systems is the same. That is why further we will restrict ourselves to the first model (4) only.

The Fig. 1 represents the typical regimes observed in that system. The left column represents waveforms of the modulus of complex wave amplitude A, the medium one — power spectra and the last one — the accumulating sums Σ_k versus time. In periodic regimes all LEs were proved to be negative (a), quasi-periodic motion is characterized by one zero LE (b), in chaotic regimes we obtained positive LEs (c, d). We emphasize, that the dimension, calculated with the help of Kaplan-Yorke formula (3) in hyperchaotic regimes, turns to be extremely high (more than 10). That fact is clearly seen from the Fig. 2(a), where we have plotted the sum of n first LEs versus n. The intersection with the horizon line gives the Lyapunov dimension D.

Our calculations of the Lyapunov exponents spectrum revealed that hyperchaotic regimes occur only if the modulation instability in such a system turns from a convective to absolute type (that can take place only near a critical frequency). Therefore one can distinguish chaotic regimes caused by different mechanisms: when modulation instability is convective, the feedback plays the crucial role, and chaos originates from the interaction between perturbations that propagates in one direction (line 1 in Fig. 2(a)). However with the approach to the threshold value of the input amplitude corresponding to the change of the character of modulation instability (see [7] for details) there appear a large number of unstable perturbations that propagate towards the main wave, that leads to the increase of the dimension (line 2 and 3 in Fig. 2(a)).

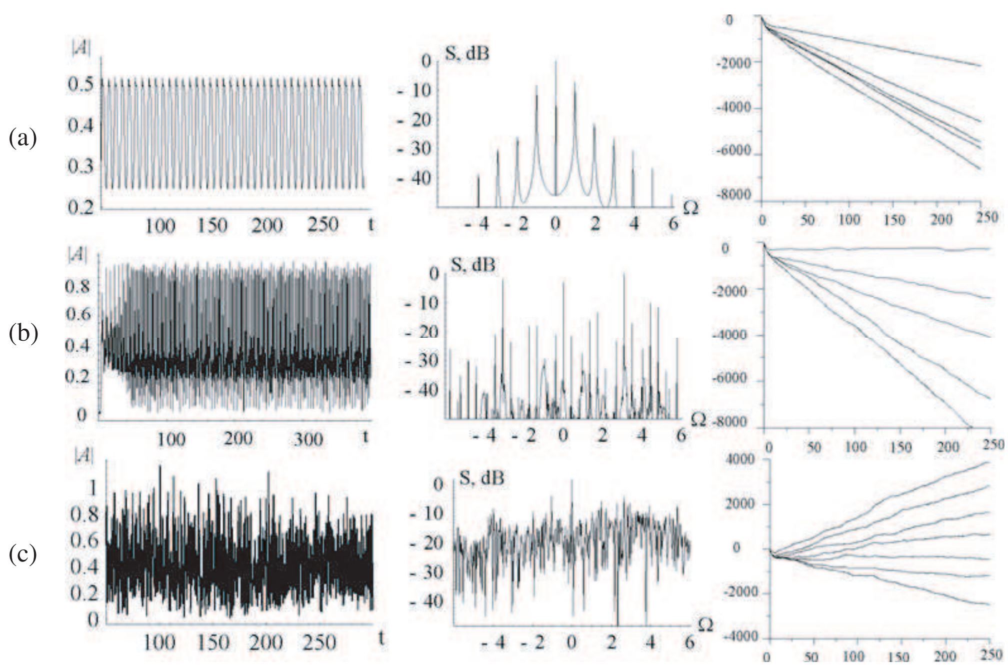

Figure 1: The dynamics of the nonlinear ring cavity. Self-modulation odulation regime, $A = 0.45$ (a), quasiperiodic self-modulation, $A = 0.6$ (b), hyperchaos $A = 1.4$ (c).

At the end of this section, we want to note the results of numerical study of a gyrotron with non-fixed field structure and reflections from the output horn. As is know, typically, this device operates near cutoff. A general statement of the problem and the results of numerical simulations of complex dynamics in the gyrotron with reflections one can find, for instance, in [5]. Previous studies of a gyrotron show that depending on two control parameters (the mismatch parameter Δ and the beam current I_0) one observes different scenarios for the onset of chaos. At $\Delta = 0.0$, the transition to chaos occurs via a cascade of period-doubling bifurcations. Since the dynamic regimes are based on the fundamental mode, we observe the period doubling of the self-modulation. At $\Delta > 0.6$, the transition to chaos occurs via the destruction of quasiperiodic motion, involving the generation of several eigenmodes of the distributed cavity.

It also have been established that, in addition to a chaotic regime characterized by a single positive LE ("weak" chaos), the gyrotron can also feature the regimes with several positive LEs as well as in the TWT [3] and in the nonlinear ring cavity. In Fig. 2(b) plots of sums of Lyapunov exponents versus their numbers are shown. Case 1 corresponds to "weak" chaotic oscillations with one positive exponent, whereas case 2 corresponds to hyperchaos. In both cases, the dimensions of chaotic attractors are high (more than 10). This phenomenon is connected with the excitation of a large number of high-Q eigenmodes, that weakly interact with electron beam. Thus in the spectrum of LEs there is the corresponding number of small LEs, and consequently the dimension of the attractor increases greatly (see for details [5]).

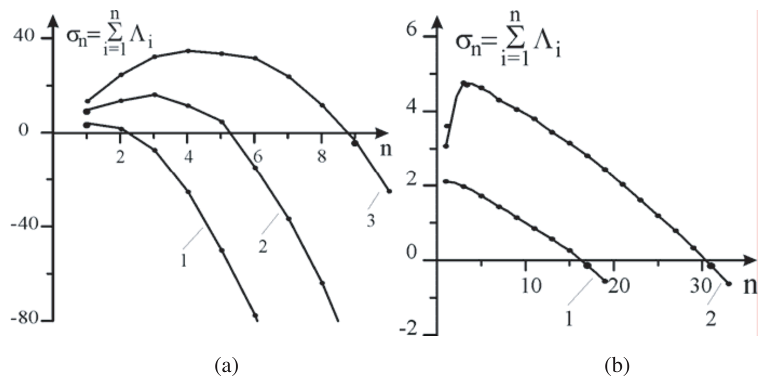

Figure 2: Sums σ_n versus the number of Lyapunov exponents. (a) chaotic regimes in the nonlinear ring cavity: $A = 0.6$ (1), 0.8 (2), 1.4 (3). (b) chaotic regimes in a gyrotron: $\Delta = 0.0$, $I_0 = 0.0365$ (1), $\Delta = 1.0$, $I_0 = 0.11$ (2).

4. CONCLUSION

Here, we have presented the results of numerical simulation of different regimes with corresponding Lyapunov exponents spectra. We have observed regimes of periodic oscillations (with all exponents being negative), quasi-periodic motion (with zero LE), chaos (one positive LE) and hyperchaos (the case when system possesses more than one positive LEs). The last phenomenon had been already observed in numerical simulation of backward wave oscillator [3] and in a gyrotron with non-fixed longitudinal field structure [5]. We have also found that in some hyperchaotic regimes Kaplan-Yorke dimension of the attractor is extremely high. Since all discussed models demonstrate complex behavior while operating near cut-off frequency, we can assume that the same phenomena will occur in other microwave self-oscillator operating near a cutoff frequency.

ACKNOWLEDGMENT

The authors thank S. P. Kuznetsov, A. G. Rozhnev, and N. M. Ryskin for useful discussions. This work was supported by the RFBR grants 05-02-16931, 06-02-16773. A.A. Balyakin's work was also supported by CRDF grant Y3-P-06-02 and grant of President of Russian Federation MK-4945.2006.2.

REFERENCES

1. Ott, E., *Chaos in Dynamical Systems*, Cambridge press, 1993.
2. Farmer, J. D., "Chaotic attractors of an infinite-dimensional dynamical system," *Physica D*, Vol. 4, No. 3, 366–393, 1982.
3. Kuznetsov, S. P. and D. I. Trubetskov, "Chaos and hyperchaos in a backward-wave oscillator," *Radiophys. Quantum Electron*, Vol. 47, No. 5–6, 341–355, 2004.

4. Dronov, V., M. R. Hendrey, T. M. Antonsen, and E. Ott, "Communication with a chaotic traveling wave tube microwave generator," *Chaos*, Vol. 14, No. 1, 30–37, 2004.
5. Blokhina, E. V., S. P. Kuznetsov, and A. G. Rozhnev, "High-dimensional chaos in a gyrotron," *IEEE Trans. on Electron Devices*, Vol. 54, No. 2, 188–192, 2007.
6. Ott, E., B. R. Hunt, I. Szunyogh, A. V. Zimin, E. J. Kostelich, M. Corazza, E. Kalnay, D. J. Patil, and J. A. Yorke, "A local ensemble Kalman filter for atmospheric data assimilation," arxiv.org/abs/physics/0203058.
7. Balyakin, A. A. and N. M. Ryskin, "Modulation instability in a nonlinear dispersive medium near cut-off frequency," *Nonlinear Phenomena in Complex Systems*, Vol. 7, No. 1, 34–42., 2004.

Improving the Accuracy of PHEMT Models Using Corrective Artificial Neural Networks

J. Dobeš and L. Pospíšil
Czech Technical University in Prague, Department of Radio Engineering
Technická 2, 16627 Praha 6, Czech Republic

Abstract— In the recent PSpice-family programs, only a class of five types of the MESFET model is available for a pHEMT representation. In the paper, a precise procedure is suggested for modeling the pHEMT using a corrective neural network working attached to an updated analytic MESFET model. The accuracy of the procedure is assessed by extracting model parameters for a typical TriQuint pHEMT. A sequence of analyses is also performed for determining an optimal structure of the artificial neural network from the point of view its structure and complexity.

1. INTRODUCTION

The Sussman-Fort, Hantgan, and Huang [1] equations can be considered a good compromise between model complexity and accuracy. Therefore, they can be used as an appropriate base for a corrective neural network, but they must be slightly modified in advance for modeling the special microwave elements as pHEMT working at tens of gigahertz.

However, the accuracy of the updated model functions is still of a percentage order. To be more precise, using the corrective neural network with the suitably modified analytic model can be an efficient and relatively simple way to obtain sufficiently accurate model.

2. MODIFYING THE ANALYTIC MESFET MODEL

The primary voltage-controlled drain-source current source of the MESFET model I_d can be defined for the forward mode ($V_\mathrm{d} \geqq 0$) by the formulae [1] with a simple but efficient update — see Fig. 1:

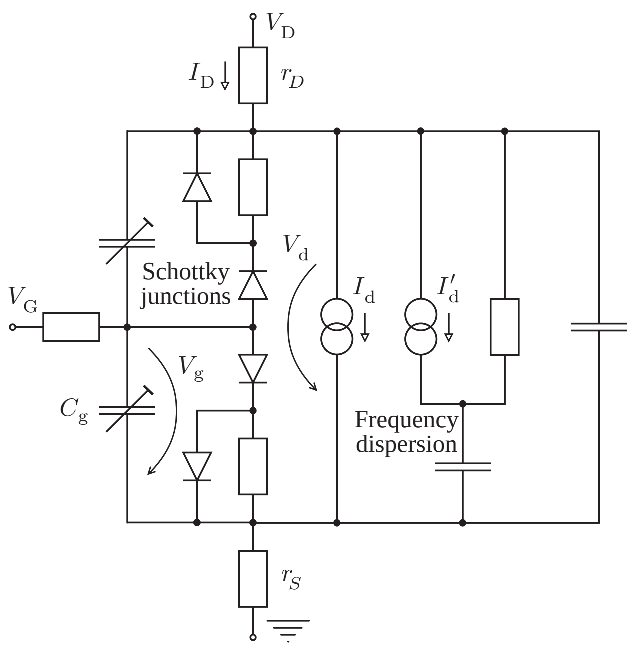

Figure 1: Diagram of the MESFET model including the frequency dispersion, which is usable as an analytical base for the application of the corrective neural network.

$$V_T = V_{T0} - \sigma V_\mathrm{d}, \tag{1a}$$

$$I_\mathrm{d} = \begin{cases} 0 & \text{for } V_\mathrm{g} \leqq V_T, \\ \beta(V_\mathrm{g} - V_T)^{n_2}(1 + \lambda V_\mathrm{d})\tanh(\alpha V_\mathrm{d}) & \text{otherwise.} \end{cases} \tag{1b}$$

The model parameters V_{T0}, β, n_2, λ, and α have already been defined in [1], the parameter σ used in (1a) represents the simple update of the original formulae necessary for modeling potential negative conductance in the output characteristics. Although the updated Equation (1) is relatively simple, it contains an improvement in comparison with the Curtice model [2] (by n_2 parameter which characterizes gate voltage influence on I_{d}), and also in comparison with the Statz model [3] (by σ parameter which characterizes drain voltage influence on I_{d}).

The modification (1a) enables the model to be utilized as the pHEMT approximation as shown in Fig. 2. The parameter extraction process has given the values $V_{T0} = -1.64\,\mathrm{V}$, $\beta = 0.102\,\mathrm{A\,V^{-2}}$, $n_2 = 0.991$, $\lambda = -0.0288\,\mathrm{V^{-1}}$, $\alpha = 1.16\,\mathrm{V^{-1}}$, $\sigma = 0.00797$, $r_D = 0.3\,\Omega$, and $r_S = 0.2\,\Omega$ with the error of the percentage order — see Fig. 2.

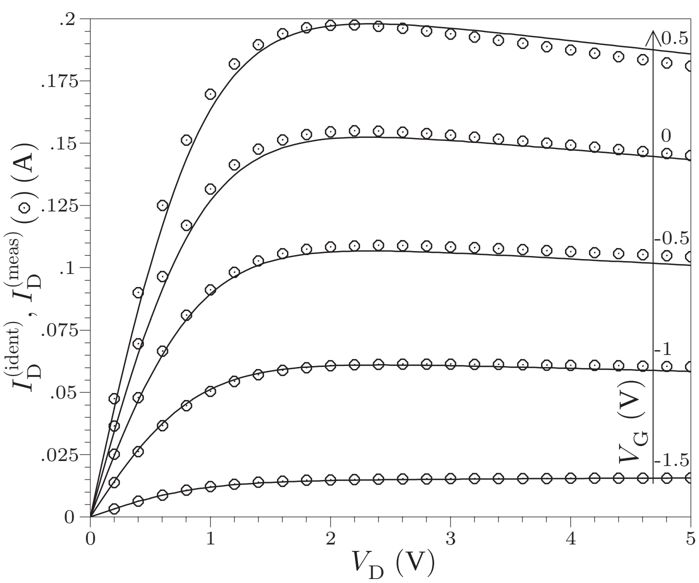

Figure 2: Results of the AlGaAs/InGaAs/GaAs power pHEMT [4] model identification using (1) (with the errors rms = 2.38% and $\delta_{\max} = 8.24\%$).

The model (1) represents the pHEMT with the root mean square (rms) error of a percentage order and is slightly more accurate than the TriQuint one [4]. On the other hand, at very high frequencies, the s_{22} parameter does *not* match the DC curves. Therefore, a secondary current source I'_{d} must be added, which is identified using a system of measured s parameters of the pHEMT.

3. SELECTING THE NUMBERS OF NETWORK LAYERS AND THEIR ELEMENTS

The rms deviations from measured data for the analytic models can be of the percentage order, which is clearly illustrated above. To obtain lesser values, the artificial neural networks can be used for modeling the devices. A detailed description of the concept of the neural networks can be found in [5] with the emphasis to modeling the nonlinear microwave devices. There can be more methods for using the artificial neural networks — the most precise one uses the network as a correction tool of the *difference* between the measured data and the previously identified analytic model.

Determining the number of elements in the individual layers of the corrective artificial neural networks attached to the modified analytical model is not a simple task. In this section, an illustrative example is demonstrated. The optimal network has been found experimentally in this example without a systematic procedure. We are now working on an automation of that process with the intention to find the optimal corrective artificial neural network to a given analytic model in a systematic way.

The tests have been performed for the AlGaAs/InGaAs/GaAs power microwave pHEMT, whose analytic model has been identified above. The results are summarized in Table 1 [6]. The rms error is the best for the structure MLP-2-8-8-6-1. However, the overall results are better for the simpler structure MLP-2-4-6-4-1 because of its lesser value of $\delta_{\max}$ — for this reason, this structure can be considered best result of this experimental process.

The good values rms and $\delta_{\max}$ promise that even simpler network can be used. In Table 2, the results for the four-layer network are summarized. For that network, a systematic procedure has been used that goes through all possible configurations. The rms error is the best for the structure MLP-2-4-6-1. However, the very accurate results are also obtained for another similar structure MLP-2-3-7-1, so we can obtain several networks which get sufficient results.

Table 1: Experimental searching for the optimal number of elements in the five-layer corrective artificial neural network.

Type of network	Relative deviations of networks with 500 training epochs	
	rms (%)	$\delta_{\max}$ (%)
MLP-2-2-2-2-1	3.781	57.75
MLP-2-2-4-2-1	1.891	16.91
MLP-2-2-4-4-1	0.1363	0.8966
MLP-2-4-4-4-1	0.0233	0.2150
MLP-2-4-6-4-1	**0.0204**	**0.1607**
MLP-2-4-6-6-1	0.1788	3.065
MLP-2-6-6-6-1	0.2588	1.272
MLP-2-6-8-6-1	0.0368	0.2614
MLP-2-8-8-6-1	**0.0057**	**0.3452**
MLP-2-8-10-6-1	0.0386	0.7587

Table 2: Systematic searching for the optimal number of elements in the four-layer corrective artificial neural network.

Type of network	Relative deviations of networks with 500 training epochs	
	rms (%)	$\delta_{\max}$ (%)
MLP-2-2-2-1	12.02	192.2
MLP-2-2-3-1	5.683	91.11
MLP-2-2-4-1	2.271	14.98
MLP-2-2-5-1	4.742	36.08
MLP-2-2-6-1	0.9973	**7.196**
MLP-2-2-7-1	2.78	37.67
MLP-2-2-8-1	**0.7249**	9.49
MLP-2-3-2-1	0.8675	5.982
MLP-2-3-3-1	1.418	10.46
MLP-2-3-4-1	0.4432	5.532
MLP-2-3-5-1	0.552	5.728
MLP-2-3-6-1	1.866	14.06
MLP-2-3-7-1	**0.0422**	**0.8029**
MLP-2-3-8-1	1.024	7.29
MLP-2-4-2-1	1.214	13.91
MLP-2-4-3-1	0.2465	2.235
MLP-2-4-4-1	0.3087	4.255
MLP-2-4-5-1	0.0829	1.337
MLP-2-4-6-1	**0.0331**	0.5998
MLP-2-4-7-1	0.1378	2.342
MLP-2-4-8-1	0.0427	**0.4804**

The results in Table 2 validate that an optimal structure of the corrective artificial neural network can be experimentally determined, and this optimal structure should not be too complicated. Moreover, finding the optimal structure is not too time-consuming and can be well automated.

4. CONCLUSION

The experiments confirm that the precision of the analytic models cannot be better than of a percentage order. Enhancing the precision is possible and relatively easy by corrective artificial neural networks. A sequence of experiments has been performed, which demonstrates that an optimal structure of the network can be systematically found.

ACKNOWLEDGMENT

This paper has been supported by the Grant Agency of the Czech Republic, grant No. 102/05/0277, and by the Czech Technical University fund for the specific research with MSc and PhD students.

REFERENCES

1. Sussman-Fort, S. E., J. C. Hantgan, and F. L. Huang, "A SPICE model for enhancementand depletion-mode GaAs FET's," *IEEE Trans. Microwave Theory Tech.*, Vol. 34, No. 11, 1115–1119, 1986.
2. Curtice, W. R., "GaAs MESFET modeling and nonlinear CAD," *IEEE Trans. Microwave Theory Tech.*, Vol. 36, No. 2, 220–230, 1988.
3. Statz, H., P. Newman, I. W. Smith, R. A. Pucel, and H. A. Haus, "GaAs FET device and circuit simulation in SPICE," *IEEE Trans. Electron Devices*, Vol. 34, No. 2, 160–169, 1987.
4. Cao, J., X. Wang, F. Lin, H. Nakamura, and R. Singh, "An empirical pHEMT model and its verification in PCS CDMA system," *Proc. of 29th European Microwave Conference*, 205–208, Munich, Germany, Oct. 1999.
5. Zhang, Q. J. and K. C. Gupta, *Neural Networks for RF and Microwave Design*, Artech House, Boston, 2000.
6. Dobeš, J. and L. Pospíšil, "Accurate modeling of the special microwave structures using artificial neural networks," *Proc. of 13th IEEE Mediterranean Electrotechnical Conference*, 149–152, Malaga, Spain, May 2006.

A Dual Resonance Three Segment Rectangular Dielectric Resonator Antenna

S. Jarchi[1], **J. Rashed-Mohassel**[1], **M. H. Neshati**[2], **and C. Lucas**[3]

[1]Center of Excellence on Applied Electromagnetic Systems, ECE Department
University of Tehran, Iran
[2]University of Sistan and Baluchestan, Iran
[3]University of Tehran, Iran

Abstract— A three-segment rectangular dielectric resonator antenna with equal segment dimensions and different dielectric constants is investigated. The dielectric constant of each segment is optimized with two different optimization algorithms, genetic algorithm and an optimization algorithm inspired from weed colonization in order to improve bandwidth. A dual resonance frequency response with improved bandwidth is obtained.

1. INTRODUCTION

Dielectric resonator antennas are suitable for a variety of applications. DRAs have small size and low cost. They can be easily coupled to almost all types of transmission lines [1]. DRAs have high radiation efficiency, since the only loss for a DRA is that due to the imperfect material of the DRA which can be very small in practice [2]. They have wider impedance bandwidth in comparison to microstrip antennas. For a typical DRA with dielectric constant of 10 the impedance bandwidth of 10% can be achieved. Avoidance of surface waves is another attractive advantage of DRAs over microstrip antennas.

There are a variety of feed configurations, which electromagnetic fields can be coupled to DRAs. Most common feed arrangements are microstrip aperture coupling, direct microstrip coupling, probe coupling and conformal strip coupling. Among these feed configurations, aperture coupling is more suitable for MMW applications. In aperture coupling configuration, since the DRA is placed on the ground plane of the microstrip feed, parasitic radiation from the microstrip line is avoided. Isolation of the feed network from the radiating element is another advantage of the aperture coupling method.

In DRAs bandwidth is a challenge. Several works have been done on improving bandwidth of DRAs. In this paper a three segment rectangular DRA with the help of genetic algorithm is designed to improve bandwidth.

2. ANTENNA STRUCTURE

The antenna structure is shown in Figure 1. A dielectric resonator is placed on the ground side of a microstrip line. The feed applied to the microstrip line and electromagnetic energy is coupled to the DRA via an aperture which is etched on the ground plane.

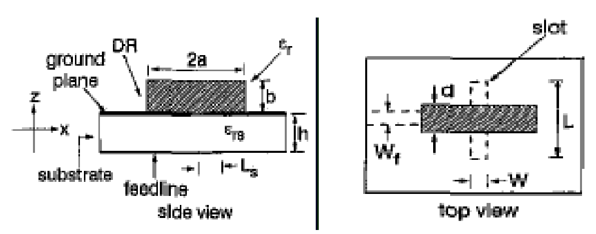

Figure 1: Single DRA [3].

There isn't any analytical formula for computing bandwidth of DRAs and numerical techniques should be employed. In this work for investigating DRAs, CST Microwave Studio is used. CST is based on the finite difference time domain method. The CST package has this advantage that, with a VBA editor its environment can be controlled and in this paper for optimizing purposes, optimization programs are developed in VBA in order to have direct access to the CST simulation environment.

Rectangular DRAs with aperture coupling have been commonly studied in literature [4]. Rectangular DRA with parameters: $\varepsilon_{rs} = 10.2$, $\varepsilon_r = 10.8$, $2a = 15\,\text{mm}$, $b = 7.5\,\text{mm}$, $d = 3\,\text{mm}$, $L = 6.1\,\text{mm}$, $L_s = 2.2\,\text{mm}$, $w = 1.2\,\text{mm}$, $w_f = 0.64\,\text{mm}$ and $h = 0.64\,\text{mm}$ is simulated in [5] with FDTD method and the resultant frequency response is shown in Figure 2. This antenna is also simulated here with CST and the frequency response is plotted in Figure 3. agreement between two figures is good and the bandwidth is 9%.

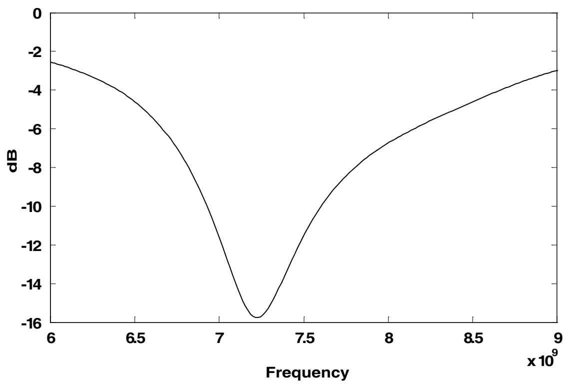

Figure 2: Return loss of the single DRA [5].

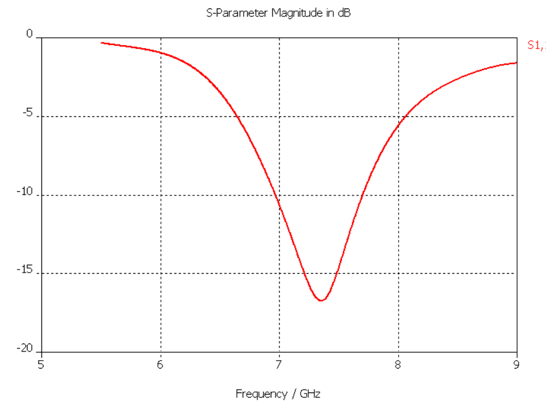

Figure 3: Return loss of the single DRA simulated with CST.

In order to obtain improved bandwidth, the DRA is subdivided into three segments with equal dimensions and different dielectric constants. The structure of the three-segment DRA is shown in Figure 4. This structure is optimized with two methods, genetic algorithm and an optimization algorithm inspired from weed colonization which is recently developed in [6] and the results of both methods are compared.

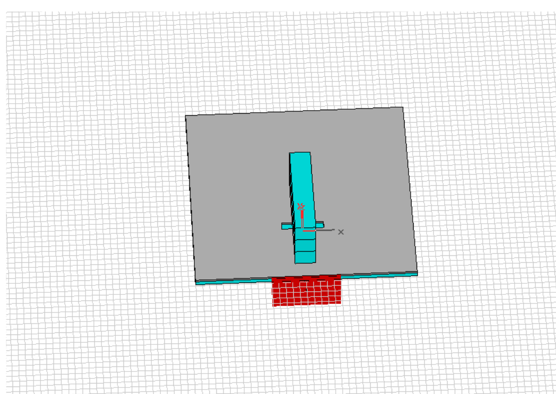

Figure 4: Three segment DRA.

3. OPTIMIZATION ALGORITHMS

As stated in previous paragraphs the antenna structure is optimized with two different methods.

3.1. Genetic Algorithm

To implement genetic algorithm binary coding was chosen and number of individuals in each population was selected to be 20.

Firstly the whole population was initialized randomly. Then fitness function, which is the DRA bandwidth, was evaluated for each individual in the population, and the population was sorted in the order of better fitness. Then 50% better individuals were selected as parents and the other 50% of parents were obtained with a 2-element tournament selection applied on whole population. Afterwards one-point cross-over and mutation algorithms with probabilities of 0.7 and 0.05, respectively, were applied on whole parents in order to produce new generations. After 9 generations, the GA converged to an acceptable answer. The plot of mean bandwidth of each generation is shown in Figure 5. This figure shows acceptable convergence of GA for the three-segment DRA problem. Parameters of the best individual in 15th generation are: $\varepsilon_{r1} = 18.7451$, $\varepsilon_{r2} = 10.5098$ and $\varepsilon_{r3} = 15.41176$. With these parameters the DRA is simulated with CST Microwave Studio and the resultant frequency response is shown in Figure 6. A dual resonance is observed in Figure 6, which is a technique commonly used in antennas to improve bandwidth, and the improved bandwidth is 1.085 GHz which is 16.5%.

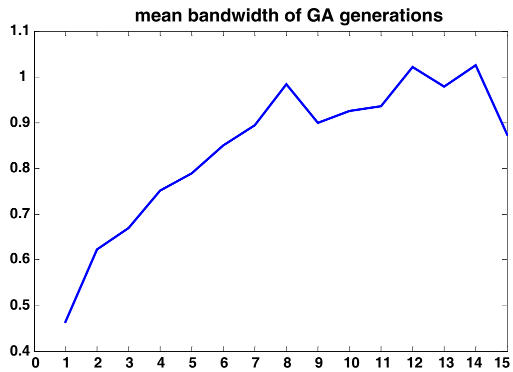

Figure 5: Mean bandwidth of generations for GA algorithm.

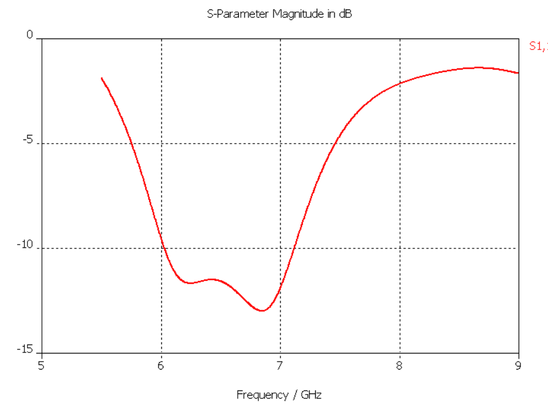

Figure 6: Three segment DRA optimized with GA.

3.2. An Optimization Algorithm Inspired from Weed Colonization

An optimization algorithm inspired from weed colonization has been proposed in [6]. For the antenna problem three dimensional search space which consists of three dielectric constants exists.

Firstly the population was initialized randomly. The number of individuals in initial population was selected to be 30. The initial population was sorted in order of better fitness, which is a higher bandwidth for the antenna problem. In this population the first 5 individuals produce 3 seeds, the second 5 individuals produce 2 seeds, the third 5 individuals produce 1 seed and the other individuals produce no seeds. The seeds are generated with a Gaussian distribution function with standard deviation (SD), σ and mean, μ. Where μ is the dielectric constant of parent plant. In each iteration, the standard deviation has been calculated with the following nonlinear equation [6]:

$$\sigma_{iter} = \frac{(iter_{\max} - iter)^n}{(iter_{msx})^n} (\sigma_{initial} - \sigma_{final}) + \sigma_{final} \tag{1}$$

Table 1: Setup of Weed Colonization algorithm.

Symbol	**Quantity**	**Value**
N_0	Number of initial population	30
$\mathrm{it}_{\max}$	Maximum number of iterations	6
dim	Problem dimension	3
$\mathrm{P}_{\max}$	Maximum number of plant population	30
$\mathrm{s}_{\max}$	Maximum number of seeds	3
$\mathrm{s}_{\min}$	Minimum number of seeds	0
n	Nonlinear modulation index	2
$\sigma_{\mathrm{initial}}$	Initial value of standard deviation	3
σ_{final}	Final value of standard deviation	0.01
$\mathrm{x}_{\mathrm{ini}}$	Initial search area	$10 < x < 20$

where $iter_{\max}$ is the maximum number of iterations, σ_{iter} is the SD at the present time step and n is the nonlinear modulation index. For the antenna problem n is selected to be 2. Parameters of this algorithm are summarized in Table 1.

After 15 generations the algorithm converged to an acceptable solution. The final dielectric constants are $\varepsilon_{r1} = 18.64311$, $\varepsilon_{r2} = 11.52842$ and $\varepsilon_{r3} = 14.07712$ with the bandwidth of 1.092 GHz, which is 16.6%. The frequency response is shown in Figure 7. A dual resonance is obtained.

The plot of mean bandwidth in each population is shown in Figure 8. This figure describes a reasonable convergence. In this algorithm, modulation index and initial and final values of standard deviation was selected without any further investigations. With an optimum choice of these parameters, the performance of the algorithm can be improved.

The two methods discussed above are compared in Table 2 and the results of both optimization methods are summarized in Table 3.

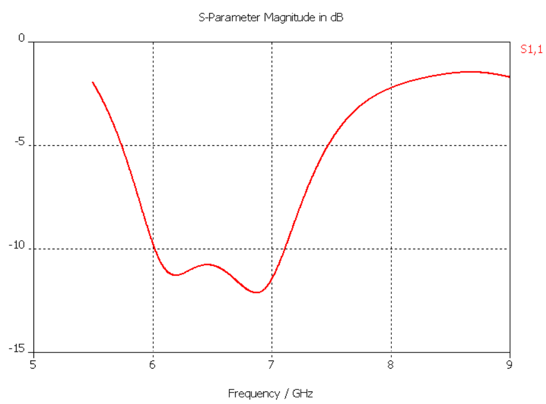

Figure 7: Three segment DRA optimized with weed colonization algorithm.

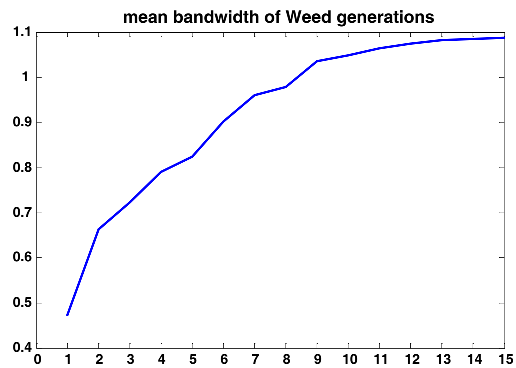

Figure 8: Mean bandwidth of generations for weed colonization algorithm.

Table 2: Comparison of GA and weed colonization.

	Number of individuals	**Number of iterations**	**Number of fitness evaluation**	**bandwidth**
GA	20	15	300	16.5%
Weed colonization	30	15	450	16.6%

Table 3: Results of GA and weed colonization algorithms.

	Bandwidth	**Number of resonances**
Single DRA	9%	1
GA optim.	16.5%	2
Weed colonization optim.	16.6%	2

4. CONCLUSION

A three segment rectangular dielectric resonator antenna with equal segments and different dielectric constants was investigated. Dielectric constant of each segment was optimized with two optimization algorithms, genetic algorithm and an optimization algorithm inspired from weed colonization. A dual resonance with improved bandwidth was obtained with both methods.

REFERENCES

1. Ittipiboon, A., R. K. Mongia, Y. M. M. Antar, P. Bhartia, and M. Cuhaci, "Aperture fed rectangular and triangular dielectric resonators for use as magnetic dipole antennas," *Electronics Letters*, Vol. 29, No. 23, 2001–2002, 11th November, 1993.
2. Luk, K. M. and K. W. Leung, *Dielectric Resonator Antennas*, Research Studies Press LTD., 2003.
3. Guo, Y. X., K. M. Luk, and K. W. Leung, "Mutual coupling between rectangular dielectric resonator antennas by FDTD," *IEE Proc. — Microw. Antennas Propag.*, Vol. 146, No. 4, 292–294, August 1999.
4. Gentili, G. B., M. Morini, and S. Selleri, "Relevance of coupling effects on DRA array design," *IEEE Trans. on Antennas and Propagation*, Vol, 51, No. 3, 399–404, March 2003.
5. Jarchi, S., J. Rashed-Mohassel, and M. H. Neshati, "Mutual coupling of DRA's in staggered configuration," *Proceedings of ANTEM/URSI 2006*, 245–248, Montreal, QC, Canada, July 2006.
6. Mehrabian, A. R. and C. Lucas, "A novel numerical optimization algorithm inspired from weed colonization," *Ecological Informatics*, 2006.

Design and Comparison of Exposure Chambers for Verification of Microwave Influence on Biological Systems

Lukáš Víšek, Paolo Togni, Jan Vrba, and Ladislav Oppl
Department of Electromagnetic Field, Czech Technical University
Technická 2, 166 27 Prague, Czech Republic

Abstract— The main aim of our work is to design and simulate an exposure chamber in order to analyze the influence of electromagnetic field on mice which can simulate mobile phone emission patterns. We use two types of structures and compare their properties to find the best design for our future work.

1. INTRODUCTION

In today's modern world various sophisticated devices emitting microwave electromagnetic field are ubiquitous. These devices are used in many fields such as industry, medicine (for therapeutic and diagnostic purposes) and communication. Almost everyone has a mobile phone or a wi-fi card in notebook. The pervasiveness of electromagnetic pollution and its possible impact on human health therefore raises a growing concern in our society.

There are two general classes of microwave effects: thermal and non-thermal. For thermal effect applies — the intensity of exposure produces heating of tissues due to energy absorption leading to a temperature rise. Nonthermal effects are the actual effects of electromagnetic field which are much more complicated to study due to various possible sites and ways of interaction. Due to an increasing daily exposure of humans many researchers focus on non-thermal effects and investigate its influence on biological tissues. To determine the exact impact of electromagnetic field it is required to eliminate some conditions affecting the results such as stress and to accurately determine the exposure. Although many researches have achieved significant results, we point out some flaws below.

First, to determine the exposure of animals, tabular values of absorption are used. However, by mere putting on the emitting device and use of tabular values it is not possible to determine how much energy is in fact absorbed. Some part of the energy is reflected and by using mobile phones as emitting source a part of energy is also radiated to the surroundings. Second, animals are fixed to emitting device in such a way that they can not move. This condition induces stress in the animals and the stress itself can affect the results. Also anesthesia is not a good solution because of its stressful influence.

2. MATERIALS AND METHODS

The main goal of our work is to design and to simulate an exposure chamber in order to analyze the impact of electromagnetic field on mice which can simulate mobile phone emission patterns and also eliminate the conditions mentioned above. We follow the following assumptions: working frequencies 900 MHz and 1800 MHz, dimensions to assure enough space for mice movement due to a non-stressful condition, possibility to measure reflected and transmitted power and homogenous electromagnetic field distribution to assure an accurate exposure. To accomplish these requirements we decided to design two types of exposure chambers and compare their properties in order to find the best solution for our future work. As the most appropriate chambers we choose parallel plate and waveguide structures.

The first chamber consists of a parallel plate structure (Figure 1) terminated by a matched load. The chamber is supplied by N-connector and the energy passes through parallel plate line into matched load (Figure 3). Because of energy transmission the dimensions of parallel plate line should guarantee a value of impedance in correspondence to N-connector, i.e., 50 Ohms. We set the dimensions in accordance with formula (1): $d = 2.5\,\text{mm}$ and $W = 18.85\,\text{mm}$.

$$Z_0 = \frac{d}{W}\sqrt{\frac{\mu}{\varepsilon}} \tag{1}$$

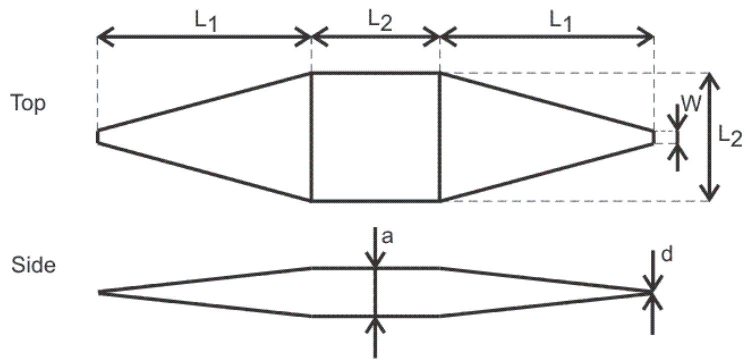

Figure 1: Parallel plate structure.

The tapered lines are used as a linear impedance transformer. Because of zero reflection coefficient magnitude a length of taper lines is chosen $L_1 = k\lambda$ where λ is a wavelength in the parallel plate structure and $k = 1$ (for 900 MHz), $k = 2$ (for 1800 MHz).

There are many possible modes to excite. And so exposure chamber dimensions were computed and chosen so that only TEM mode is excited at both frequencies. We chose TEM mode because of constant power extending over the whole aperture. To avoid excitation of the next mode TE_{10} it is needed to reach its cut-off frequency f_c greater than 1800 MHz (for TEM mode for both frequencies $f_c = 0$) in accordance with formula (2).

$$f_{cTE_{10}} = \frac{1}{2a \cdot \sqrt{\mu\varepsilon}} \tag{2}$$

We set a dimension $a = 75$ mm and a dimension $L_2 = 200$ mm in such way to assure enough space for mice movement. For measuring the power passed it is possible to connect a power meter to the matched load.

The second chamber is a rectangular waveguide resonator (resonant frequencies 900 MHz and 1800 MHz). It consists of two identical waveguides connected together (Figure 4). To achieve a homogenous electromagnetic field distribution it is possible to excite TE_{10} mode only. Due to this requirement we are not allowed to design one waveguide exposure chamber for both frequencies. According to a waveguide cut-off frequency formula (2) we set dimensions $a = 250$ mm, $b = 125$ mm for 900 MHz and $a = 125$ mm, $b = 62.5$ mm for 1800 MHz (Figure 2). For our application the support of mode TE_{103} in a resonator is the most advantageous.

$$f_{r,mnp} = \frac{c}{2\pi\sqrt{\varepsilon_r\mu_r}}\sqrt{\left(\frac{m\pi}{a}\right)^2 + \left(\frac{n\pi}{b}\right)^2 + \left(\frac{p\pi}{l}\right)^2} \tag{3}$$

By analyzing formula (3) we get dimension $l = 3\lambda/2$. We locate a feeding connector in the distance $l_1 = \lambda/4$ from a shortcut end of the waveguide. The second connector is used for measuring passed power. Due to air and light supply a row of gaps was made in lateral sides. Gap dimensions were chosen in a way not to influence the inner electromagnetic field distribution and to avoid emission in the surrounding space — width 2 mm and height $h = 2b/3$ (spatially oriented in the line of the surface current flowing). The row length is 200 mm.

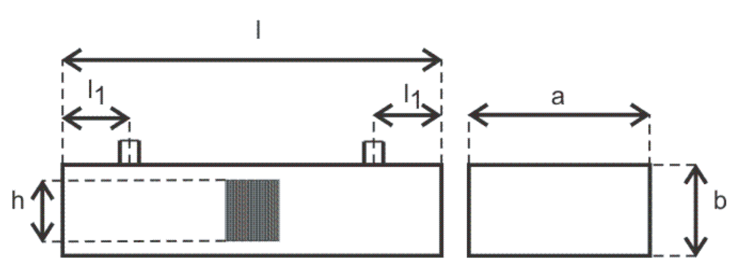

Figure 2: Waveguide structure.

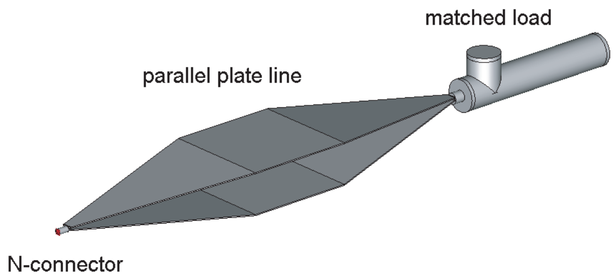

Figure 3: Model of a parallel plate chamber.

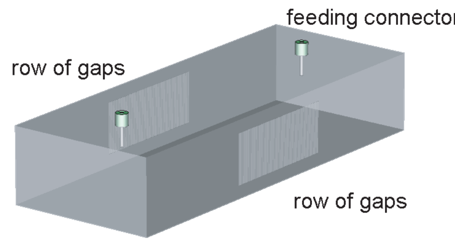

Figure 4: Model of a waveguide chamber.

3. RESULTS

To verify the basic properties of the designed chambers such as electromagnetic field distribution and impedance matching and to choose the best solution for further research by their comparison, we simulated both structures by aid of 3D electromagnetic field simulator.

We divided the analysis into two parts. In the first part exposure chambers were optimized and we verified their properties and in the second part we investigated their behavior after putting into a homogenous mouse model and compared the results. As a mouse model we used a homogenous cylinder with radius of 25 mm and length of 60 mm as a body and a cone with length of 25 mm as a head. We use electrical parameters $\varepsilon_r = 45.8$ and $\sigma = 0.76\,\mathrm{S/m}$ for both parts of the model.

Significant simulation results were mostly similar for both frequencies and we therefore show only results for 900 MHz.

Parallel plate: Figure 5 displays the impedance matching reached in an empty chamber. Parameter $S_{1,1}$ is equal to $-18.96\,\mathrm{dB}$. After putting the mouse model into chamber and changing its position, the parameter $S_{1,1}$ ranged from $-17\,\mathrm{dB}$ to $-20\,\mathrm{dB}$.

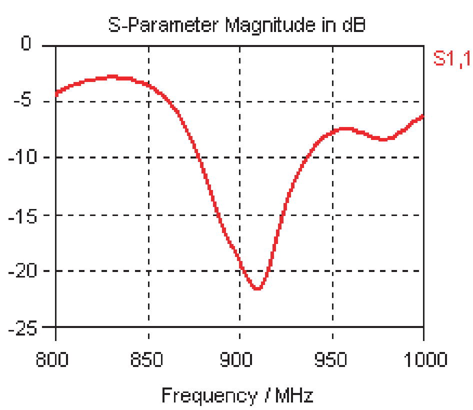

Figure 5: Impedance matching of parallel plate structure.

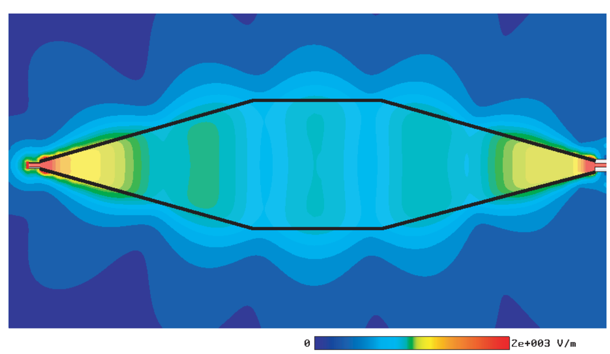

Figure 6: Distribution of electric field strength in longitudinal cutting plane (top view).

Figure 6 shows the distribution of electric field strength. It is obvious that a considerable part of energy is emitted in the surrounding space and after putting the mouse model into chamber the amount of emitted energy has grown as we can see by comparing Figure 7 and Figure 8.

Waveguide: Figure 9 displays the impedance matching reached in an empty chamber. Parameter $S_{1,1}$ is equal to $-19.12\,\mathrm{dB}$. After putting the mouse model into chamber the resonance frequency has changed significantly (value $S_{1,1} = -0.5\,\mathrm{dB}$) and we had to reach again resonance frequency. But during next "mouse movement" some positions caused a significant change of a resonance frequency. Figure 10 displays the distribution of electric field strength and shows that insignificant amount of power is emitted in the surrounding space.

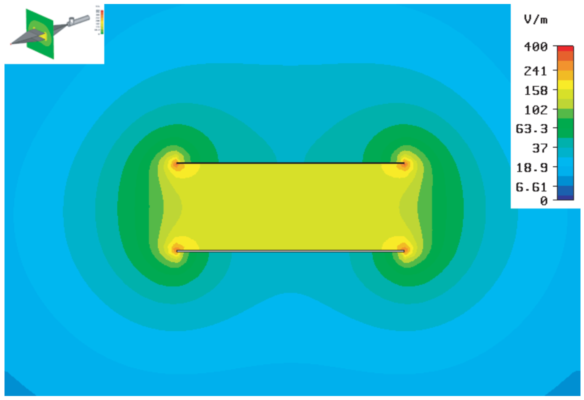

Figure 7: Distribution of electric field strength without mouse model in a transverse cutting plane structure (parallel plate structure — front view).

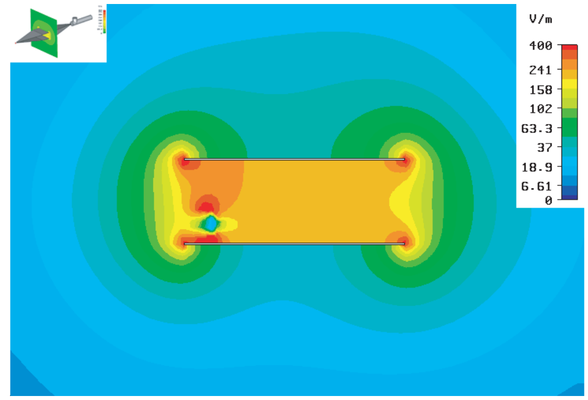

Figure 8: Distribution of electric field strength with mouse model in a transverse cutting plane (parallel plate structure — front view).

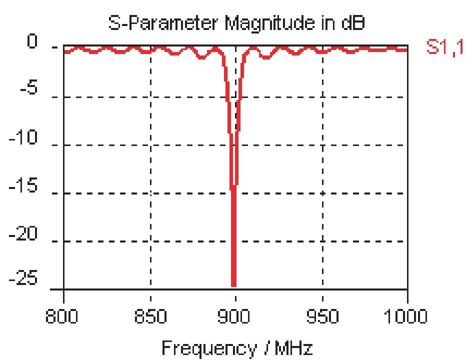

Figure 9: Impedance matching of waveguide resonance structure.

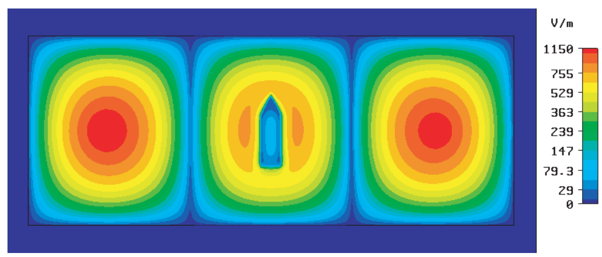

Figure 10: Distribution of electric field strength with mouse model in a longitudinal cutting plane (waveguide resonance structure — top view).

4. CONCLUSIONS

In the designed parallel plate chamber it is possible to excite both frequencies within one structure. Constant power is extended over the whole aperture (Figure 7) and thus we can use the whole space for mice and mice movement does not have an impact on the impedance matching. On the other hand, open lateral sides emit inconsiderable amount of energy in the surrounding space and we are not allowed to measure accurate power balance.

We need one special waveguide chamber for each frequency. Power is concentrated in the centre of aperture. We can use only 50 percent of this aperture. Impedance matching is strongly influenced by mouse movement. Insignificant amount of power is emitted in the surrounding space. Waveguide chamber has only a problem with impedance matching. A solution to this problem could be to add a loss material to enlarge the resonance band width or a usage of a nonresonance microwave structure.

The main aim of this work was to find a direction for our future progress in the design of an exposure chamber. This problem is very complex and a lot of issues remain unsolved.

ACKNOWLEDGMENT

This work was supported by the Czech Academy of Sciences, Institutional Research Concepts No. AV0Z50200510 and by the grant of Czech Academy of Sciences IAA500200510: "Hyperthermia and anticancer immunomodulation, morpho-functional study of microenvironmental interactions in melanoma model".

REFERENCES

1. Vrba, J., *Úvod do Mikrovlnné Techniky*, CTU Press, 2003.
2. Salford, L. G., A. E. Brun, J. L. Eberhardt, L. Malmgren, B. R. R. Persson, "Nerve cell damage in mammalian brain after exposure to microwaves from GSM mobile phones," [on-line] URL: ⟨http://www.ehponline.org⟩, 2003.
3. Vrba, J., *Měření na centimetrových vlnách*, SNTL, Prague, 1958.
4. Pozar, D. M., *Microwave Engineering*, third edition, John Wiley & Sons, Inc., 2005.

The Effects of 884 MHz GSM Wireless Communication Signals on Spatial Memory Performance: An Experimental Provocation Study

Clairy Wiholm[1,2], Arne Lowden[4], Lena Hillert[3], Niels Kuster[5], Bengt B. Arnetz[1,2] Torbjörn Åkerstedt[4], and Scott D. Moffat[6,7]

[1]Department of Family Medicine and Public Health Sciences
Division of Occupational and Environmental Health
Wayne State University, USA
[2]Department of Public Health and Caring Sciences
Uppsala University, Uppsala, Sweden
[3]Department of Public Health Sciences, Division of Occupational Medicine
Karolinska Institute, Stockholm, Sweden
[4]Institute of Psychosocial Medicine (IPM), Karolinska Institutet, Stockholm, Sweden
[5]IT'IS Foundation for Research on Information Technologies in Society
Swiss Federal Institute of Technology (ETH), Zurich, Switzerland
[6]Institute of Gerontology, Wayne State University, USA
[7]Department of Psychology, Wayne State University, USA

Abstract— We investigated the effects from a double-blind radiofrequency (RF) exposure (884 MHz, GSM exposure with a temporal change between non-DTX and DTX at a time averaged peak spatial SAR of 1.4 W/kg) on spatial memory and learning. The exposure was conducted in the evening between 7.30 p.m. until 10.30 p.m. (i.e., for three hours). The purpose of this study was to investigate whether exposure to radio RF fields, equal to GSM mobile phone use had any direct impact on spatial memory performance in human adults.

The participants were daily mobile phone users, men and women age 18 to 45, with and without symptoms (headache, dizziness and concentration difficulties) they associated with mobile phone use.

The primary outcome measure was a computerized "virtual" spatial navigation task (vMWT) modeled after the Morris Water Task (MWT), administrated on a standard desktop computer. The task environment was a circular pool surrounded by several cues, which could be used to guide navigation. Hidden beneath the surface of the arena was a platform, and participants were required to locate the platform as quickly as possible. On each of seven trials participants were placed in a different position of the area and facing a different orientation and were informed to locate the platform as quickly and as accurately as possible. The primary dependent variable used in the analysis was the distance traveled on each trial and the amount of improvement (i.e., learning) from trial 1 to 7. The test was conducted twice per test session, before (6 p.m.) and at the end of exposure (10.00 p.m).

A significant RF exposure effect on distance travelled during the 7 trials was found for the symptomatic group. RF exposure had no significant effect on the amount of improvement (i.e., learning) from trial 1 to 7 on neither of the groups, compared to sham.

The results of this double-blind intervention study suggest that the simulated GSM exposure at 884 MHz performance. Dosimetry modeling of GSM RF suggest that parts of the brain of relevance for executive functioning, including the pre-frontal cortex and the para-limbic area are exposed. This is compatible with the known dependence of spatial memory performance on limbic/hippocampal and pre-frontal systems. Our findings suggest that, under conditions representative of real-life mobile phone exposure, certain cognitive functions of interest are affected. Further studies are needed to pin point the brain mechanisms that may underlie these effects, for example identifying which specific parts of the brain are most affected by GSM exposure.

1. INTRODUCTION

The effect of electromagnetic fields (EMF) from digital mobile phones on cognitive functioning is an area receiving increased interest. Significant effects of RF exposure on specific cognitive functions and brain processes were reported [1–3], but in some studies no effect was observed [4–7]. The different study designs regarding exposure power, exposure time, exposure location (right or left hemisphere), and choose of study population most likely contribute to the variation in reported results. In addition there are considerable differences between studies in the selection of cognitive tests and cognitive domains of interest. This double blind mobile phone-related RF exposure study involved extended exposure periods under more realistic worst-case scenario and a novel cognitive measure, the virtual Morris Water Task.

At previous PIER meetings in Cambridge MASS, USA 2006 and in Beijing, China 2007 the study design, methology as well as general findings have been presented.

2. METHOD

The applied exposure simulated the maximum human exposure during a GSM phone conversation at a carrier frequency of 884 MHz, i.e., a temporal change between GSM basic at a peak spatial absorption rate averaged over 10 g (psSAR10 g) of 1.95 W/kg (average interval duration of 11 seconds) and DTX at psSAR10 g of 0.23 W/kg (average duration of 5 s) resulting in time averaged psSAR10 g of 1.4 W/kg. Hence, the exposure was well within the ICNIRP guidelines of 2 W/kg (ICNIRP, 1998). The exposure was applied by a patch antenna simultaneously exposing all possible exposure footprints of mobile phones [8] as well as the deeper brain structures. The exposure simulated the modulation of the GSM frame structures but not the higher frequencies as introduced by rondom code modulation.

For the behavioral navigation testing, all subjects completed a Virtual Morris Water Task (vMWT) that has been developed and validated previously [9, 10]. The task was modeled after the Morris Water Task [11] in which a participant must navigate and locate a particular point in space over a number of trials. Before beginning the navigation task, practice trials were allowed to familiarize subjects with movement through the environment and to be certain that participants were comfortable with the computer-administered task. The task environment was a circular arena surrounded by several cues, which could be used to guide navigation. Hidden beneath the surface of the arena was a platform, and the task required the participant to locate the platform as quickly as possible (Fig. 1). A total of seven trials were conducted. Before testing, participants were informed that the platform remained in the same location on each trial and that they should try to remember its location. On each of seven learning trials, participants were "placed" into one of the three quadrants of the pool, which did not contain the platform and facing a different orientation on each trial. The primary dependent measure was the distance traveled on each trial. Multiple repeated measures ANOVA's were used. Variables in the models included group (symptomatic vs. non-symptomatic), exposure (RF vs. Sham), time (baseline 6 p.m. vs. late 10.00 p.m.), trial (distance traveled on each of 7 vMWT trials).

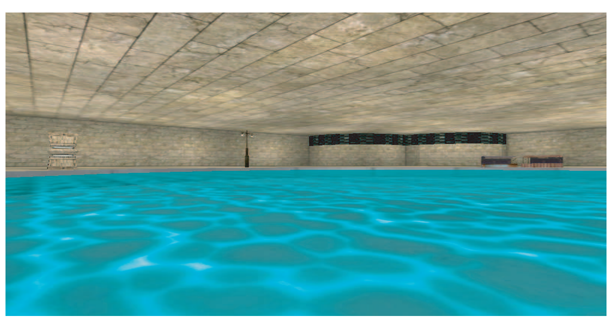

Figure 1: A typical scene from within the virtual environment. Participants view the environment from a first-person perspective.

3. MATERIAL

The participants ($N = 55$) were men and females, daily mobile phone users, age 18 to 45 years (mean age 29+/−7), with (symptomatic) and without (non-symptomatic) symptoms (headache, dizziness and concentration difficulties) they associated with mobile phone use. Exclusion criteria were attribution of symptoms to other electrical equipment than mobile phones, medical or psychological illness where current symptoms could not be excluded, earlier brain injury, present medication, sleeps disorders, hypertension and ongoing pregnancy. The inclusion criteria thus excluded subjects with environmental illness, since we were interested in including subjects specifically relating their symptoms to mobile phone use.

4. RESULTS

A main RF exposure effect [$F = 5,354$; $p < .026$)] and a RF exposure*group effect on distance travelled during the 7 trials was found [$F = 5,444$; $p < .025$)]. The symptomatic group improved their perforamance under RF exposure while there was no such effects of the RF exposure for the non symptomatic group. RF exposure had no significant effect on the amount of improvement (i.e., learning) from trial 1 to 7 in neither of the groups.

5. DISCUSSION

The results of the present study reveal main effects from RF exposure (RF. vs. Sham) on spatial performance as measured by distance traveled in a human analog of the Morris Water Task. However, it seems that only those with self-reported mobile phone related symptoms improved there performance. Considering amount of improvement from the first to the last trial, RF exposure (as compared to sham) was associated with improved rate of learning.

Spatial navigation is a complex cognitive function that depends on several neural and cognitive systems for successful completion. Functional neuroimaging and lesion studies have identified a network of structures that are involved in spatial navigation. The proposed network includes the hippocampus, parahippocampal gyrus, cerebellum, parietal cortex, posterior cingulate gyrus, prefrontal cortex, retrosplenial cortex and other cortical and subcortical regions. Successful navigation requires the selection of an appropriate search strategy and is also dependent on appropriate behavioral monitoring and alterations of searching behavior if the selected strategy proves unsuccessful. Furthermore navigation involves significant working memory demands because, within a trial, participants must remember preceding moves and locations and continually update this information to avoid immediately returning to the same (incorrect) locations [10]. The current study provides some support for cognitive and possibly neural effects of GSM like RF emissions. This represents an important novel finding in the expanding literature regarding cognitive effects of RF exposure in the GSM band and more broadly on the debate regarding the possible biological impact of mobile phone use. Future research should more specifically focus on the spatial peak SAR ratio of the exposed hemisphere and the studied functions. This approach would give a clearer picture of possible cause and effect.

ACKNOWLEDGMENT

Mobile Manufacturers Forum (/MMF) has funded the study.

REFERENCES

1. Eliyahu, I., R. Luria, R. Hareuveny, M. Margaliot, N. Meiran, and G. Shani, "Effects of radiofrequency radiation emitted by cellular telephones on the cognitive functions of humans," *Bioelectromagnetics*, Vol. 27, No. 2, 119–26, 2006.
2. Preece, A. W., S. Goodfellow, M. G. Wright, S. R. Butler, E. J. Dunn, Y. Johnson, et al., "Effect of 902 MHz mobile phone transmission on cognitive function in children," *Bioelectromagnetics*, Suppl 7, S138–43, 2005.
3. Smythe, J. W. and B. Costall, "Mobile phone use facilitates memory in male, but not female, subjects," *Neuroreport*, Vol. 14, No. 2, 243–6, 2003.
4. Besset, A., F. Espa, Y. Dauvilliers, M. Billiard, and R. de Seze, "No effect on cognitive function from daily mobile phone use," *Bioelectromagnetics*, Vol. 26, No. 2, 102–8, 2005.
5. Jauchem, J. R., "Health effects of microwave exposures: a review of the recent (1995–1998) literature," *J. Microw. Power Electromagn. Energy*, Vol. 33, No. 4, 263–74, 1998.
6. Jauchem, J. R., "A literature review of medical side effects from radio-frequency energy in the human environment: involving cancer, tumors, and problems of the central nervous system," *J. Microw. Power Electromagn. Energy*, Vol. 38, No. 2, 103–23, 2003.
7. Wilen, J., A. Johansson, N. Kalezic, E. Lyskov, and M. Sandstrom, "Psychophysiological tests and provocation of subjects with mobile phone related symptoms," *Bioelectromagnetics*, Vol. 27, No. 3, 204–14, 2006.
8. Kuster, N., J. Schuderer, A. Christ, P. Futter, and S. Ebert, "Guidance for exposure design of human studies addressing health risk evaluations of mobile phones," *Bioelectromagnetics*, Vol. 25, No. 7, 524–529, 2004.
9. Moffat, S. and S. Resnick, "Effects of age on virtual environment place navigation and allocentric cognitive mapping," *Behavioral Neuroscience*, Vol. 116, No. 5, 851–859, 2002.

10. Moffat, S. D., K. Kennedy, K. Rodrigue, and N. Raz, "Extra-hippocampal contributions to age differences in human spatial navigation," *Cerebral Cortex*, 2007, (in press).
11. Morris, R., P. Garrud, J. Rawlins, and J. O'Keefe, "Place navigation impaired in rats with hippocampal lesions," *Nature*, Vol. 297, 681–683, 1982.

EBG Substrate in Unilateral Fin Line Resonator

Humberto C. C. Fernandes, **Davi B. Brito**, and **Joêmia L. G. Medeiros**

Department of Electrical Engineering, Universidade Federal do Rio Grande do Note
P. O. Box 1583, 59.078-970-Natal/RN, Brazil

Abstract— The fin line resonator with EBG — Electromagnetic Bandgap substrate, is analyzed using the TTL — Transverse Transmission Line-method. Compared to other full wave methods the TTL is an efficient tool to determine the resonance frequency, making possible a significant algebraic simplification of the equations involved in the process. The results obtained for this application and the conclusions are presented.

1. INTRODUCTION

Electromagnetic Bandgap (EBG) structures have emerged as a new class of periodic dielectric structures where propagation of electromagnetic waves is forbidden for all frequencies in the photonic band gap [1]. This material has a periodic arrangement of cylinders immersed in air with diameters and spacing of less than one wave length [2–4]. This substrate can improve the band width and eliminate the propagation of undesirable modes. Many integrated circuits for millimeter wave applications can be made using the fin line techniques. This includes, beyond the fin line circuit, circuits inserted in metal and other standards circuits, mounted in the wave guides E-plane [5].

This work presents an application of the 2D layer-by-layer EBG crystal: the efficient rectangular unilateral fin line resonator, shown in the Fig. 1. The analysis is made using the TTL method and the coupling definitions.

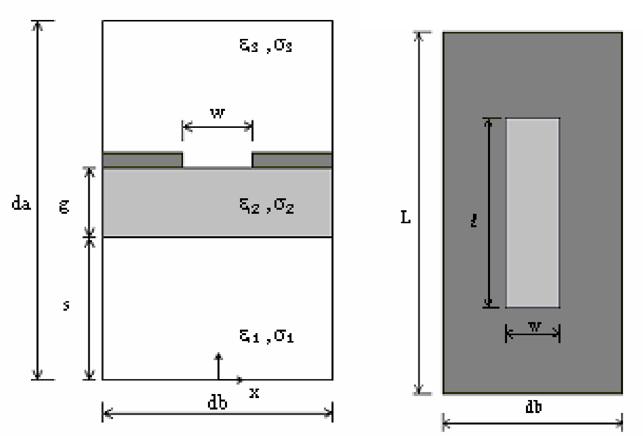

(a) (b)

Figure 1: (a) Transverse section (b) superior view.

2. THEORY

Starting for the Maxwell equations the electromagnetic fields are developed. The "x" and "z" field equations in the Fourier Transform Domain for the structures ith regions are obtained using the

TTL method:

$$\tilde{E}_{xi} = \frac{1}{\gamma_i^2 + k_i^2}\left[-j\alpha_n \frac{\partial}{\partial y}\tilde{E}_{yi} + \omega\mu\beta_k \tilde{H}_{yi}\right] \tag{1}$$

$$\tilde{E}_{zi} = \frac{1}{\gamma_i^2 + k_i^2}\left[-j\beta_k \frac{\partial}{\partial y}\tilde{E}_{yi} - \omega\mu\alpha_n \tilde{H}_{yi}\right] \tag{2}$$

$$\tilde{H}_{xi} = \frac{1}{\gamma_i^2 + k_i^2}\left[-j\alpha_n \frac{\partial}{\partial y}\tilde{H}_{yi} - \omega\varepsilon\beta_k \tilde{E}_{yi}\right] \tag{3}$$

$$\tilde{H}_{zi} = \frac{1}{\gamma_i^2 + k_i^2}\left[-j\beta_n \frac{\partial}{\partial y}\tilde{H}_{yi} + \omega\varepsilon\alpha_n \tilde{E}_{yi}\right] \tag{4}$$

where: $\gamma_i^2 = \alpha_n^2 + \beta_k^2 - k_i^2$, is the propagation constant in "y" direction;
α_n is the spectral variable in "x" direction;
β_k is the spectral variable in "z" direction;
$k_i^2 = \omega^2\mu\varepsilon = k_0^2\varepsilon_{ri}^*$, is the wave number of ith term of dielectric region;
$\varepsilon_{ri}^* = \varepsilon_{ri} - j\frac{\sigma_i}{\omega\varepsilon_0}$, is the relative dielectric constant of the material with losses;
$\omega = \omega r + j\omega i$, is the dielectric constant of the ith region;

The solutions of the field's equations for the three regions in study are given by:
For region 1:

$$\tilde{E}_{y1} = A_{1e}\cdot\cosh(\gamma_1 y) \tag{5}$$

$$\tilde{H}_{y1} = A_{1h}\cdot\cosh(\gamma_1 y) \tag{6}$$

For region 2:

$$\tilde{E}_{y2} = A_{2e}\cdot\sinh(\gamma_2 y) + B_{2e}\cosh(\gamma_2 y) \tag{7}$$

$$\tilde{H}_{y2} = A_{2h}\cdot\sinh(\gamma_2 y) + B_{2h}\cosh(\gamma_2 y) \tag{8}$$

For region 3:

$$\tilde{E}_{y3} = A_{3e}\cdot\cosh[\gamma_3(da - y)] \tag{9}$$

$$\tilde{H}_{y3} = A_{3h}\cdot\cosh[\gamma_3(da - y)] \tag{10}$$

For the determination of the unknown constants described above the boundary conditions are applied in the structure shown in Fig. 1(b), in $y = s$ and $y = t$. The electromagnetic fields general equations as function of $\tilde{E}_{xt}$ and $\tilde{E}_{zt}$, which are the tangential components of the electric fields are obtained to calculate the propagation constant. The magnetic boundary conditions are applied.

$$\tilde{H}_{x2} - \tilde{H}_{x3} = \tilde{J}_{zt} \tag{11}$$

$$\tilde{H}_{z2} - \tilde{H}_{z3} = -\tilde{J}_{xt} \tag{12}$$

where $\tilde{J}_{xt}$ and $\tilde{J}_{zt}$ are the electric current densities in the fins.

Substituting the magnetic fields equations in the above equations and isolating the terms in the electric fields, were find the equations that can be written through the admittance functions:

$$Y_{xx}\tilde{E}_{xt} + Y_{xz}\tilde{E}_{zt} = \tilde{J}_{zt} \tag{13}$$

$$Y_{zx}\tilde{E}_{xt} + Y_{zz}\tilde{E}_{zt} = \tilde{J}_{xt} \tag{14}$$

This system can be written in the matrix form:

$$\begin{bmatrix} Y_{xx} & Y_{xz} \\ Y_{zx} & Y_{zz} \end{bmatrix}\begin{bmatrix} \tilde{E}_{xt} \\ \tilde{E}_{zt} \end{bmatrix} = \begin{bmatrix} \tilde{J}_{zt} \\ \tilde{J}_{xt} \end{bmatrix} \tag{15}$$

Were for example:

$$Y_{xx} = \frac{-j}{\omega\mu\left(\gamma_2^2+k_2^2\right)}\left[\left(\frac{-\beta_k^2\gamma_2 d_1}{B}+\frac{k_2^2\alpha_n^2 e_1}{A}\right)\cosh\left(\gamma_2 g\right)+\right.$$
$$\left.+\left(\frac{-\beta_k^2\gamma_2 f_1}{B}+\frac{k_2^2\alpha_n c^1}{A}\right)\sinh\left(\gamma_2 g\right)\right]-\frac{j\left(k_3^2-\beta_k^2\right)}{\omega\mu\gamma_3}\cot gh(\gamma_3 d) \quad (16)$$

where A e B are give by:

$$A = \gamma_1 \sinh\left(\gamma_1 s\right)\cdot\cosh(\gamma_2 s)+\gamma_2\frac{\varepsilon_1}{\varepsilon_2}\cosh(\gamma_1 s)\cdot\sinh(\gamma_2 g) \quad (17)$$
$$B = \sinh(\gamma_1 s)\cdot\cosh(\gamma_2 g)+\frac{\gamma_1}{\gamma_2}\cosh(\gamma_1 s)\cdot\sinh(\gamma_2 g) \quad (18)$$

The $\tilde{E}_{xt}$ and $\tilde{E}_{zt}$ fields are expanded in terms of base functions,

$$\tilde{E}_{xt} = \sum_{i=1}^{n} a_{xi}\cdot\tilde{f}_{xi}\left(\alpha_n,\beta_k\right) \quad (19)$$
$$\tilde{E}_{zt} = \sum_{j=1}^{m} a_{zj}\cdot\tilde{f}_{zj}\left(\alpha_n,\beta_k\right) \quad (20)$$

where n and m, are positive integers.

As the fields have the contribution of two slots, they can be written as:

$$\tilde{E}_{xt} = a_x\cdot\tilde{f}_x\left(\alpha_n,\beta_k\right) \quad (21)$$
$$\tilde{E}_{zt} = a_z\cdot\tilde{f}_z\left(\alpha_n,\beta_k\right) \quad (22)$$

where the 1 and 2 indexes are related to the first and second slots.

Continuing, the scalar product of Equation (15) is made by the set of base functions according to the Galerkin method, the particular case of moment method. With this, the current densities turn out zero and a new matrix equation is obtained.

$$\begin{bmatrix} K_{xx} & K_{xz} \\ K_{zx} & K_{zz} \end{bmatrix}\cdot\begin{bmatrix} a_x \\ a_z \end{bmatrix} = \begin{bmatrix} 0 \\ 0 \end{bmatrix} \quad (23)$$

where for example:

$$K_{xx} = \sum_{-\infty}^{\infty}\tilde{f}_x\cdot Y_{xx}\cdot\tilde{f}_x^* \quad (24)$$

These procedures are described for the general cases utilizing two components of the electric field for any chosen base function. When we deal with purely real functions the scalar product is the fiction itself and his conjugated are ignored.

So that, for the system (18) to have a non trivial solution, the matrix determinant of the K coefficients must be equal to zero. The characteristic equation solution gives, the complex angular frequency that make possible to find the resonance frequency.

3. EBG STRUCTURE

For a non-homogeneous structure, the incident wave undergoes a process of multiple scattering. A solution can be obtained through of the numerical process of homogenization [2–5]. The process is based on the theory related to the diffraction of an incident electromagnetic plane wave imposed by the presence of air immersed cylinders in a homogeneous material.

In the homogenization [5] process the bidimensional medium is reduced to a one-dimensional medium. To do so, let us imagine that the crystal is made of a stack of diffraction gratings (what we now deal with is an infinite structure in the x direction). Numerically, we observe that the last gap corresponds to a range of wavelengths that give rise to only one diffraction order for such gratings. Consequently, forgetting the evanescent waves leads to the conclusion that each grating behaves as a homogeneous slab.

The problem is to specify an effective index for this slab. In fact, what is done consists in "homogenizing" the crystal slice by slice, as depicted in Fig. 2. It should be noted here that the wavelength is not very large with respect to the size of the scatterers, meaning that, properly speaking, we are not in the rigorous framework of homogenization theory. Nevertheless, let us try to apply the homogenization rules so as to get an effective index. The rods with permittivity ε_1 are embedded in a medium of permittivity ε_2. The procedure consists in dividing the structure into a superposition of homogenized layers. The layers containing the rods are broken up into cells hose y size (resp. x size) is the diameter of a rod $(2r)$ (resp. the period d).

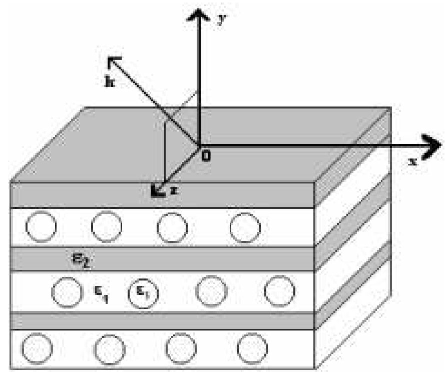

Figure 2: Homogenized bidimensional PBG crystal.

According to homogenization theory the effective permittivity depends on the polarization [5]. For the s and p polarization, respectively, we have:

$$\begin{aligned}\varepsilon_{eq} &= \beta\left(\varepsilon_1-\varepsilon_2\right)+\varepsilon_2\\ \frac{1}{\varepsilon_{eq}} &= \frac{1}{\varepsilon_1}\left\{1-\frac{3\beta}{\frac{2/\varepsilon_1+1/\varepsilon_2}{1/\varepsilon_1-1/\varepsilon_2}+\beta-\frac{\alpha(1/\varepsilon_1-1/\varepsilon_2)}{4/3\varepsilon_1+1/\varepsilon_2}\beta^{10/3}+O\left(\beta^{14/3}\right)}\right\}\end{aligned} \tag{25}$$

β is defined as the ratio between the area of the cylinders and the area of the cells, α is an independent parameter whose value is equal to 0.523.

4. RESULTS

To calculate the numerical results it was developed a computational program in Fortran PowerStation language, according to the previous theoretical analyses. In this work results for the phase constant, effective dielectric permittivity, for the even and odd modes, and coupling are shown.

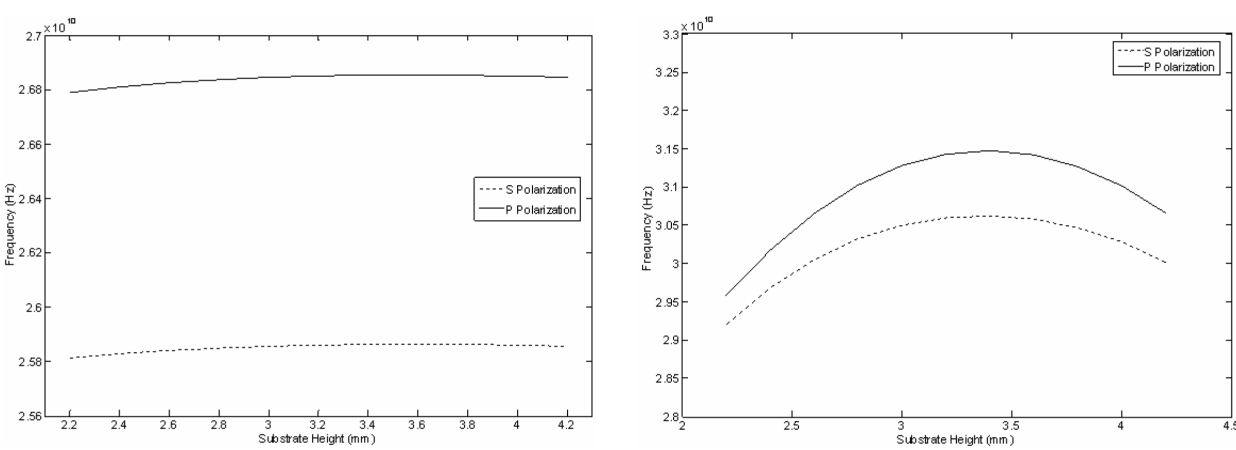

(a) (b)

Figure 3: Resonance frequency vs. substrate height in a WR-28 wave guide, (a) even mode (b) odd mode.

The new results are related to a unilateral fin line with EBG substrate, with two coupled slots, in a WR-28 millimeter wave guide with $g = 0.254$ mm, $s = 3.302$ mm (region 1 width), $w = 0.2$ mm, $\varepsilon_{r2} = 8.7209$ for the p polarization and $\varepsilon_{r2} = 10.233$ for the s polarization. The figures show the results with an excellent convergence with the theoretical results, Fig. 3(a) show the resonance attenuation for the even mode, and Fig. 3(b) show the resonance frequency for the odd mode.

5. CONCLUSION

Theoretical and numerical results have been presented for the unilateral fin line directional coupler with 2D EBG photonic substrate. The full wave transverse transmission line (TTL) method was used to the characterization of the unilateral fin line directional resonator, together with the method of the Moments. The full wave TTL method was used to the electromagnetic fields determination. Numerical results for the resonance frequency were presented. Finally new results can be obtained for this structure.

ACKNOWLEDGMENT

This work was partially supported by CNPQ and CAPES, Brazilian Agencies.

REFERENCES

1. Ramalho, P. A. dos S. and C. L. da S. S. Sobrinho, "FDFDmethod for analysis of TM modes,in periodics structure 2-D," *(In Portuguese) Telecommunications Journal*, Vol. 07, No. 02, Dec. 2004.
2. Wiersma, D. S., P. Bartolini, Ad. Lagendijk, and R. Righini, "Localization of light in a disordered medium," *Letters to Nature*, Vol. 390, 18/25 Dec., 1997.
3. Grüning, U., V. Lehmann, S. Ottow, and K. Busch, "Macroporous silicon with a complete two dimensional photonic band gap centered at 5 μm," *Appl. Phys. Lett.*, Vol. 68, Feb. 1996.
4. Radisic, V., Y. Qian, R. Coccioli, and T. Itoh, "Novel 2-D Photonic Bandgap Structure for Mictostrip Lines," *IEEE Microwave and Guided Wave Letters*, Vol. 8, No. 2, Feb 1998.
5. Centeno, E. and D. Felbacq, "Rigorous vector diffraction of electromagnetic waves by bidimensional photonic crystals," *J. Optical Soc. American A*, Vol. 17, No. 2, 320–327, February 2000.
6. Brat, B. and S. K. Koul, *Analysis, Design and Applications of Fin Lines*, 383–471, Artech House, Inc., Norwood, MA, USA, 1987.
7. Fernandes, H. C. C., L. C. de Freitas Jr., and S. A. P. Silva, "An efficient educational program for a finline coupler on semiconductor," *MSWM'98*, Kharkov, Ukraine, 1998.
8. Wiersma, D. S., P. Bartolini, Ad. Lagendijk, and R. Righini, "Localization of light in a dimensional medium," *Letters to Nature*, Vol. 390, 18/25 Dec., 1997.
9. Guillouard, K., M. F. Wong, V. F. Hanna, and J. Citerne, "Diakoptics using finite element analysis," *MWSYM 96*, Vol. 1, 363–366, 1996.
10. Rocha, A. R. B. and H. C. C. Fernandes, "Analysis of antennas with PBG substrate," *International Journal of Infrared and Millimeter Waves*, Vol. 24, 1171–1176, USA, Jul. 2003.
11. Tan, J. and G. Pan, "A general functional analysis to dispersive structures," *MWSYM 96*, Vol. 2, 1027–1030, 1996.

Time Reversal in Lossy Material: An Assessment

I. Scott, A. Vukovic, and P. Sewell
George Green Institute for Electromagnetics Research, School of Electrical and Electronic Engineering
University of Nottingham, University Park, Nottingham, NG7 2RD, UK

Abstract— This paper presents both an analytical and numerical analysis of errors caused by time reversal of electromagnetic waves. Analytical results describing spatial resolution limitations due to the loss of evanescent waves is presented for a two-dimensional parallel plate metal waveguide filled with an ideal and subsequently a lossy dielectric. An analytic model for a cylindrical problem space is also given, which exhibits the same effects observed for the waveguide problem. The properties of biological materials, specifically human Grey Matter, in relation to time reversal design techniques are also analyzed. The Transmission Line Modelling method is used to evaluate the numerical error of practical source reconstruction with respect to the modal content present in the forward simulation.

1. INTRODUCTION

Time reversal is used for a wide range of applications encompassing ultrasound, imaging, scatterer detection, material characterization and optimization [1–6]. Reversal of the TLM process proceeds by defining a Time Reversal Mirror (TRM) along the boundaries of the computation space [7]. Typically within an iterative design loop, signals incident upon the TRM are stored during a conventional forward time simulation of a given scatterer configuration, which, after perturbation toward the desired scattering profile, are re-injected during the time reverse process with a view to revealing the ideal scatterer geometry. However, the accuracy of the time-reversal procedure relies heavily on the practical size of a problem and on the finite machine precision of the forward stage of the simulation, a factor which is often overlooked when time-reversal techniques are deployed. An arbitrary problem will contain a finite number of local guided and evanescent fields which are propagated to the TRM in the forward simulation. The effective capture of these fields by the TRM is determined by the issues just mentioned. Any loss of modal content of the fields will limit the resolution with which the scatterer geometry is subsequently resolved and limits the scope for design optimization. Furthermore, it is often stated that time reversal techniques are only valid for lossless systems. However, a variety of time reversal simulations applied to biological simulations have been reported [4] demonstrating that time reversal is still possible, although the validity and the effect of material losses on the accuracy of the results has yet to be fully examined.

In this paper a simple analytical analysis of the time reversal spatial resolution error caused by the loss of the modes due to the finite machine precision is performed. Two canonical problems are analyzed, namely point source excitation of both a parallel plate metal waveguide and free space described in two dimensional (2D) cylindrical coordinates. For the case of the parallel plate waveguide an analysis of the effect of material loss on the time reversal simulation error is also presented. A biological load having the same parameters as human grey matter for different operating frequencies is examined and finally, the modal loss in the time-reversal process is demonstrated in context using the Transmission Line Modeling (TLM) method.

The paper begins with a short introduction to the TLM method, which is used here to demonstrate the effects of time reversal loss, although it is noted that the effects are prominent in any equivalent numerical time reversal algorithm. The paper then introduces the analytical approach based upon the modes within a parallel plate metal waveguide and cylindrical geometries which are used to obtain analytical predictions for evanescent mode loss for different propagation lengths and numerical precision simulations. The numerical loss of modes will be demonstrated in a numerical context using the TLM method and the metal waveguide excited by a Gaussian pulse of different widths. This will be followed with an analytical analysis of the effect of material loss on time-reverse simulations.

2. THE TLM METHOD

The TLM method is a differential time domain numerical technique based on the analogy between the field quantities and the propagation of voltages and currents on a mesh of interconnected transmission lines [8]. For 2D analyses, the problem space is typically divided into a uniform square grid, each cell of which contains a transmission line node at its center. The transmission lines have the characteristic impedance of free space and other material properties are modeled by introducing additional inductances, capacitances and losses implemented by adding appropriate shunt or series transmission line stubs to the network.

The TLM method, can be algorithmically separated into three stages namely; initialisation, scattering and connection [8]. Initialization defines the sources and initial wave values; scattering determines the reflection of voltage waves at all network nodes and connection propagates voltage waves between adjacent nodes. This process can be described mathematically as a matrix multiplication:

$$\underline{V}^s(t) = \underline{\underline{\mathbf{S}}}\,\underline{V}^i(t) \qquad \underline{V}^i(t+\Delta t) = \underline{\underline{C}}\,\underline{V}^r(t) \tag{1}$$

where the subscripts s denotes the scattered voltage, i denotes the incident voltage, r is the reflected voltage and S is the scatter matrix, which for each node of a 2D shunt network joining four transmission lines is locally:

$$[S] = \frac{1}{2}\begin{bmatrix} -1 & 1 & 1 & 1 \\ 1 & -1 & 1 & 1 \\ 1 & 1 & -1 & 1 \\ 1 & 1 & 1 & -1 \end{bmatrix} \tag{2}$$

For lossless systems, $[S]^{-1} = [S]$ which allows time reversal of the TLM procedure, without change to the TLM algorithm.

3. ANALITICAL MODE LOSS MODELS

In order to analytically demonstrate the error caused by a finite problem space and finite machine precision, two analytical models are considered namely a parallel plate metal waveguide shown in Fig. 1 and a 2D cylindrical description of free space. If the metal waveguide is excited by a point source the total field can be expressed as

$$E_T = \sum_{n=0,1,.}^{N} A_n \cos\left(\frac{n\pi x}{W}\right) e^{-j\gamma_n z} \tag{3}$$

where γ_n are the modal propagation constants, x the transverse coordinate, z the longitudinal coordinate, n is the mode number and A_n the appropriate modal amplitudes.

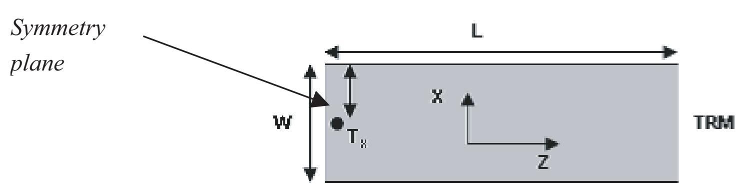

Figure 1: Parallel plate metal waveguide of width W and length L excited by a point source T_x.

The propagation constants γ, can be found as:

$$\gamma_n = \sqrt{\frac{n\pi}{W} - \omega^2 \varepsilon\mu} \tag{4}$$

where W is the width of the waveguide and ω the angular frequency. In a lossless material γ_n can be either purely real or imaginary corresponding to propagating and evanescent modes respectively and in the case of a lossy material, γ_n is a complex number implying that even the propagating modes will decay with distance from the source.

In a finite precision numerical simulation, using for example the TLM method, only a fixed number of significant digits will be used. For single precision (7 significant digits), an evanescent mode in the presence of a unit amplitude propagating mode is lost after a length L when $e^{-\gamma_n L} < 10^{-7}$, i.e.,

$$L = \ln\left(10^{\frac{7}{\gamma_n}}\right). \tag{5}$$

If the TRM is located after this distance in the waveguide, then the mode will never be detected and in the time reversal phase is not re-injected and its contribution to the source reconstruction is missing.

In the case of cylindrical coordinates a similar phenomenon is observed if the factor $e^{-j\gamma_n z}$ is replaced by the corresponding Hankel function, $H_n^{(2)}(kr)$, where r is the radial distance from the source and k is the radial wavenumber, and each spatial cosine by its corresponding angular counterpart.

4. ANALYTICAL RESULTS

4.1. Modal Loss

In order to give an insight into the behavior of the numerical simulations, an analytical model of the modal loss in the forward simulation is used and a predictable artificial precision and sampling equal to that of the numerical models is enforced. The parallel plate metal waveguide has width $W = 0.07\,\mathrm{m}$ and a transverse sampling of $\Delta x = 0.002\,\mathrm{m}$ is used. A point source of unit amplitude E_T excites the structure and Fig. 2 shows the relative error, $|E_T - E_T'|$, of the point source amplitude reconstructed after time reversal for different lengths of the waveguide L. The dotted line shows the distances at which modes are predicted to be lost calculated using (5). As can be seen, the error in the total field reconstruction has a step like behavior with the propagating distance confirming the utility of the simple analytical predictions.

The same process is repeated for the case of a 2D cylindrical cavity and shown in Fig. 2(b)), with spatial sampling of 0.005 m, the error measure is plotted against increasing radius of the cavity at which the TRM is placed and shows the same behavior.

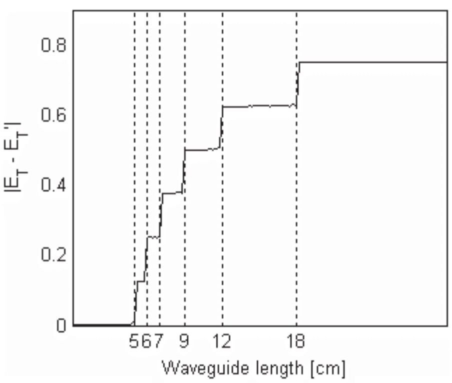

(a)

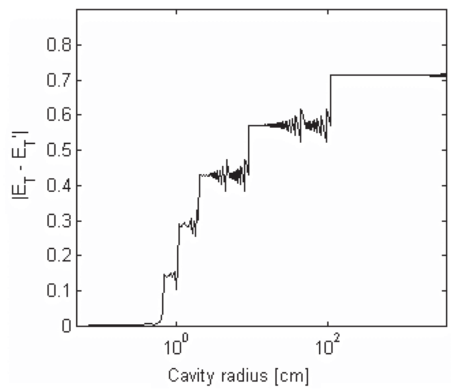

(b)

Figure 2: Error of the total field reconstruction in time reversal in (a) the metal waveguide as a function of distance and for the case of single precision and (b) in 2D cylindrical cavity.

Figure 3 shows the numerical simulation obtained using the TLM method for both forward and reverse simulations. The metal waveguide shown in Fig. 1 is excited by a Gaussian pulse of spatial half width W_{gin} located on the symmetry plane and spanning a number of transverse sampling nodes of the air filled waveguide. As in the case of a point source excitation, the modal content comprises both propagating and evanescent modes and the loss of each decaying mode is expected after a certain length in the forward simulation which causes spatial broadening of the reconstructed Gaussian excitation pulse after reverse time propagation. An analytical prediction is performed with waveguide parameters, $W = 0.07\,\mathrm{m}$, $L = 0.90\,\mathrm{m}$ and $\Delta x = 0.00016\,\mathrm{m}$. To mimic the effect of finite precision calculations, the modal amplitudes of the signal after forward time propagation are analytically evaluated and those which are 7 digits smaller than the dominant term are removed. The pulse is then analytically propagated in reverse time and the half width of the reconstructed Gaussian pulse is calculated. The ratio of the recovered Gaussian half width to the initial half width for different input pulses is shown in Fig. 3. The results obtained using the TLM method for the propagation is also shown on the same graph. The TLM mesh size sampling is taken to be 0.00053 m and the time step $\Delta t = 1.79 \times 10^{-7}$. It can be seen that the TLM results show the same behavior and the discrepancy is attributed to the finite run time that is needed to reach steady state and the fact that in practice the loss of each mode is not exactly the sharp phenomenon described by (5), rather a progressive yet rapid deterioration. Overall the simple analytical prediction using (5) is successful in determining the resolution of the source/scatterer reconstruction and this must be taken into account in setting convergence criteria for the iterative design of scatterers.

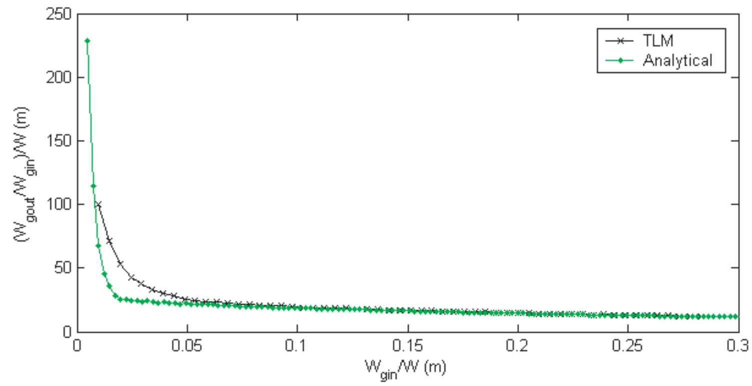

Figure 3: (a) Analytical prediction of mode loss estimated through the change of the width of the reconstructed Gaussian pulse compared to width at the input. Waveguide width is 0.07 m, length 0.90 m and spatial sampling is 0.00016 m, (b) TLM simulation of identical scenario with spatial sampling of 0.00053 m.

4.2. Effect of the Material Loss

Figure 4 examines the effect of the material loss on the relationship between the propagation length, single precision and propagation constants. A simple plot of the propagation factors for each mode in the complex plane can prove particularly useful for assessing the effect of material loss on the simulation. Eq. (5) defines a cut-off level for the simulation in terms of modes; i.e., any mode whose decay rate is greater than the cut-off value will be lost completely in the reverse simulation. Generally, the higher order modes are lost first and increasing either the material loss or propagation length causes a progressive loss in spatial resolution. Fig. 4(a)) plots the propagation constants in the complex plane for a waveguide with parameters $W = 0.17$ m, $L = 0.12$ m, filled with lossless and lossy material with conductivity $\sigma = 3$ and 4.5. The dotted line shows the cut-off level after which the modes are lost with 7 digit precision. Increasing the loss causes more modes to be lost for the same waveguide length. Fig. 4(b)) considers the specific case of human grey matter with dielectric properties equivalent to 100 MHz ($\varepsilon_r = 80.14$, $\sigma = 0.559$ S/m), 500 MHz ($\varepsilon_r = 55.83$, $\sigma = 0.779$ S/m) and 1 GHz ($\varepsilon_r = 52.28$, $\sigma = 0.985$ S/m). It can be seen that at higher operating frequencies the material is more lossy and the propagation constants migrate further into the complex plane. However, with increased operating frequency, the propagation constants also shift to the right side of the plane which reduces the modal loss.

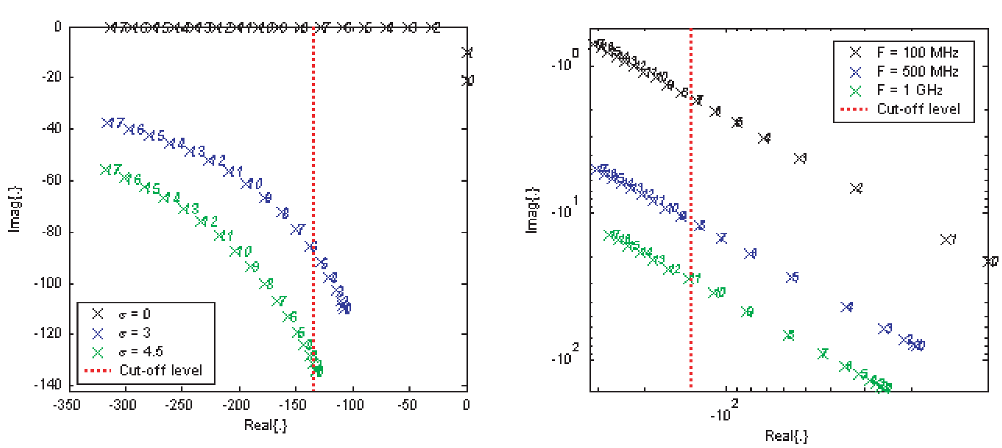

(a) (b)

Figure 4: Propagation constants in the complex plane obtained for a waveguide $W = 0.17$ m, $L = 0.12$ m and (a) filling of free space with varying loss; (b) for the case of human grey matter at frequencies of 100 MHz, 500 MHz and 1 GHz.

5. CONCLUSION

The paper examines the effect the evanescent mode loss has as a consequence of the finite machine precision on the accuracy of time reversal simulations. The effect has been analyzed analytically for the case of a 2D parallel plate metal waveguide and 2D cylindrical cavity and then shown numerically using the TLM method. The inclusion of loss in the simulation is shown to exaggerate the case of the lossless simulation.

REFERENCES

1. Forest, M. and W. J. R. Hoefer, "A novel synthesis technique for conducting scatterers using TLM time reversal," *MTT*, Vol. 43, No. 6, 1371–1378, 1995.
2. Liu, D., G. Kang, L. Li, Y. Chen, S. Vasudevan, W. Joines, Q. H. Liu, J. Krolik, and L. Carin,, "Electromagnetic time-reversal imaging of a target in a cluttered environment," *IEEE Trans. Antennas and Propagation*, Vol. 53, No. 9, 3058–3066, 2005.
3. Cassereau, D. and M. Fink, "Time-reversal of ultrasonic fields-part III: Theory of the closed time-reversal cavity," *IEEE Trans. Ultrasonics, Ferroelectrics, and Frequency Control*, Vol. 39, No. 5, 579–592, 1992.
4. Kosmas, P. and C. M. Rappaport, "Time reversal with the FDTD method for microwave breast cancer detection," *MTT*, Vol. 53, No. 7, 2317–2323, 2005.
5. Sorrentino, R., L. Roselli, and P. Mezzanotte, "Time reversal in finite difference time domain method," *IEEE Microwave and Guided Wave Letters*, Vol. 3, No. 11, 402–404, 1993.
6. Popovic, M. and A. Taflove, "Two-dimensional FDTD inverse scattering scheme for determination of nera surface material properties at microwave frequencies," *IEEE Trans of Antennas and Propagation*, Vol. 52, No. 9, 2366–2373, 2004.
7. Scott, I., A. Vukovic, and P. Sewell, "Reducing numerical limitations in time-reversal simulations," To appear, *The Fourth IASTED Confer. on Antennas Radar and Wave Propagation (ARP)*, May 2007.
8. Christopoulos, C., *The Transmission-line Modeling Method: TLM*, Oxford University Press, Oxford, 1995

Eigenfunction Expansions of Source-excited Electromagnetic Fields on Open Cylindrical Guiding Structures in Unbounded Gyrotropic Media

A. V. Kudrin[1], **E. Yu. Petrov**[1], **and T. M. Zaboronkova**[2]

[1]University of Nizhny Novgorod, Russia
[2]Technical University of Nizhny Novgorod, Russia

Abstract— We consider electromagnetic fields excited by spatially bounded, arbitrary given sources in the presence of a cylindrical guiding structure immersed in an infinitely extended homogeneous gyrotropic medium whose permittivity and permeability are both describable by tensors with nonzero off-diagonal elements. The axis of symmetry of the considered cylindrical structure is assumed to coincide with the gyrotropic axis. The total field is sought in terms of the vector modal solutions of source-free Maxwell's equations. By demanding completeness of the modal spectrum and using a continuity argument, we determine the content of the modal spectrum and obtain an eigenfunction expansion of the source-excited field in terms of discrete- and continuous-spectrum modes.

1. INTRODUCTION

Gyrotropic structures capable of guiding electromagnetic waves have been an important research topic for a long time because of many applications including, in particular, those related to the characteristics of whistler-mode waves in density ducts in laboratory and space plasmas, helicon waves in magnetized metals and semiconductors, waves in ferrites, modes of gyrotropic fibers, etc. The theory of excitation of closed waveguides filled with gyrotropic media has received much careful study, and there are many accounts of it (see, e.g., [1, 2] and references therein). Open gyrotropic waveguides surrounded by an isotropic outer medium have been discussed in [3]. Recently, open gyrotropic guiding structures located in a gyrotropic background medium have attracted considerable interest [4–6]. Several authors have discussed representations of the dyadic Green's functions for such structures [5]. Another approach is to obtain eigenfunction expansions of source-excited fields without preliminary calculations of the dyadic Green's functions [6, 7].

This paper extends methods, initially developed for representing source-excited electromagnetic fields in the presence of cylindrical guiding structures immersed in a gyroelectric medium [6, 7] such as a magnetoplasma, for example, to the case where spatially bounded, given sources are located in a gyrotropic medium whose permittivity and permeability are both describable by tensors with nonzero off-diagonal elements. The medium can be homogeneous or radially inhomogeneous inside a cylinder of given radius, and is homogeneous outside it. The axis of symmetry of such a cylindrically stratified structure is parallel to the gyrotropic axis of the medium.

2. FORMULATION OF THE PROBLEM AND BASIC EQUATIONS

Consider time-harmonic ($\sim \exp(i\omega t)$) given electric and magnetic currents with densities $\boldsymbol{j}^{\mathrm{e}}(\rho,\phi,z)$ and $\boldsymbol{j}^{\mathrm{m}}(\rho,\phi,z)$, respectively, in a gyrotropic medium described by the permittivity and permeability tensors

$$\boldsymbol{\varepsilon} = \epsilon_0 \begin{pmatrix} \varepsilon_1 & i\varepsilon_2 & 0 \\ -i\varepsilon_2 & \varepsilon_1 & 0 \\ 0 & 0 & \varepsilon_3 \end{pmatrix}, \qquad \boldsymbol{\mu} = \mu_0 \begin{pmatrix} \mu_1 & i\mu_2 & 0 \\ -i\mu_2 & \mu_1 & 0 \\ 0 & 0 & \mu_3 \end{pmatrix}, \tag{1}$$

where ρ, ϕ, and z are cylindrical coordinates and ϵ_0 and μ_0 are the electric and magnetic constants, respectively. Note that such tensors are typical of a general bigyrotropic anisotropic medium whose distinguished axis is parallel to the z axis. Let the elements of the tensors be functions only of the radial coordinate ρ for $\rho < a$ and constant for $\rho > a$, where a is the radius of the cylindrical structure considered. In what follows we denote the elements of the tensors $\boldsymbol{\varepsilon}$ and $\boldsymbol{\mu}$ in the inner region ($\rho < a$) and in the outer medium ($\rho > a$) by $\tilde{\varepsilon}_{1,2,3}$, $\tilde{\mu}_{1,2,3}$ and $\varepsilon_{1,2,3}$, $\mu_{1,2,3}$, respectively. We will consider only the case where $\varepsilon_1^{-1}\varepsilon_2 + \mu_1^{-1}\mu_2 \neq 0$. A peculiar case $\varepsilon_1^{-1}\varepsilon_2 = -\mu_1^{-1}\mu_2$ where the outer medium has the property of uniaxial anisotropy needs separate consideration and will not be discussed here.

Solutions of source-free Maxwell's equations in such a cylindrically stratified medium can be sought in terms of the vector functions

$$\begin{bmatrix} \boldsymbol{E}_{m,s,\alpha}(\boldsymbol{r},q) \\ \boldsymbol{H}_{m,s,\alpha}(\boldsymbol{r},q) \end{bmatrix} = \begin{bmatrix} \boldsymbol{E}_{m,s,\alpha}(\rho,q) \\ \boldsymbol{H}_{m,s,\alpha}(\rho,q) \end{bmatrix} \exp[-im\phi - ik_0 p_{s,\alpha}(q)z], \tag{2}$$

where k_0 is the wave number in free space, q is the normalized (to k_0) transverse wave number in the outer medium, m is the azimuthal index ($m = 0, \pm 1, \pm 2, \ldots$), the functions $p_{s,\alpha}(q)$ describe the dependence of p, the axial wave number normalized to k_0, on the transverse wave number q for two normal waves of the outer medium (hereafter, these waves are denoted by the subscript values $\alpha = 1$ and $\alpha = 2$), the subscript s designates the wave propagation direction ($s = -$ and $s = +$ denote waves propagating in the negative and positive directions of the z axis, respectively), and $\boldsymbol{E}_{m,s,\alpha}(\rho,q)$ and $\boldsymbol{H}_{m,s,\alpha}(\rho,q)$ are the vector wavefunctions describing the radial distribution of the field of an eigenwave corresponding to the transverse wave number q and the indices m, s, and α. The functions $p_{s,\alpha}(q)$ obey the relation $p_{+,\alpha}(q) \equiv p_\alpha(q) = -p_{-,\alpha}(q)$, where

$$\begin{aligned} p_\alpha(q) &= 2^{-1/2}\left[\tau_{\rm e}\kappa_{\rm e}^2 + \tau_{\rm m}\kappa_{\rm m}^2 + \tau_{\rm g}^2\kappa^2 - (\tau_{\rm e}+\tau_{\rm m})q^2 + \chi_\alpha R_p(q)\right]^{1/2}, \quad \chi_1 = -\chi_2 = -1, \\ R_p(q) &= \left\{(\tau_{\rm e}-\tau_{\rm m})^2 q^4 - 2\left[(\tau_{\rm e}+\tau_{\rm m})(\tau_{\rm e}\kappa_{\rm e}^2 + \tau_{\rm m}\kappa_{\rm m}^2 + \tau_{\rm g}^2\kappa^2) - 2\tau_{\rm e}\tau_{\rm m}(\kappa_{\rm e}^2+\kappa_{\rm m}^2)\right] q^2 \right. \\ &\quad \left. + (\tau_{\rm e}\kappa_{\rm e}^2 + \tau_{\rm m}\kappa_{\rm m}^2 + \tau_{\rm g}^2\kappa^2)^2 - 4\tau_{\rm e}\tau_{\rm m}\kappa_{\rm e}^2\kappa_{\rm m}^2\right\}^{1/2}. \end{aligned} \tag{3}$$

Here,

$$\begin{aligned} \tau_{\rm e} &= \frac{\varepsilon_1}{\varepsilon_3}, \quad \tau_{\rm m} = \frac{\mu_1}{\mu_3}, \quad \tau_{\rm g} = \frac{\varepsilon_2}{\varepsilon_1} + \frac{\mu_2}{\mu_1}, \\ \kappa_{\rm e} &= \left(\varepsilon_3 \frac{\mu_1^2 - \mu_2^2}{\mu_1}\right)^{1/2}, \quad \kappa_{\rm m} = \left(\mu_3 \frac{\varepsilon_1^2 - \varepsilon_2^2}{\varepsilon_1}\right)^{1/2}, \quad \kappa = (\varepsilon_1\mu_1)^{1/2} \end{aligned} \tag{4}$$

(see [8]). It is assumed that $\operatorname{Re} R_p(q) > 0$ and $\operatorname{Im} p_\alpha(q) < 0$.

The transverse components of the vector wavefunctions $\boldsymbol{E}_{m,s,\alpha}(\rho,q)$ and $\boldsymbol{H}_{m,s,\alpha}(\rho,q)$ are readily expressed in terms of their axial components $E_{z;m,s,\alpha}(\rho,q)$ and $H_{z;m,s,\alpha}(\rho,q)$. In the homogeneous outer medium ($\rho > a$), the components $E_{z;m,s,\alpha}(\rho,q)$ and $H_{z;m,s,\alpha}(\rho,q)$ satisfy the following system of equations:

$$\hat{L}_m E_{z;m,s,\alpha} + k_0^2(\kappa_{\rm e}^2 - \tau_{\rm e}^{-1}p_\alpha^2)E_{z;m,s,\alpha} = ik_0^2\tau_{\rm g}\mu_3 p_{s,\alpha} Z_0 H_{z;m,s,\alpha}, \tag{5}$$

$$\hat{L}_m H_{z;m,s,\alpha} + k_0^2(\kappa_{\rm m}^2 - \tau_{\rm m}^{-1}p_\alpha^2)H_{z;m,s,\alpha} = -ik_0^2\tau_{\rm g}\varepsilon_3 p_{s,\alpha} Z_0^{-1} E_{z;m,s,\alpha}, \tag{6}$$

where Z_0 is the impedance of free space and

$$\hat{L}_m = \frac{\partial^2}{\partial\rho^2} + \frac{1}{\rho}\frac{\partial}{\partial\rho} - \frac{m^2}{\rho^2}.$$

To find the eigenvalues q and the corresponding eigenwaves (2) it is required that the functions $\boldsymbol{E}_{m,s,\alpha}(\rho,q)$ and $\boldsymbol{H}_{m,s,\alpha}(\rho,q)$ obtained as a result of solution of Maxwell's equations be regular on the z axis and satisfy both the boundary conditions, which consist in the continuity of the components $E_{\phi;m,s,\alpha}(\rho,q)$, $E_{z;m,s,\alpha}(\rho,q)$, $H_{\phi;m,s,\alpha}(\rho,q)$, and $H_{z;m,s,\alpha}(\rho,q)$ at the discontinuity points of the permittivity- and permeability-tensor elements, and the following boundedness conditions at $\rho \to \infty$ [6]:

$$\rho^{1/2}\left|\boldsymbol{E}_{m,s,\alpha}(\rho,q)\right| < R_{m,\alpha}^{(1)}, \qquad \rho^{1/2}\left|\boldsymbol{H}_{m,s,\alpha}(\rho,q)\right| < R_{m,\alpha}^{(2)}, \tag{7}$$

where $R_{m,\alpha}^{(1)}$ and $R_{m,\alpha}^{(2)}$ are certain constants. It can be shown that the total field yielded by summing (integrating) eigenwaves over the found values of q satisfies the radiation condition at infinity ($r = (\rho^2+z^2)^{1/2} \to \infty$). We emphasize that conditions (7) turn out to be sufficient for finding the eigenvalues q and the corresponding eigenwaves in contrast to the case of an isotropic outer medium where, along with the boundedness conditions, certain additional conditions should be imposed on the desired fields of eigenwaves [3].

3. DISCRETE- AND CONTINUOUS-SPECTRUM MODES

Solving equations (5) and (6), we can write the axial field components in the outer medium as follows:

$$E_{z;m,s,\alpha}(\rho,q) = \frac{i}{\varepsilon_3}\Big[\sum_{k=1}^{2} C^{(k)}_{m,s,\alpha}(q) n^{(1)}_{s,\alpha} q H^{(k)}_m(k_0 q\rho) + C_{m,s,\alpha}(q) n^{(2)}_{s,\alpha} q_\alpha H^{(2)}_m(k_0 q_\alpha \rho)\Big],$$

$$H_{z;m,s,\alpha}(\rho,q) = -\frac{1}{Z_0\mu_3}\Big[\sum_{k=1}^{2} C^{(k)}_{m,s,\alpha}(q) q H^{(k)}_m(k_0 q\rho) + C_{m,s,\alpha}(q) q_\alpha H^{(2)}_m(k_0 q_\alpha \rho)\Big]. \tag{8}$$

Here, $C^{(1)}_{m,s,\alpha}$, $C^{(2)}_{m,s,\alpha}$, and $C_{m,s,\alpha}$ are coefficients to be determined and $H^{(1)}_m$ and $H^{(2)}_m$ are Hankel functions of the first and second kinds, respectively, of order m. Other quantities in (8) are given by the formulas

$$n^{(1,2)}_{s,\alpha}(q) = \Big[\mu_3^{-1}\big(q^{(1,2)}_\alpha\big)^2 + \mu_1^{-1} p^2_\alpha(q) + \varepsilon_1^{-1}(\varepsilon_2^2 - \varepsilon_1^2)\Big]\Big[\tau_{\rm g} p_{s,\alpha}(q)\Big]^{-1},$$

$$q^{(1)}_\alpha = q, \quad q^{(2)}_\alpha = q_\alpha(q) = \Big[\kappa^2_{\rm m} - \tau^{-1}_{\rm m} p^2_\alpha(q) - \varepsilon_3\tau_{\rm g} p_{s,\alpha}(q)\big(n^{(1)}_{s,\alpha}(q)\big)^{-1}\Big]^{1/2}. \tag{9}$$

In the above expressions, we put $\operatorname{Im} q_\alpha(q) < 0$. Because of such a choice of the branches of $q_\alpha(q)$, we rejected the solution comprising $H^{(1)}_m(k_0 q_\alpha\rho)$ to ensure that the functions $\boldsymbol{E}_{m,s,\alpha}(\rho,q)$ and $\boldsymbol{H}_{m,s,\alpha}(\rho,q)$ do not contradict the boundedness conditions (7).

If the medium in the inner region is homogeneous, then the axial field components for $\rho < a$ can be written as

$$E_{z;m,s,\alpha}(\rho,q) = \frac{i}{\tilde\varepsilon_3}\sum_{k=1}^{2} B^{(k)}_{m,s,\alpha}(q)\,\tilde n^{(k)}_{s,\alpha}\,\tilde q^{(k)}_\alpha J_m(k_0\tilde q^{(k)}_\alpha\rho),$$

$$H_{z;m,s,\alpha}(\rho,q) = -\frac{1}{Z_0\tilde\mu_3}\sum_{k=1}^{2} B^{(k)}_{m,s,\alpha}(q)\,\tilde q^{(k)}_\alpha J_m(k_0\tilde q^{(k)}_\alpha\rho). \tag{10}$$

Here, J_m are Bessel functions of the first kind of order m, $B^{(1)}_{m,s,\alpha}$ and $B^{(2)}_{m,s,\alpha}$ are coefficients to be determined, and $\tilde q^{(1)}_\alpha$ and $\tilde q^{(2)}_\alpha$ are the transverse wave numbers in the inner region, which correspond to the axial wave number $p_\alpha(q)$:

$$\tilde q^{(1,2)}_\alpha(q) = 2^{-1/2}\left[\tilde\kappa^2_{\rm e} + \tilde\kappa^2_{\rm m} - \big(\tilde\tau^{-1}_{\rm e} + \tilde\tau^{-1}_{\rm m}\big)p^2_\alpha(q) + \chi_{1,2}R_q\big(p_\alpha(q)\big)\right]^{1/2},$$

$$R_q(p) = \left\{\left(\frac{1}{\tilde\tau_{\rm e}} - \frac{1}{\tilde\tau_{\rm m}}\right)^2 p^4 - 2\left[\left(\frac{1}{\tilde\tau_{\rm e}} + \frac{1}{\tilde\tau_{\rm m}}\right)(\tilde\kappa^2_{\rm e} + \tilde\kappa^2_{\rm m}) - 2\left(\frac{\tilde\kappa^2_{\rm e}}{\tilde\tau_{\rm m}} + \frac{\tilde\kappa^2_{\rm m}}{\tilde\tau_{\rm e}} + \tilde\varepsilon_3\tilde\mu_3\tilde\tau^2_{\rm g}\right)\right]p^2 + \big(\tilde\kappa^2_{\rm e} - \tilde\kappa^2_{\rm m}\big)^2\right\}^{1/2}. \tag{11}$$

The quantities $\tilde\tau_{\rm e}$, $\tilde\tau_{\rm m}$, $\tilde\tau_{\rm g}$, $\tilde\kappa_{\rm e}$, $\tilde\kappa_{\rm m}$, and $\tilde n^{(1,2)}_{s,\alpha}$ are obtained from the formulas for $\tau_{\rm e}$, $\tau_{\rm m}$, $\tau_{\rm g}$, $\kappa_{\rm e}$, $\kappa_{\rm m}$, and $n^{(1,2)}_{s,\alpha}$ in (4) and (9) if we replace $\varepsilon_{1,2,3}$, $\mu_{1,2,3}$, and $q^{(1,2)}_\alpha$ by $\tilde\varepsilon_{1,2,3}$, $\tilde\mu_{1,2,3}$, and $\tilde q^{(1,2)}_\alpha$, respectively.

Calculating the transverse components of the field and satisfying the continuity conditions for the tangential field components on the boundary $\rho = a$, we arrive at a system of linear equations for unknown coefficients $B^{(1,2)}_{m,s,\alpha}$, $C^{(1,2)}_{m,s,\alpha}$, and $C_{m,s,\alpha}$. This system can thus be represented in matrix form:

$$\mathbf{S}\cdot\boldsymbol{G} = C^{(1)}_{m,s,\alpha}\boldsymbol{F}. \tag{12}$$

where the components of the column vector $\boldsymbol{G}$ are given by the expressions $G_{1,2} = B^{(1,2)}_{m,s,\alpha}$, $G_3 = C^{(2)}_{m,s,\alpha}$, and $G_4 = C_{m,s,\alpha}$. The elements of the matrix $\mathbf{S}$ and the components of the column vector $\boldsymbol{F}$, which are not written here, are expressed in terms of cylindrical functions entering the representations of the tangential fields at $\rho = a$. The coefficients $B^{(1,2)}_{m,s,\alpha}$, $C^{(1,2)}_{m,s,\alpha}$, and $C_{m,s,\alpha}$ are determined up to a factor independent of spatial coordinates. It is convenient to put $C^{(1)}_{m,s,\alpha} = \det|\mathbf{S}|$. Then other coefficients are easily calculated. Their expressions turn out to be very cumbersome and are not presented here for brevity.

In the case of an inhomogeneous inner region, two independent sets of solutions should be found numerically instead of those represented by Bessel functions in (10). The solutions of the two sets are distinguished by their behavior near the axis $\rho = 0$, in the vicinity of which they are described by Bessel functions with the arguments $k_0\tilde{q}^{(1)}_\alpha\rho$ or $k_0\tilde{q}^{(2)}_\alpha\rho$, where $\tilde{q}^{(1)}_\alpha$ and $\tilde{q}^{(2)}_\alpha$ correspond to the parameters of the medium at $\rho = 0$. Next, satisfying the boundary conditions at $\rho = a$, we again arrive at an equation in form (12).

The obtained field representation allows us to find the spectrum of eigenvalues q and the corresponding eigenfunctions of the guiding structure. First, it is easy to verify that the field (8) satisfies the boundedness conditions (7) for all real transverse wave numbers q. Next, based on the results of the analysis performed in [6], it can be shown that $\boldsymbol{E}_{m,s,\alpha}(\rho, q\exp(\pm i\pi)) = \boldsymbol{E}_{m,s,\alpha}(\rho, q)$ and $\boldsymbol{H}_{m,s,\alpha}(\rho, q\exp(\pm i\pi)) = \boldsymbol{H}_{m,s,\alpha}(\rho, q)$, whence it follows that the negative values of q can be excluded from the analysis. Thus, all positive values of q constitute the continuous eigenvalue spectrum.

Along with the continuous spectrum of the values of q, conditions (7) can also be satisfied for certain discrete complex values $q = q_{m,n}$ $(n = 1, 2, \ldots)$ which are roots of the equations

$$C^{(1)}_{m,s,\alpha}(q_{m,n}) = 0 \quad \text{for} \quad \operatorname{Im} q_{m,n} < 0 \tag{13}$$

and

$$C^{(2)}_{m,s,\alpha}(q_{m,n}) = 0 \quad \text{for} \quad \operatorname{Im} q_{m,n} > 0. \tag{14}$$

With allowance for the properties of Hankel functions, it can easily be verified that roots of equation (14) do not yield new solutions for the field and can therefore be rejected. As in the case of a gyroelectric medium [6, 7], we assume that the discrete part of the spectrum of eigenvalues q is constituted only by the roots of equation (13) for which the inequality $|\operatorname{Im} q_{m,n}| < |\operatorname{Im} q_\alpha(q_{m,n})|$ takes place (see [6] for details). The subscript α for which this inequality holds will be denoted by $\hat{\alpha}$. It is evident that the waves corresponding to the discrete values $q_{m,n}$ are localized eigenmodes (discrete-spectrum modes) of the considered guiding structure. The eigenmode fields are obtained by putting $q = q_{m,n}$ and $\alpha = \hat{\alpha}$ in (2) and will further be denoted as $\boldsymbol{E}_{m,n_s}(\boldsymbol{r})$ and $\boldsymbol{H}_{m,n_s}(\boldsymbol{r})$, where the indices $n_+ = n > 0$ and $n_- = -n < 0$ mark discrete-spectrum modes propagating in the positive and negative directions of the z axis, respectively.

4. EXPANSION OF THE TOTAL SOURCE-EXCITED FIELD IN TERMS OF DISCRETE- AND CONTINUOUS-SPECTRUM MODES

With allowance for the above analysis, the total field outside the source region can be expanded in the form

$$\begin{bmatrix}\boldsymbol{E}(\boldsymbol{r})\\ \boldsymbol{H}(\boldsymbol{r})\end{bmatrix} = \sum_{m=-\infty}^{\infty}\left(\sum_{n_s} a_{m,n_s}\begin{bmatrix}\boldsymbol{E}_{m,n_s}(\boldsymbol{r})\\ \boldsymbol{H}_{m,n_s}(\boldsymbol{r})\end{bmatrix} + \sum_\alpha\int_0^\infty a_{m,s,\alpha}(q)\begin{bmatrix}\boldsymbol{E}_{m,s,\alpha}(\boldsymbol{r},q)\\ \boldsymbol{H}_{m,s,\alpha}(\boldsymbol{r},q)\end{bmatrix} \mathrm{d}q\right), \tag{15}$$

where a_{m,n_s} and $a_{m,s,\alpha}$ are the expansion coefficients of the discrete- and continuous-spectrum modes, respectively. In (15), one should put $n_s = n > 0$ and $s = +$ for positive z and $n_s = -n$ and $s = -$ for negative z outside the source region.

The discrete- and continuous-spectrum modes entering expansion (15) satisfy some orthogonality relations. The orthogonality relations have precisely the same form as that obtained for open waveguides in a gyroelectric medium [6, 7] and can be established through a similar argument. Using the orthogonality relations and the well-known method for finding the expansion coefficients of modes of closed and open waveguides on the basis of Lorentz's theorem (see, e.g., [3, 6]), we get

$$a_{m,\pm n} = \frac{1}{N_{m,n}}\int\left[\boldsymbol{j}^{\mathrm{e}}(\boldsymbol{r})\cdot\boldsymbol{E}^{(\mathrm{T})}_{-m,\mp n}(\boldsymbol{r}) - \boldsymbol{j}^{\mathrm{m}}(\boldsymbol{r})\cdot\boldsymbol{H}^{(\mathrm{T})}_{-m,\mp n}(\boldsymbol{r})\right]\mathrm{d}\boldsymbol{r}, \tag{16}$$

$$a_{m,\pm,\alpha}(q) = \frac{1}{N_{m,\alpha}(q)}\int\left[\boldsymbol{j}^{\mathrm{e}}(\boldsymbol{r})\cdot\boldsymbol{E}^{(\mathrm{T})}_{-m,\mp,\alpha}(\boldsymbol{r},q) - \boldsymbol{j}^{\mathrm{m}}(\boldsymbol{r})\cdot\boldsymbol{H}^{(\mathrm{T})}_{-m,\mp,\alpha}(\boldsymbol{r},q)\right]\mathrm{d}\boldsymbol{r}. \tag{17}$$

Here, integration is performed over the region occupied by currents, the superscript (T) denotes fields taken in an auxiliary ("transposed") medium described by the transposed tensors $\boldsymbol{\varepsilon}^{\mathrm{T}}$ and $\boldsymbol{\mu}^{\mathrm{T}}$, and the normalization quantities for the corresponding modes are given by the formulas

$$N_{m,n} = 2\pi \int_0^\infty \left[\boldsymbol{E}_{m,n}(\boldsymbol{r}) \times \boldsymbol{H}^{(\mathrm{T})}_{-m,-n}(\boldsymbol{r}) - \boldsymbol{E}^{(\mathrm{T})}_{-m,-n}(\boldsymbol{r}) \times \boldsymbol{H}_{m,n}(\boldsymbol{r})\right] \cdot \hat{\boldsymbol{z}}_0 \, \rho \, \mathrm{d}\rho, \tag{18}$$

$$N_{m,\alpha}(q) = -\frac{16\pi}{Z_0 k_0^2} \left(\frac{\mathrm{d}p_\alpha(q)}{\mathrm{d}q}\right)^{-1} \left[\mu_3^{-1} + \varepsilon_3^{-1} \left(n^{(1)}_{s,\alpha}\right)^2\right] C^{(1)}_{m,s,\alpha}(q) C^{(2)}_{m,s,\alpha}(q). \tag{19}$$

It is worth nothing that the quantities $N_{m,n}$ and $N_{m,\alpha}(q)$ are related by

$$N_{m,n} = \frac{1}{2\pi i} \frac{\mathrm{d}N_{m,\hat{\alpha}}}{\mathrm{d}q}\bigg|_{q=q_{m,n}}. \tag{20}$$

For the sake of brevity, we do not present expressions for the field inside the source region since they can easily be found using the standard method described in [3, 6].

5. CONCLUSION

In this paper, we presented the complete eigenfunction expansion of the total electromagnetic field excited by spatially bounded given sources in a cylindrically stratified gyrotropic medium. The field has been expanded in terms of modes whose spectrum comprises both the discrete and continuous parts and the expansion coefficients of discrete- and continuous-spectrum modes have been calculated. Our analysis extends the theory of excitation of open waveguides in a gyroelectric medium [6, 7] to the case of open guiding structures located in a generalized gyrotropic medium whose permittivity and permeability are both described by tensors with nonzero off-diagonal elements. Although the problem of excitation of guiding structures in such a medium, also called bigyrotropic, can be solved using the dyadic Green's functions (see, e.g., [5]), the approach developed herein makes it possible to immediately obtain the source-excited field without preliminary calculation of the dyadic Green's functions, which significantly facilitates evaluation of the field.

ACKNOWLEDGMENT

This work was supported by the Russian Foundation for Basic Research (project No. 07–02–00436-a) and the Program for the State Support of the Leading Scientific Schools of the Russian Federation (project No. NSh–1087.2006.2).

REFERENCES

1. Felsen, L. B. and N. Marcuvitz, *Radiation and Scattering of Waves*, Prentice-Hall, Englewood Cliffs, 1973.
2. Liu, S., L. W. Li, M. S. Leong, and T. S. Yeo, "Theory of gyroelectric waveguides," *Progress In Electromagnetics Research*, PIER 29, 231–259, 2000.
3. Manenkov, A. B., "Irregular magneto-optical waveguides," *IEEE Trans. Microwave Theory Tech.*, Vol. MTT-29, No. 9, 906–910, 1981.
4. Manenkov, A. B., "Orthogonality relations for the eigenmodes of lossy anisotropic waveguides (fibres)," *IEE Proc.-J*, Vol. 140, No. 3, 206–212, 1993.
5. Tan, E. L. and S. Y. Tan, "Cylindrical vector wave function representations of the dyadic Green's functions for cylindrical multilayered gyrotropic bianisotropic media," *Progress In Electromagnetics Research*, PIER 26, 199–222, 2000.
6. Kondrat'ev, I. G., A. V. Kudrin, and T. M. Zaboronkova, *Electrodynamics of Density Ducts in Magnetized Plasmas*, Gordon and Breach, Amsterdam, 1999.
7. Zaboronkova, T. M., A. V. Kudrin, and M. Yu. Lyakh, "Excitation of nonsymmetric waves by given sources in a magnetoplasma in the presence of a cylindrical plasma channel," *Radiophys. Quantum Electron.*, Vol. 46, Nos. 5–6, 407–424, 2003.
8. Przeździecki, S. and R. A. Hurd, "Diffraction by a half plane perpendicular to the distinguished axis of a gyrotropic medium (oblique incidence)," *Can. J. Phys.*, Vol. 59, No. 3, 403–424, 1981.